Dissertation
submitted to the
Combined Faculties of the Natural Sciences and Mathematics
of the Ruperto-Carola-University of Heidelberg, Germany
for the degree of
Doctor of Natural Sciences

Put forward by
Andreas Dörr
born in: Filderstadt, Germany
Oral examination: January 21, 2015

PENTATRAP:
A novel Penning-trap system for high-precision mass measurements

Referees: Prof. Dr. Klaus Blaum
Prof. Dr. Selim Jochim

Abstract

The novel Penning-trap mass spectrometer PENTATRAP aims at mass-ratio determinations of medium-heavy to heavy ions with relative uncertainties below 10^{-11}. From the mass ratios of certain ion species, the corresponding mass differences will be determined with sub-eV/c^2 uncertainties. These mass differences are relevant for neutrino-mass experiments, a test of special relativity and tests of bound-state QED. Means to obtain the required precision are very stable trapping fields, the use of highly-charged ions produced by EBITs, a non-destructive cyclotron-frequency determination scheme employing detectors with single-ion sensitivity and a five-trap tower, that allows for measurement schemes being insensitive to magnetic field drifts.

Within this thesis, part of the detection electronics was set up and tested under experimental conditions. A single-trap setup was realized. A Faraday cup in the trap tower enabled the proper adjustment of the settings of the beamline connecting the EBIT and the Penning-trap system, resulting in the first trapping of ions at PENTATRAP. A stabilization of switched voltages in the beamline and detailed studies of ion bunch characteristics allowed for reproducible loading of only a few ions. Detection of the axial oscillation of the trapped ions gave hints that in some cases, even single ions had been trapped. Furthermore, valuable conclusions about necessary modifications of the setup could be drawn.

Zusammenfassung

Das neuartige Penningfallen-Massenspektrometer PENTATRAP hat die Bestimmung von Massenverhältnissen mittelschwerer bis schwerer Ionen mit relativen Ungenauigkeiten $< 10^{-11}$ zum Ziel. Mit den Massenverhältnissen bestimmter Ionen werden die entsprechenden Massendifferenzen mit sub-eV/c^2-Unsicherheiten bestimmt werden. Diese Massendifferenzen sind für Neutrinomassen-Experimente, einen Test der speziellen Relativitätstheorie und Tests der QED gebundener Zustände von Bedeutung. Die benötigte Präzision soll mit den folgenden Mitteln erreicht werden: Sehr stabile Speicherfelder, hochgeladene Ionen aus EBITs, ein nicht-destruktives Zyklotronfrequenzbestimmungsschema, welches Detektoren mit Einzelionensensitivität nutzt, und ein Fünffallenturm, der Messschemata ermöglicht, die insensitiv gegenüber Magnetfelddrifts sind.

Im Rahmen dieser Arbeit wurde ein Teil der Detektionselektronik aufgebaut und unter Experimentbedingung getestet. Ein Einzelfallenaufbau wurde realisiert. Mit Hilfe eines Faradaybechers im Fallenturm konnten die passenden Einstellungen der Strahlführung zwischen der EBIT und dem Penningfallenaufbau gefunden werden, was zum ersten Speichern von Ionen an PENTATRAP führte. Die Stabilisierung gepulster Spannungen in der Strahlführung und die detailierte Untersuchung der Eigenschaften von Ionenpaketen ermöglichte reproduzierbares Laden von nur wenigen Ionen. Der Nachweis axialer Oszillationen gefangener Ionen gab Hinweise darauf, dass in einigen Fällen sogar einzelne Ionen geladen worden waren. Zudem konnten wertvolle Schlüsse über notwendige Modifikationen des Aufbaus gezogen werden.

Contents

List of Figures

List of Tables

List of Abbreviations

AC	Alternating current
CE	Correction electrode
CS	Control system
DAC	Digital-to-analog converters
DC	Direct current
EBIT	Electron beam ion trap
EC	Endcap
FC	Faraday cup
FET	Field-effect transistor
FWHM	Full width at half maximum
HCI	Highly-charged ion
HV	High-voltage
LAN	Local area network
LCI	Low-charged ion
LHe	Liquid helium
LO	Local oscillator
MCP	Microchannel plate
MIVOC	Metal ions from the volatile compounds
PE	Protective earth
PnA	Pulse 'n' amplify
RE	Ring electrode
RF	Radio-frequency
SNR	Signal-to-noise ratio
TOF	Time of flight
VCA	Voltage-controlled amplifier

1. Introduction and motivation

1.1. A brief history of Penning traps

The intention of this introduction is to give a brief overview over the history of Penning traps, i.e. to discuss some high-precision Penning-trap measurements and the technical developments that enabled them (and which are in most cases still of relevance today). In the first ∼20 years, the field was mainly driven by measurements of the electron's magnetic moment. From around 1980 on, mass spectrometry became an additional driving force. Since then, the precision-limit of mass-ratio measurements with long-lived light isotopes has been pushed towards and in a few cases even beyond the 10^{-11}-barrier. Aim of the novel Penning-trap mass spectrometer PENTATRAP, which is the subject of this thesis, is to extend the range of ultra-high-precision mass-ratio measurements to medium-heavy and heavy isotopes.

The electron's anomalous magnetic moment In the 1950s, there was considerable interest in the electron's anomalous magnetic moment: QED calculations of the anomaly were advancing (see e.g. [1, 2]) and experiments tried to keep up with the precision of the theoretical predictions. Experimental values of μ_e at that time stemmed from indirect determinations via the electron-proton magnetic-moment ratio [3, 4] and the proton's magnetic moment [5, 6]. To complement these experimental efforts, Dehmelt decided to head for a direct determination of the magnetic moment of the free electron.

First g_e-determination using free electrons In his first experiment, Dehmelt used spin exchange collisions with polarized sodium atoms to detect spin-flips of free polarized electrons in an external magnetic field of strength B: Applying magnetic radiofrequency fields at the Larmor frequency $\nu_L = g_e \mu_B B/h$ changed the mean electron polarization and thus also the mean sodium polarization. This in turn altered the absorption of circularly polarized light from a sodium arc [7]. The g_e he obtained had a relative uncertainty of $3 \cdot 10^{-5}$ and was less precise than the indirectly determined values. Dehmelt's measurement was limited by the maximum usable time of 0.1 s after electron creation. This time was determined by the amount of argon buffer gas with which the glass bulb containing the sodium vapor was filled. A certain argon pressure was needed to keep the wall diffusion time of the electrons sufficiently long. On the other hand, interaction with the argon gas was the main electron-polarization relaxation mechanism, limiting the obtainable spin-flip signal.

Introduction of the Penning trap His search for a way to both reduce the argon pressure and obtain a sufficiently long observation time lead Dehmelt to build his first Penning trap[1] in 1959. He realized that the shift of the cyclotron frequency of an electron in a homogeneous magnetic field due to a superimposed quadrupolar electrostatic field would be independent of the position in the trap [10]. In this combination of fields, the electron motion is a superposition of three harmonic eigenmotions: A fast circular motion in the plane perpendicular to the magnetic field at the frequency ν_+, which is basically the cyclotron frequency ν_c being slightly reduced by the radial electrostatic field, an (axial) oscillation along the magnetic field lines at frequency ν_z, being determined by the electron's charge-to-mass ratio e/m_e and the depth of the electrostatic potential, and a slow circular (magnetron) drift in the radial plane at frequency ν_-, being mainly determined by the magnetic field strength and the radial electrostatic field strength.

First g_e-determination with electrons in a Penning trap In 1968 the first determination of g_e using electrons stored in a Penning trap was reported by Gräff, Major, Roeder and Werth [11]. Although the experimental precision of $\delta g_e/g_e \approx 2 \cdot 10^{-6}$ was not yet competitive compared to other techniques (for an overview see [12]), the principal capability of the Penning trap to confine charged particles to a small volume for extended time periods (several minutes) to carry out precision measurements had been proven. In this experiment, the cyclotron frequency of the electrons (as a measure of the magnetic field strength) was determined by searching for the frequencies, at which electric RF fields most effectively excited the eigenmotions of the electrons, leading to a loss of electrons from the trap. The oscillation amplitude of an externally excited LC-circuit connected between the endcaps[2] of the trap was used as a measure for the number of trapped electrons: Whenever the axial oscillation frequency of the electrons was tuned to the resonance frequency of the LC-circuit, the electrons effectively shorted the circuit, leading to an electron-number dependent damping of the circuit's oscillation (for details see [13]). The electron polarization and the Larmor frequency determination in this experiment still involved polarized sodium atoms.

Non-destructive bolometric detection Also in 1968, Dehmelt presented a novel detection technique to determine the eigenfrequencies of electrons in a Penning trap[3] [15]. In this technique, called *bolometric detection*, an LC-circuit is connected across the endcaps, which is not excited externally, but only by it's own thermal noise and the image current induced by the axial motion of the electron cloud, being tuned to the resonance frequency of the LC-circuit. Monitoring the integrated power on top of the LC-circuit while attempting to excite the eigenmotions of the electrons can be used to determine the eigenfrequencies: In case one of the eigenmotions is excited

---

[1] Dehmelt named the superposition of a homogeneous magnetic field and a quadrupolar electrostatic field "Penning trap" in recognition of the work of Frans Penning, inventor of the Penning pressure gauge [8]. The first one to recognize the trapping capability of this field configuration was John Pierce [9].

[2] The two endcap electrodes are enclosing the trapping volume in axial direction, i.e. in the direction of the magnetic field lines.

[3] Before, Dehmelt had applied a technique similar to the one described in [13] to probe the presence of electrons in RF traps (see e.g. [14]), and presumably also in Penning traps.

at the right frequency, the noise level of the LC-circuit rises. Collisions within the electron cloud lead to a coupling of the radial modes to the axial mode, which is necessary to determine the radial frequencies. A major benefit of this technique is that it is non-destructive, i.e. no electron loss is involved.

a_e-determination without atomic beam, isolation of a single electron and trap improvements In the following decade, huge progress was made within the group of Dehmelt towards a high-precision determination of g_e. In 1973 Walls and Stein published the results of their determination of the g_e-anomaly $a_e = (g_e - 2)/2 = (\nu_L - \nu_c)/\nu_c$ using an electron cloud stored in a cryogenic Penning trap[4] [16]. a_e was determined from the directly measured anomaly frequency $\nu_a = \nu_L - \nu_c$ and the cyclotron frequency ν_c. In contrast to [11], no atom beam was required for polarization and spin flip detection in their measurement scheme, which is described in the following. First, both spin states were equally populated within the cloud by a strong radial magnetic RF field at ν_L. Then it was attempted to couple the excited spins to the cloud's thermalized cyclotron motion by means of a radial magnetic RF field. Successful coupling at ν_a lead to a heating of the cyclotron motion, which could be detected bolometrically. The uncertainty $\delta a_e/a_e \approx 2.1 \cdot 10^{-5}$, corresponding to an uncertainty of $\delta g_e/g_e \approx 2.4 \cdot 10^{-8}$, was limited by space-charge effects. It was still an order of magnitude higher than the uncertainty of the at that time accepted value [17]. Also in 1973, Wineland, Ekstrom and Dehmelt succeeded in isolating a single electron, which paved the way towards a determination of g_e not being limited by space charge effects [18]. Another important improvement was the introduction of an additional set of electrodes to improve the harmonicity of the electrostatic trapping potential, allowing for a determination of the electrons' eigenfrequencies with greatly improved precision [19].

a_e-determination with a single electron, sideband cooling and continuous Stern-Gerlach-effect In 1976, Van Dyck, Ekstrom and Dehmelt published the result of their determination of a_e using a single electron [20]. This measurement had been enabled by two new methods, which addressed the fact that for a single electron there is no inherent coupling mechanism between the axial and the radial modes like collision-induced coupling in an electron cloud. The first new method was sideband coupling between the axial and the magnetron motion by means of suitably oriented RF fields at $\nu_z + \nu_-$ [21]. With this method, energy can be transferred between the magnetron mode and the axial mode (which is directly damped through an LC-circuit at 4 K), leading to a reduction of the magnetron radius. The second method was to superimpose a weak magnetic bottle directed in axial direction onto the homogeneous magnetic field to couple both the modified cyclotron motion and the electron's spin to the axial motion. An increase in the modified cyclotron energy (e.g. due to a resonant excitation) was then accompanied by a small axial frequency change and spin flips could be detected by small axial frequency jumps[5]. The uncertainty in this

---

[4] In fact, all following g_e-Penning-trap experiments were measuring a_e instead of g_e.

[5] This effect is commonly called *continuous Stern-Gerlach-effect.*

measurement was $\delta a_e/a_e \approx 4.3 \cdot 10^{-6}$, corresponding to $\delta g_e/g_e \approx 5.0 \cdot 10^{-9}$. Shortly after, a small change in the experimental procedure resulted in a massive precision enhancement ($\delta a_e/a_e \approx 1.7 \cdot 10^{-7}$, corresponding to $\delta g_e/g_e \approx 2.0 \cdot 10^{-10}$) [22].

Proton-electron mass ratio and the g-factor of the positron While early work in Penning traps was mainly focused on g_e, the field started to become wider. In 1978 Gärtner and Klempt used a Penning trap to determine the proton-electron mass ratio. For this purpose, they measured the cyclotron frequencies of both protons and electrons in the same trap. From the cyclotron frequency ratio they deduced the mass ratio with an uncertainty of $\sim 2.9 \cdot 10^{-6}$, mainly limited by space-charge effects in the determination of the proton-cyclotron frequency [23]. The determination of the eigenfrequencies in this experiment was still based on the RF-absorption technique that had been used in the g_e-factor determination of 1968 [11].

With some modifications to the setup of Gärtner and Klempt, the proton-electron mass ratio was measured again in 1980 by Gräff, Kalinowsky and Traut [24]. To determine the cyclotron frequencies, a novel technique was used: They applied RF excitations at different frequencies around $\nu_+ + \nu_-$ (which in an ideal trap is ν_c), ejected the particles and observed the time of flight (TOF) to a channelplate detector being placed outside the strong magnetic field. When the excitation was at the right frequency, the modified-cyclotron energy and thereby the orbital magnetic moment increased, leading to an acceleration in the magnetic field gradient on the way to detector[6]. Thus excitation at the right frequency led to a dip in the TOF-spectrum. The mass-ratio uncertainty of $\sim 6 \cdot 10^{-7}$ was mainly limited by a lack of understanding of the $\nu_c(e^-)$-resonance lineshape.

In 1981, Van Dyck and Schwinberg presented preliminary results of their determination of the proton-electron mass-ratio, using bolometric detection [25]. For the determination of the eigenfrequencies of the electron, they used their usual detection scheme involving a weak magnetic bottle and an axial detector. In the case of the proton, they used separate detectors for the axial and the modified cyclotron mode. The uncertainty of $1.4 \cdot 10^{-7}$ was mainly limited by the magnetic bottle in combination with the uncertainty of the agreement of the electrons' and the protons' center positions[7].

Also in 1981, Schwinberg, Van Dyck and Dehmelt published the result of their determination of the positron-g-factor, which had an uncertainty of only $5 \cdot 10^{-11}$ [27]. The result was in excellent agreement with a previously determined value of

---

[6] It is not clarified in [24] how the "excitation" at $\nu_+ + \nu_-$ leads to an increase in the modified cyclotron energy. For an "excitation" by quadrupolar coupling at this sideband, the magnetron motion must have been initially excited. For the protons it can be speculated, that the initial magnetron energy of the protons, being produced by electron impact on the trap surfaces, was sufficient. For the electrons, the broadening of the cyclotron resonance (several 10 kHz resonance width) was such that at the quoted magnetron frequency of 760 Hz probably coupling at both sidebands as well as direct excitation of the modified cyclotron frequency occurred simultaneously.

[7] In retrospect, this systematic shift was underestimated by a factor of 1/2 [26]. This already gave a hint of how difficult mass spectrometry with non-mass doublets can be in an inhomogeneous magnetic field.

g_e. Thus, a first high-precision test of CPT-invariance[8] had been carried out with Penning traps.

Detailed studies and an ultra-high-precision e^-/e^+-g-factor measurement In the following years, different properties of the Penning trap were studied in detail. For instance, eigenfrequency shifts due to a tilt between the electrostatic and the magnetic field were calculated and found to cancel perfectly in the so-called invariance theorem $\nu_c^2 = \nu_+^2 + \nu_z^2 + \nu_-^2$ [28]. Calculations of electrostatic properties of traps with hyperbolic electrodes and of traps with cylindrical and disk-electrodes were carried out. The interaction of the electron with the cavity being formed by the trap electrodes was investigated. In 1986, these and many more topics were summarized by Brown and Gabrielse in a review article [29].

In 1987, Van Dyck, Schwinberg and Dehmelt published the result of a new determination of the electron- and positron-g-factors [30]. Due to many major or minor improvements in the trap setup, in experimental procedures and in the theoretical understanding of the resonance lineshapes, they were able to measure the g-factors with an outstanding precision of $4.3 \cdot 10^{-12}$, being mainly limited by an uncertainty in the correction for cavity shifts, and to compare them with a precision of $2.1 \cdot 10^{-12}$. Still today, this is the most precise CPT-test with charged particles. The g-factors and detailed calculations were combined for a determination of the fine-structure constant that was unrivaled for many years [31]. Only two years later, Dehmelt received the Nobel prize. He shared half of the prize with Wolfgang Paul *"for the development of the ion trap technique"*. The other half went to Norman Ramsey [32].

New mass-spectrometry applications In 1986, a collaboration around Gabrielse succeeded in trapping antiprotons from the Low Energy Antiproton Ring at CERN [33]. This was the starting point for a series of technical developments and measurements heading towards a high-precision comparison of the charge-to-mass ratios of protons and antiprotons as a test of CPT-invariance (see Sec. 1.3). Furthermore it was a first crucial step towards the production of cold antihydrogen.

In 1987, Bollen *et al.* published the masses of several unstable isotopes that had been determined by Penning-trap mass spectrometry [34]. The different Rb- and Sr-isotopes, having lifetimes as short as 3.7 min, were provided by the on-line mass separator ISOLDE at CERN. Cyclotron frequencies were determined by the same TOF-method that had been used by Gräff *et al.* for the determination of the proton-electron mass ratio. Many more Penning-trap mass spectrometers for short-lived isotopes would be following, for instance SHIPTRAP at the SHIP velocity filter at GSI [35], JYFLTRAP at the IGISOL-facility of the University of Jyväskylä [36] or TITAN at the radioactive ion beam facility ISAC at TRIUMF [37]. Over the years, the limits of minimum required ion lifetime (as low as 8.8 ms [38]), of minimum required production yield (as low as one particle per minute [39]) and of mass resolution and experimental precision (improvements e.g. due to the use of highly-charged ions [37] or novel detection techniques [40]) have been pushed further and further. For a

---

[8] Invariance of physical processes under simultaneous charge conjugation, parity and time reversal

discussion of the manifold applications of high-precision mass measurements with short-lived isotopes, the reader is referred to [41].

Ultra-high-precision Penning-trap mass spectrometry Another field that made enormous progress at the end of the 1980's was ultra-high-precision Penning-trap mass spectrometry with stable or long-lived ions[9]. The experiments in this field can be separated into those using the destructive TOF detection technique and those using non-destructive image-current detection techniques. Early work on the former type of experiments was done by Gerz, Wilsdorf and Werth at Mainz around 1990 [42]. Around 1995, another experiment of this type, named SMILETRAP, was put into operation at Stockholm [43, 44]. In more recent years, several high-precision mass-ratio measurements with long-lived or stable isotopes have been performed at SHIPTRAP in offline mode [45, 46]. Some measurements that have been performed at SMILETRAP and SHIPTRAP will be discussed in Sec. 1.3.

The highest-precision mass- and mass-ratio measurements[10] have been carried out with single ions and non-destructive image-current detection techniques. In 1989, two groups reported on first mass/mass-ratio measurements of that type. The group of Pritchard at MIT reported on a mass-ratio measurement of the molecular ions CO^+ and N_2^+, where the mass ratio was determined with an uncertainty of $4 \cdot 10^{-10}$ [47]. The group of Van Dyck, operating the University of Washington Penning-trap mass spectrometer (UW-PTMS), reported a new proton mass with an uncertainty of $3 \cdot 10^{-9}$, which had been deduced from the mass ratio of protons and C^{4+}-ions[11] [48]. Both experiments were limited by magnetic field drifts[12]. In the following years, the two experiments followed quite different directions to reduce the influence of magnetic field instabilities. The MIT-group reduced the time to switch between two ion species in a mass-ratio measurement [49], and ultimately realized simultaneous cyclotron frequency determinations with one ion of each species trapped at the same time [50, 51]. The Van Dyck-group on the other hand put a lot of effort into the stabilization of the magnet, which allowed them to perform cyclotron frequency measurements with the same ion species for several 10 hours before switching to the other species [52].

The most precise mass or mass-ratio measurements with uncertainties near or below 10^{-11} have all been carried out with rather light ions (for a broader overview see [53] and references therein): The Van Dyck-group determined the masses of ^{16}O and ^{4}He with relative uncertainties of $1.2 \cdot 10^{-11}$ and $1.6 \cdot 10^{-11}$, respectively [54]. The MIT-

---

[9] From this point on, only developments in this field will be discussed. Important achievements in other fields, like the determination of bound-electron g-factors, improved determinations of the free-electron g-factor or determinations of the proton-g-factor will be discussed in Sec. 1.3.

[10] The distinction between mass and mass-ratio measurements is slightly artificial, since mass measurements are actually mass-ratio measurements with one ion serving as a mass reference.

[11] In these measurements, actually only one ν_c-determination was carried out with a single C^{4+}-ion. In the other ν_c-determinations, space charge shifts had to be accounted for.

[12] Although magnetic field drifts were a major issue back then and are an issue still today, one should not be misled to think, that the magnets in use are poorly engineered. The great success of Penning-trap mass spectrometry is based on the fact, that the mass of an ion can be linked to a frequency (which can be measured to high precision) that is extraordinarily stable due to the stability of the superconducting magnets in use.

group has determined the mass ratios m(CO^+)/m(N_2^+) [55], m($^{14}N_2^+$)/m($^{13}C_2^+H_2^+$) [51], m($^{33}S^+$)/m($^{32}SH^+$) and m($^{29}Si^+$)/m($^{28}SiH^+$) [56] with relative uncertainties of $1.5 \cdot 10^{-11}$, $7 \cdot 10^{-12}$, $8.9 \cdot 10^{-12}$ and $6.5 \cdot 10^{-12}$, respectively.

PENTATRAP – extending the range of ultra-high-precision mass-ratio measurements to medium-heavy and heavy isotopes As will be discussed in Sec. 1.4, ultra-high-precision mass ratios of medium-heavy to heavy isotopes are required in many different applications. It is planned to determine the required mass ratios with the novel Penning-trap mass spectrometer PENTATRAP, which is the subject of this thesis, with relative uncertainties below 10^{-11}. Currently, there are only two experiments worldwide that have demonstrated the capability to perform mass-ratio measurements at this level of precision, namely THe-Trap (the former UW-PTMS), being situated like PENTATRAP at the Max-Planck-Institut für Kernphysik in Heidelberg and FSU-Trap (the former MIT-Trap), being situated at the Florida State University in Tallahassee. However, for both experiments mass-ratio determinations with relative uncertainties around or below 10^{-11} are currently restricted to light ions. One reason for this is that high ion charge states are required with present techniques to perform mass-ratio determinations with medium-heavy or heavy ions at this level of uncertainty, as will be outlined below. Neither THe-Trap nor FSU-Trap currently has access to highly-charged ions.

To perform mass-ratio determinations with medium-heavy or heavy ions with the aimed-at uncertainties is challenging: As will be discussed in detail in Sec. 3.2.1, a high-precision mass-ratio measurement with current state-of-the-art techniques requires that the cyclotron frequency of the ion is at least one order of magnitude larger than the axial frequency. For technical reasons, axial frequencies cannot be much lower than a few 100 kHz when image-current detection is applied. Thus, cyclotron frequencies should be at least several MHz or preferably, a few ten MHz. At PENTATRAP, a superconducting magnet with a field strength of 7 T will be employed, leading to a cyclotron frequency of $\sim 107.5 \frac{q}{m}$ MHz, where q is the charge state of the ion and m the ion's mass in atomic units. Since not much higher field strength can be obtained with commercial superconducting magnets, high charge states are required to obtain cyclotron frequencies of a few ten MHz with heavy ions. In the case of PENTATRAP, these ions will be delivered by electron-beam ion traps. Due to Coulomb interaction between the ions, the very elegant method of performing simultaneous cyclotron frequency determinations with both ions of interest in one trap to suppress magnetic field fluctuations is not applicable with highly-charged ions. At PENTATRAP, it was thus decided to employ two complementary strategies to reduce the influence of magnetic field fluctuations: First of all, various measures are taken to minimize the fluctuations (see Sec. 3.4.1). Second, simultaneous cyclotron frequency measurements in two traps of a five-trap tower will be used to further suppress the influence of the fluctuations. The combination of access to highly-charged heavy ions, simultaneous cyclotron frequency measurements, highly-stable magnetic as well as electrostatic trapping fields and detections systems with single-ion sensitivity open up very exciting perspectives.

1.2. Outline of the thesis

The thesis is organized as follows: Within the rest of this chapter, an overview over Penning-trap measurements for fundamental studies is given. In the last part of the chapter, fundamental studies requiring ultra-high-precision mass-ratio measurements with medium-heavy to heavy elements are presented. In Chapter 2, the properties of ideal Penning traps and the imperfections of real Penning traps will be discussed. Chapter 3 provides a detailed overview over the experimental setup: In Sec. 3.2, the necessity to use highly-charged ions and their production are discussed. Sec. 3.3 addresses the beamline for the transport of ions from the source to the Penning traps as well as related diagnostic tools. In Sec. 3.4, the actual Penning trap setup is introduced. Particular emphasis is laid on possible implementations and implications of simultaneous cyclotron-frequency determinations in two traps of the five-trap setup and on the detection system which was partly set up within this thesis. Furthermore modifications of the setup due to conclusions that were drawn from first commissioning experiments are outlined. During these experiments, which were carried out within the framework of this thesis and which are described in Chapter 4, first trapping of ions was realized. Sec. 4.1 focuses on the transport studies that enabled a reliable loading of only a few to single ions. Sec. 4.2 describes measurements that were carried out with trapped ions and discusses limitations of these measurements. The thesis is concluded with a summary and an outlook in Chapter 5.

1.3. Penning traps for fundamental studies

It has been outlined in Sec. 1.1 that Penning traps are perfectly suited for many fundamental studies. Main reasons for that are the connection between fundamental quantities (like masses or g-factors) and highly-stable frequencies and the ability to measure these frequencies very accurately and precisely. The last point is closely related to the fact, that these measurements can be carried out with single particles at very low energies. In the following, a selection of fundamental studies that were/will be carried out with or with the aid of Penning traps is presented.

1.3.1. Tests of quantum electrodynamics

g-factor Penning-trap experiments and QED-calculations have been challenging each other for several decades now to reach higher and higher precisions.

The g-factor of the electron After the e^-/e^+-g-factor measurement published by the Dehmelt-group in 1987 [30], it took nearly 20 years, until the experimental uncertainty in the determination of g_e could be improved by the Gabrielse-group [57]. In 2008, the same group published a further improved value [58]. In this work an uncertainty of $\delta g_e/g_e \approx 2.8 \cdot 10^{-13}$ was reached, being limited by a (not fully understood) lineshape broadening and the widths of the resonances due to the thermal axial motion. Together with a high-precision calculation of g_e, having a similar uncertainty, a new value of the fine-structure constant α was determined which had an uncertainty of $3.7 \cdot 10^{-10}$. This value of α has the highest weight of all values contributing to the currently accepted α [59]. The technical developments that enabled this precise measurement are summarized in [60]. Attempts to further improve the measurement are in preparation [61, 62].

A further improved value of g_e in combination with an even higher-order QED calculation [63] could be used for an even more precise determination of α. On the other hand, with an independent determination of α (see Sec. 1.3.3) Standard Model predictions of g_e could be put at test. In [64] for instance it is pointed out that a slightly more precise determination of a_e in combination with an independent value of α could be used to test whether certain non-Standard Model contributions to the muon g-factor anomaly a_μ also contribute to a_e[13].

g-factors of bound electrons Bound-electron g-factors are altered compared to the free-electron g-factor by the interaction of the electron with the nucleus and the electron shell. Particularly interesting are bound-state g-factors in highly-charged ions, because already for rather light isotopes the electric field strength at the position of the electron exceeds the field strengths that can be obtained in the laboratory e.g. with intense lasers [65]. Furthermore, calculations on few-electron systems can be performed with high precision.

In bound-state-g-factor Penning-trap experiments, the g-factor anomaly is not directly accessible. The measurable quantities are the Larmor-frequency of the bound electron and the cyclotron frequency of the ion. The g-factor is then given by

$$g = \frac{\nu_L}{\nu_c} \frac{q}{e} \frac{m_e}{M_\text{ion}}, \tag{1.1}$$

where q is the charge of the ion and M_ion is its mass. A measurement of the g-factor of the 1s-electron in hydrogen-like $^{28}\text{Si}^{13+}$ with an uncertainty of $4 \cdot 10^{-10}$, which is in excellent agreement with the theoretical value, is to date the most stringent test of bound-state QED [66]. The uncertainty was at the time of the publication limited by the uncertainty in m_e. This measurement, as well as other noteworthy bound-electron g-factor experiments (for instance the most precise test of bound-state QED calculations for a lithiumlike ion [67] or the most precise determination of the electron mass (see below)) were carried out at the University of Mainz.

Future g-factor experiments like ALPHATRAP at MPIK [68] or ARTEMIS at GSI [69] will perform g-factor measurements with heavy highly-charged ions, thus putting QED at test in even stronger electromagnetic fields.

1.3.2. Neutrino-physics related studies

Since the first observation of neutrino oscillations [70] it is known that neutrinos are massive particles, which is in contrast to the predictions of the standard model. However, from neutrino oscillation experiments only squared mass-differences between the three mass-eigenstates can be deduced and the absolute mass scale of the neutrino

---

[13] This is of course only under the assumption that the discrepancy between $a_\mu(\text{exp})$ and $a_\mu(\text{SM})$ is due to non-SM physics and not due to some systematic errors in previous a_μ measurements.

masses is still unclear [71]. Another important question is which non-Standard Model mechanism leads to finite neutrino masses. This finally leads to the question whether neutrinos are Majorana- or Dirac-particles [71].

Investigations of the mass of electron (anti-) neutrinos The most direct way to determine the mass (or an upper mass-limit) of the electron (anti)neutrino is to study for a β^--decay or an electron capture-transition the probability density function of the energy of all final-state particles but the emitted neutrino. A finite neutrino mass alters the shape of the spectrum. The most pronounced effect can be found near the endpoint of the spectrum - only there, the mass gives a significant contribution to the energy $\sqrt{p^2c^2 + m^2c^4}$ of the neutrino.

The most investigated decay for this purpose is the β^--decay of tritium. For some time it was thought, that a determination of the $\bar{\nu}_e$-mass could be carried out by determining the endpoint of the β-spectrum (with the spectrum being obtained by a kinematic analysis of the emitted electrons) and subtracting it from the ^{3}H-^{3}He mass difference[14]. However, the smallness of the neutrino mass and the tiny event rates near the endpoint of the kinetic energy spectrum prohibit a precise enough direct determination of the endpoint [73]. Instead one has to perform a fit of the theoretical lineshape to the data near the endpoint of the spectrum to extract the neutrino mass. This however changes the role of an independent Q-value, that can be measured by Penning-trap mass spectrometry[15]: In [73] it was shown, that an uncertainty of the independent Q-value of below 5 meV would be needed to increase the sensitivity of the next-generation β-spectrometer KATRIN, that aims at a neutrino-mass sensitivity of 0.2 eV/c^2. But even if an independent Q-value is not precise enough to increase the sensitivity of a β-spectrometer, it might still serve for calibration purposes (see below).

The tritium-helium Q-value determination has so far been carried out with two Penning-trap mass spectrometers, namely the UW-PTMS and SMILETRAP. The measured Q-values had uncertainties of 1.7 eV [74] and 1.2 eV [75], respectively. This however was not precise enough to influence the sensitivity of the to-date most precise β-spectrometers that established an upper $\bar{\nu}_e$ mass-limit of 2.3 eV/c^2 (see [73] and references therein). Efforts towards a more precise Q-value are underway at the MPIK, where the UW-PTMS setup was moved in 2008 [76]. While an uncertainty of the Q-value of 5 meV currently seems to be out of reach, an uncertainty of 30 meV seems feasible. This would constitute a sensible calibration check of critical voltages

---

[14] In his biography, 2001 Nobel laureate Eric Cornell, one of the first Ph.D. students at the MIT-trap, recalls: *"In the spring of 1985, shopping around for a graduate school and a research project, I met Dave Pritchard at MIT. He spun me a wonderful yarn: by very precisely measuring the mass difference between the helium-3 and tritium, one can determine the total amount of energy released in the beta decay of tritium. Combine this mass measurement with a determination (no big deal, Dave implied) of the endpoint of the beta-ray spectrum, and one has measured the rest mass of the electron neutrino! There were hints, in those days, that the neutrino might have a rest mass as large as ten eV, a value of cosmological significance."* [72].

[15] Q-values and mass ratios are linked as follows: $Q = m_1 - m_2 = m_2(\frac{m_1}{m_2} - 1)$. In the last term, the quantity that needs to be determined with highest precision is the mass ratio, whereas the absolute mass usually has to be known with much smaller precision.

in the KATRIN-experiment [73].

Alternatives to the tritium β-decay, namely the β-decay ^{187}Re$\rightarrow^{187}$Os and the electron capture-transition ^{163}Ho$\rightarrow^{163}$Dy, and the role of high-precision Pennning-trap mass spectrometry in neutrino-mass experiments planning to employ these transitions will be discussed in Sec. 1.4.

Are neutrinos Majorana- or Dirac-particles? As pointed out before, one fundamental question in neutrino physics is, whether neutrinos are Majorana- or Dirac-particles. In the former case, neutrinos would be their own antiparticles, while in the latter case, they would not. A large number of experiments try to answer this question by searching for indications of neutrinoless double-beta decays ($0\nu 2\beta$) [77]. Precise knowledge of the Q-value is very helpful in the search for $0\nu 2\beta$-decays, since this would be the energy of the two emitted electrons. In case of the ^{76}Ge$\rightarrow^{76}$Se-decay, which is a very promising candidate for the $0\nu 2\beta$-search, the Q-value was determined by means of Penning-trap mass spectrometry with an uncertainty of only 7 eV [78].

An interesting alternative to $0\nu 2\beta$-decays are neutrinoless double-electron capture (0ν2EC) transitions. However, lifetimes of these transitions are only experimentally attractive, when the decay rates are resonantly enhanced by a degeneracy of the initial and the final excited states [79]. To decide upon the suitability of a candidate for 0ν2EC, the Q-value (among other things) has to be known precisely. Therefore, numerous Q-value measurements were carried out by four Penning-trap mass spectrometers: SHIPTRAP, TRIGATRAP, JYFLTRAP and FSU-Trap (see [45] and references therein). One possible candidate is ^{152}Gd$\rightarrow^{152}$Sm, which would have a half-life of less than 10^{27} years for an effective Majorana neutrino mass of 1 eV. In comparison, the GERDA experiment was recently able to determine the half-live of the $0\nu 2\beta$-transition in ^{76}Ge to be larger than $2.1 \cdot 10^{25}$ years [80].

1.3.3. Determination of fundamental constants

The ability to perform high-precision g-factor and mass-ratio measurements makes Penning traps a valuable tool for the determination of different fundamental constants.

The mass of the electron The mass of the electron m_e has been determined with Penning traps both by means of direct mass measurements as well as by bound-electron g-factor measurements. The most precise direct mass measurement dates back to 1995: The van Dyck-group compared the cyclotron-frequencies of a single C^{6+}-ion and a small cloud of electrons. The uncertainty in m_e was $2.2 \cdot 10^{-9}$, limited, among other factors, by cloud effects [81].

An alternative way to determine m_e opened up with the introduction of high-precision bound-electron g-factor measurements in Penning traps. It can be seen from Eq. (1.1) that m_e can be derived from the g-factor, the ion's mass and the Larmor- to cyclotron-frequency ratio. Since the g-factors of electrons in hydrogenlike ions can be calculated to high precision and with high accuracy within the framework of QED, the g-factors come from theory. The latest determination of this kind yielded an uncertainty of only $3 \cdot 10^{-11}$ for m_e, limited by statistical uncertainty [82]. This improved value of m_e allows, among other things, for a very precise determination of α (see below) and even more precise comparisons of calculated and measured bound-electron g-factors in highly-charged ions.

The fine-structure constant As pointed out in Sec. 1.3.1, the most precise determination of α was obtained by comparing a high-precision determination of the electron g-factor anomaly and the corresponding QED-calculations [58, 63]. From this side, further improvements can be expected [61, 62].

The second most precise determination of α is based on the relation [83]

$$\alpha^2 = \frac{2R_\infty}{c}\frac{m_{\mathrm{Rb}}}{m_e}\frac{h}{m_{\mathrm{Rb}}}. \tag{1.2}$$

Thus α can be obtained from high-precision measurements of the Rydberg constant R_∞, the mass of the electron m_e, the mass of ^{87}Rb and the ratio h/m_{Rb}, with h being Planck's constant. In [83], a new value of h/m_{Rb} was reported, that was obtained by measuring the recoil velocity $\hbar k/m_{\mathrm{Rb}}$ of Rb-atoms after having absorbed a photon of momentum $\hbar k$. The relative uncertainty of the determined value of h/m_{Rb} of $6.3 \cdot 10^{-10}$ was the limiting factor in the resulting determination of α. The above discussed extremely precise determination of m_e has ensured, that even with massive progress in the recoil measurements, the precision of m_e won't be a limitation. The quantity with the second-highest relative uncertainty of $1.2 \cdot 10^{-10}$ is the mass of ^{87}Rb [84]. Although still being a factor of five better than the uncertainty in h/m_{Rb}, a mass determination with a relative uncertainty comparable to that of m_e would ensure that it won't become the major limitation in such a determination of α in the near future.

In [85], the possibility to determine α by means of differences in bound-electron g-factors of B- and H-like ions of certain heavy isotopes is discussed. Experimental input could be provided by the ALPHATRAP-experiment.

1.3.4. Tests of special relativity

Many Penning-trap mass spectrometry applications implicitly use Einstein's famous equation [86]

$$E = mc^2, \tag{1.3}$$

e.g. when nuclear binding energies are deduced from mass differences. In other applications, the equation is used the other way around: For instance, the masses of many short-lived isotopes are determined from energy releases in nuclear decays. If on the other hand, both mass differences and binding energies are available, the equation can be put to the test.

The most precise test of this kind was performed by determining the sums of energies of γ-rays emitted after neutron captures in ^{28}Si and ^{32}S and comparing them with the mass differences[16] $m(^{28}\mathrm{Si}) + m(\mathrm{n}) - m(^{29}\mathrm{Si})$ and $m(^{32}\mathrm{S}) + m(\mathrm{n}) - m(^{33}\mathrm{S})$, respectively

---

[16] To clarify the experimental idea, the description of the experiment is slightly simplified. Since the neutron is a neutral particle, its mass cannot be determined to high precision by means of standard mass-spectrometry methods. Instead, the neutron mass has to be determined from the

[56]. The γ-ray wavelengths were measured with the crystal Bragg spectrometer *GAMS4* at ILL, Grenoble. The mass differences of the silicon- and sulphur-isotopes were determined by means of Penning-trap mass spectrometry[17], using the MIT-Trap. The final result yielded a precision of $4.4 \cdot 10^{-7}$, being limited by the precision of γ-ray measurements. Besides confirming Eq. (1.3) on the obtained level of precision, the result can also be interpreted as a test of the assumption of special relativity, that the limiting velocity for matter c_{mat} (entering Eq. (1.3) as Δmc^2_{mat}) equals the speed of electromagnetic waves in vacuum c_{em} (entering Eq. (1.3) as hc_{em}/λ) [87].

1.3.5. Tests of CPT-invariance

One implication of the CPT-theorem is, that the charge-to-mass ratio and the magnetic moment of a particle and its antiparticle should be of equal magnitude with opposite sign [88]. Any violation of this prediction could be a hint towards an explanation for the matter-antimatter-asymmetry in the universe.

Comparison of the magnetic moments of electrons and positrons The most precise test of CPT-invariance in the lepton sector has been carried out by comparing the g-factors of electrons and positrons in a Penning trap, as described in Sec. 1.1. The comparison yielded $g(e^-)/g(e^+) = 1 + (0.5 \pm 2.1) \cdot 10^{-12}$ [30]. A new comparison of $g(e^-)$ and $g(e^+)$ is underway [61, 62].

Comparison of the q/m of the proton and the antiproton The most precise test of CPT-invariance in the baryon sector has been carried out by comparing the charge-to-mass ratios of p and $\bar{p}$. The most precise comparison was actually carried out with a $\bar{p}$ and an H$^-$-ion to avoid systematic shifts related to the reversal of the trapping potential. With corrections for the electrons in H$^-$, a q/m-ratio between $\bar{p}$ and p of $-0.99999999991(9)$ was stated [89]. Some years later, the published value had to be corrected to $-0.99999999984(9)$ [90] since a shift due to the polarizability of the H$^-$-ion had been overlooked [55]. This result certainly calls for a new comparison with improved precision, which could be carried out by the two groups heading for a high-precision comparison of the magnetic moments of p and $\bar{p}$ (see below).

Comparison of the magnetic moments of the proton and the antiproton Another possible test of CPT-invariance in the baryon sector is to compare the magnetic moments of p and $\bar{p}$. Two groups, BASE [91] and ATRAP, are aiming for a comparison on the 10^{-9}-level. These measurements are particularly challenging due to the smallness of the $p/\bar{p}$ magnetic moments compared to the e^-/e^+ magnetic moments. While the BASE-group succeeded in determining g_p with an uncertainty of only $3.3 \cdot 10^{-9}$ [92],

---

mass difference between deuterium and hydrogen (or two other suitable isotopes) with a binding energy correction determined by a neutron capture/γ-ray spectroscopy experiment. Thus on the mass side of the comparison, there is actually m(D)-m(H) instead of m(n), and on the γ-ray side, the neutron binding energy in deuterium has to be subtracted.

[17] Actually, the mass-ratio measurements were not carried out with ^{28}Si$^+$ and ^{32}S$^+$, but with ^{28}SiH$^+$ and ^{32}SH$^+$ in order to have mass-doublets.

the ATRAP-group was already able to perform a $g_{\bar{p}}$ measurement (with an uncertainty of $4.4 \cdot 10^{-6}$) [93].

1.4. Applications of ultra-high-precision mass ratios of medium-heavy to heavy isotopes

The novel PENTATRAP setup will offer the unique possibility to perform mass-ratio measurements with uncertainties below 10^{-11} even with medium-heavy to heavy isotopes. In the following, some applications requiring such ultra-high-precision mass ratios are presented.

1.4.1. Neutrino mass investigations

The β-decay of ^{187}Re As mentioned in Sec. 1.3 the β-decay of ^{187}Re to ^{187}Os is a promising alternative to the tritium β-decay for direct neutrino mass investigations. The decay is promising insofar as it has a Q-value of only $\sim$2.5 keV, compared to a tritium Q-value of $\sim$18.6 keV, and the number of decays in an energy range ΔE below the endpoint (where the sensitivity to $m(\bar{\nu}_e)$ is the largest) scales as $(\Delta E/Q)^3$ [94]. However, since ^{187}Re has a half-life of 43.3 billion years [95] the required source mass is too big for a kinematic analysis of emitted electrons. Instead, a calorimetric[18] detection of the kinetic energy of the recoiling nucleus and the emitted electron can be used to determine the β-spectrum. The so far most precise determination of an upper bound of $m(\bar{\nu}_e)$ from the β-decay of ^{187}Re was carried out with cryogenic microcalorimeters and yielded $m(\bar{\nu}_e) \leq 15$ eV (90 % confidence limit) [96].

The MARE[19]-project plans to set up a large-scale ^{187}Re microcalorimeter array with a sensitivity to $m(\bar{\nu}_e)$ of at least 0.2 eV/c^2 [94]. After an initial R&D-phase, recently the first phase of the experiment has started. In this phase it should be possible to obtain an upper bound of $m(\bar{\nu}_e)$ of a few eV/c^2 [97].

Penning-trap mass spectrometry can support these efforts by Q-value measurements on two different precision scales: With a precision of a few 10 eV, a long-standing discrepancy of the Q-values determined by microcalorimeters and the Q-values determined by proportional counters can be resolved (see [98] and references therein). Recently, the case was decided in favor of the microcalorimeters by a mass-ratio determination at SHIPTRAP. The resulting Q-value had an uncertainty of only 34 eV [46]. As the statistical sensitivity of MARE to $m(\bar{\nu}_e)$ has a strong Q-dependence, the new Q-value allows for proper dimensioning of the experiment concerning the number of arrays and the measurement time needed.

The final goal of the MARE-experiment will be supported by PENTATRAP by determining the Q-value with an uncertainty of 1 eV or less. Thus a measurement of the mass ratio $R = m(^{187}\mathrm{Re}^{q+})/m(^{187}\mathrm{Os}^{q+}) = (m(^{187}\mathrm{Os}^{q+}) + Q'/c^2)/m(^{187}\mathrm{Os}^{q+})$

---

[18] Calorimeters determine the change of the temperature of an absorber due to energy being deposited in the absorber e.g. by charged particles or photons. From the temperature change the total energy deposited in the absorber can be deduced.

[19] Microcalorimeter Arrays for a Rhenium Experiment

with a highly challenging relative uncertainty of

$$\frac{\delta R}{R} = \frac{\delta Q / m(^{187}\mathrm{Os}^{q+})c^2}{R} = \frac{\delta Q}{m(^{187}\mathrm{Re}^{q+})c^2} \leq 5.7 \cdot 10^{-12} \tag{1.4}$$

will have to be carried out. The mass difference Q' between the highly-charged rhenium- and osmium-ions will have to be corrected for binding energy differences to finally obtain the neutral Q-value that is relevant for the microcalorimetric β-decay study. Whether the Q-value obtained by PENTATRAP will be used as a systematics check or will serve as a fixed parameter in a lineshape fit to increase the statistical sensitivity to $m(\bar{\nu}_e)$ will strongly depend on both the final precision obtained by PENTATRAP and the final sensitivity of MARE.

The MARE-collaboration is currently focusing on feasibility studies for a new experiment employing the electron capture in ^{163}Ho for placing bounds on $m(\nu_e)$ (see next paragraph) [97, 99]. Whether the original plans with ^{187}Re will be further pursued will probably depend on the outcome of these studies.

The electron capture in ^{163}Ho Another alternative to the tritium β-decay for neutrino mass studies is the electron capture in ^{163}Ho. In this process, the nucleus captures an electron from the shell which leads to a transition of a proton to a neutron, leading to a ^{163}Dy-nucleus. The excited shell de-excites consecutively, for instance by emission of X-rays or Auger electrons. The spectrum of the total de-excitation- and recoil-energy is influenced by $m(\nu)$ in a similar fashion as in the case of β^--decays. Appealing features of this transition are a small Q-value[20] of around 2.5 keV and a (compared to ^{187}Re) short lifetime of only 4570 years [95].

Cryogenic microcalorimeters are particularly suitable for the determination of the de-excitation/recoil energy spectrum, since they directly measure the sum of all energies in the de-excitation process. There are two major advantages of ^{163}Ho over ^{187}Re for the use in neutrino mass studies with microcalorimeters:

1. The ^{163}Ho-lifetime is much shorter than the ^{187}Re-lifetime. Thus much less source material is needed to obtain the same number of events within a certain time interval [97]. In contrast to ^{187}Re, the source material does not have to be part of the absorber, so that the absorber material can be chosen freely. Furthermore, absorbers can be much smaller without a degradation of the decay rate per absorber [97, 99, 101]. Smaller absorbers have less heat capacity and are thus more sensitive.

2. The ^{163}Ho-spectrum shows sharp de-excitation lines and is thus self-calibrating, while calibration by means of external sources is needed to properly assign energies in the ^{187}Re-spectrum [97].

---

[20] In the case of ^{163}Ho, there is no simple Q-scaling of the statistical $m(\nu_e)$-sensitivity of the near-endpoint spectrum as in the case of ^{187}Re. This is due to a resonant enhancement of the sensitivity in case the Q-value is close to the highest-energy de-excitation line [100].

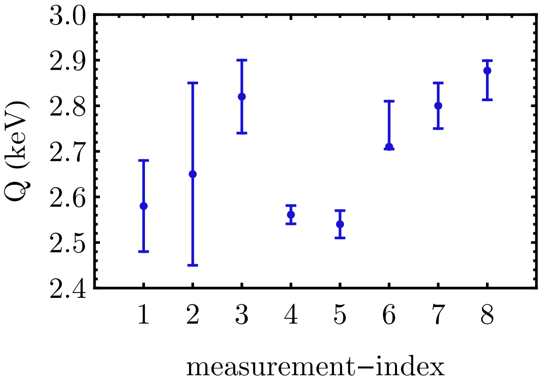

Figure 1.1.: Some Q-values of the electron capture in ^{163}Ho reported in the literature are shown (see [98] and references therein as well as [102]).

The feasibility of a large-scale ^{163}Ho experiment is currently investigated by two groups/collaborations, namely ECHo[21] and HOLMES[22]. In the following, activities of the ECHo-collaboration are summarized.

At the heart of the experiment are metallic magnetic calorimeters (MMCs) [101]. They consist of an erbium-gold-absorber, into which the ^{163}Ho is implanted. The absorber is strongly thermally coupled to a temperature sensor. The sensor employs the temperature-dependent magnetization of a paramagnetic alloy in a weak magnetic field at temperatures below 50 mK. The magnetization is read out by a SQUID magnetometer. As a near future goal, an array of about 100 MMCs, read out by one SQUID in a multiplexing scheme, will be set up. The array has the prospect to reach a statistical sensitivity of below 10 eV/c^2 on $m(\nu_e)$.

In the case of ^{163}Ho, the support by Penning-trap mass spectrometry is crucial. Again, Q-value determinations on two precision scales are needed. First of all, the Q-values reported in literature span over a range of several 100 eV and are in parts mutually exclusive (see Fig. 1.1). As was shown in [100] by means of Monte Carlo methods, the statistical sensitivity with Q being close to the highest-energy de-excitation line shows a rather extreme Q-dependence: A change of Q from 2200 eV to 2400 eV would increase the required statistics to obtain a certain statistical sensitivity on $m(\nu_e)$ by about two orders of magnitudes[23]. Thus a direct Q-value determination with an uncertainty of a few 10 eV would clarify how a ^{163}Ho microcalorimeter experiment would have to be dimensioned in order to obtain a statistical sensitivity on $m(\nu_e)$ in the sub-eV range. Such a Q-value determination is planned with SHIPTRAP in the near future.

The final goal of ECHo to obtain a sensitivity on $m(\nu_e)$ in the sub-eV range will be supported by PENTATRAP by determining the Q-value of the decay with an uncertainty of 1 eV or less. This will require a mass-ratio measurement with again a highly challenging relative uncertainty of less than $6.6 \cdot 10^{-12}$. Whether the Q-value

---

[21] Electron Capture ^{163}Ho - http://www.kip.uni-heidelberg.de/echo/

[22] https://artico.mib.infn.it/holmes

[23] For higher Q-values, the Q-dependence is less extreme.

obtained by PENTATRAP will be used for a systematics-check or as a fixed parameter in the lineshape-fit to increase the sensitivity on $m(\nu_e)$ will depend on several factors:

- The exact uncertainty of the measured Q-value.
- The sensitivity of the measured de-excitation spectrum without an independent Q-value[24].
- The Q-value itself: Resonant enhancement for Q being close to the highest-energy de-excitation line changes the sensitivity to Q.

Further contributions to ECHo are a detailed theoretical investigation of the de-excitation spectrum and, since ^{163}Ho is not naturally occurring, the production of a sufficient amount of radiochemically pure ^{163}Ho [101]. To summarize, the perspectives for a high-precision neutrino mass study employing the electron capture in ^{163}Ho seem to be very good. However, the required statistics to obtain sub-eV sensitivity strongly depends on the not yet accurately known Q-value.

1.4.2. A test of special relativity and a precise determination of the neutron mass

A test of special relativity, similar to the one described in Sec. 1.3.4, could be carried out by comparing the mass difference[16] $m(^{35}\mathrm{Cl}) + m(n) - m(^{36}\mathrm{Cl})$ with the sum of energies of the γ-rays emitted after the neutron capture in ^{35}Cl.

The γ-ray energies can be determined with a high-resolution double crystal spectrometer. In [103], the total neutron binding energy was determined with an uncertainty of 1.8 eV, corresponding to a relative uncertainty of $2.1 \cdot 10^{-7}$, using the *Gams4* spectrometer at ILL. It is estimated that the improved spectrometer *Gams6* will be able to reach a relative uncertainty of $1 \cdot 10^{-8}$, corresponding to an absolute uncertainty of 86 meV.

PENTATRAP aims at the first direct determination of the mass difference between ^{36}Cl and ^{35}Cl by measuring their mass ratio. To obtain an uncertainty in the mass difference[25] of less than 1.8 eV/c^2, a mass-ratio measurement with a relative uncertainty of less than $5.3 \cdot 10^{-11}$ has to be carried out. To keep up with the anticipated precision of *Gams6* the relative uncertainty in the mass ratio would even have to be below $2.5 \cdot 10^{-12}$. This goal is highly ambitious not only due to this never before achieved ultra-low uncertainty, but also because the isotopes have a mass difference of 1 u. Thus, many systematic shifts that cancel to high precision for mass doublets will have to be corrected for in the mass-ratio determination.

Furthermore, a conversion of the mass ratio to a mass difference with an uncertainty of less than 86 meV/c^2 would require a reduction of the uncertainty of the absolute

---

[24] A detailed discussion of experimental parameters like detector resolution or unresolved pile-up fraction which influence the sensitivity besides mere statistics goes beyond the scope of this thesis. For this discussion, the reader is referred to [100].

[25] Within this section, using eV/c^2 as a mass unit is somehow sloppy - the proper unit would be atomic mass units. It is however more convenient to use eV/c^2, since it makes the comparison of masses and energies much easier

^{35}Cl mass by more than a factor of ten to at least 3 eV/c^2, corresponding to a relative uncertainty of $\sim 9 \cdot 10^{-11}$. This mass determination could be carried out at PENTATRAP by performing a mass-ratio measurement between e.g. the q/m-doublets $^{35}\text{Cl}^{10+}$ and $^{28}\text{Si}^{8+}$. ^{28}Si would be a suitable reference, since its mass is known with an uncertainty of only ~ 0.4 eV/c^2 [104].

However, if both PENTATRAP and *Gams6* were able to reach uncertainties of below 86 meV/c^2 and 86 meV, respectively, the uncertainty in the test of Eq. (1.3) would be limited by the neutron mass, or to be more specific, by the uncertainty in the neutron binding energy in deuterium. However, the neutron binding energy in ^{36}Cl and the $^{36}\text{Cl} - {}^{35}\text{Cl}$ mass difference could then be used to determine the neutron mass with a four times smaller uncertainty than the currently accepted value [104].

1.4.3. Binding energies and QED-tests

As pointed out before, the mass differences that PENTATRAP determines are mass differences between highly-charged ions. In most applications of high-precision mass ratios, however, mass differences of neutral atoms are required. Thus, the mass differences determined by PENTATRAP have to be corrected for binding energy differences between the ions. For this, one will have to resort in most cases to theory. Thus, both precise and accurate calculations of binding energy differences are of utmost importance.

The further development of numerous theoretical approaches to this task (see e.g. [105–108] and references therein) will be assisted by PENTATRAP as follows: The ionization energy $E_i(n)$ of the charge state q of some isotope A can be determined by measuring the mass difference between $A^{(q+1)+}$ and A^{q+}:

$$E_i(q) = m(A^{(q+1)+})c^2 - m(A^{q+})c^2 - m_e c^2, \tag{1.5}$$

where m_e is the electron mass. Ionization energies for several consecutive charge states and several isotopes can then be used as a benchmark for different theoretical approaches. If the isotope were ^{163}Dy for instance, an uncertainty in the ionization energy of less than 1 eV would require to determine the mass ratio between two neighboring charge states with a relative uncertainty of less than $6.6 \cdot 10^{-12}$. Due to the different charge states (and hence charge-to-mass ratios), achieving such a precision will require detailed studies of many different systematic eigenfrequency shifts.

Particularly interesting are binding energies in heavy highly-charged ions, since these can test the predictions of bound-state QED in the regime of extremely strong electromagnetic fields. One of the most impressive experimental results in this field was the determination of the ground-state Lamb shift in hydrogenlike uranium by means of X-ray spectroscopy with ions stored in the ESR storage ring at GSI [109]. However, since the uncertainty of 4.6 eV was about an order of magnitude higher than the uncertainty of the theoretical predictions at that time, the measurement was not able to challenge theory.

In order to determine the binding energy of the 1s electron in hydrogenlike $^{238}\text{U}^{91+}$ with an uncertainty below 0.5 eV at PENTATRAP, the mass ratio between $^{238}\text{U}^{92+}$

and $^{238}\mathrm{U}^{91+}$ would have to be determined with a relative uncertainty of $\sim 2.2 \cdot 10^{-12}$. In order to judge the feasibility of such a measurement extensive studies of systematic frequency shifts - especially the ones having a strong charge state dependence - will have to be carried out.

2. Penning trap basics

2.1. Ideal Penning traps

Ion motion and frequencies An ion[1] of mass m and charge q in a homogeneous magnetic field $\vec{B} = B\vec{e}_z$ performs under the influence of the Lorentz force[2]

$$\vec{F} = q\vec{v} \times \vec{B} \tag{2.1}$$

a circular motion in the xy-plane at the free-space cyclotron frequency[3]

$$\nu_c = \frac{1}{2\pi}\frac{qB}{m}. \tag{2.2}$$

Knowing the strength of the magnetic field and the charge of the ion, a measurement of the free-space cyclotron frequency yields the mass of the ion.

In order to perform high-precision measurements of the free-space cyclotron frequency, confinement of the ion in all spacial directions is necessary. With a magnetic field in z-direction, a confinement in the radial plane (the plane perpendicular to the magnetic field) is obtained. In a Penning trap, confinement in axial direction (the direction of the magnetic field) is realized by means of a superimposed electrostatic quadrupolar potential

$$\Phi = c_2 U_0 \left(z^2 - \frac{x^2+y^2}{2}\right) \equiv c_2 U_0 \left(z^2 - \frac{\rho^2}{2}\right), \tag{2.3}$$

where c_2, being of dimension 1/length^2, gives a length scale and U_0 provides a potential scale. In the last equation, the potential was written in cylindrical coordinates. The ion is confined in z-direction if $c_2 q U_0 > 0$.

The overall equations of motion of an ion in a Penning trap are thus given by

$$\begin{pmatrix} \ddot{x} \\ \ddot{y} \\ \ddot{z} \end{pmatrix} = \frac{qc_2U_0}{m}\begin{pmatrix} x \\ y \\ -2z \end{pmatrix} + \frac{qB}{m}\begin{pmatrix} \dot{y} \\ -\dot{x} \\ 0 \end{pmatrix}. \tag{2.4}$$

---

[1] In this section, the term *ion* could be replaced at any point by the term *charged particle.*

[2] Within this paragraph, the ion-motion is treated non-relativistically. Special relativity will be taken into account at the end of this section.

[3] Within this thesis, the term *free-space cyclotron frequency* stands for the frequency ν_c (see Eq. (2.2)) of the circular motion of an ion in a homogeneous magnetic field, while the term *cyclotron frequency* stands for the frequency ν_+ (see Eq. (2.7)) of one of the radial motions of an ion in a Penning trap. ν_+ is often also called *modified cyclotron frequency* or *trap cyclotron frequency.*

The solution to these equations is a superposition of three independent harmonic eigenmotions:

$$\begin{pmatrix} x(t) \\ y(t) \\ z(t) \end{pmatrix} = a_+ \begin{pmatrix} \sin(\omega_+ t + \phi_+) \\ \cos(\omega_+ t + \phi_+) \\ 0 \end{pmatrix} + a_- \begin{pmatrix} \sin(\omega_- t + \phi_-) \\ \cos(\omega_- t + \phi_-) \\ 0 \end{pmatrix} + a_z \begin{pmatrix} 0 \\ 0 \\ \sin(\omega_z t + \phi_z) \end{pmatrix}, \tag{2.5}$$

where a denotes the amplitude, ω the frequency and ϕ the phase of the corresponding eigenmotion. An ion trajectory is sketched in Fig. 2.1.

The eigenmotions have the following properties:

- The *axial motion* at the frequency[4]

  $$\omega_z = \sqrt{\frac{2c_2 q U_0}{m}} \tag{2.6}$$

  is the oscillation of the ion in the harmonic electrostatic potential in z-direction.

- The *cyclotron motion* at the frequency

  $$\omega_+ = \frac{\omega_c}{2} + \sqrt{\frac{\omega_c^2}{4} - \frac{\omega_z^2}{2}} \tag{2.7}$$

  is similar to the free-space cyclotron motion, with a correction due to the radial electrostatic field.

- The *magnetron motion* at the frequency

  $$\omega_- = \frac{\omega_c}{2} - \sqrt{\frac{\omega_c^2}{4} - \frac{\omega_z^2}{2}} \tag{2.8}$$

  is similar to the motion of the ion in a (radial) Wien filter, consisting of the radial electrostatic field and the magnetic field.

From both Eq. (2.7) and Eq. (2.8), the following criterion for a stable motion of the ion in a Penning trap can be deduced:

$$\omega_z < \frac{\omega_c}{\sqrt{2}}. \tag{2.9}$$

In most Penning trap experiments, the following hierarchy of eigenfrequencies is given:

$$\omega_+ \gg \omega_z \gg \omega_-. \tag{2.10}$$

Although the free-space cyclotron frequency ω_c is not an eigenfrequency of the ion in a Penning trap, it can be deduced from the ion's eigenfrequencies by means of the relations:

$$\omega_c = \sqrt{\omega_+^2 + \omega_-^2 + \omega_z^2}, \tag{2.11}$$

$$\omega_c = \omega_+ + \omega_-. \tag{2.12}$$

---

[4] Within this thesis, both angular frequencies, denoted by ω, as well as measurable frequencies, denoted by ν, are simply called *frequencies*. They are related by $\omega = 2\pi\nu$.

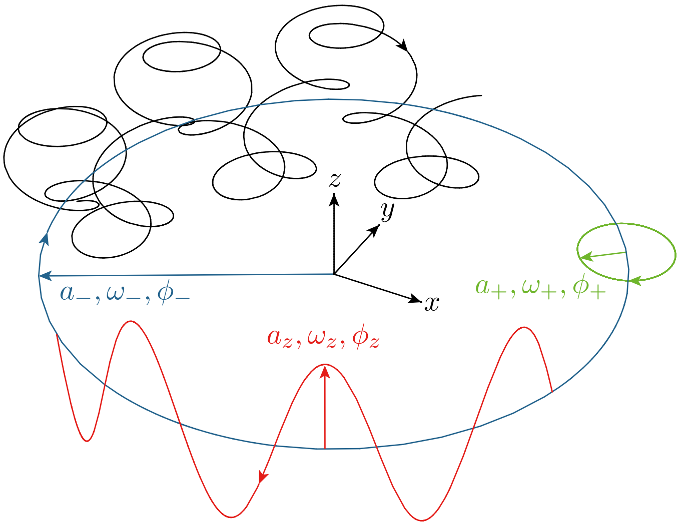

Figure 2.1.: The sketch of a trajectory of an ion in a Penning trap is shown. The ion motion (black trajectory) is a superposition of three harmonic eigenmotions at frequencies ω_+, ω_- and ω_z. The z-direction is the direction of the magnetic field. For further details see text.

These two relations are at the heart of Penning-trap mass spectrometry. In Sec. 2.2 it will be shown that Eq. (2.11) is valid exactly even for Penning traps with certain imperfections, while Eq. (2.12) is valid to high precision in many cases.

Energies and actions In the classical picture of the ion motion in a Penning trap, the energy of the ion is given by

$$E = \underbrace{\frac{1}{2}m\omega_+^2 a_+^2 - \frac{1}{4}m\omega_z^2 a_+^2}_{E_+} + \underbrace{\frac{1}{2}m\omega_-^2 a_-^2 - \frac{1}{4}m\omega_z^2 a_-^2}_{E_-} + \underbrace{\frac{1}{2}m\omega_z^2 a_z^2}_{E_z}. \tag{2.13}$$

Note that for a stable trap (i.e. Eq. (2.9) is fulfilled), the magnetron energy is dominated by the potential energy and is thus negative. Therefore, the magnetron motion is metastable: A reduction of its energy leads to an increase in radius. The energy of the cyclotron motion on the other hand is dominated by kinetic energy.

Although the classical picture of the ion motion in a Penning trap is an accurate description for the experimental conditions at PENTATRAP, it is convenient in some cases to resort to a quantum-mechanical picture [29]. Since the three eigenmotions are three harmonic oscillations, the ion's energy can be written as follows:

$$E = \underbrace{\left(n_+ + \frac{1}{2}\right)\hbar\omega_+}_{E_+} - \underbrace{\left(n_- + \frac{1}{2}\right)\hbar\omega_-}_{E_-} + \underbrace{\left(n_z + \frac{1}{2}\right)\hbar\omega_z}_{E_z}, \tag{2.14}$$

where n is the quantum number of the corresponding motion. Spin-dependent contributions to the ion's total energy have been left aside, since they are not relevant for mass spectrometry.

Table 2.1.: Absolute values of the classical actions of the three eigenmotions of an ion in a Penning trap are listed. Expressions are taken from [111]

eigenmotion	$\lvert \oint p\, dq \rvert$
cyclotron	$\pi m \omega_+ a_+^2$
magnetron	$\pi m \omega_+ a_-^2$
axial	$\pi m \omega_z a_z^2$

Besides the energy of an eigenmotion, its classical action

$$J = \oint p\, dq \tag{2.15}$$

is an important parameter. It is conserved under adiabatic variations of the trapping fields [110]. This fact is of particular relevance for an adiabatic transport of ions between traps and for the lowering of the electrostatic potential for the ejection of ions with large axial energies. Furthermore, the action is exchanged between eigenmotions for resonant quadrupolar radio-frequency (RF) fields (see Sec. 2.3). Absolute values of the actions are listed in Tab. 2.1.

Relativistic frequency shifts In the first two paragraphs, the ion motion has been treated non-relativistically. Although energies are usually quite small[5], there is in principle no non-relativistic regime: Whether or not special relativity has to be taken into account depends on the ion energy and the measurement precision.

Since relativistic effects are usually small, they can be treated by means of perturbative methods, resulting in the following shifts of the eigenfrequencies [112]:

$$\frac{\Delta\omega_z}{\omega_z} = -\frac{1}{4c^2}\left((\omega_+ a_+)^2 + (\omega_- a_-)^2 + \frac{3}{4}(\omega_z a_z)^2\right), \tag{2.16}$$

$$\frac{\Delta\omega_\pm}{\omega_\pm} = \mp\frac{\omega_\pm}{\omega_+ - \omega_-}\frac{(\omega_\pm a_\pm)^2 + 2(\omega_\mp a_\mp)^2 + (\omega_z a_z)^2/2}{2c^2}. \tag{2.17}$$

Usually the most significant contribution is the dependence of the cyclotron frequency on the cyclotron energy. For a typical hierarchy of eigenfrequencies, the shift is given by:

$$\frac{\Delta\omega_+}{\omega_+} \approx -\frac{E_+}{mc^2}. \tag{2.18}$$

Thus, relativistic shifts become less severe the heavier the ion is.

---

[5] Depending on measurement scheme and eigenmotion, energies are typically in a (rather wide) range from 10^{-8} to 100 eV. All of these energies are many orders of magnitude below the energy equivalent to the rest mass of any ion.

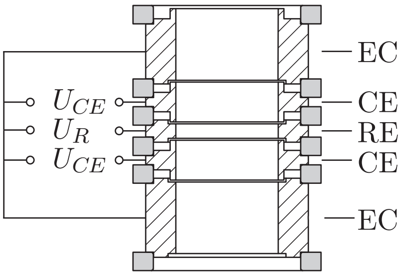

Figure 2.2.: A set of five cylindrical electrodes with suitable voltages applied can be used to generate an electrostatic trapping field. The sectional drawing shows one of the PENTATRAP Penning traps. The abbreviations stand for endcap (EC), correction electrode (CE) and ring electrode (RE).

2.2. Real Penning traps

In the implementation of a Penning trap, the magnetic field is usually provided by a superconducting magnet. The electrostatic quadrupolar potential can be generated using a set of cylindrical electrodes [113], with suitable voltages applied (see Fig. 2.2). Both the magnetic as well as the electrostatic field will deviate from the fields in an ideal Penning trap:

- The trap's rotational symmetry axis $\vec{e}_z^{\,trap}$ will be tilted to some degree relative to the direction of the magnetic field $\vec{e}_z^{\,mag}$.
- The radial electrostatic potential won't be perfectly rotationally symmetric, but might be slightly elliptic.
- The electrostatic potential won't be perfectly harmonic.
- The magnetic field won't be perfectly homogeneous.
- The ion induces image charges on the electrode surfaces that alter the trapping potential.

Besides that, there are further factors complicating mass spectrometry with real Penning traps:

- The magnetic field strength is only known to finite precision.
- The magnetic and electrostatic fields will fluctuate/drift over time.

In the following, these imperfections will be dealt with. Other imperfections will be treated later on (see Sec. 3.4.4.7). Furthermore it will be explained within this section, how mass-ratio measurements can reduce the influence of certain shortcomings of real Penning traps. The issue of magnetic/electrostatic field-fluctuations and -drifts will be discussed in Sec. 3.4.3.1 and Sec. 3.4.5.

Tilted and elliptic traps Major sources of systematic shifts of the eigenfrequencies in a Penning trap are a misalignment between $\vec{e}_z^{\,trap}$ and $\vec{e}_z^{\,mag}$ as well as an ellipticity of the radial electrostatic potential, arising e.g. from charge patches on the trap electrodes [28]. In a coordinate system, in which $\vec{e}_z^{\,trap}$ coincides with the z-axis and the major axis of the radial elliptical potential coincides with e.g. the x-axis, the electrostatic potential and the magnetic field can be written as:

$$\Phi = c_2 U_0 \left(z^2 - \frac{x^2+y^2}{2} - \epsilon \frac{x^2-y^2}{2} \right), \tag{2.19}$$

$$\vec{B} = B \begin{pmatrix} \sin(\theta)\cos(\phi) \\ \sin(\theta)\sin(\phi) \\ \cos(\theta) \end{pmatrix}. \tag{2.20}$$

ϵ is the ellipticity-parameter and ϕ and θ are the angles between the magnetic field and the x- and z-axes, respectively. In [28] it was shown that Eq. (2.11) holds also for the frequencies $\bar{\omega}_{\pm,z}(\epsilon,\theta,\phi)$ measured in an imperfect Penning trap, i.e. the following relation is fulfilled

$$\omega_c^2 = \bar{\omega}_+^2(\epsilon,\theta,\phi) + \bar{\omega}_-^2(\epsilon,\theta,\phi) + \bar{\omega}_z^2(\epsilon,\theta,\phi). \tag{2.21}$$

This relation is called *the invariance theorem* [29]. It enables high-precision free-space cyclotron frequency measurements in imperfect Penning traps.

For free-space cyclotron frequency determinations by means of the invariance theorem, all three eigenfrequencies have to be measured. A small fluctuation[6]/uncertainty[7] $\Delta\omega_i$ in one of the eigenfrequencies ω_i affects the free-space cyclotron frequency as follows:

$$\frac{\Delta\omega_c}{\omega_c} = \frac{1}{\omega_c}\frac{\partial\omega_c}{\partial\omega_i}\Delta\omega_i = \left(\frac{\omega_i}{\omega_c}\right)^2 \frac{\Delta\omega_i}{\omega_i}. \tag{2.22}$$

How various small fluctuations/uncertainties have to be added to a total $\Delta\omega_c/\omega_c$ depends on correlations between these fluctuations/uncertainties and the exact experimental procedures. An important feature of Eq. (2.22) is that contributions of the axial and the magnetron mode to the total $\Delta\omega_c/\omega_c$ are suppressed by factors $(\omega_z/\omega_c)^2$ and $(\omega_-/\omega_c)^2$. Thus, for a typical hierarchy of eigenfrequencies, the cyclotron frequency has to be determined with roughly the relative precision that is aimed-at for the free-space cyclotron frequency, whereas the axial and magnetron frequencies have to be determined with orders of magnitude smaller relative precisions.

If Eq. (2.12) is used instead of Eq. (2.11) to determine the free-space cyclotron frequency, i.e. only ω_+ and ω_- are measured, shifts due ϵ, ϕ and θ do not cancel out. Nevertheless, high-precision mass ratio measurements are possible in elliptic and tilted traps using Eq. (2.12): In [114] it was shown by means of the invariance theorem

---

[6] By fluctuation, a fluctuation of an operating parameter of the experimental apparatus that influences an eigenfrequency is meant.

[7] By uncertainty, an uncertainty in the determination of an eigenfrequency or in the correction for a systematic shift is meant.

that the measured mass ratio[8] of ion A and B is shifted relative to the true mass ratio by the amount

$$\Delta\frac{m_A}{m_B} \approx \left(\frac{1}{2}\epsilon^2 - \frac{9}{4}\theta^2\right)\left(\frac{\bar{\omega}_+^B - \bar{\omega}_+^A}{\bar{\omega}_+^A}\right)\frac{\bar{\omega}_-^A}{\bar{\omega}_+^B}. \tag{2.23}$$

The second and the third factor in this equation suppress the influence of ϵ and θ usually by many orders of magnitude and enable high-precision mass-ratio measurements.

For the alignment of $\vec{e}_z^{\,trap}$ with $\vec{e}_z^{\,mag}$, the behavior of any of the frequencies $\bar{\omega}_{\pm,z}(\epsilon,\theta,\phi)$ for different angles θ can be employed. Assuming $\epsilon \ll 1$, the axial frequency for instance is given by [28]

$$\bar{\omega}_z(\theta) \approx \omega_z\sqrt{1 - \frac{3}{2}\sin^2(\theta)}. \tag{2.24}$$

For best alignment, $\bar{\omega}_z$ thus has to be maximized.

Electrostatic anharmonicities In a trap as shown in Fig. 2.2, the electrostatic potential won't be perfectly harmonic, but its series expansion will also contain anharmonic terms. Due to the mirror symmetry of the trap with respect to the radial plane going through the center of the trap, odd terms will usually be negligible compared to even terms. Thus, the potential in cylindrical coordinates can be written as [115]:

$$\begin{aligned}\Phi(\rho,z)/U_0 = c_0 &\\ &+ c_2\left(z^2 - \frac{1}{2}\rho^2\right)\\ &+ c_4\left(z^4 - 3\rho^2z^2 + \frac{3}{8}\rho^4\right)\\ &+ c_6\left(z^6 - \frac{15}{2}\rho^2z^4 + \frac{45}{8}\rho^4z^2 - \frac{5}{16}\rho^6\right)\\ &+ \ldots\,.\end{aligned} \tag{2.25}$$

While c_0 is an offset of no relevance for the trapping, the c_2-term gives the sought-after quadrupolar potential. The anharmonic terms c_{2n} with $n > 2$ lead to energy-/amplitude-dependent shifts of the eigenfrequencies. A detailed discussion of the pertubative calculation of these shifts can be found in [116]. Here only the results of this article are stated, adapted to the definition of the potential given in Eq. (2.25).

The relative shifts of the eigenfrequencies due to the c_4-term are given by:

$$\frac{\Delta\omega_+}{\omega_+} = -\frac{3}{2}\frac{c_4}{c_2}\frac{\omega_-}{\omega_+ - \omega_-}\left(2a_z^2 - a_+^2 - 2a_-^2\right) \tag{2.26}$$

$$\frac{\Delta\omega_-}{\omega_-} = \frac{3}{2}\frac{c_4}{c_2}\frac{\omega_+}{\omega_+ - \omega_-}\left(2a_z^2 - a_-^2 - 2a_+^2\right) \tag{2.27}$$

$$\frac{\Delta\omega_z}{\omega_z} = \frac{3}{4}\frac{c_4}{c_2}\left(a_z^2 - 2a_+^2 - 2a_-^2\right). \tag{2.28}$$

---

[8] Mass ratio measurements will be discussed at the end of this section.

The relative shifts of the eigenfrequencies due to the c_6-term are given by:

$$\frac{\Delta\omega_+}{\omega_+} = -\frac{15}{8}\frac{c_6}{c_2}\frac{\omega_-}{\omega_+ - \omega_-}(3a_z^4 + a_+^4 + 3a_-^4 - 6a_+^2 a_z^2 - 12a_-^2 a_z^2 + 6a_+^2 a_-^2) \tag{2.29}$$

$$\frac{\Delta\omega_-}{\omega_-} = \frac{15}{8}\frac{c_6}{c_2}\frac{\omega_+}{\omega_+ - \omega_-}(3a_z^4 + a_-^4 + 3a_+^4 - 6a_-^2 a_z^2 - 12a_+^2 a_z^2 + 6a_+^2 a_-^2) \tag{2.30}$$

$$\frac{\Delta\omega_z}{\omega_z} = \frac{15}{16}\frac{c_6}{c_2}(a_z^4 + 3a_+^4 + 3a_-^4 - 6a_+^2 a_z^2 - 6a_-^2 a_z^2 + 12a_+^2 a_-^2). \tag{2.31}$$

Magnetic field inhomogeneities The superconducting magnets that are employed in high-precision Penning-trap mass spectrometers usually have, besides the main coils, additional shimming coils to make the magnetic field as homogeneous as possible. Nevertheless, there are always inhomogeneous magnetic field terms left, e.g. due to imperfect shimming or magnetic materials in the field of the magnet, that have to be dealt with at a certain level of precision. A series-expansion of the magnetic field around the center of a trap yields [116]:

$$\begin{aligned} \vec{B}(\rho, z) = {} & B_0\vec{e}_z \\ & + B_1\left(z\vec{e}_z - \frac{1}{2}\rho\vec{e}_\rho\right) \\ & + B_2\left(\left(z^2 - \frac{1}{2}\rho^2\right)\vec{e}_z - z\rho\vec{e}_\rho\right) \\ & + \dots\,. \end{aligned} \tag{2.32}$$

The effect of the various inhomogeneity terms can be calculated by means of perturbation theory. While even terms ($B_{2,4,\ldots}$) give rise to energy-/amplitude-dependent shifts in the eigenfrequencies already in a first-order perturbative calculation, the odd terms ($B_{1,3,\ldots}$) give rise to shifts only from second order[9] on [116] (which does not imply that these shifts are necessarily less important).

The shifts arising from the B_2-term are given by [116]:

$$\frac{\Delta\omega_+}{\omega_+} = \frac{B_2}{2B_0}\frac{\omega_+ + \omega_-}{\omega_+ - \omega_-}\left(a_z^2 - a_+^2 - a_-^2\left(1 + \frac{\omega_-}{\omega_+}\right)\right) \tag{2.33}$$

$$\frac{\Delta\omega_-}{\omega_-} = -\frac{B_2}{2B_0}\frac{\omega_+ + \omega_-}{\omega_+ - \omega_-}\left(a_z^2 - a_+^2\left(1 + \frac{\omega_+}{\omega_-}\right) - a_-^2\right) \tag{2.34}$$

$$\frac{\Delta\omega_z}{\omega_z} = \frac{B_2}{4B_0}\frac{\omega_+ + \omega_-}{\omega_+\omega_-}\left(a_-^2\omega_- + a_+^2\omega_+\right). \tag{2.35}$$

Usually, the shifts arising from B_2 dominate over shifts arising from B_4 [65, 87]. If nonetheless shifts arising from $B_{4,6,\ldots}$ have to be calculated, the reader is referred to [116].

The shifts arising from B_1 can be estimated as follows: The magnetic moment due to the cyclotron motion couples to the axial magnetic field gradient, giving an energy

---

[9] Examples of shifts that would appear in second order are the below mentioned B_1-shift or the so-called equilibrium position shift (see Sec. 3.4.4.7).

dependent axial force, which shifts the center of the axial oscillation. Due to B_1 and the shift of the center, the effective magnetic field seen by the ion is changed, which leads to a shift of the cyclotron frequency [117]:

$$\frac{\Delta\omega_+}{\omega_+} \approx -\frac{1}{2}\left(\frac{B_1}{B_0}\right)^2 \left(\frac{\omega_+^2}{\omega_z^2} - \frac{1}{2}\right) a_+^2. \tag{2.36}$$

For the inhomogeneities at the trap positions in the PENTATRAP setup, derived from an NMR-probe measurement [118], the shifts arising from the B_1-terms are much smaller than the shifts arising from the B_2-terms. Nevertheless, the B_1-terms can be critical: If the axial equilibrium positions of different ion species is different in a trap, they effectively experience different magnetic field strengths due to B_1 (see Sec. 3.4.4.7). Or, as another example, if B_1 is different for two different traps, the magnetic field ratio between these two traps will change when the traps are moving relative to the magnets' coils. This is of relevance for the two-trap measurement scheme, that will be employed at PENTATRAP (see Sec. 3.4.3.1).

Image charge shifts An ion in a Penning trap induces image charges in the trap electrodes. The additional electrostatic potential due to these image charges shifts the eigenfrequencies. In a cylindrical Penning trap, only the radial eigenfrequencies are shifted by [66, 119]

$$\Delta\omega_\pm \approx \mp K \frac{q^2}{8\pi\epsilon_0 m a^3 \omega_c}, \tag{2.37}$$

where a is the trap radius and K is a trap-geometry dependent factor. The cyclotron frequency as determined by the invariance theorem Eq. (2.11) is shifted by

$$\frac{\Delta\omega_c}{\omega_c} = \left(-\frac{\omega_+}{\omega_c} + \frac{\omega_-}{\omega_c}\right) K \frac{q^2}{8\pi\epsilon_0 m a^3 \omega_c^2} \approx -K \frac{m}{8\pi\epsilon_0 a^3 B^2}. \tag{2.38}$$

For a typical hierarchy of eigenfrequencies (see Eq. (2.10)), the image charge shift just depends on the mass of an ion.

Mass ratio measurements To determine the mass of an ion A with a certain precision, the strength of the magnetic field has to be known to at least the same precision. For the calibration of the magnetic field, an ion B of known mass can be used. Thus, instead of measuring only the free-space cyclotron frequency $\nu_{c,A}$, one measures the free-space cyclotron frequency ratio

$$R = \frac{\nu_{c,A}}{\nu_{c,B}} = \frac{m_B}{m_A}. \tag{2.39}$$

The last equality holds under the assumption of equal charge states, constant magnetic field and no systematic shifts.

But there is more to mass-ratio measurements than just magnetic field calibration: Both ions will experience systematic shifts $\Delta\nu_{c,A}$ and $\Delta\nu_{c,B}$, which change the measured free-space cyclotron frequency ratio as follows:

$$R = \frac{\nu_{c,A} + \Delta\nu_{c,A}}{\nu_{c,B} + \Delta\nu_{c,B}} \approx \frac{\nu_{c,A}}{\nu_{c,B}} \left(1 + \frac{\Delta\nu_{c,A}}{\nu_{c,A}} - \frac{\Delta\nu_{c,A}}{\nu_{c,A}}\right). \tag{2.40}$$

Thus, if ion A and ion B are of similar mass, they will experience similar systematic shifts, and the effect of the systematic shifts will be largely suppressed.

In many cases, the mass ratio itself is the quantity of interest and there is no need to determine the absolute masses of ion A and ion B with the same relative precision as the mass-ratio (see Sec. 1.4).

2.3. Radio-frequency excitations

Dipolar excitation A dipolar electric RF-field

$$\vec{E}(t) = E_0 \sin(\omega t + \phi)\hat{e}_i \tag{2.41}$$

with a frequency ω at/near one of the eigenfrequencies $\omega_{\pm,z}$ can be used to excite (or more generally manipulate) the amplitude of the corresponding eigenmotion. For axial dipolar excitation the field has to be oriented in z-direction ($\hat{e}_i = \hat{e}_z$). For the excitation of one of the radial modes, the field has to be oriented in some radial direction. The fields can be generated by applying an RF-signal at the corresponding frequency to a suitable electrode[10].

Depending on the relative phase of the excitation and the motion of the ion, the motional amplitude will either at first decrease or increase [120]. In the first case, the amplitude will reach zero after some time and then afterwards increase. After some time, the motional amplitude will increase linearly in time for any phase.

Dipolar excitations can be used, among other things, to imprint a certain phase to an eigenmotion (see Sec. 3.4.4.2) or to drive ions to large amplitudes for cleaning purposes (see Sec. 4.2.3).

Quadrupolar coupling/excitation Quadrupolar electric RF-fields

$$\vec{E}(t) = E_0 \sin(\omega_{coup} t + \phi)\,(x_i \vec{e}_j + x_j \vec{e}_i) \tag{2.42}$$

can be used to couple (and excite in some cases) the eigenmotions of an ion in a Penning trap.

Pure coupling occurs, when the frequency of the RF-field is at/near the sum or the difference of two eigenfrequencies, depending on the eigenmotions involved (see Tab. 2.2). In this case, the actions of the eigenmotions (see Sec. 2.1) are exchanged periodically at half of the modified Rabi-frequency [111, 121]

$$\Omega = \sqrt{\Omega_0^2 + \delta^2}, \tag{2.43}$$

which results in a modulation of the amplitudes of the eigenmotions at the same frequency. δ is the detuning from the true sideband frequency and Ω_0 is the Rabi-frequency, which for axial-radial coupling is given by [111, 121]

$$\Omega_0 = \frac{qE_0}{m} \frac{1}{2\sqrt{\omega_z \omega_\pm}}. \tag{2.44}$$

---

[10] For radial dipolar excitation, the RF-signal has to be applied to a part of a radially split electrode.

Table 2.2.: Sideband frequencies, at which quadrupolar coupling of two eigenmodes occurs as well as sideband frequencies, at which quadrupolar coupling and excitation of the eigenmodes occurs are listed.

eigenmotions	coupling	coupling & excitation
cyclotron, magnetron	$\omega_+ + \omega_-$	$\omega_+ - \omega_-$
cyclotron, axial	$\omega_+ - \omega_z$	$\omega_+ + \omega_z$
axial, magnetron	$\omega_z + \omega_-$	$\omega_z - \omega_-$

For the coupling of the magnetron motion and the cyclotron motion, the Rabi frequency is given by [122]:

$$\Omega_0 = \frac{qE_0}{m} \frac{1}{\omega_+ - \omega_-}. \tag{2.45}$$

If the coupling is realized by means of an RF-pulse, and the strength E_0 and the duration τ of the pulse are chosen such that $\Omega\tau = \pi$, the actions of the two coupled modes will be completely exchanged. Such pulses are called π-pulses [111].

When the sum/difference in the sideband frequency is turned into a difference/sum for a quadrupolar RF-field, the pure coupling turns into a coupling accompanied by an excitation of the two motions (see Tab. 2.2). The use of both sidebands will be discussed in Sec. 3.4.4.2. Quadrupolar RF-fields can be generated by applying an RF-signal to a part of a radially split electrode.

Parametric excitation Parametric excitation can occur, when the depth of the electrostatic trapping potential is modulated at a frequency approximately twice the axial frequency of the trapped ion. Including a damping force due to some cooling mechanism, the axial equation of motion reads:

$$\ddot{z}(t) + \gamma_z \dot{z}(t) + \omega_z^2 (1 + h\cos(\omega_d t)) z(t) = 0, \tag{2.46}$$

where γ_z is the damping constant and $\omega_d \approx 2\omega_z$ is the frequency of the drive. If the ion motion were undamped, and the trap were perfectly harmonic, the amplitude would just increase exponentially in time [123]. If damping is taken into account, parametric excitation occurs only, when the drive exceeds a certain threshold [124]:

$$h > h_T \equiv \frac{2\gamma_z}{\omega_z}. \tag{2.47}$$

For multiple ions, the threshold scales linearly with the number of ions - therefore, the threshold amplitude can be used to count ions in a trap. If the trap is not perfectly harmonic, anharmonic terms will limit the exponential growth of the axial amplitude. The ω_d-dependence of the axial amplitude in response to a drive at frequencies around $2\omega_z$ can be used to estimate the anharmonic potential terms $c_{4,6,...}$ [123, 124].

3. Experimental setup

3.1. Overview

In Fig. 3.1, a schematic overview of the PENTATRAP setup is shown. The setup can be separated into three parts:

- Ion production
- Ion transport including tools for diagnostics
- Penning traps including detection systems.

One of the outstanding features of PENTATRAP is the access to highly-charged ions (HCIs) over the whole mass-range. With this, it is possible to carry out ultra-high-precision mass-ratio measurements even in the range of medium- to high-Z elements (see Sec. 3.2.1). HCIs are produced with two different electron beam ion traps (EBITs), the *Dresden EBIT-W* and the Heidelberg EBIT (see Sec. 3.2). These EBITs are both situated in the EBIT-hall on ground level.

The ions are transported into the trap region through a beamline, which includes ion-optics for focusing, steering and deceleration of ion bunches. Furthermore, it includes diagnostic tools: Faraday cups and microchannel plates (MCPs) with phosphor screens are used to optimize the ion production and the efficiency of the transport. The beamline will be addressed in Sec. 3.3.

The Penning-trap laboratory is situated in the basement below the EBIT hall. The superconducting 7-T magnet (see Sec. 3.4.1) hosts parts of the beamline, the trap setup incorporating five cylindrical Penning traps (see Sec. 3.4.3) and the ultra-sensitive cryogenic first-stage detection electronics (see Sec. 3.4.4). The magnet's bore has a direct connection to the liquid helium (LHe) reservoir of the magnet, such that its interior is cooled to 4.2 K. This allows for the use of superconducting detection coils and ensures good vacuum conditions by means of cryogenic pumping. Besides the cryogenic and room temperature detection electronics (see Sec. 3.4.4), the setup incorporates further electronic devices, which are at room temperature (see Sec. 3.4.5): Ultra-stable trap voltage-sources, power supplies, function generators and communication devices. The control system to control and read out most of the devices incorporated in the setup will be addressed in Sec. 3.5.

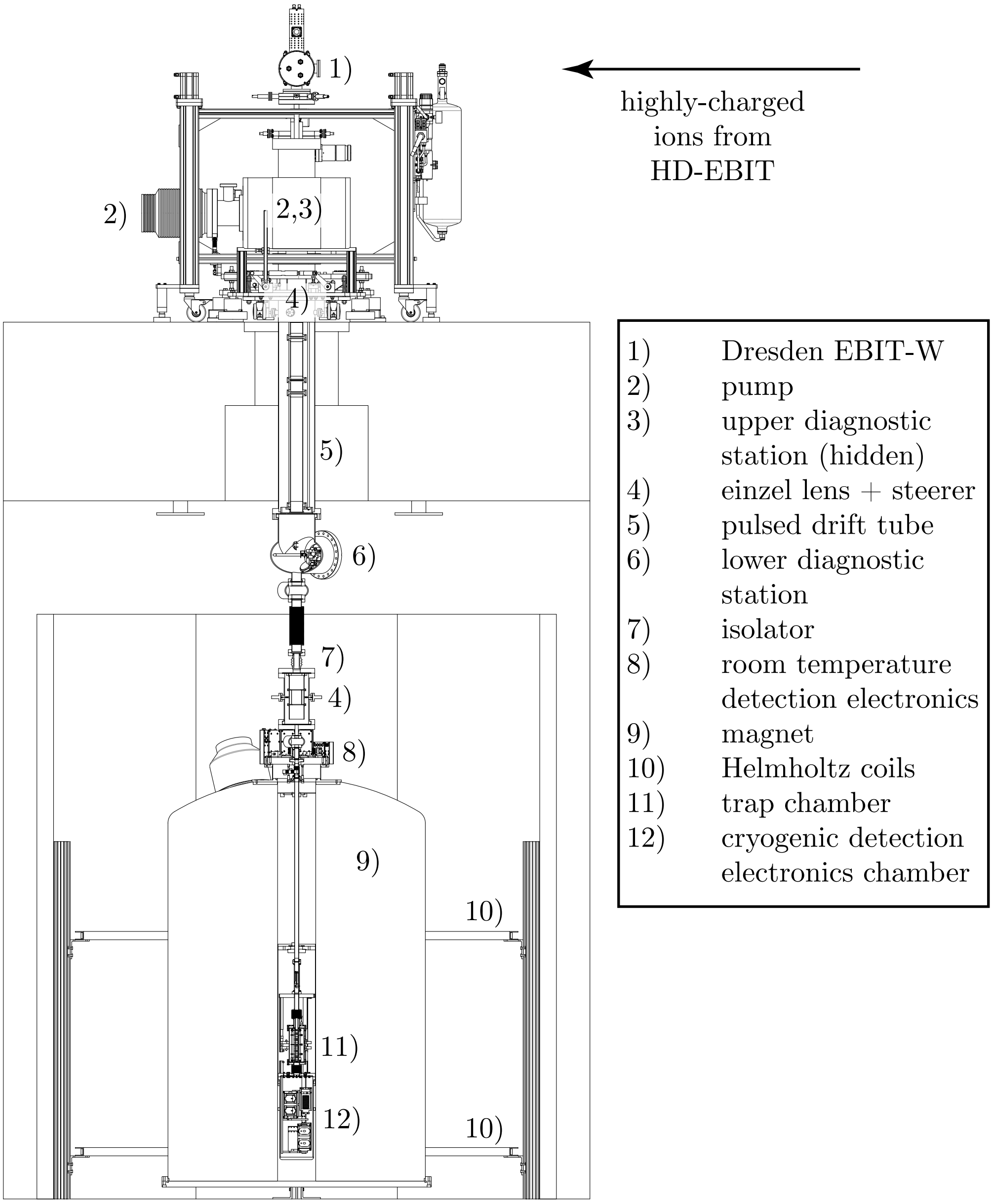

Figure 3.1.: An overview over the PENTATRAP experimental setup is shown. On the upper floor, two EBITs are situated for the production of highly-charged ions (HCIs). The beamline to the HD-EBIT is not shown. The HCIs are guided into the trap region with various ion-optical elements like einzel lenses or pulsed drift tubes. Diagnostic tools like MCPs are used for the optimization of transport settings. The homogeneous magnetic field for the Penning trap is provided by a cold-bore 7-T superconducting magnet. The trap chamber containing the 5-trap stack and the cryogenic detection electronics chamber are immersed in the liquid helium of the cold bore.

3.2. Ion production

3.2.1. Why highly-charged ions?

The temporal stabilities of both the magnetic and the electrostatic trapping fields are critical for high-precision Penning-trap mass spectrometry. The relative stability of state-of-the-art voltage sources employed to generate the electrostatic field is 10^{-8} over the time-scale of a ν_c-determination at best (see Sec. 3.4.5), while relative magnetic field stabilities below 10^{-12}/h have been achieved [125]. Therefore, suppressing the influence of voltage fluctuations is of major importance to perform cyclotron frequency ratio measurements at the precision-level that PENTATRAP aims at[1]. The motivation for the use of highly-charged ions is related to this suppression, as will be explained in the following.

A change ΔU_0 of the electrostatic trapping potential depth U_0 affects the three eigenfrequencies as follows:

$$\Delta\nu_z = \nu_z \frac{\Delta U_0}{2U_0}, \tag{3.1}$$

$$\Delta\nu_+ = -\frac{\nu_z^2}{\nu_+ - \nu_-}\frac{\Delta U_0}{2U_0}, \tag{3.2}$$

$$\Delta\nu_- = \frac{\nu_z^2}{\nu_+ - \nu_-}\frac{\Delta U_0}{2U_0}. \tag{3.3}$$

If all three eigenfrequencies could be measured simultaneously, the changes of the eigenfrequencies due to voltage fluctuations/drifts would cancel out exactly in the determination of ν_c by means of the invariance theorem Eq. (2.11) (as can be seen by combining Eq. (3.1), Eq. (3.2) and Eq. (3.3) with Eq. (2.22)). The same holds true for simultaneous cyclotron and magnetron frequency measurements and a determination of ν_c by means of the sum-relation given in Eq. (2.12).

Although very elaborate techniques have been developed to perform free-space cyclotron frequency determinations by means of quasi-simultaneous eigenfrequency measurements [126], high-precision free-space cyclotron frequency determinations by truly simultaneous eigenfrequency measurements cannot be carried out with current state-of-the-art techniques[2]. Thus, eigenfrequencies have to be measured independently, and the contributions of Eq. (3.1), Eq. (3.2) and Eq. (3.3) to the free-space cyclotron frequency determination have to be treated independently.

At PENTATRAP, free-space cyclotron frequencies will be determined by means of the invariance theorem (Eq. (2.11)). Voltage-instabilities[3] ΔU_0 during the determination of ν_+ affect ν_c as follows (using Eq. (2.22)):

$$\frac{\Delta\nu_c}{\nu_c} = -\left(\frac{\nu_+}{\nu_c}\right)^2 \frac{\nu_z^2}{\nu_+(\nu_+ - \nu_-)}\frac{\Delta U_0}{2U_0}. \tag{3.4}$$

---

[1] The question of magnetic field instabilities will be addressed in Sec. 3.4.3.1.

[2] A detailed discussion of this topic is beyond the scope of this thesis.

[3] The abstract term *voltage instability* will be used within this section for both drifts and fluctuations. How eigenfrequencies are affected exactly by drifts and fluctuations has to be discussed within the context of a definite free-space cyclotron frequency determination scheme. The following discussion is only intended as a rough estimate of the effect of any voltage instability on ν_c.

During the determination of ν_z, the effect is:

$$\frac{\Delta\nu_c}{\nu_c} = \left(\frac{\nu_z}{\nu_c}\right)^2 \frac{\Delta U_0}{2U_0}. \tag{3.5}$$

During the determination of ν_-, the effect is:

$$\frac{\Delta\nu_c}{\nu_c} = \left(\frac{\nu_-}{\nu_c}\right)^2 \frac{\nu_+}{\nu_+ - \nu_-} \frac{\Delta U_0}{U_0}. \tag{3.6}$$

Thus in order to suppress the effect of voltage instabilities on the determination of ν_c by means of the invariance theorem, a pronounced hierarchy of eigenfrequencies (see Eq. (2.10)) is required:

$$\nu_- \ll \nu_z \ll \nu_+. \tag{3.7}$$

PENTATRAP aims at free-space cyclotron frequency ratio measurements of ions over the whole mass-range at a relative precision-level below 10^{-11}. As pointed out before, the voltage sources in use provide a relative voltage stability of 10^{-8} over the time-scale of one ν_c-determination cycle at best. Thus, all "suppression-factors" to $\Delta U_0/U_0$ in Eq. (3.4), Eq. (3.5) and Eq. (3.6) have to be below 10^{-3} at least.

In Fig. 3.2, the voltage-instability suppression-factor $\nu_z^2/2\nu_c^2$ of Eq. (3.5) is plotted exemplarily for a ^{187}Os-ion at an axial frequency of 400 kHz[4] in a magnetic field of 7 T for different charge states q. It can be seen that for a suppression-factor below 10^{-3}, charge states $q \geq 11$ are required. For a suppression-factor below 10^{-4}, charge states $q \geq 35$ are required. Thus, highly-charged ions are required to carry out free-space cyclotron frequency ratio measurements with heavy ions at the aimed-at precision under the above sketched boundary conditions.

3.2.2. Electron beam ion traps

Principle The production of HCIs by means of an EBIT is based on successive electron-impact-ionization. Ions are trapped in one direction in an electrostatic potential minimum created by a set of trap electrodes with suitable voltages applied. An intense electron beam in direction of the trap symmetry axis serves both for ionization and electrostatic radial confinement of the ions. Confinement times being sufficient to breed ions to very high charge states are achieved through evaporation of low-charged ions (LCIs), being mainly rest-gas ions. The evaporative cooling counteracts heating caused by plasma instabilities and ion-electron collisions [127]. In order to keep the charge-exchange rate between HCIs and neutral gas low, the whole setup is placed in an ultra-high vacuum[5]. With EBITs, ions as highly-charged as bare uranium [128] or even Cf^{96+} [129] have been produced.

---

[4] Much lower axial frequencies are not feasible for technical reasons which are for instance related to the axial frequency detector (see Sec. 3.4.4.4). For a detailed discussion see [115].

[5] The vacuum pressure is a compromise between a low charge-exchange rate and a high cooling-rate by means of LCI.

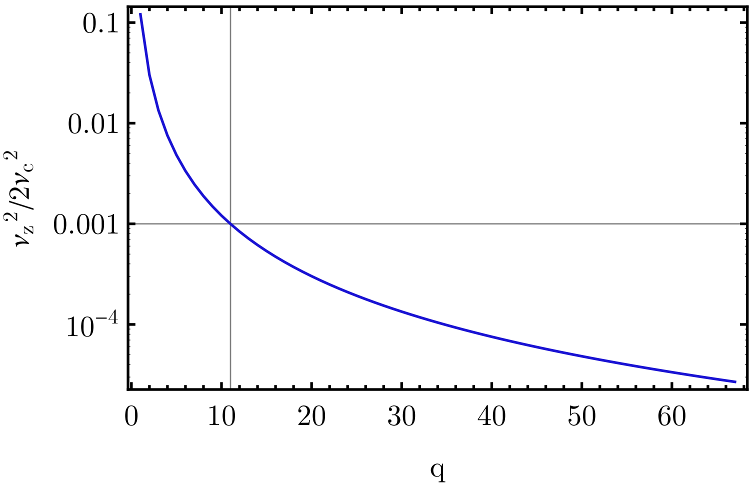

Figure 3.2.: The voltage-instability suppression-factor of Eq. (3.5) is plotted exemplarily for ^{187}Os-ions at an axial frequency of 400 kHz in a field of 7 T for different charge states. The vertical line and the horizontal line show that for a suppression-factor below 10^{-3} at least an 11+ charge state is required. For details see text.

Setup A schematic setup of an EBIT is shown in Fig. 3.3. The cathode produces the electron beam. It is situated in a region of low magnetic field, whereas the trap is placed in a strong magnetic field. Therefore, the electron beam gets radially compressed on its way from the cathode to the center of the trap. This enhances the electron current density in the center of the trap and thereby the ionization rates. The potential difference between the cathode and the central trap electrode defines the energy of the electron beam. Since electron-impact-ionization cross sections are energy dependent, the electron energy can be used to enhance the breeding of a certain charge state. Behind the trap, electrons are picked up by a collector electrode. In Fig. 3.3, the axial potential minimum is created by three cylindrical electrodes where the outer ones are on the same potential, whereas the inner one is on a lower potential. The injection of the species of interest will be addressed in Sec. 3.2.3 and Sec. 3.2.4.

Ion ejection If required, ions can be ejected from an EBIT either as a continuous beam or in bunches. The energy of the ejected ions can be set by means of an offset to the trap electrode-voltages[6]. For extraction of a continuous beam, one of the outer trap electrodes can be set to a potential slightly below the potential of the other one, such that hot ions continuously leak out of the trap. To obtain an ion-bunch, one of the trap electrodes has to be pulsed either up or down, depending on the electrode chosen. This is the operation mode of choice for PENTATRAP since it allows for deceleration of the ion bunches with pulsed drift-tubes in the beamline connecting the EBIT and the Penning traps. The EBIT-extraction trigger serves as zero-time for the timing of the corresponding pulses.

---

[6] The trap voltages are relative to the ground of the beamline following the EBIT.

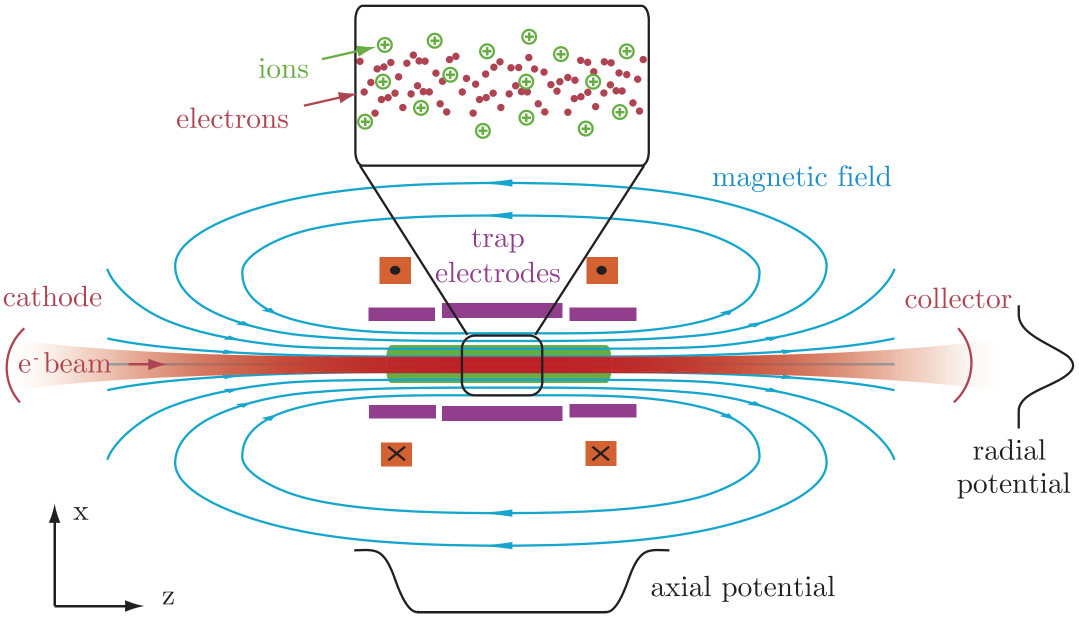

Figure 3.3.: The core elements of an EBIT are shown schematically. An electron beam is created by a cathode, accelerated towards the center of the trap and then dumped on a collector behind the trap. Ions are trapped electrostatically by a radial potential minimum created by the electron beam and an axial potential minimum created by an electrode structure with suitable voltages applied. The ions get successively ionized by the electron beam. To obtain high current densities, the electron beam gets compressed by means of a strong magnetic field. For further details, see text. Picture taken and modified with permission from [118].

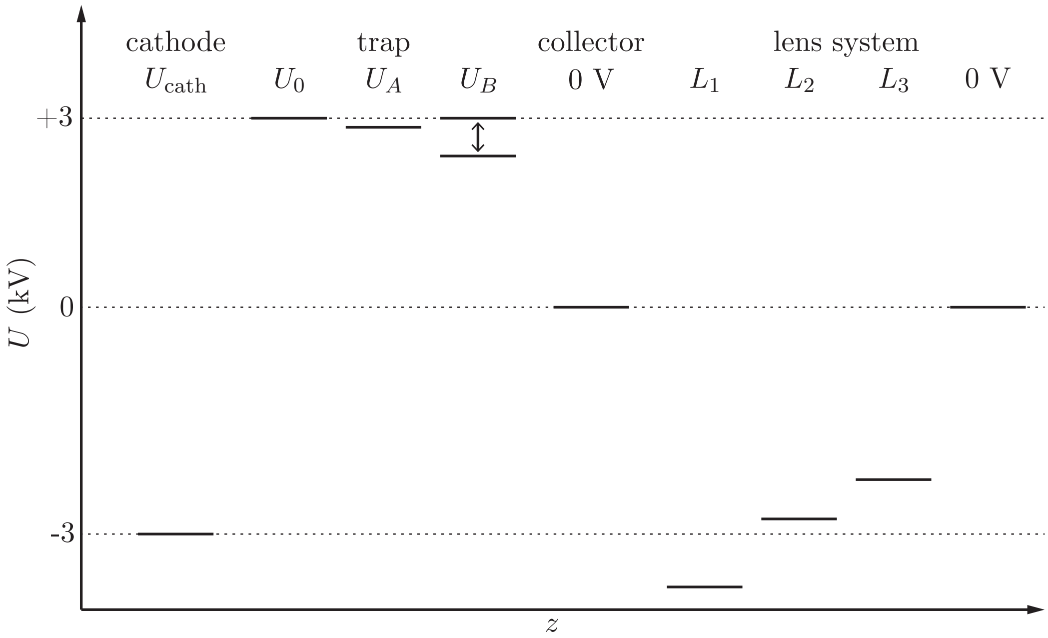

Figure 3.4.: A sketch of the voltages applied to the electrode system of the *Dresden EBIT-W* (without Wien filter) is shown. The voltage levels are indicated by solid bars. The cathode is usually set to a voltage of -3 kV. The electrostatic trapping potential is formed by the three following electrodes, with the voltages U_0, U_A and U_B applied. For extraction of ions, U_B is pulsed to a value below U_A. Between the grounded electron collector and the Wien filter, a set of four electrodes serves as an ion optical extraction system, with the electrode closest to the Wien filter being grounded. The voltages at the different electrodes agree with those that have been used in most of the experiments presented in Chapter 4.

3.2.3. The Dresden EBIT-W

Setup One of the EBITs in use is the commercially available *DREEBIT Dresden EBIT-W* [130]. It is a room-temperature EBIT with an integrated Wien filter [131]. The cathode delivers an electron current of up to 50 mA. The magnetic field strength in the trap region, produced by permanent magnets, is 250 mT. The maximum achievable current density is <300 A/cm^2. The maximum electron energy is 15 keV.

An overview over the voltages applied to the electrode system of the *Dresden EBIT-W* is shown in Fig. 3.4. The cathode is set to the recommended voltage of -3 kV [132]. The trap consists of three cylindrical electrodes. Since the cathode potential is fixed, the voltage at the central electrode U_A determines both the electron energy and the energy of ejected ions. The voltage difference between the outer electrodes and the inner electrode $U_0 - U_A = U_B - U_A$ determines the depth of the trap. For ion ejection, U_B is pulsed below U_A using a *Behlke GHTS 100A* solid-state switch. Ions are typically ejected with an energy of several keV/q. The electron collector is a water-cooled grounded electrode, with a small hole in the middle to let ions through. It is situated in a low magnetic field, such that the electron beam is widened before hitting the collector. The collector is followed by four electrodes, which serve as the extraction system for the ions. While the electrode closest to the Wien filter is grounded, the others are usually set to negative voltages down to -8 kV. The electrode next to the collector should be on a voltage below -3 kV in order to reflect electrons passing the collector. Except for the cathode voltage, which is supplied by a *DREEBIT* high-voltage (HV) supply, all voltages applied to the EBIT and the extraction system are supplied by *CAEN A1526P/N* HV-modules.

The Wien filter consists of entrance and exit apertures, two opposing electrodes with voltages of equal magnitude but opposing sign applied, and a magnetic field being both perpendicular to the electric field and the ion flight direction. The magnetic field of strength ~0.5 T is created by permanent magnets. The aperture size can be either 0.5, 1 or 1.5 mm. With aperture sizes of 0.5 and 1 mm, the resolution of the filter ranges from 20 to 100 [131]. The Wien filter voltages are supplied by *CAEN 1737P/N* HV-modules[7].

Injection of element of interest During all commissioning experiments, gas containing the element of interest was leaked through a fine-dosing valve and a capillary into the EBIT volume. For Xe- and Ar-ions, which were produced in the course of the experiments presented within this thesis, common Xe- and Ar-gas was used, respectively. For Re-ions, which were produced during the EBIT-start-up phase, the so-called MIVOC-technique[8] [133] was applied where Re is contained in a volatile compound ($C_8H_5O_3Re$ - see [118] for further details) being continuously pumped. The gas being produced in this process is mainly pumped away, but some of it leaks through the fine dosing valve into the EBIT. Under the influence of the intense electron beam of the EBIT, the compound gets fragmented and charge breeding of its' contents takes place. For details on the gas inlet system, see [118].

Performance The *Dresden EBIT-W* has proven to be a flexible ion source for commissioning experiments at PENTATRAP: For atomic numbers up to $Z{\approx}30$, any charge-state can be produced. Furthermore it is a very reliable source - during the experiments performed within this thesis, it has run for more than half a year almost continuously.

Although not the highest charge states can be obtained for heavy elements, the performance of the *Dresden EBIT-W* is sufficient in many cases, e.g. for the planned ^{187}Re-^{187}Os Q-value measurement (see Sec. 1.4): Charge breeding studies have shown that e.g. $^{187}\mathrm{Os}^{52+}$ can be obtained [118]. An osmium ion in this charge state would have a cyclotron frequency of ~30 MHz, being ~75 times higher than an axial frequency of 400 kHz. This would correspond to a suppression of the axial frequency uncertainty in the determination of ν_c by a factor of $4.5 \cdot 10^{-5}$ (see Eq. (2.22)).

---

[7] If their voltage range of 0 V to ±250 V is sufficient, these modules are preferred over the formerly used *CAEN 1733P/N* 3kV-modules, since the voltages are more stable.

[8] Metal Ions from the VOlatile Compounds

3.2.4. The Heidelberg EBIT

Setup The Heidelberg EBIT (HD-EBIT) at the Max-Planck-Institut für Kernphysik in Heidelberg is one of few EBITs that can go to the highest charge states even for heavy elements. It is situated in the EBIT hall in a separate Faraday room. It was designed to produce an electron beam at an energy of up to 350 keV [134]. With a recently installed new cathode a current of up to ~500 mA can be produced [135]. Usual extraction energies are in the range of 5 to 10 keV/q. For the coupling of PENTATRAP to the HD-EBIT, a new beamline has been designed, which will be installed in the near future [136].

Injection of species of interest Similar to the *Dresden EBIT-W*, gas can be leaked into the trap volume. The gas is either naturally occurring or produced by means of the MIVOC-method. In the near future, a wire probe technique, which is very economical regarding sample material consumption, will be tested. In this technique, a thin wire, plated with a thin layer of the sample material, is inserted into the trap near the electron beam. Sample atoms are sputtered off the wire by ion impact [137]. This technique is particularly interesting in cases where only a very limited amount of sample material is available. For instance, a ^{163}Ho-sample will contain not more than a few 10^{16} atoms.

Performance The maximum electron beam energy that has so far been obtained with the HD-EBIT is 125 keV [138]. This would be sufficient to produce bare lead. The new cathode has delivered currents up to $\sim$ 420 mA at an electron energy of 20 keV. Although the bucking coil for the reduction of the magnetic field at the position of the cathode is broken, stable ion-currents on the order of pA have been obtained for helium-like xenon [135]. With the upcoming repair of the coil, even higher yields are expected.

3.3. Ion transport

The PENTATRAP beamline interfaces the *Dresden EBIT-W* with the trap setup[9]. It ranges from the Wien filter all the way down into the magnet and ends at the Faraday cup below the trap tower. An overview of the beamline is shown in Fig. 3.5. In Sec. 3.3.1, the ion optics to control various ion bunch parameters is described. In Sec. 3.3.2, diagnostic tools are discussed.

3.3.1. Ion optics

Electrode system Below the upper diagnostic station, a combined einzel lens- and steerer-unit is placed, consisting of four cylindrical electrodes. The focus of an ion bunch can be varied by changing the voltage at the second electrode (called D1). The third electrode is quartered. The bunches can be steered towards the Penning

---

[9] At a later stage, the beamline will be extended to the HD-EBIT. The beamline-extension is part of the PhD-thesis of H. Bekker [136].

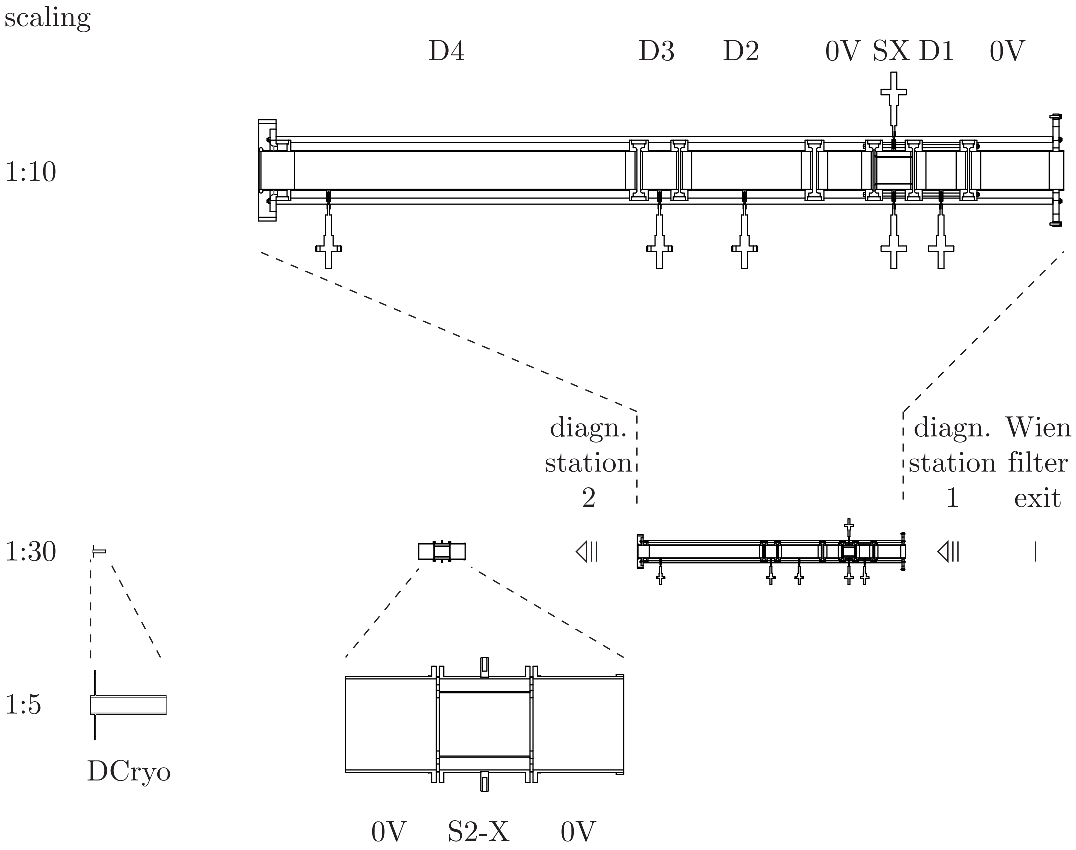

Figure 3.5.: A schematic overview of the beamline is shown. To give an idea of the length scales, the scaling factors are given to the left. The total length of the beamline from the Wien filter exit to the cryogenic drift tube is about 3.7 m. For further details, see text.

traps by changing the voltages at the four segments (called S1, S2, S3 and S4) of this electrode.

The three cylindrical electrodes (called D2, D3 and D4) following this unit can be used as drift tubes for the deceleration of ion bunches. Usually, D4 is chosen for deceleration, since it is the longest electrode, having a length of 50 cm at a diameter of 5 cm. This results in a ∼20 cm long field free drift region. With this drift tube, ions are decelerated from several keV/q to energies below 200 eV/q.

Closely above the magnet's top flange, an einzel lens with quartered central electrode is placed. By changing the voltage-offset at all four quarters of the central electrode (called S2-1, S2-2, S2-3 and S2-4), the focus of an ion bunch can be modified. By varying the individual voltages around the offset, the bunch can be steered towards the central axis of the trap.

A few mm above the trap tower, a drift tube (called DCryo) of length 5 cm with a diameter of 1 cm is placed. With this drift tube, ions are decelerated to energies of a few eV/q, such that they can be captured in the trap.

HV supplies and switches All electrodes of the beamline are supplied either by *CAEN A1526P*-modules (0 → +15 kV), *CAEN A1733P/N*-modules (0 → ±3 kV) or *CAEN 1737P/N*-modules (0 → ±250 V), which are incorporated in two *CAEN SY2527*-frames. To minimize absolute voltage fluctuations, the module with the smallest possible voltage-range was chosen for each electrode[10].

In the beamline, the voltages at the two drift tubes and at the S4-steering electrode (which occasionally was used as an ion-gate by setting the electrode either to ground or to some arbitrary high voltage) were switched using *Behlke GHTS100A*-switches. The trigger-pulse pattern was generated by a *National Instruments* FPGA-card.

During the efforts to transport ions from the EBIT to the trap region, difficulties in the interplay between the HV-supplies and the *Behlke*-switches occurred. These difficulties were related to the fact that the buffer capacitances C_B at both inputs of the switches are only 10 nF, while the load capacitances C_L, formed by electrodes, feedthroughs and cables, were usually several 100 pF. If the switch is supposed to switch from voltage U_+ to voltage U_-, the finite ratio C_L/C_B leads to an intermediate output voltage U_im of

$$U_\mathrm{im} \approx U_- + \frac{C_L}{C_B}(U_+ - U_-). \tag{3.8}$$

The fast switching happens between the voltages U_+ and U_im, not between U_+ and U_-. After the fast switching, the output voltage should slowly approach U_-, with the speed depending on the current that the HV-supply can deliver. Unfortunately, this was not the case with the *CAEN*-supplies. The short-term deviation of the monitored voltage from the set voltage of several percent led to significant fluctuations of the long-term output voltage of the *CAEN*-supplies, probably due to improper voltage regulation.

---

[10] For channels of all three modules, there can be deviations between the set and the internally monitored voltage. These deviations are different from channel to channel and change over time. For the *A1526P*-modules, they are specified to be ±0.3%±1 V [139]. For the *A1733P/N*-modules, they are specified to be ±0.3%±0.25 V [140]. For the *A1737P/N*-modules, they are specified to be ±0.3% [141].

To overcome this problem, the buffer capacitances at all switches (including the one for the EBIT-endcap) were increased by factors of 10 to 100 with externally connected HV-capacitors. With this measure, the voltages became much more stable. This enabled the loading of single ion bunches and ultimately of only a few ions (see Sec. 4.2.4).

Alignment Along the ion flight path, two bellows are used to connect three different parts of the experiments, which are:

A) the *Dresden EBIT-W* including Wien filter,

B) the beamline part ranging from the upper to the lower diagnostic station,

C) the lower einzel lens and the cryogenic insert.

The internal alignment of these parts and the alignment between them are crucial for the successful transport and capture of the ions. Part B) can be aligned with respect to C) by means of a translation- and tilt-stage. The alignment of A) with respect to B) and C) is very critical. Without proper alignment, the behavior of the beam after deceleration is unpredictable - a slight change in the drift tube voltage will require completely different steerer settings to transport ions into the cryogenic region. In the first place, this prevented us from transporting slow ions to the trap region. In the coming setup, it will be possible to perform this alignment with a dedicated translation- and tilt-stage for the EBIT [142].

In the course of the thesis work, an internal alignment of the *Dresden EBIT-W* including the cathode, the trap, the extraction system and the Wien filter had to be carried out once. This was done after the electron current hitting the first trap electrode had become excessively high and the production rates had become too low.

3.3.2. Beam diagnostics

3.3.2.1. Beamline diagnostic stations

In the beamline, there is the option to mount two diagnostic stations - one below the EBIT and one below the upper drift tube (see Fig. 3.1). Each station (see Fig. 3.6) contains a Faraday cup and an MCP detector with a phosphor screen (*El-Mul Technologies*). These devices can be moved into the beam path with a one-axis manipulator. In the following, the MCP and the phosphor screen will be addressed. The Faraday cups will be addressed in Sec. 3.3.2.2.

The MCP acts as a charge amplifier. The current that is drawn when a bunch of ions hits the MCP is converted to a voltage with a resistor of several MΩ. This voltage is amplified with a fast amplifier (*ORTEC VT120C*). A constant-fraction discriminator (*ORTEC 935*) is used to convert the pulses generated by individual ions into rectangular pulses with an amplitude of -0.8 V. A multichannel scaler (*ORTEC MCS-pci*), which is triggered by the EBIT-extraction-pulse, counts the number of pulses in preset time-bins. By this, a time-of-flight (TOF) spectrum of the ions extracted from the EBIT can be recorded.

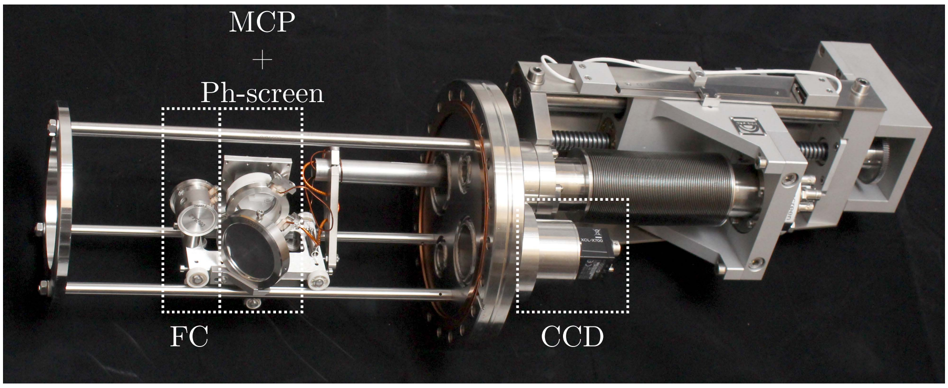

Figure 3.6.: A photograph of a diagnostic station is shown. A Faraday cup and an MCP detector with phosphor screen (both shown from the back) are mounted on a slide, that can be moved into the beam and out of the beam with a one-axis manipulator. Next to the phosphor screen, there is a mirror such that the image of the phosphor screen can be seen through a viewport and recorded with a CCD-camera.

An ion impinging onto the MCP initiates an electron avalanche at the impact site. Since the phosphor screen is on a more positive potential than the back plane of the MCP-stack, the electron avalanche is guided onto the screen, thereby generating fluorescence light. The diagnostic station contains a mirror below the phosphor screen and a viewport, such that this light can be recorded with a CCD-camera (*MATRIX VISION*). The read-out of the camera is triggered by the EBIT-extraction-pulse. The phosphor screen image can be used to monitor the shape and the position of an ion bunch extracted from the EBIT. Further details on the diagnostic stations can be found in [118].

3.3.2.2. Faraday cups

At PENTATRAP, Faraday cups are versatile tools for the optimization of the ion production and the transport of the ions from the source to the trap region. There is a Faraday cup installed in each diagnostic station (see Fig. 3.6) and one in the trap tower in the cryogenic region. Since these Faraday cups have been used extensively within the presented thesis work, the following two paragraphs are dedicated to details on Faraday cup measurements.

Measurement principle The principle of a Faraday cup is the following: When ions hit the Faraday cup, their charge changes the total charge Q of the cup. Since the cup has a certain capacitance C to ground, a voltage drop

$$U = \frac{Q}{C} \tag{3.9}$$

due to the total charge Q can be measured across C. The lower C is, the higher the sensitivity of the Faraday cup.

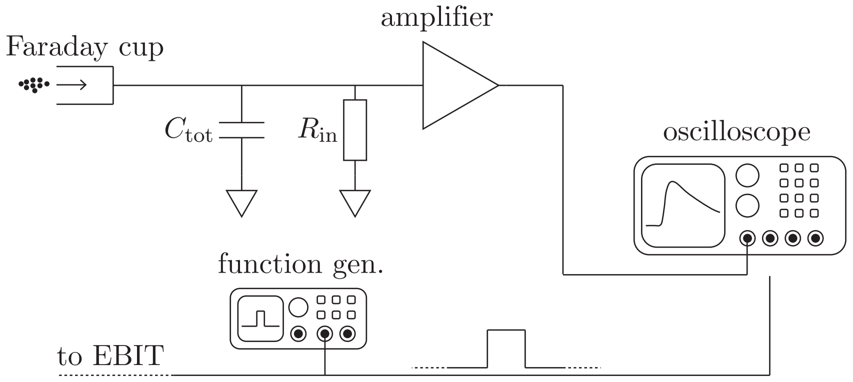

Figure 3.7.: A schematic setup of the Faraday cup and its readout is shown. Ions are extracted from the EBIT in bunches. The function generator triggering the extraction with a rectangular pulse also triggers the readout of the amplified Faraday cup voltage with an oscilloscope. The total capacitance to ground C_{tot} that the ions charge up is given by the sum of the Faraday cup's capacitance, cable capacitances and the amplifier's input capacitance. The input resistance of the amplifier gradually discharges the Faraday cup.

A complete measurement setup is shown schematically in Fig. 3.7. Since the EBITs at PENTATRAP are operated in bunched mode, the signal triggering the bunch extraction can be used to trigger the readout of the Faraday cup voltage with an oscilloscope. The signal is usually quite small (in the µV-range, but sometimes even below) and therefore has to be amplified with a low-noise amplifier. Cables and the input capacitance of the amplifier increase the total capacitance to ground C_{tot} that is charged up by the ions. The input resistance of the amplifier R_{in} gradually discharges the Faraday cup.

Signal shape A typical signal of the cryogenic Faraday cup is shown exemplarily in Fig. 3.8. The signal contains two important information:

1. The minimum-to-maximum amplitude (see Fig. 3.8) is a measure for the charge contained in a bunch[11].

2. The rising edge contains information about the TOF distribution of a bunch.

Knowing the TOF distribution/probability density function at the Faraday cup $p(t)$ where $t = 0$ is the extraction-time, the signal $U(t)$ is governed by the following differential equation:

$$\frac{dU(t)}{dt} = \frac{Q}{C_{\text{tot}}} p(t) - \frac{U(t)}{\tau}, \tag{3.10}$$

---

[11] Only when the rise time of the signal is much smaller than the time constant of the discharge, the minimum-to-maximum amplitude is a reliable measure. In all experiments performed within this thesis, this prerequisite was fulfilled.

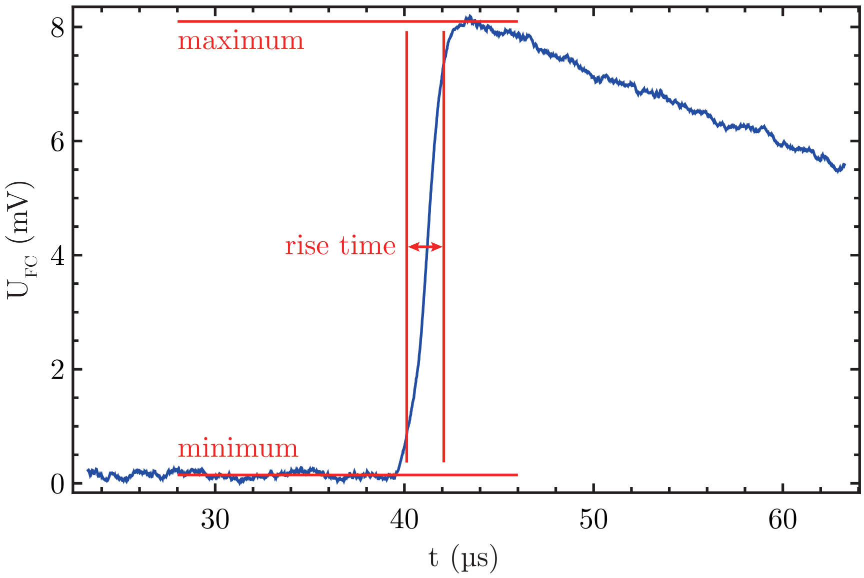

Figure 3.8.: A signal measured with the cryogenic Faraday cup is shown exemplarily. Times are relative to the time, when the ion bunch was extracted from the EBIT. The minimum and maximum signal amplitude as well as the 10%-90% rise time are marked. For further details see text.

where the amplification has been left aside for simplicity. The last term accounts for the discharge of the Faraday cup with the time constant τ, being determined by the input resistance R_{in} of the amplifier and the total capacitance C_{tot} of the Faraday cup, the cabling and the amplifier input. The shape of the signal is then given by:

$$U(t) = \frac{Q}{C_{\text{tot}}} e^{-t/\tau} \int_0^t e^{t'/\tau} p(t') dt'. \tag{3.11}$$

Since the width of the TOF distribution $p(t)$ (or equivalently the rise time of the signal) is usually much smaller than the discharge time constant τ, information about $p(t)$ is mainly encoded in the rising edge of the signal.

3.4. Penning traps

3.4.1. Magnet system

Superconducting magnet The superconducting PENTATRAP magnet (see Fig. 3.9) provides a field of strength ~7 T. In a volume with a radius of 2.5 mm and a length that covers the three inner of the five traps, it has a homogeneity of <25(1) ppm [118]. Absolute values of the magnetic bottle terms B_2 in the trap centers are roughly in the range of 10 to 100 nT/mm^2 for the three inner traps. The absolute values of the magnetic field gradients in the trap centers B_1 are typically a few µT/mm. To compare these values, the lowest reported magnetic field inhomogeneities at FSU-TRAP were $B_2 = -42(26)$ nT/mm^2 and $B_1 = -0.15(4)$ µT/mm [143]. In the

Figure 3.9.: A photograph of the cold-bore 7-T superconducting PENTATRAP magnet is shown. For details, see text.

future, the homogeneity of the magnetic field of the PENTATRAP magnet might be improved by either using compensation coils or ferroshims [143]. The 16 cm-diameter bore of the magnet is cold, i.e. it is filled with LHe due to a direct connection to the LHe-reservoir of the magnet.

Stabilization measures Several measures are taken to stabilize the field of the intrinsically already very stable magnet and to prevent disturbances due to external sources:

- The LHe-level and the He-gas pressure in the bore are actively stabilized [142, 144]. This stabilizes the temperature distribution along the cryogenic insert being placed in the bore (see Sec. 3.4.2). Therefore the temperature-dependent magnetic susceptibility of the materials used for the cryogenic insert is stabilized. With the UW-PTMS/THe-TRAP magnet, a magnetic field stability of a few tenths of a ppt/h was achieved by means of these measures [125].
- To reduce the influence of low-frequency changes of the large-scale external magnetic field, arising for instance from variations of the earth's magnetic field or the movement of a crane in the EBIT-hall, a compensation system consisting

1)	beamtube
2)	trap chamber (hidden)
3)	translation- and tilt-stage
4)	detection electronics chamber

Figure 3.10.: A photograph of the cryogenic insert with all main components marked is shown. The fragile cables are protected by PTFE-sleeves, which can be seen all over the setup. For details, see text.

of a fluxgate magnetometer, control electronics and a pair of Helmholtz coils will be used [145]. It is estimated that this compensation system, together with the self-shielding of the magnet, will give a total shielding factor of ∼10000 [118].

- For the shielding from high-frequency magnetic fields (and also for the shielding from stray electric fields), the magnet is situated in an aluminum housing.
- Temperature-variations of less than 100 mK both in the aluminum housing and in the rest of the magnet laboratory are achieved by means of active temperature stabilization. This limits, among other things, the following mechanisms:
    - Thermal expansion or shrinkage of parts of the setup, leading to relative shifts between the traps and the magnets' coils (see App. A),
    - pressure changes in the pressure reference for the LHe-level and He-pressure stabilization system,
    - temperature induced drifts of the magnetic field strength measured by the fluxgate magnetometer [118].

  Furthermore temperature stabilization is required for various electronic devices, e.g. for the ultra-stable trap voltage sources (see Sec. 3.4.5). From long-term temperature measurements in the aluminum housing (in an otherwise empty laboratory), an Allan deviation of ∼0.02 K on a time-scale of one day has been obtained [146].
- The three magnet-feet are situated on rubber-damped concrete cylinders embedded in the floor. Vibration amplitudes of the cylinders are ≤ 1 µm [146].
- In the future, a self-shielding superconducting compensation coil might further increase the magnetic field stability [147, 148].

3.4.2. Cryogenic insert

Components The cryogenic insert, which is shown in Fig. 3.10, can be separated into the following parts:

- Beamtube: The beamtube, which is made of stainless steel, connects the room temperature part of the beamline with the cryogenic part of the beamline and the trap. Furthermore, the tube holds radiation shields as well as the resonator, which is required for the LHe-level determination [142].
- Trap chamber: The trap chamber, which is made of OFHC-copper, hosts the trap tower (see Sec. 3.4.3), as well the cryogenic drift tube. A HV-feedthrough in the top lid is used to apply a voltage to the drift tube. The chamber has edge-welded bellows on top and below, such that it can be positioned in the magnetic field by means of a translation- and tilt-stage. Through the lower bellow, a direct connection to the detectors in the detection electronics chamber is provided.

- Translation- and tilt-stage: The translation- and tilt-stage, which is described in detail in [118], can be used to shift the trap chamber in the radial plane and to align the trap chamber with the magnetic field. Although free-space cyclotron frequency determinations by means of the invariance theorem are insensitive to tilts of the trap symmetry axis with respect to the magnetic field direction (see Sec. 2.2), a proper alignment is required to transport ions between traps without a significant increase of the magnetron radius.

- Detection electronics chamber: The detection electronics chamber hosts up to four axial and four cyclotron detectors (see Sec. 3.4.4). Besides the detectors, it consists of a vacuum-enclosure and a flange with 20 four-pin feedthroughs (see Fig. 3.11), which are required for the trapping voltages and the detectors. Most parts are made of OFHC-copper. The seal between the flange and the vacuum-enclosure, like all other cryogenic vacuum-seals in the setup, is realized with 1 mm thick indium wire.

- Cabling: A large number of cables is going from the room-temperature magnet flange down to the cryogenic region, e.g. for trapping voltages, RF excitations, the drift tube voltage or the supply of detection electronics. For all DC-voltages, varnish insulated manganin wire is used. For all AC-voltages, low temperature coaxial cable (*GVL Cryoengineering GVLZ034*) is used. For the voltage applied to the drift tube, this cable can be used as well. Since all cables in use are rather fragile, they are protected with PTFE-sleeves.

Past modifications The cryogenic insert has been subject to a number of modifications, which were mainly related to two issues: First, problems to lower the setup into the bore occurred due to a too large overall diameter. Second, vacuum leaks occurred.

The diameter of the magnet's bore is 160 mm. Initially, the maximum diameter of the cryogenic insert was specified to be 158 mm. The very first setup had three flanges and six radiation shields which were at this limit over (almost) the whole circumference. With this setup, it was not possible to lower the setup into the bore. The reasons for that were most probably air ice frozen to the bore, blocking the setup, and a too low conductance for He-gas, which is produced in vast amounts during the cool down of the insert. Since the He-gas could not flow out of the bore properly, the insert probably was standing on a gas cushion. In the following, the diameter at each point was reduced as much as possible[12]. After that, the setup was successfully lowered into the bore twice.

The experiment's Achilles' heel is the cryogenic feedthrough-flange on top of the resonator chamber (see Fig. 3.11). Twenty feedthroughs (custom made by *Kyocera*) consisting of an OFHC-copper jacket, a ceramic insulator and four 1 mm-diameter OFHC-copper pins are mounted to the flange. During the production of two flanges, both soldering and welding of the feedthroughs to the flange were tested (for details see [146]). For the second flange, the soldering was carried out by a specialized

---

[12] With a few exceptions, the diameter is now $\leq$156 mm at most points

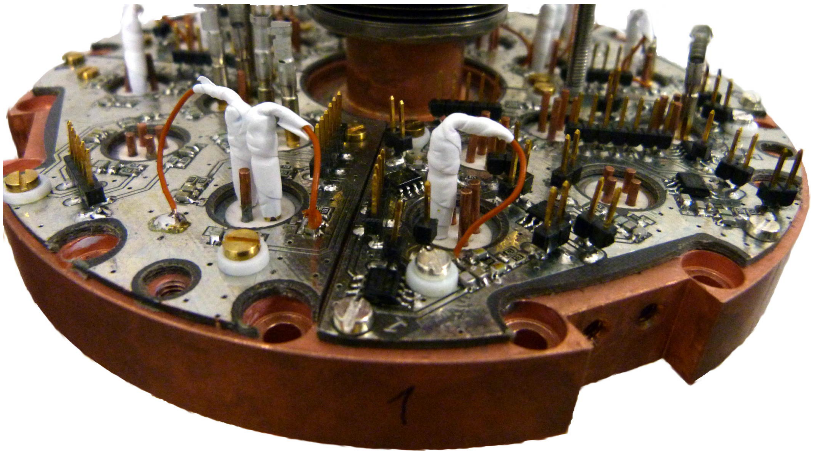

Figure 3.11.: The cryogenic feedthrough-flange, which is situated on top of the resonator chamber, is shown (without trap chamber flange). Filter boards for various DC-voltages and RF-signals are mounted on top of the flange. Cables and feedthrough-pins are connected by means of plugs.

company (*Reuter*). To exclude a damaging of the feedthroughs during the cabling process, soldering of cables to the pins was replaced by the use of plugs. Despite all of these measures, leaks were detected at multiple feedthroughs after several cool-downs of the setup. Single-pin feedthroughs of the same manufacturer have proven to be very reliable in the proton g-factor experiment [121]. But it has to be pointed out that in the proton g-factor experiment, cool-down times are much longer than at PENTATRAP where the setup is directly lowered into a bath of LHe. Thus the high failure-rate is either due to the four-pin-geometry or due to the rapid cool-down. Since the cool-down procedure cannot be altered, the feedthroughs will be removed in a future version of the setup. For a more detailed discussion of the cryogenic-feedthrough problem see App. B.

Future modifications For the near future, the following modifications of the existing setup, which address the problem of too short storage times caused by vacuum problems (see Sec. 4.2.5), are planned:

- New detection-electronics-chamber flange: All cryogenic feedthroughs will be removed from the detection-electronics-chamber flange (the former feedthrough-flange). Instead, feedthroughs will be placed in the room-temperature region and cables from the room-temperature region to the cryogenic region will be guided in the vacuum through stainless steel and copper capillaries.

- Pre-vacuum chamber: A pre-vacuum chamber around the cryogenic setup will significantly reduce the sensitivity of the vacuum in the trap region to leaks.

- Pumping barrier: A pumping barrier in the cryogenic region will reduce the gas-flow from the room-temperature vacuum region to the cryogenic vacuum region. Furthermore, the pumping barrier will address the problem of too large initial radial amplitudes of the ions in the trap (see Sec. 4.2.5).

- Charcoal absorbers: The charcoal absorbers in the cryogenic region, which are intended to increase the surface for cryogenic pumping, will be removed since they cannot be activated in the setup.

Further details about the listed modifications can be found in App. C.

For a future setup (PENTATRAP V2), which is currently under construction, all the concepts that will be tested in the next setup, are planned to be adopted with slight alterations. Furthermore, to reduce the difficulties in the lowering process, the maximum diameter of the interior of the pre-vacuum chamber will be 140 mm. Parts of the setup will be modified as follows:

- Detection electronics chamber: The diameter of the resonator chamber will shrink according to the maximum diameter. This calls for smaller replacements of the so far used resonators (see Sec. 3.4.4). The development of these resonators will be part of the master's thesis of Rima Schüssler [149].

- Translation and tilt stage: The current translation and tilt stage has to be replaced by a more compact version. Different concepts for the stage are currently under discussion, for instance a translation and tilt stage based on a hexapod, driven by cryogenic piezomotors.

For further details on PENTATRAP V2, the reader is referred to [150].

3.4.3. Trap tower

A core ingredient of the PENTATRAP experiment is the trap tower containing five identically constructed Penning traps, each consisting of five cylindrical electrodes. The traps allow for simultaneous free-space cyclotron frequency determinations, which will be addressed in Sec. 3.4.3.1. Design aspects will be summarized in Sec. 3.4.3.2. The realization of the five-trap tower and a simpler single-trap version that was used for the measurements presented in Chapter 4 will be discussed in Sec. 3.4.3.3.

3.4.3.1. Simultaneous free-space cyclotron frequency determinations using a two-trap scheme

In high-precision Penning-trap mass-ratio measurements, the statistical uncertainty is usually limited by magnetic field fluctuations [53]. Complementary approaches to push this limit are the stabilization of the magnetic field (see Sec. 3.4.1) and the minimization of the time between free-space cyclotron frequency determinations of the two ion species, of which the mass ratio should be determined.

The definite limit for the second approach is to determine both free-space cyclotron frequencies simultaneously. One way to realize this is by trapping of two ions on a shared magnetron orbit in a single trap [87, 151]. This method allowed for the to-date most precise mass-ratio measurements [56]. At PENTATRAP, this method would suffer from overly large systematic shifts due to ion-ion interaction, since mass-ratio measurements are going to be performed with highly-charged ions. Instead, simultaneous free-space cyclotron frequency determinations will be realized with a multi-trap technique, which will be described in the following.

Principle In Fig. 3.12, a scheme for the mass-ratio determination using two traps, named A and B, is shown. In each measurement cycle n, the free-space cyclotron frequencies $\nu_{c,\mathrm{A},n}$ and $\nu_{c,\mathrm{B},n}$ of the ions (indicated as *red* and *green* dots in Fig. 3.12) in trap A and B are determined simultaneously. Their ratio R_n is given by:

$$R_n = \frac{\nu_{c,\mathrm{A},n,\mathrm{green}}}{\nu_{c,\mathrm{B},n,\mathrm{red}}} = \frac{B_{\mathrm{A},n}}{B_{\mathrm{B},n}} \frac{q_{\mathrm{green}} m_{red}}{q_{\mathrm{red}} m_{green}} \equiv \rho_n \frac{q_{\mathrm{green}} m_{red}}{q_{\mathrm{red}} m_{green}}, \tag{3.12}$$

where $B_{\mathrm{A},n}$ ($B_{\mathrm{B},n}$) is the average magnetic field during the measurement of the cyclotron frequency in trap A (B). In the next measurement cycle $n+1$, the ion species in trap A and B are interchanged, the free-space cyclotron frequencies are determined simultaneously, and again the ratio R_{n+1} is calculated:

$$R_{n+1} = \frac{\nu_{c,\mathrm{A},n+1,\mathrm{red}}}{\nu_{c,\mathrm{B},n+1,\mathrm{green}}} = \frac{B_{\mathrm{A},n+1}}{B_{\mathrm{B},n+1}} \frac{q_{\mathrm{red}} m_{green}}{q_{\mathrm{green}} m_{red}} \equiv \rho_{n+1} \frac{q_{\mathrm{red}} m_{green}}{q_{\mathrm{green}} m_{red}}. \tag{3.13}$$

From two consecutive ratio determinations, one obtains:

$$R \equiv \sqrt{\frac{R_n}{R_{n+1}}} = \sqrt{\frac{\rho_n}{\rho_{n+1}}} \frac{q_{\mathrm{green}} m_{red}}{q_{\mathrm{red}} m_{green}}. \tag{3.14}$$

Under the assumption that the ratio of magnetic field strengths in trap A and trap B is constant over time, i.e. any (relative) change in the magnetic field is the same for both traps, this equation reduces to

$$R = \frac{q_{\mathrm{green}} m_{red}}{q_{\mathrm{red}} m_{green}}. \tag{3.15}$$

This means that the mass-ratio determination is unaffected by magnetic field fluctuations, as long as they affect the magnetic fields in trap A and trap B in the same way.

Magnetic field ratio fluctuations and drifts As pointed out in the last paragraph, Eq. (3.15) holds only in case the ratio ρ of the magnetic field strengths in the two traps is constant over time. However, there are potential sources of drifts and statistical fluctuations of ρ. One practical example of such a source is the stainless steel beam-tube (see Sec. 3.4.2): When the temperature gradient along the tube changes, e.g. due to a change in the temperature of the laboratory, the relative position of the traps and the magnetic field might change due to thermal expansion of the tube. In case the magnetic field gradients B_1 in both traps are different, the magnetic field ratio ρ will

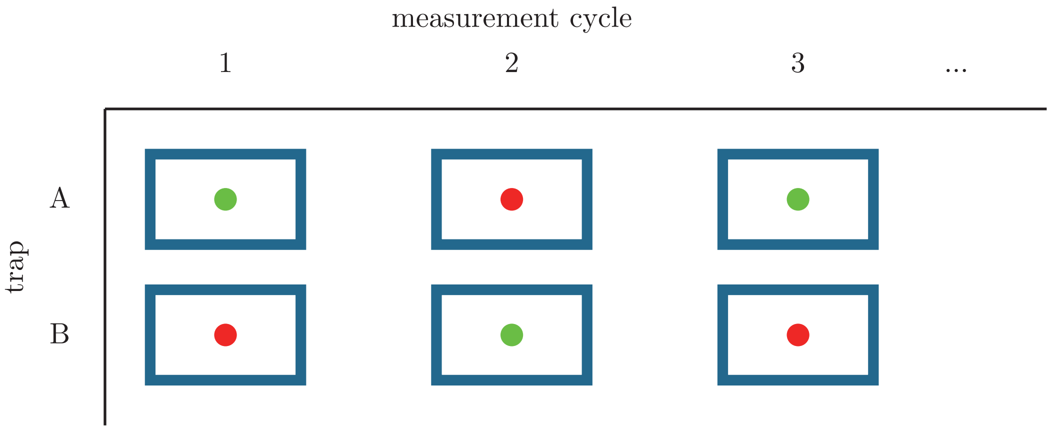

Figure 3.12.: A general scheme for the mass-ratio determination by means of simultaneous free-space cyclotron frequency measurements in two traps is shown. Two ions, indicated by *red* and *green* dots, are alternately trapped in trap A and B, indicated by blue boxes. In each measurement cycle n, the free-space cyclotron frequency of the ion in trap A ($\nu_{c,\mathrm{A}}$) and the free-space cyclotron frequency of the ion in trap B ($\nu_{c,\mathrm{B}}$) are determined simultaneously. For further details see text.

change because of that (see App. A). When the laboratory temperature fluctuates, ρ will fluctuate. And if the temperature drifts, ρ will drift[13].

While the uncertainty in the mass ratio due to statistical fluctuations could be reduced by repeated measurements, drifts would introduce a systematic shift in the mass ratio as determined by Eq. (3.14): If for instance ρ would be drifting linearly at a rate that results in a difference $\Delta\rho$ between successive measurements, this would lead to a relative shift of $-\Delta\rho/2\rho$ of the mass ratio determined by Eq. (3.14).

A change in the analysis can circumvent this problem: Instead of combining two successive measurements of R_n to one mass ratio, the measured values of R_n can be divided into two subsets, one with all measurements where n is odd and one with all measurements where n is even. Referring to the situation displayed in Fig. 3.12, this means that the odd-subset contains all cyclotron-frequency ratios where ion *green* is in trap A and ion *red* is in trap B, while the even-subset contains all cyclotron-frequency ratios where ion *red* is in trap A and ion *green* is in trap B. The mass ratio can then be extracted from simultaneous fits of the functions

$$R_{\mathrm{odd}}(t) = R \cdot \rho(t) \equiv R \sum_{i=0}^{m} a_i t^i \tag{3.16}$$

---

[13] This emphasizes the importance of a highly homogeneous magnetic field (see Sec. 3.4.1) and a well-stabilized temperature of both the laboratory and the LHe-bath, into which the beam-tube and the rest of the cryogenic insert are immersed (see Sec. 3.4.2).

and

$$R_{\text{even}}(t) = \frac{1}{R} \cdot \rho(t) \equiv \frac{1}{R} \sum_{i=0}^{m} a_i t^i \tag{3.17}$$

to the two subsets. Free parameters in the fit are the mass ratio R (see Eq. (3.15)) and the coefficients of the polynomial to model the drift of ρ. For the problem of finding the proper polynomial order m, the reader is referred to [115], where this problem is discussed in the context of modeling magnetic field drifts.

Implementation A possible implementation of the two-trap scheme using a stack of five traps is shown in Fig. 3.13. Traps 2 and 3 are used for simultaneous free-space cyclotron frequency determinations. Traps 1 and 4 are used as containers. Between measurement cycle 1 and 2, the ions in trap 1, 2 and 3 are transported adiabatically to traps 2, 3 and 4, respectively. Between cycle 2 and 3, the transport happens in reverse direction. If the initial loading of traps 1, 2, 3 with three ions of two different species (*red* and *green*) is carried out as indicated in cycle 1, the ion species is interchanged in the measurement traps after each cycle. Trap 5 can be used for monitoring of the magnetic field or of the trap voltage supply with the most suitable ion species (*black*).

An alternative implementation of the two-trap scheme using five traps is shown in Fig. 3.14. Traps 2 and 4 are used for simultaneous free-space cyclotron frequency determinations. When the initial loading of traps 1, 2, 3, 4 with four ions of two different species (*red* and *green*) is carried out as indicated in cycle 1, the interchange of ion species in the measurements traps can again be realized by simple adiabatic transport of the ions to their neighboring trap in up- or downward direction, depending on the cycle number. In this scheme, traps 1, 3 and 5 are not solely used as containers, but they can be used for ion preparation. For instance, time-consuming direct cooling of the cyclotron mode[14] can be carried out prior to the transport of an ion into the measurement traps. Therefore, the measurement in traps 2 and 4 can start right after the transport without any further preparation.

Besides these two schemes, one can think of other schemes, as well. For instance, in case the magnetic field is extremely stable and one trap is highly preferable over the others, one could think of performing sequential measurements in this trap instead of simultaneous measurements in two traps. Which scheme will be applied will depend on various factors. In the following, three of these factors are named exemplarily:

- Magnetic field configuration: The magnetic field inhomogeneities vary from trap to trap. This alters systematic shifts and makes some traps preferable over others.

- Trapping potentials: Although the trap electrodes have been manufactured with very high precision (see Sec. 3.4.3.3), electrostatic anharmonicities might be different for each trap due to remaining manufacturing uncertainties or mounting errors. Furthermore, the potential of charge patches will be different for each trap. This might make some traps preferable over others.

---

[14] Cyclotron cooling times can be several 100 s.

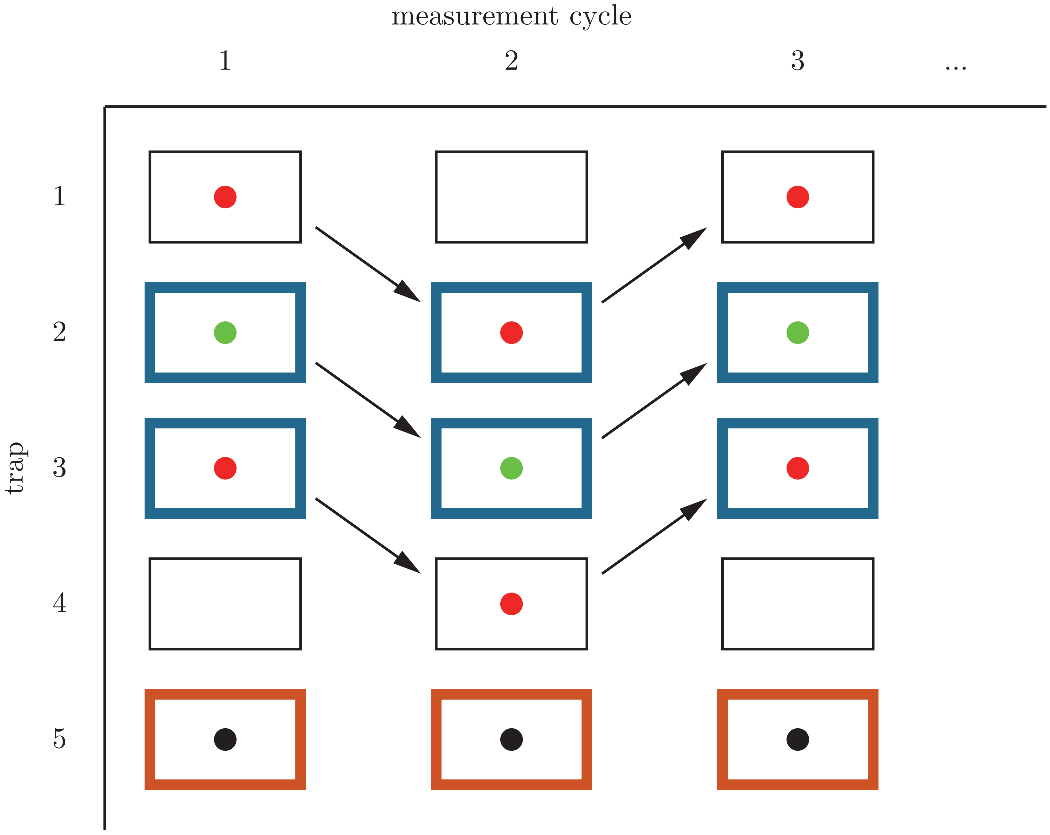

Figure 3.13.: A possible implementation of the two-trap scheme using a stack of five traps is shown. The traps are indicated by boxes and the ions by dots where the color indicates the ion species. The two measurement traps 2 and 3 are highlighted blue, the monitor trap 5 is highlighted in red. Traps 1 and 4 are used as container traps. Adiabatic transport of an ion to a neighboring trap between measurement cycles is indicated by an arrow. For further details see text.

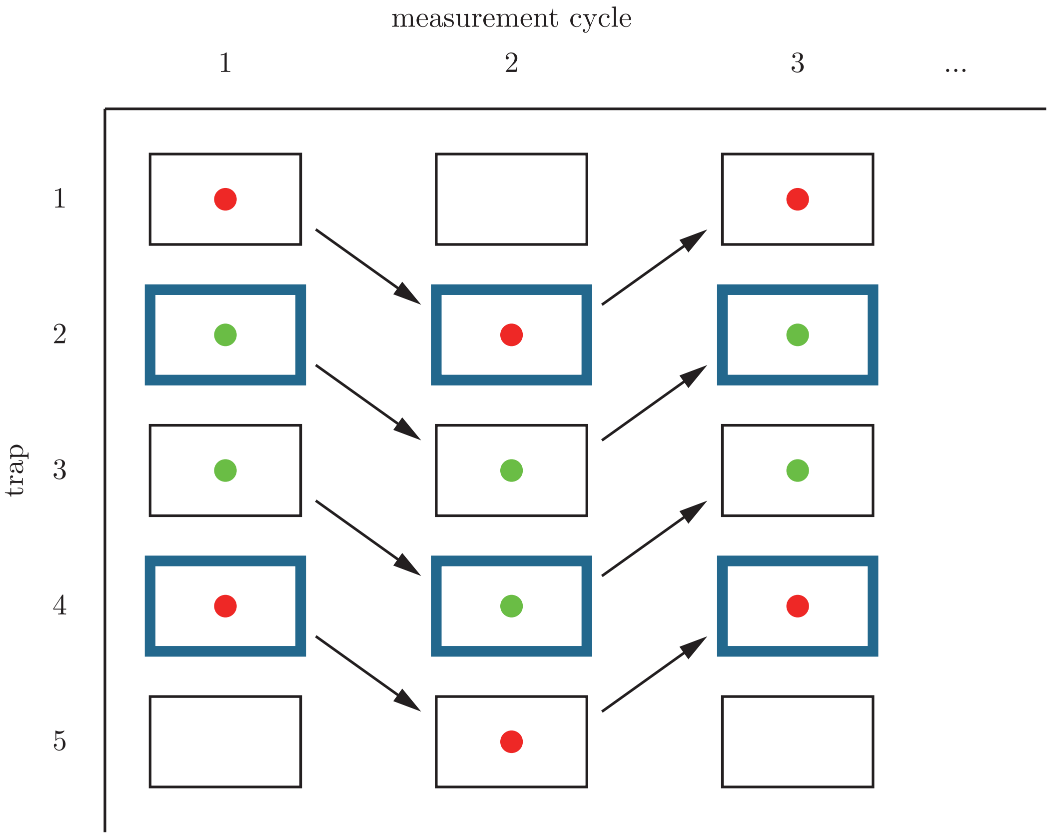

Figure 3.14.: An alternative implementation of the two-trap scheme using a stack of five traps is shown. The traps are indicated by boxes and the ions by dots where the color indicates the ion species. The two measurement traps 2 and 4 are highlighted blue, the preparation-traps 1, 3 and 5 are non-highlighted. Adiabatic transport of an ion to a neighboring trap between measurement cycles is indicated by an arrow. For further details see text.

- Mass or charge-to-mass ratio difference: Which characteristics of the traps matter the most will depend on how close or far the two ions of interest are in charge-to-mass ratio or in mass. Some systematic shifts will cancel out in the ratio to very high precision in cases of the ions being a mass-doublet, while being highly relevant for non-mass-doublets.

Systematic shifts in the two-trap scheme A relative systematic free-space cyclotron frequency shift δ shifts two successively measured cyclotron frequency ratios R_n and R_{n+1}, as defined in Eq. (3.12) and Eq. (3.13), as follows:

$$\frac{\Delta R_n}{R_n} \approx \delta_A(green) - \delta_B(red), \tag{3.18}$$

$$\frac{\Delta R_{n+1}}{R_{n+1}} \approx \delta_A(red) - \delta_B(green), \tag{3.19}$$

where A and B are trap-indices. Since a number of shifts δ will be different for trap A and B, δ_A and δ_B will usually not cancel in a single determination of R_n, even for mass-doublets. $\Delta R_n/R_n$ and $\Delta R_{n+1}/R_{n+1}$, however, will usually be nearly identical for mass-doublets. Therefore, the influence of δ will be strongly suppressed in this case. This is of course only true for time-independent shifts.

For non-mass-doublets, some shifts which are suppressed for mass-doublets will play a role. In this case, depending on the stability of the magnetic field and the uncertainty in the correction for the shift, a mass-ratio determination by means of alternating free-space cyclotron frequency determinations in the trap with the smaller systematic shifts might be favorable. This, however, doesn't require a change of the measurement procedure: The same measurement scheme as shown in Fig. 3.12 can be applied, the data is just analyzed independently for one of the traps. Thus the decision whether to use the two-trap scheme or an alternating scheme for the mass-ratio determination is not a matter of how to do the measurement, but rather a matter of data analysis.

3.4.3.2. Design aspects and calculated properties

The PENTATRAP traps should fulfill the following requirements (for a more detailed discussion see [115, 119]):

1. They should allow for different implementations of the two-trap scheme introduced in Sec. 3.4.3.1.

2. They should allow for loading of externally produced ions (see Sec. 3.2) and adiabatic transport of ions between the traps (see Sec. 3.4.3.1).

3. To avoid shifts of the eigenfrequencies due to electrostatic anharmonicities (see Sec. 2.2), the traps should be *compensated*, i.e. at a certain tuning ratio[15] T_{ideal},

---

[15] The tuning ratio T is defined as the ratio of the voltage U_{CE} that is applied to the correction electrodes and the voltage U_R that is applied to the central ring electrode: $T = U_{CE}/U_R$. For a definition of the electrodes, see Fig. 2.2.

Table 3.1.: Calculated properties of a PENTATRAP trap are shown. The values $c_{4,6,8}$ are calculated at T_{ideal}. The values in parenthesis are errors due to an estimated machining-precision of ±5 µm. For further details see text.

T_{ideal}	0.881032
c_2 (mm^{-2})	$-1.496(0.007) \cdot 10^{-2}$
d_2 (mm^{-2})	$-0.025(1.241) \cdot 10^{-4}$
c_4 (mm^{-4})	$0.000(4.199) \cdot 10^{-6}$
d_4 (mm^{-4})	$-8.406(0.001) \cdot 10^{-4}$
c_6 (mm^{-6})	$-0.008(1.892) \cdot 10^{-7}$
d_6 (mm^{-6})	$3.579(0.019) \cdot 10^{-5}$
c_8 (mm^{-8})	$1.672(0.077) \cdot 10^{-7}$
d_8 (mm^{-8})	$-1.196(0.010) \cdot 10^{-6}$

the two leading anharmonicity coefficients c_4 and c_6 should vanish simultaneously

4. For experimental reasons (which are discussed for instance in [121]), the trap should be *orthogonal*, i.e. the axial frequency should not depend on T.

5. Even for mass differences as big as one atomic unit, image charge shifts (see Eq. (2.38)) should not preclude mass-ratio measurements on a 10^{-12}-precision level.

The first two requirements lead to a trap stack consisting of five identical cylindrical traps [113], each consisting of five electrodes. For the third and fourth requirement, an analytical solution could be found [115]. To fulfill the fifth requirement, a trap diameter of 10 mm was chosen. Details on the trap geometry can be found in [115].

In Tab. 3.1, important electrostatic trap properties, calculated for the ideal trap geometry with 1 µm-rounding for manufacturing, are summarized. $c_{2,4,6,8}$ are the coefficients of the potential written in the form of Eq. (2.25) at the tuning ratio T_{ideal} where c_4 vanishes. In case T deviates from T_{ideal}, the coefficients $c_{2,4,6,8}$ are given by $c_{2,4,6,8}(T_{\text{ideal}}) + d_{2,4,6,8}(T - T_{\text{ideal}})$. The values in parenthesis are errors due to an estimated machining precision of ±5 µm. All values are taken from [115, 119] with a correction of the sign of d_4 [152].

While the ideal values are of no concern, it is still unclear whether the values including the machining error are critical or not: Since these errors were obtained by means of error propagation using the analytical form of the c- and d-coefficients and their dependence on different lengths of the trap geometry, it is not clear how the different errors are correlated. Furthermore it is unclear, how assembling errors influence the trap performance. In order to draw a final conclusion about the expected trap performance, these two question should be clarified in the near future.

3.4.3.3. Realization

Electrodes and insulators The trap electrodes are made of OFHC copper. The purity of the copper is >99.999% to minimize the magnetic permeability caused by impurities. The electrodes are plated with 20 µm of gold to avoid oxidized regions that could charge up and disturb the trapping potential. The insulators between the electrodes are cylindrical sapphire-rings. The final tolerance of the gold-plated electrodes is ±5 µm, while the tolerance of the sapphire rings is ±1 µm. A detailed discussion of the construction and the manufacturing of the trap electrodes can be found in [118].

Trap tower The trap tower is held by two gold-plated OFHC copper plates. The interfaces of these plates to the endcaps are of endcap-like shape, such that similar electrostatic boundary conditions are provided for the outer traps like for the three inner traps. The plates are held together by three posts made of CuSn8. At the lower plate, the rods are fixed with copper nuts, while at the upper plate, beryllium copper disk springs between the plate and the nut compensate for a ∼0.3 mm different shrinkage of the posts and the trap tower. Whether the springs are necessary will be tested in the near future: Other experiments (see e.g. [121]) do not compensate for a different shrinkage of (copper-)posts and the trap stack without cracking the sapphire insulators. Furthermore, insufficient compression of the trap stack could result in gaps between the electrodes being larger than specified. In [115] it has been pointed out that deviations from the ideal gap sizes are the most severe sources of error in the trapping potential.

For the experiments carried out within this thesis, a simplified trap stack was constructed. It consisted of a single trap, a Faraday cup (being a copper cup with the contours of a trap) below the trap and three dummies (long cylindrical copper electrodes with outer contours of a trap). A cut through the setup is shown in Fig. 3.15a. Due to time constraints, the dummies and the Faraday cup weren't gold-plated.

In the next experimental run, the trap stack containing all five traps (see Fig. 3.15b) will be utilized. As will be shown in Sec. 4.1, the Faraday cup is a very helpful tool for the optimization of the ion transport and capturing. Therefore, a Faraday cup that can be incorporated into the five-trap stack has been constructed [142].

3.4.4. Detection electronics

At PENTATRAP, eigenfrequencies are measured with a non-destructive image-current detection technique. With this technique and the ultra-high vacuum in the trap region that is anticipated with the future modifications presented in Sec. 3.4.2, free-space cyclotron frequency ratio determinations can be performed over and over again with the same set of ions. Furthermore single-ion sensitivity is achievable with this method. Thus, free-space cyclotron frequency shifts due to ion-ion-interaction are of no concern.

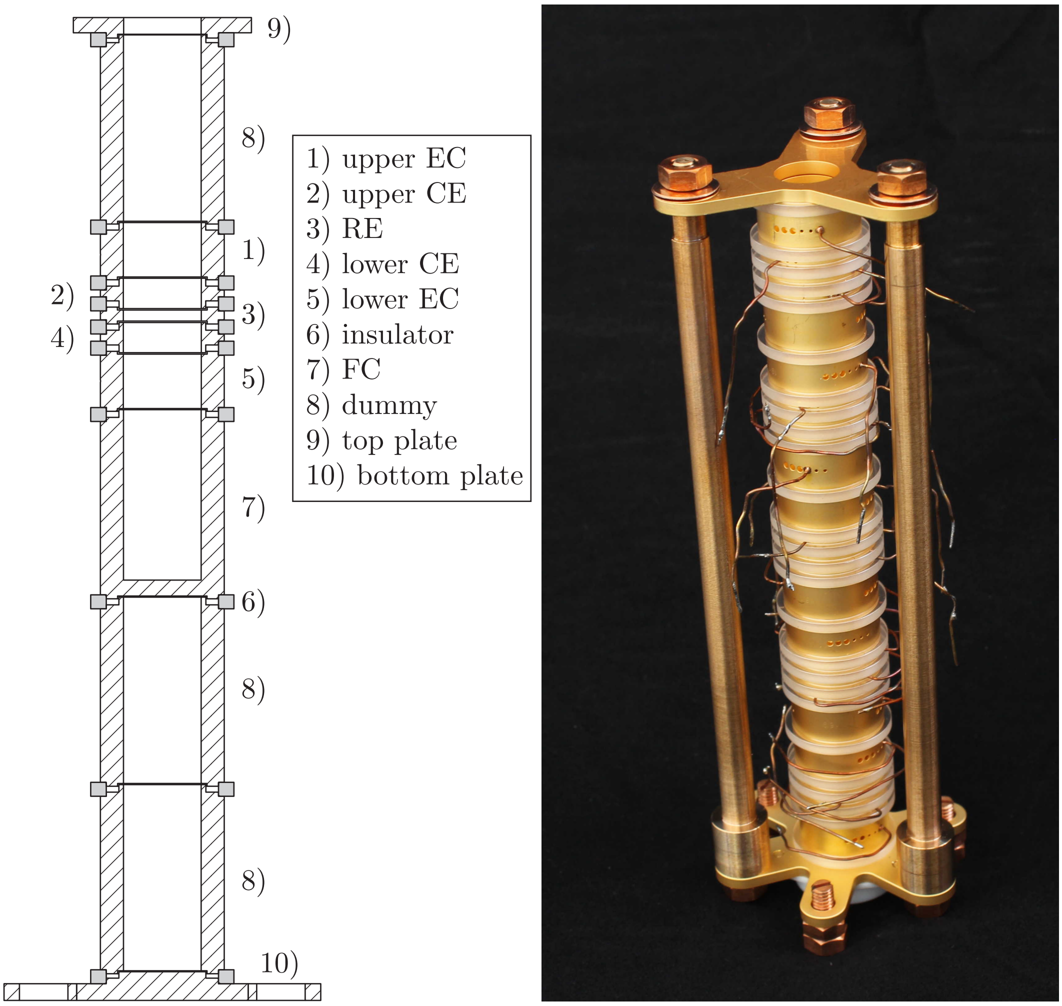

(a) (b)

Figure 3.15.: In (a) a cross-sectional drawing of the trap stack used for the first commissioning experiments is shown. It incorporates one trap, a Faraday cup (FC) and three trap-dummies. In (b) the five-trap stack with the newly constructed Faraday cup mounted below (of which only the PTFE-holder can be seen) is shown. For further details, see text.

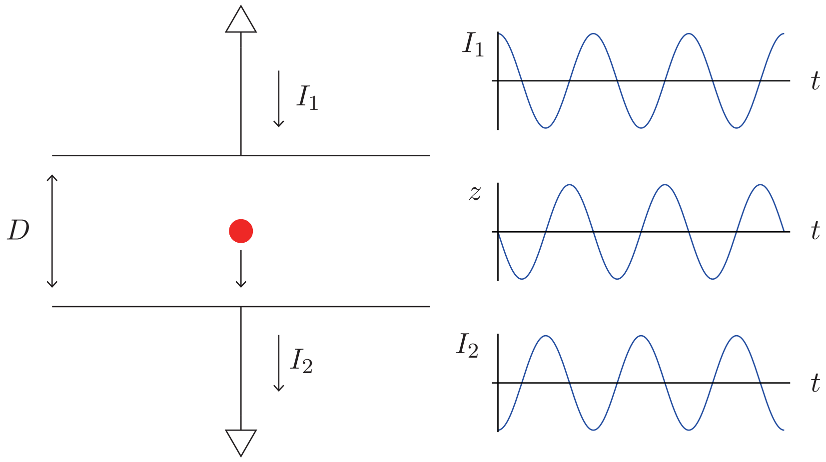

Figure 3.16.: The principle of image-current detection is illustrated. The ion oscillates between to infinitely extended grounded conducting plates, separated by a distance D. The currents flowing to the conductors due to varying image charges induced on them oscillate at the same frequency as the ion. For further details see text.

3.4.4.1. Detection principle

Image currents An ion being situated between conductors that are held on fixed potentials induces surface charges on these conductors, such that the potentials on the surfaces stay constant. Therefore, if the ion moves relative to the conductors, currents will flow to the conductors to compensate for changing integrated surface charges. A very simple case of an ion of charge q and mass m moving between two infinitely extended parallel grounded conducting plates, separated by a distance D, is shown in Fig. 3.16. Using the Shockley-Ramo theorem [153, 154], the current to plate 1 and 2 is

$$I_{1,2} = \pm \frac{q\vec{v}\hat{e}_z}{D} = \pm \frac{qv_z}{D}. \tag{3.20}$$

If the ion performs a harmonic oscillation between the two plates with an amplitude z_0 at frequency ω_0, the current oscillates at the same frequency:

$$I_{1,2} = \pm \frac{qz_0\omega_0}{D} \sin(\omega_0 t). \tag{3.21}$$

The exchange of the two-plate setup by a cylindrical Penning trap is simply accompanied by an exchange of D with the effective electrode distance D_{eff} [155]. The effective electrode distances of different electrodes of the PENTATRAP traps will be given in Sec. 3.4.6. Analytic expressions for effective electrode distances have been derived in [121].

Peak detection Image currents induced by a single ion are typically on the order of 10 fA. To convert these tiny currents into measurable voltages, an inductor with

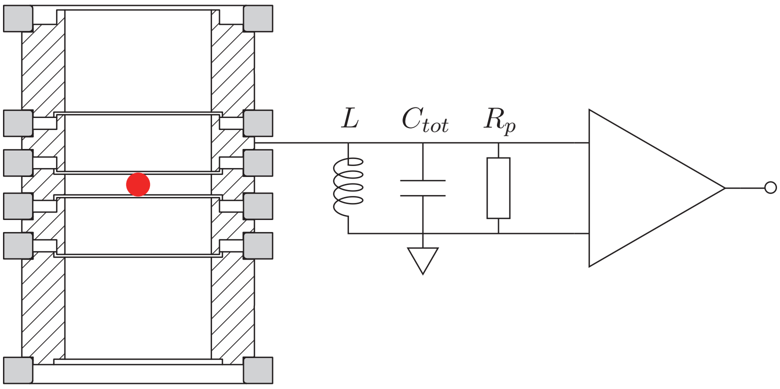

Figure 3.17.: A system for the detection of image currents induced by the motion of an ion in a Penning trap is shown schematically. The detection system consists of a high-Q resonator connected to the trap and an amplifier. For further details see text.

inductance L is connected to the trap. Together with the total capacitance in parallel C_{tot}, being the sum of the trap capacitance, the inductor's self-capacitance and further capacitances, a parallel LCR-circuit is formed (where the parallel-resistance R_p arises from resistive and dielectric losses). Usually, an amplifier is attached to the resonator, which determines the signal-to-noise ratio (see Sec. 3.4.4.3) and decouples the resonator from following signal-transmission lines. A complete detection system is shown schematically in Fig. 3.17.

The flow of the image-current I at the frequency $\nu = \omega/2\pi$ through the complex impedance Z of the LCR-circuit leads to a voltage drop

$$\begin{aligned} U &= I \cdot Z_{LCR}(\omega) && (3.22)\\ &= I \cdot (R_p^{-1} + (i\omega L)^{-1} + i\omega C)^{-1} && (3.23)\\ &= I \cdot \omega L \left(\frac{1}{\frac{1}{Q} - i\left(1 - \frac{\omega^2}{\omega_{LCR}^2}\right)} \right), && (3.24) \end{aligned}$$

where in the last equation, the LCR-circuits' resonance frequency $\omega_{LCR} = (LC)^{-1/2}$ and quality factor (Q-value) $Q = R_p/\omega_{LCR}L$ have been introduced. In Fig. 3.18 it can be seen that the image current signal appears as a sharp peak at the ion's frequency on top of the thermal noise spectrum of the detection circuit. The thermal noise[16] spectrum is of the form [156, 157]

$$U_J(\omega) = \sqrt{4k_BT\,\mathfrak{Re}(Z_{LCR}(\omega))\Delta\nu}, \tag{3.25}$$

where T is the temperature of the detection circuit and $\Delta\nu$ is the measurement bandwidth.

---

[16] also called Johnson-noise or Nyquist-Johnson-noise

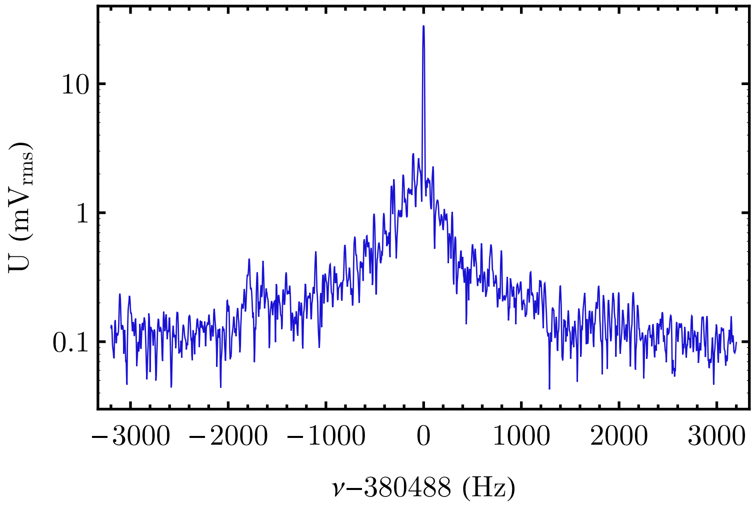

Figure 3.18.: A frequency spectrum of the detector signal with the image current-peak of (parametrically excited) ions at the center of the detector is shown. The background spectrum is the thermal noise of the detector. For further details see text.

Ion cooling and signal in thermal equilibrium The ion's equation of motion is altered by the interaction with the detector in two ways:

1. The voltage drop $U = I \cdot Z_{LCR}(\omega)$ across the detection circuit acts back on the ion by means of a decelerating electric field $-U/D_{\mathrm{eff}}$.
2. The thermal noise U_J of the detector is driving the ion by means of the electric field $-U_J/D_{\mathrm{eff}}$.

The resulting equation of motion, which is exemplarily shown for the axial mode, reads:

$$\ddot{z} + \frac{q^2 Z_{LCR}(\omega_z)}{m D_{\mathrm{eff}}^2}\dot{z} + \omega_z^2 z = -\frac{q U_J}{m D_{\mathrm{eff}}}. \tag{3.26}$$

The complex damping term arising from the image current back action has two consequences: First, the imaginary part of the damping leads to a shift of the resonance frequency - this issue will be discussed separately in Sec. 3.4.4.7. Second, the real part of the damping term

$$\gamma = \frac{q^2\,\mathfrak{Re}(Z_{LCR}(\omega))}{m D_{\mathrm{eff}}^2} \tag{3.27}$$

leads to an actual damping of the axial oscillation, with the energy of the ion being dissipated in the resistor. Neglecting the thermal noise driving force for a hot ion, the energy of the ion is reduced exponentially with the time constant

$$\tau = \frac{m D_{\mathrm{eff}}^2}{q^2\,\mathfrak{Re}(Z_{LCR}(\omega))} = \gamma^{-1}, \tag{3.28}$$

until the ion is in thermal equilibrium with the detector, i.e. the mean dissipation power equals the mean thermal noise driving power.

In thermal equilibrium, it is convenient to model the ion with an equivalent series-LC circuit [158]. This can be motivated by rewriting Eq. (3.26) in terms of the image current:

$$0 = \frac{mD_{\text{eff}}^2}{q^2}\dot{I}(t) + Z_{LCR}(\omega)I(t) + \frac{\omega^2 mD_{\text{eff}}^2}{q^2}\int I(t')dt' + U_J \tag{3.29}$$

$$= l\dot{I}(t) + Z_{LCR}(\omega)I(t) + \frac{1}{c}\int I(t')dt' + U_J, \tag{3.30}$$

where in the last equation, the ion's equivalent inductance l and the ion's equivalent capacitance c have been introduced. In Fig. 3.19a, the trap and the detector arrangement with the ion replaced by its equivalent series-LC circuit is shown. Using this model, the lineshape of the ion signal which shows up in the thermal noise spectrum of the resonator can be calculated (see Fig. 3.19b). Both the case where the ion is on-resonance ($\omega_z = \omega_0$) and off-resonance ($\omega_z \neq \omega_0$) are discussed in great detail elsewhere (see e.g. [121, 158, 159]). Here only the result for the on-resonance case is summarized. In this case, a dip appears in the center of the detector's thermal noise spectrum. The dip has a Lorentzian lineshape with a width of [158]

$$\Delta\nu = \frac{n}{2\pi}\frac{q^2 R_p}{mD_{\text{eff}}^2} = \frac{n\gamma}{2\pi}, \tag{3.31}$$

where γ is the real damping constant on resonance and n is the number of ions. Thus, the width of the dip can be used to count the number of ions being trapped. The dip-method will be used at PENTATRAP to determine the axial frequency. The choice of the proper dip width is discussed in [115].

3.4.4.2. Indirect cooling and detection methods

The axial motion as well as the cyclotron motion can be detected and cooled by means of the method described in the previous section. This is not possible for the magnetron mode, since it is meta-stable: Direct coupling to a dedicated detector would increase the magnetron radius, leading to increased systematic shifts or even particle loss. For the magnetron motion, indirect cooling and detection methods have to be applied, in which the magnetron motion is coupled to one of the other motions by means of quadrupolar RF-fields at the proper sideband-frequency (see Sec. 2.3). For the other two motions, indirect cooling and detection can be beneficial as well, as will be explained in the following.

Sideband cooling As discussed in Sec. 2.3, all eigenmotions of an ion in a Penning trap can be coupled using quadrupolar RF-fields, such that the actions of the eigenmotions are exchanged periodically. Assuming that one of the eigenmotions (called A) is initially excited and the other eigenmotion (called B) is in contact with a detector at temperature T_B, energy is constantly removed from the coupled system until the

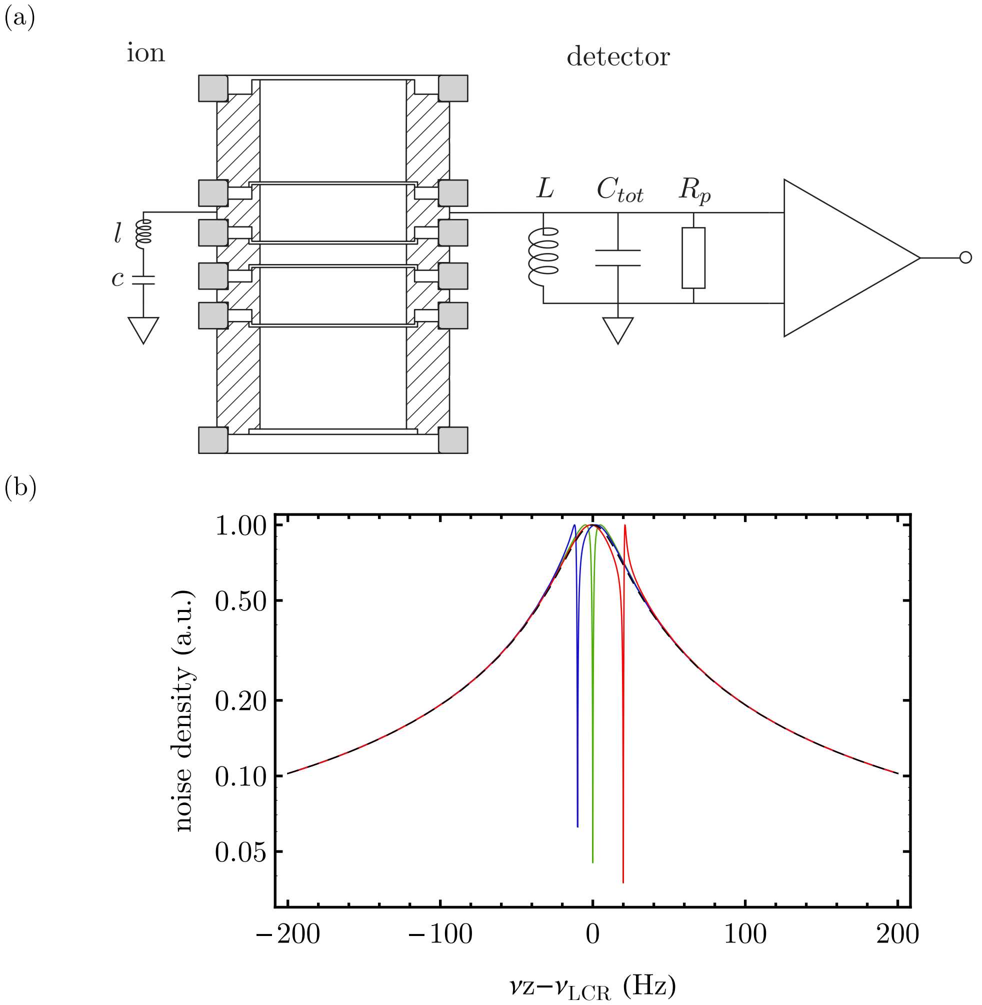

Figure 3.19.: In (a) an equivalent circuit for the description of the interaction of a thermalized ion with the detector is shown. In (b) the resulting thermal noise spectrum is shown for various detunings between resonator and ion frequency (green: no detuning, blue: -10 Hz, red: +20 Hz). The ion shows up as a dip in the thermal noise spectrum of the detector. The black dashed line is the thermal noise spectrum of the detector only. For further details, see text.

Table 3.2.: Temperatures achievable by means of sideband cooling are shown exemplarily for an $^{40}\mathrm{Ar}^{8+}$-ion with eigenfrequencies $\nu_+ \approx 21.5$ MHz, ν_z=400 kHz and $\nu_- \approx 3.7$ kHz assuming detector temperatures of 4.2 K. For further details see text.

coupling to	axial detector		cyclotron detector	
mode	sideband	temperature	sideband	temperature
magnetron	$\nu_z + \nu_-$	39 mK	$\nu_+ + \nu_-$	0.7 mK
axial	-	4.2 K	$\nu_+ - \nu_z$	78 mK
cyclotron	$\nu_+ - \nu_z$	226 K	-	4.2 K

cooling limit is reached. In [29] it has been shown that the cooling limit is reached, when the time-averaged quantum numbers in the coupled modes are the same. From this, it can be deduced that in the cooling limit, the temperature of the eigenmotion A (neglecting any sign-issues related to the negative magnetron energy) is:

$$T_A = \frac{\omega_A}{\omega_B} T_B. \tag{3.32}$$

Temperatures achievable at PENATRAP are shown exemplarily in Tab. 3.2. With this method, cooling below the physical temperatures of the detectors can be achieved.

Multi-dip method The coupling of eigenmotions using quadrupolar RF-fields at the respective sideband frequencies cannot only be used to cool ions, but also to detect the eigenfrequency of the motion that is not directly detected. A (near-)resonant coupling of two eigenmotions leads to a modulation of the amplitudes of both eigenmotions [111]. This results in a splitting of the detected signal in two signals (which can either be peaks [111] or energy-wise more favorable dips [160]). If e.g. the axial signals are detected, the signal-frequencies will be $\omega_{l,r} = \omega_z + \epsilon_{l,r}$ with

$$\epsilon_{l,r} = -\frac{1}{2}\left(\delta \pm \sqrt{\Omega_0^2 + \delta^2}\right), \tag{3.33}$$

where δ is the detuning from the true sideband frequency ω and Ω_0 is the Rabi-frequency (see Eq. (2.44)).

If for instance the cyclotron motion is coupled to the axial motion at the frequency $\omega_{coup} = \omega_+ - \omega_z + \delta$, the cyclotron frequency can be calculated as follows:

$$\omega_+ = \omega_{coup} + \omega_l + \omega_r - \omega_z. \tag{3.34}$$

It can be seen that an independent determination of the axial frequency is required for the determination of the cyclotron frequency.

Difficulties can arise from the instability of the axial frequency during the determination of the double-dip frequencies, which can partly be overcome by sandwiching the double-dip measurement between two axial frequency measurements or by the use of triple-/quintuple-dip methods [126, 160]. The statistical uncertainty in the determination of the cyclotron frequency by means of this method is finally limited by the uncertainty in the frequency determination from the dips. For eigenfrequencies similar to those at PENTATRAP, a limit on the order 10^{-10} was found [65].

Phase sensitive PnA method As has been pointed out in Sec. 2.2, a determination of the free-space cyclotron frequency of an ion with an uncertainty of a few parts in 10^{12} requires a determination of the cyclotron frequency with roughly the same uncertainty. Therefore the uncertainty in the determination of the cyclotron frequency achievable with multi-dip methods is too large for the precision that is aimed at.

Therefore a novel phase-sensitive method called PnA (standing for Pulse 'n' Amplify) [161] will be used. In this method, the cyclotron motion, being initially cold, is first excited with a dipolar excitation of defined phase to imprint a certain starting phase to the motion. The phase is then allowed to evolve undetected for a certain phase evolution time T. After this time, the cyclotron motion and the axial motion, being initially cold as well, are coupled with a quadrupolar RF-field at/near the sum-frequency $\nu_+ + \nu_z$. This leads to a coupling and a coherent amplification of both motions. After this, the axial oscillation is detected and its phase is determined.

The cyclotron frequency can be deduced by adding the appropriate multiples of 2π to this phase (details on this so-called phase unwrapping can be found in [65, 161]), correcting the phase for the offset obtained through the coupling procedure, and dividing the resulting phase by the phase evolution time T. It has to be pointed out that in this method, in contrast to a similar method [47], the amplitude during the phase evolution can be smaller than the amplitude required for detection, which reduces systematic shifts.

There are two main advantages of this method over multi-dip methods: First, the axial frequency does not directly enter the determination of the cyclotron frequency, making this method less sensitive to trapping voltage fluctuations. Second, the frequency resolution is given by

$$\Delta\nu_+ = \frac{\Delta\phi}{2\pi T}, \tag{3.35}$$

where $\Delta\phi$ is the phase-uncertainty, mainly arising from the uncertainty in the initial phase (due to a non-zero initial cyclotron amplitude) and from the uncertainty in the detected phase arising from the axial phase prior to the mode-coupling. Since this phase uncertainty is basically independent of the phase evolution time, the uncertainty in ν_+ can be reduced below the uncertainty-limit of the multi-dip methods with a suitably chosen phase evolution time.

To the end of this paragraph, it should be mentioned that this method is not limited to the cyclotron frequency. In principle it can also be applied e.g. to the axial motion. This would have the benefit that the axial motion could be sideband-cooled through coupling to the cyclotron resonator before the measurement, such that the energy during the measurement could be below $k_B \cdot 4.2$ K. Furthermore, the achievable frequency resolution would not be limited by the uncertainty of the frequency determination from a dip. Further benefits will be mentioned in Sec. 3.4.4.7.

3.4.4.3. Resonator-amplifier coupling

In Fig. 3.20, an equivalent circuit for the image current detection system is shown. It contains the ion represented by a current source, the parallel LCR-circuit and the amplifier, having an input resistance R_{in} and an input capacitance C_{in}. A voltage and a current source represent the amplifiers' input-related voltage noise density e_n and current noise density i_n, respectively. The coupling between the LCR-circuit and the amplifier can be influenced by the coupling capacitor C_c or the tap at the coil.

In an analysis of the equivalent circuit by means of Kirchhoffs' laws for typical axial and cyclotron detector parameters, the following relations are obtained:

- The ratio between the voltage at the amplifier input U_{in} and the voltage across the LCR-circuit U_{LCR} is given by:

  $$\frac{U_{in}}{U_{LCR}} \approx \frac{L_2}{L_1 + L_2} \frac{C_c}{C_{\mathrm{in}} + C_c} \equiv \kappa_L \kappa_C \equiv \kappa, \tag{3.36}$$

  where the inductive and capacitive coupling factors κ_L and κ_C as well as the total coupling factor κ have been introduced.

- The input resistance of the amplifier loads the LCR-circuit. The effective parallel resistance $R_{p,\mathrm{eff}}$ of the coupled detector is given by:

  $$R_{p,\mathrm{eff}} \approx R_p || \frac{R_{\mathrm{in}}}{\kappa^2} = \frac{1}{\frac{1}{R_p} + \frac{\kappa^2}{R_{\mathrm{in}}}}. \tag{3.37}$$

- The input capacitance C_{in} of the amplifier and the coupling capacitor C_c, being connected in series, add to the total capacitance of the coupled detector as follows:

  $$C_{p,\mathrm{eff}} \approx C_p + \kappa_L^2 \frac{C_{\mathrm{in}} C_c}{C_{\mathrm{in}} + C_c}. \tag{3.38}$$

- At the detector's resonance frequency, the amplifier's input-related current-noise i_n causes a noise-voltage u_n at the amplifier input given by

  $$u_n = \kappa^2 R_{p,\mathrm{eff}} i_n. \tag{3.39}$$

To decide for a certain resonator-amplifier coupling, several factors have to be considered:

- For the detection of a dip, the coupling influences two important parameters: The dip-width by means of $R_{p,\mathrm{eff}}$ and the signal-to-noise ratio (SNR).

  The first parameter is certainly of most importance, since a too narrow dip will smear-out during the measurement due to trapping voltage fluctuations or drifts, while for a too wide dip, the uncertainty in the fit of the theoretical

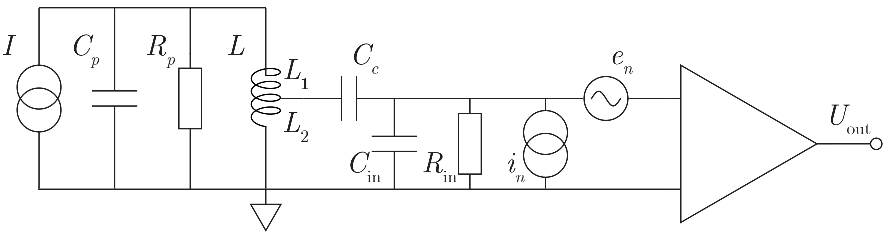

Figure 3.20.: An equivalent circuit for the image current detection system is shown. The ion is represented by a current source. The capacitance of the LCR-circuit contains coil-, trap- and cable-capacitances. The resistance of the LCR-circuit covers losses in resonator, trap and cabling. The amplifier is modeled by an input resistance, an input capacitance, a voltage source representing the input-related voltage-noise density e_n and a current source representing the input-related current-noise density. The coupling capacitor C_c as well as the tap at the coil are used to set the coupling of LCR-circuit and amplifier. For further details see text.

lineshape to the dip becomes unnecessarily big. A dip width of around 1 Hz has been estimated to be ideal [115].

A dip appears in the LCR-circuit's noise spectrum, which is an incoherent superposition of the LCR-circuit's thermal noise and the current-noise excitation of the LCR-circuit. The noise-background is given by the voltage noise e_n of the amplifier. Thus the dip-detection SNR is given by

$$\text{SNR} = \frac{\sqrt{\kappa^2 4 k_B T R_{p,\text{eff}} + \kappa^4 R_{p,\text{eff}}^2 i_n^2}}{e_n}, \tag{3.40}$$

where κ also enters through $R_{p,\text{eff}}$.

Note that also the pick-up electrode is a degree of freedom in these considerations, since it influences the dip-width by means of the effective electrode-distance D_{eff}.

- For the detection of a peak, the coupling influences two parameters: The SNR and the time constant τ of the exponential signal-decay.

  For the peak-detection, the current drop across the detector caused by the image-current I is the signal, while the sum of all incoherent noise sources is the noise background. Thus the dip-detection SNR is given by

  $$\text{SNR} = \frac{\kappa R_{p,\text{eff}} I}{\sqrt{e_n^2 + \kappa^2 4 k_B T R_{p,\text{eff}} + \kappa^4 R_{p,\text{eff}}^2 i_n^2}}. \tag{3.41}$$

  The image-current I can usually be increased only within certain boundaries, which are dictated by systematic shifts.

The time-constant τ of the signal decay can be influenced by means of $R_{p,\mathrm{eff}}$. Again, the pick-up electrode is an additional degree of freedom.

- If a detector is mainly for cooling purposes, there are two parameters of interest which can be influenced by the coupling: First of all, the cooling time constant τ and second the dip-detection SNR, which in this case defines the minimum temperature that is achievable by means of active electronic feedback (see Sec. 3.4.4.5).

For the axial detector for the first experimental run of PENTATRAP, considering the properties of the axial detection system (see Tab. 3.3 and Tab. 3.4), a coupling of $\kappa = 1/3$ was chosen.

3.4.4.4. Cryogenic axial detectors

The cryogenic axial detector, which was developed by Christian Roux [115] in close collaboration with Sven Sturm and Andreas Mooser from the g-factor experiments in Mainz [65, 162], consists of a toroidal NbTi-coil, placed in an OFHC-copper housing (both parts together are called axial resonator), and a low-noise, high-input-impedance amplifier.

Resonators The resonators are LCR-circuits in themselves, having an inductance, a self-capacitance and a parallel resistance. One major design-criterion for the resonator is a big parallel resistance, which means that all losses should be minimized. Therefore, a toroidal coil-shape has been chosen, which reduces currents induced in the housing compared to helical coils. Furthermore, the housing is made of OFHC-copper, which presents a low resistance to the induced currents. To minimize dielectric losses, PTFE with its comparably low loss-tangent has been chosen for both the toroidal body and the insulation of the 75 µm thick NbTi-wire. A third loss-mechanism are resistive AC-losses in the NbTi-wire, which are magnetic-field dependent [163]. In a test measurement it was shown that for one of the coils that will be used at PENTATRAP, the quality factor (see Eq. (3.24)) degraded from ~36000 to ~22000, going from a magnetic field of 1 T to a field of 7 T. Due to space-constraints, the four toroids cannot be placed in four separate housings, but have to be placed in two double-resonator housings. A double-resonator is shown in Fig. 3.21.

Amplifiers Besides the actual amplification, main design-criteria for the axial amplifier are a high input-impedance, low input-related voltage- and current-noise densities and a low power-consumption. The axial amplifier is based on GaAs[17] field-effect transistors (FETs). The common-source input stage consists of two parallel dual-gate FETs (*NE25139*) with their gates shorted together. Having two parallel FETs reduces any incoherent noise by a factor of $1/\sqrt{2}$, while the shorting of the gates reduces the $1/f$-noise (for a detailed discussion including input-capacitance considerations see [65]). The input-stage is followed by a common-gate stage. The two stages together

---

[17] GaAs does not suffer from charge-carrier freeze-out at LHe-temperatures.

Figure 3.21.: Two assembled axial detectors (with amplifier box lid removed) in a double-resonator housing, as well as a toroidal PTFE coil body are shown. The coils are made from PTFE-insulated 75 µm thick NbTi-wire, wound on the coil body. The torus is wrapped in PTFE-tape for mechanical stability of the coil. For further details see text.

form a cascode. With properly biased gates, this minimizes the Miller-capacitance [164]. Therefore, the coupling of the effective drain-source resistance to the gate is minimized, leading to a high input-impedance. Further measures to obtain a high input-impedance, as well as the detailed setup of the amplifier, are discussed in [115]. The amplifiers are placed in copper-boxes at the side of the resonator housing. Performance parameters of the amplifiers are summarized in Tab. 3.3.

Resonator duplication Within the presented thesis work, four toroids were wound[18] with the aim of a resonance-frequency of 600 kHz[19] when being connected to a trap and an amplifier. Test-measurements were carried out at a temperature of 3 K with a cryo-cooler (*Sumitomo SRP-062B-F-50H*). The self-resonances of the toroids were recorded using an *HP4195A* network analyzer, with the analyzers' out- and input weakly capacitively coupled to the resonator. In this configuration, the damping of the analyzer's output signal depends on the impedance of the resonator. From the -3 dB-width $\Delta\nu$ and the self-resonance frequency ν_0, the resonators Q-value can be determined:

$$Q = \frac{\nu_0}{\Delta\nu}. \tag{3.42}$$

---

[18] with patient assistance by Christine Böhm and Ralph Zilly

[19] For a detailed list of arguments favoring high/low axial detection frequencies, see [115]. This list should be reconsidered as soon as experimental experience with actual free-space cyclotron frequency determinations has been gathered.

Table 3.3.: Important parameters of the cryogenic axial amplifier are shown. P is the amplifier's power consumption. Values are taken from [115].

gain	15.6 dB
P	9 mW
e_n	$610\ \mathrm{pV}/\sqrt{\mathrm{Hz}}$ (at 680 kHz)
i_n	$3.7 \pm 3\ \mathrm{fA}/\sqrt{\mathrm{Hz}}$
R_{in}	11.3 MΩ
R_{in}	2.1 pF

Since the exact coupling between network analyzer and toroid is difficult to judge, a conservative estimate of 2% and 10% for the relative error of the resonance frequency and the Q-value were assumed, respectively.

The inductance and self-capacitance of a resonator can be determined by measuring ν_0 with an additional capacitance in parallel. For the calculation of the errors, it was assumed that the uncertainty in the capacitance of the additional capacitor at 3 K is 5%. But it has to be pointed out that the capacitance-/inductance-measurements were carried out with the same type of capacitor for all three toroids, such that the errors should be correlated. Therefore, the inductance-/capacitance-differences between the toroids should be much more reliable than the errors indicate. The properties of the four toroids are summarized in Tab. 3.4.

It can be seen that the inductances and capacitances of the toroids are quite different, although great care was taken to perform the winding in the very same manner. This was probably due to the fact that several layers had to be placed on top of each other in the 18 segments of the toroid. Since one layer was not fixed with PTFE-tape (to reduce the amount of dielectric material), before the next was wound on top, the exact position of a single winding was difficult to control. Fixing one layer, before the next layer is wound on top might lead to more reproducible results. Nevertheless, a slight axial-frequency difference between two traps might not be harmful anyway. On the contrary, it might be favorable to have differences of a few kHz such that RF-pulses in one trap don't excite the ion in the other trap.

Integration into the setup For the first experimental run, toroid 3 was placed in the upper and toroid 1 in the lower chamber of a double-resonator housing, which was situated at the bottom of the resonator chamber, i.e. in a magnetic field of 1-4 T. The amplifiers in their copper box were situated at a radial distance of ∼5 cm from the symmetry axis of the detection electronics chamber, with an angle of ∼70° between the radial unit vector and the amplifier board. There were some concerns about the radial magnetic field of several 100 mT in this place, as it was observed in test measurements that a magnetic field of several T oriented perpendicular to the amplifier board severely reduced the amplification [115]. However, no performance degradation of the amplifier in the setup was noticed.

The upper of the two toroids was connected to the lower endcap of the sole trap

Table 3.4.: The properties of four toroids are summarized. The self-resonance frequencies are directly measured. They are in good agreement with the capacitances and inductances. For further details see text.

property	toroid 1	toroid 2	toroid 3	toroid 4
windings	761	761	761	761
L (mH)	3.49(18)	3.27(17)	3.15(16)	3.18(16)
C_p (pF)	8.13(41)	8.86(45)	7.97(40)	9.20(46)
ν_0 (kHz)	933(19)	917(19)	1008(21)	928(19)
Q	53600(5360)	66600(6660)	58700(5870)	43400(4340)

in the setup with a 1 mm thick copper wire in a PTFE sleeve. The cold end of this toroid, i.e. the end that wasn't connected to the trap, was coupled to the resonator housing through two parallel 1.5 nF-capacitors. This allowed for a DC-bias of the upper toroid and therefore for a direct connection to the endcap. The cold end of the lower toroid was connected to the housing in the same way. The amplifiers were inductively coupled to the resonators with a coupling factor κ of $\sim 1/3$ using taps at the toroids.

Since the aimed at axial-detection frequency of 600 kHz is out of reach for $m/q \gtrsim 3$ with the *UM1-14* voltage source (see Sec. 3.4.5), capacitors of 27 an 21 pF were soldered in parallel to the upper and the lower coil, respectively, to reduce the detectors' resonance frequencies. For the upper coil, which was connected to the trap, a frequency of ∼380 kHz was obtained. For the lower coil, which was not connected to a trap and served for test purposes, a resonance frequency of ∼495 kHz was obtained.

Amplifier working point For the optimization of a detector, the gate voltages U_{G1} and U_{G2} at the first and the second stage of the amplifier were scanned and the resulting noise resonances were recorded. From these noise resonances, the Q-value and the dip-detection SNR were determined. Results of such a scan for the lower of the two resonators build into the setup for the first experimental run are shown in Fig. 3.22a and Fig. 3.22b. From these results it can be concluded that a good working-point of the amplifier would be e.g. U_{G1}=-0.78 V and U_{G2}=-0.7 V where both a comparably high Q-value and a high SNR can be obtained[20]. In the behavior of the Q-value around $U_{G2} = 0$ it can be seen that a not properly setup cascode decreases the input resistance of the amplifier by means of an increased Miller-capacitance. For a detailed explanation of the variation of the Q-value with the gate-voltages, see [121].

Thermal coupling of amplifiers One concern about the double resonator housings with the double amplifier boxes was that the thermal coupling of the amplifiers to the LHe-bath might be insufficient. If this was true, then the working point of one

---

[20] It has to be pointed out that the weighing of SNR, Q-value and other factors (like amplifier gain) against each other depends on the experimental boundary conditions.

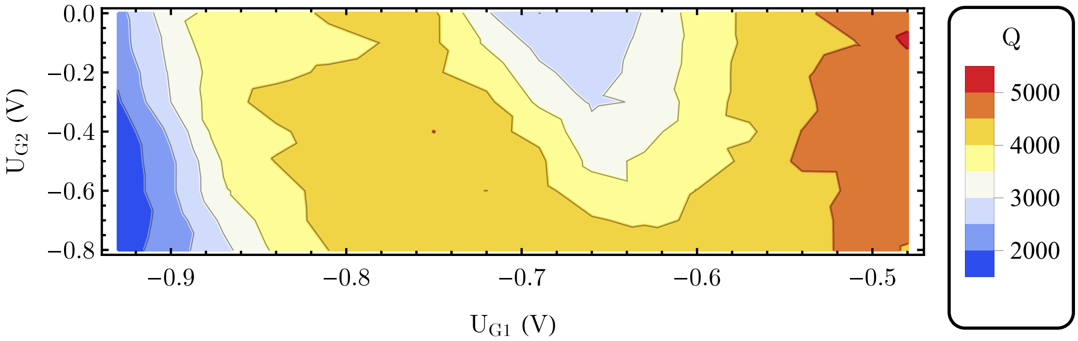

(a) Quality factor of the detector not being connected to the trap for different U_{G1} and U_{G2}.

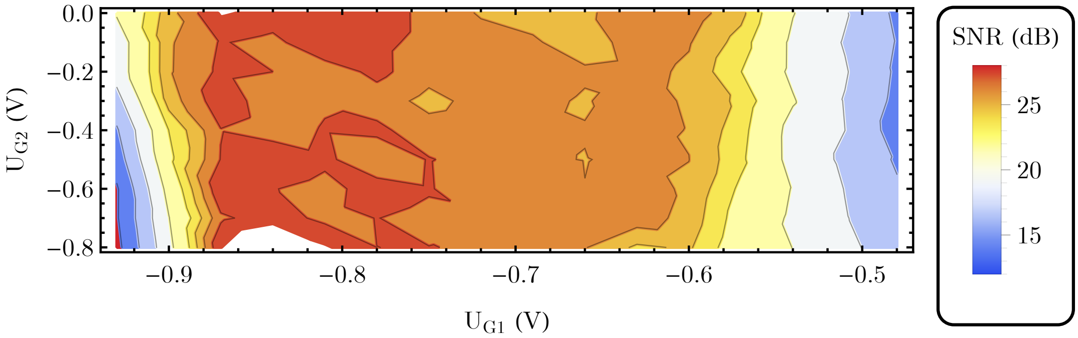

(b) SNR of the detector not being connected to the trap for different U_{G1} and U_{G2}.

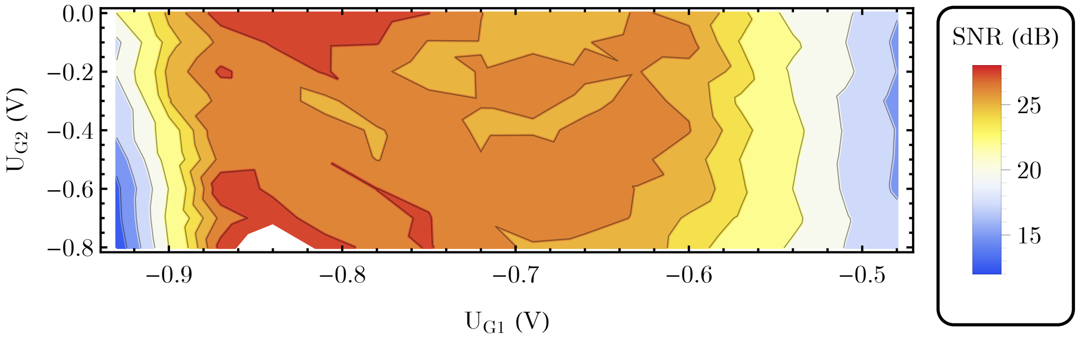

(c) SNR of the detector not being connected to the trap for different U_{G1} and U_{G2} with a power dissipation of $\sim$ 11 mW in the detector being connected to the trap.

Figure 3.22.: (a) and (b) show typical results for the Q-value and the possible SNR in case of dip-detection in a scan of U_{G1} and U_{G2}. (c) shows the same as (b), with the difference that in (b) the neighboring amplifier in the double-amplifier box was off, while during the measurements shown in (c), it was dissipating $\sim$11 mW. This comparison was done to investigate possible thermal cross-talk. At the white spaces around $U_{G2} = -0.8$ V and $U_{G1} = -0.84$ V in (b) and (c), the measurement failed. For further details, see text.

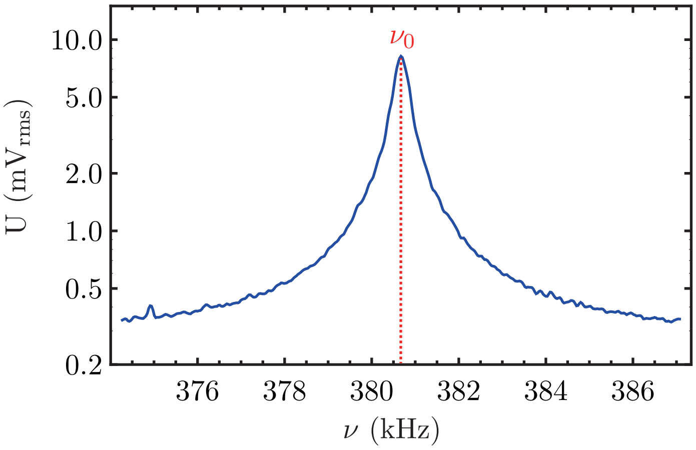

Figure 3.23.: The thermal noise of the axial detector connected to the lower endcap of the sole trap in the setup is shown. Its resonance frequency is 380.7 kHz and its Q-value is 1275. For further details see text.

amplifier might change in case the power dissipation of the other amplifier changes. Therefore, the most extreme case was tested: First, the upper amplifier was turned off, and a scan of U_{G1} and U_{G2} for the determination of the working point of the lower detector was carried out, as described above. After that, the upper amplifier was turned on with a quite high power dissipation of $\sim$ 11 mW. Neither a significant difference in the Q-values, nor in the signal-to-noise ratios (which are exemplarily shown in Fig. 3.22b and Fig. 3.22c) could be observed. Thus, in the current setup thermal coupling is not an issue.

Detector connected to the trap In Fig. 3.23, a noise-resonance of the resonator connected to the trap is shown. It has a resonance frequency of 380.7 kHz and a Q-value of 1275. This corresponds to a parallel resistance of R_p = 9.6 MΩ. In a test setup in the cold head, the detector had a much higher quality-factor of ~3000, mainly limited by the 27 pF-capacitor in parallel. It is assumed that the Q-value was mainly degraded due to the impedance to ground of the Faraday cup next to it, being capacitively coupled to the pick-up electrode with a capacitance of ~7 pF: The Faraday cup could only be grounded at the room temperature end of the cryogenic coaxial cable connected to it, which resulted in a resistance of several 10 Ω in series with the trap capacitance. An additional reason for the degradation of the Q-value might be parasitic mutual cable capacitances. These are particularly difficult to avoid in the narrow bellow between trap chamber and detection electronics chamber. A shielding of all cables going to the trap except for the ones being connected to a detector might circumvent this problem. Due to the extremely small loss tangent of sapphire [165], the trap capacitance can be excluded as a source of losses on this level.

Future modifications Although the detectors are working fine, they have to be replaced in a future version of the setup: It was pointed out in Sec. 3.4.2 that the resonator chamber will have to shrink - the inner diameter will be reduced from 136 mm to 120 mm and the length will be reduced by a few centimeters. Since the axial double resonator housings are rather big (62 mm in diameter with a height of about 110 mm) with an additional bulky amplifier box, they will not fit into the new setup. The new resonators and coils will be designed by Rima Schüssler in the context of her master's thesis in collaboration with Stefan Ulmer, who designed very compact detectors for the BASE experiment [91].

3.4.4.5. Room temperature axial detection electronics

Post-amplification, down-conversion and sampling The signal from the cryogenic amplifier is further amplified by the *Stahl electronics* *AF-DC-c* board [166, 167], which is mounted in one of the copper boxes directly at the magnet's top flange. The pre-amplifier features an ultra-low input related voltage noise density $< 0.75\ \mathrm{nV}/\sqrt{\mathrm{Hz}}$ and a gain of $\sim$33 dB - therefore, the total noise-level is mainly defined by the noise of the cryogenic amplifier. From this point on, the signal is further processed in different ways, depending on the application (see Fig. 3.24).

For the processing of the signal with an *HP 35670A* FFT-analyzer, which for instance is required for dip-detection, the signal has to be down-converted into the frequency range of 0 - 102.4 kHz. This is done with a down-converter on the *AF-DC-c* board by mixing the signal with a sinusoidal local-oscillator (LO) signal. Usually, white noise from both the frequency range below and above the LO-frequency would be down-converted into the same frequency range and would therefore add up. To prevent this reduction of the SNR, which would prolong the time to detect a dip, the *AF-DC-c* down-converter provides a high level of suppression of signals in the frequency-range below the LO-frequency: Signals in the frequency-range 3 - 23 kHz below the LO-frequency are suppressed by more than 55 dB compared to signals in the same frequency range above the LO-frequency. This works for LO-frequencies in the range 300 - 800 kHz. For further details see [167].

To see, whether an ion responds to a parametric excitation (see Sec. 2.3), it is convenient to further down-convert the signal after the *AF-DC-c* down-converter with a *Mini-Circuits ZAD-8+* mixer to frequencies of $\sim$1 Hz. The slowly varying signal can easily be detected with an oscilloscope. For further details see Sec. 4.2.2.

For the detection of the signal from the pre-amplifier with a *Rohde & Schwarz FSP3* spectrum analyzer, a down-conversion is not necessary. The signal is simply amplified by a *Mini-Circuits ZFL-500LN* amplifier.

Feedback electronics Active electronic feedback has proven to be a useful tool in Penning-trap experiments (that are employing image-current detection) to alter the effective parallel resistance and the effective temperature of the detector [65, 121, 168]. In this technique, the signal from the cryogenic amplifier is phase-shifted, damped and fed back to the LCR-circuit through a capacitor, as shown in Fig. 3.25. Leaving aside

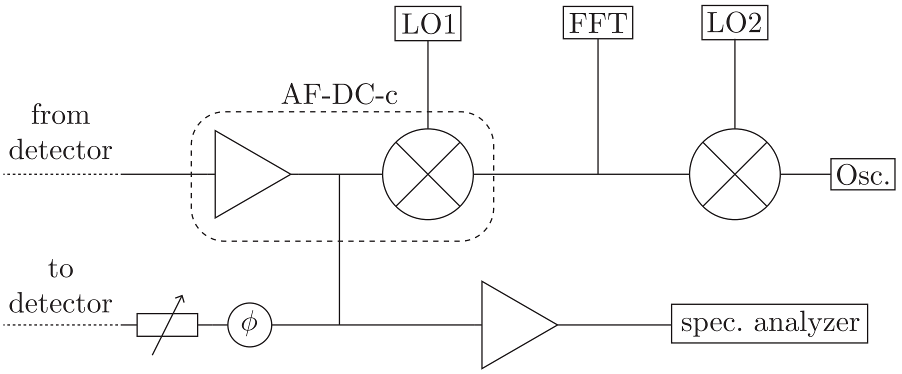

Figure 3.24.: A schematic overview over the room temperature axial detection and feedback electronics is shown. First the signal from the cryogenic amplifier is further amplified. For detection with an FFT-analyzer, the signal is down-converted into the frequency-range 3-23 kHz. To detect the ion-response to a parametric excitation, the signal is further down-converted to ∼1 Hz. For detection of the signal from the pre-amplifier with a spectrum analyzer, the signal is only amplified and not down-converted. To alter the quality-factor and the effective temperature of the resonator, the signal is phase-shifted and damped and then fed back to the cryogenic detector. For further details see text.

the ion-signal for a moment, the resulting signal is given by[21]

$$u_1(\omega) = u_J \frac{1}{1 + R(\frac{1}{i\omega L} + i\omega(C + C_f) - i\omega A C_f)}, \tag{3.43}$$

where A is the complex amplification factor, C_f is the capacitance of the feedback capacitor and

$$u_J = \sqrt{4k_B T R} \tag{3.44}$$

is the thermal noise density of the LCR-circuits resistance. For $A = 0$, the feedback-capacitor simply acts as an additional parallel capacitance. With a feedback phase (i.e. complex phase of A) of 0° and 180°, this parallel resistance is altered and thus, the resonance frequency can be changed with $|A|$. For a feedback phase of 90° or 270° and on resonance, Eq. (3.43) becomes:

$$u_1 = u_J \frac{1}{1 \pm |A| \cdot \omega_0 R C_f} \equiv \gamma u_J, \tag{3.45}$$

where the plus sign corresponds to a phase of 90° and the minus sign to a phase of 270°. When the ion current I is taken into account, the resonance case Eq. (3.45) alters as follows:

$$u_1 = \gamma(u_J + IR). \tag{3.46}$$

---

[21] The following derivation is closely following [65].

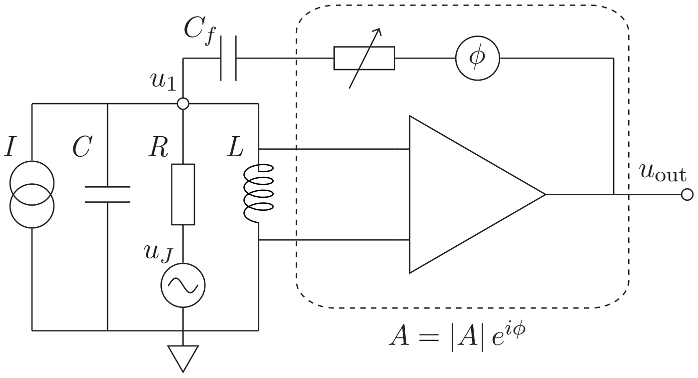

Figure 3.25.: A schematic overview over the axial feedback loop is shown. The ion is modeled as a current source. The thermal noise u_J is modeled as a voltage source in series with the resistance R of the parallel LCR-circuit. The amplifier represents all amplifiers before the phase shifter. The complex amplification factor A arises from all amplifiers, the phase shifter and the variable attenuator and incorporates both feedback gain $|A|$ and phase Φ. The feedback signal is fed to the detector through the feedback capacitor C_f. For further details see text.

From this follows an effective resistance seen by the ion of

$$R_\mathrm{eff} = \gamma R. \tag{3.47}$$

From Eq. (3.44), Eq. (3.45) and Eq. (3.47) follows an effective temperature of

$$T_\mathrm{eff} = \gamma T. \tag{3.48}$$

Thus, for a feedback phase of 270° and a feedback gain in the range of $(0, \omega_0 R C_f)$ (called positive feedback), the effective parallel resistance of the tank circuit can be increased (within technical limits) at the expense of an increased effective detector temperature. This allowed for instance to detect a cyclotron dip of a single proton [169]. More common is the usage of a feedback phase of 90° (called negative feedback), which allows for a reduction of the effective temperature seen by the particle. The decrease in temperature is at the expense of a reduced effective parallel resistance. A technical lower limit in the temperature is given by the noise of the feedback loop [65].

In [65], a down- and up-conversion scheme is used to control the feedback phase, with the phase defined by the relative phase between the two LOs. The strength of this method is its simplicity, while its main disadvantage is the additional noise on the detector due to LO-leakage and up-conversion of both sidebands. Therefore, a direct phase-shifter (being situated behind the room temperature axial pre-amplifier) has been designed within the presented thesis work. Its working principle is sketched in Fig. 3.26: The incoming signal is split into four signals, having relative phases of 0°,

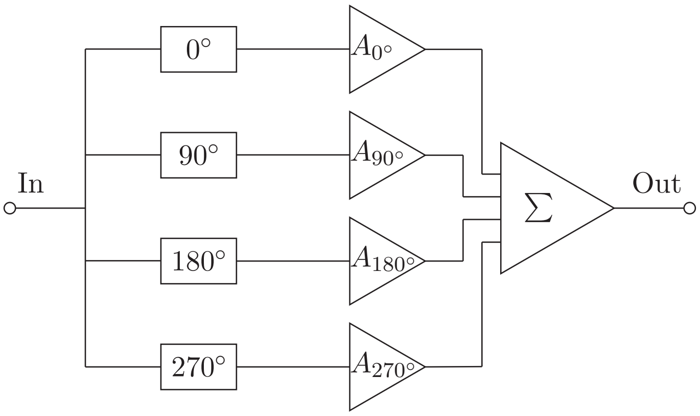

Figure 3.26.: The main components of the phase-shifter designed for the axial feedback loop are shown. The input signal is split into four signals with relative phases of 0°, 90°, 180° and 270°. These signals are independently altered in amplitude and afterwards summed up. For further details see text.

90°, 180° and 270°. To set a certain phase, these four signals are altered in amplitude individually and then added up. With a proper choice of amplitudes, any phase can be set relative to the input signal. The splitting into four phases is realized by means of a passive polyphase filter, which is also part of the *AF-DC-c* down-converter (for a detailed treatment see [167]). The amplitude control is done with voltage-controlled amplifiers (VCAs).

Prototypes of this phase-shifter (with small layout changes) were set up and tested within the diploma thesis of Christian Hökel-Schmöger [170]. Within that thesis, the phase-shifter was tested together with an axial cryogenic detector in the cold-head, and both positive and negative feedback were realized successfully. A new version of the phase-shifter with easier to control VCAs has recently been set up (see Fig. 3.27) and will tested by Rima Schüssler [149].

3.4.4.6. Cyclotron detection system

Besides the axial detectors, four detectors for the cyclotron motion will be incorporated in the detection electronics chamber. Since the cyclotron mode can be detected to extremely high precision with indirect methods (see Sec. 3.4.4.2), the main purpose of the cyclotron detectors is not frequency-determination, but cooling of both cyclotron mode (directly) and magnetron mode (indirectly). Furthermore, it is a valuable auxiliary tool - for instance, it can aid a controlled reduction of the number of trapped ions (see e.g. [121]). Besides that, the cyclotron detector might be used for an indirect phase-sensitive determination of the axial frequency. Since the cyclotron motion is a radial motion, the image current is picked up at one half of a split electrode.

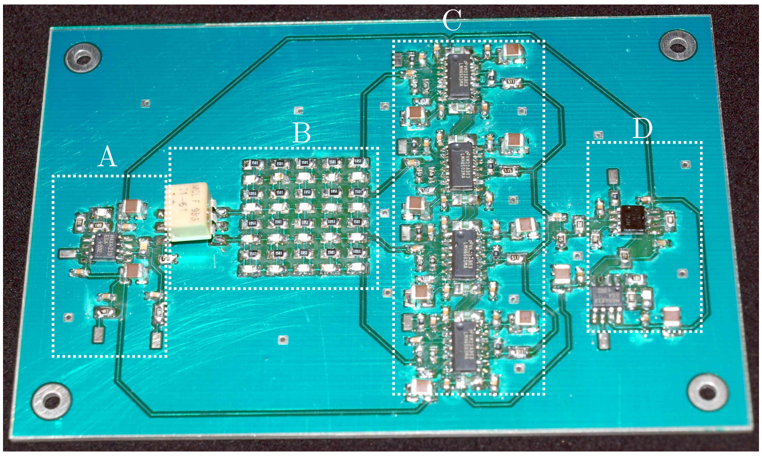

Figure 3.27.: A picture of the phase-shifter is shown. The functional blocks from left to right are an input amplifier (A), a passive polyphase filter (B), four VCAs (C) and a summation and post-amplification stage (D). The phase-shifter was set up by Rima Schüssler in the framework of her master's thesis.

Cryogenic detector The cryogenic cyclotron detector consists of a helical OFHC copper coil in a cylindrical OFHC copper housing, a GaAs-FET based amplifier and a GaAs varactor diode for resonance frequency tuning. It was developed by Christian Roux [115] closely following Stefan Ulmer's design of the cyclotron detector for the proton-g-factor experiment [121, 171].

A photograph of the resonator is shown in Fig. 3.28a, and parameters of an unloaded resonator prototype are summarized in Tab. 3.5. Although the resonators are working very well, they have to be replaced in the near future, since they are to bulky (diameter $\approx$ 50 mm, height $\approx$ 100 mm). The new, more compact resonators will be designed by Rima Schüssler. A replacement of the OFHC copper-wire by aluminum-wire as well as a toroidal shape of the coil are currently under discussion.

Like the axial amplifier (see Sec. 3.4.4.4), the cryogenic cyclotron amplifier contains a cascode input stage to suppress the Miller effect. In contrast to the axial amplifier, the cascode does not consist of several FETs, but actually uses the dual-gate feature of the *NE25139*-FET. Besides the minimization of the gate-to-drain capacitance by means of the cascode, further measures are taken to provide a high-input impedance of the amplifier:

- The amplifier board is milled on *Taconic* PTFE-copper laminate, such that the board input capacitance does not degrade the input resistance by means of dielectric losses. Furthermore, the board input capacitance is minimized as much as possible.
- To bias the gate of the common-source input stage without a degradation of the input resistance, the bias voltage is applied through a high-ohmic resistor. The formerly used 100 MΩ-resistor (*YAGEO RC0805JR-07100ML*) was found to

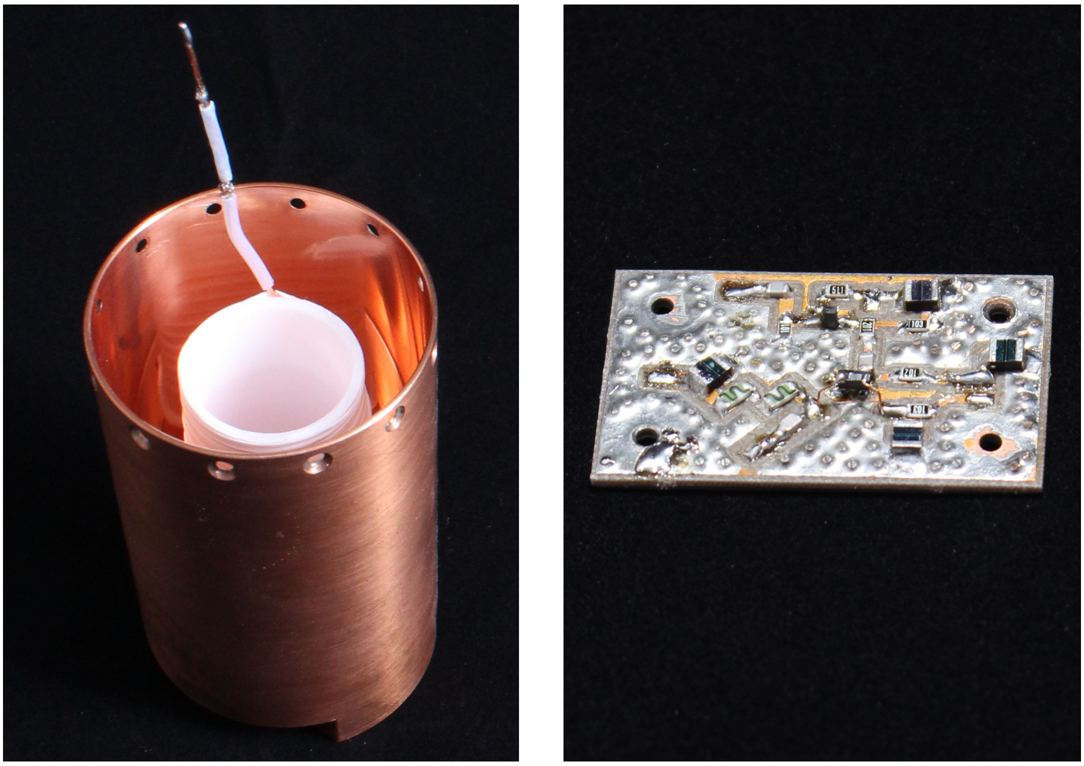

(a) (b)

Figure 3.28.: In (a) a cryogenic cyclotron resonator is shown (without lid). It consists of a helical OFHC copper coil fixed on a PTFE support structure in a OFHC copper housing. In (b) a cryogenic cyclotron amplifier is shown. Compared to a previous version (see [115]), the layout has been slightly modified. The most important changes are the vertical mounting of the FETs (which thus have some contacts that have to be connected with thin copper wire) and the two 1 GΩ-resistors in series (which have a bigger 1206 package compared to the 0805 package of all other resistors), which are used to bias the gate of the common source input stage. For further details, see text.

Table 3.5.: Important parameters of the cryogenic cyclotron detection system are shown. Values are taken from [115].

(a) Unloaded resonator prototype

Q	4000
L_p	2.3 µH
C_p	3.2 pF

(b) Amplifier

gain	15.8 dB
P	3 mW
e_n	500 pV/$\sqrt{\text{Hz}}$ ($\nu > 20$ MHz)
R_{in}	700 kΩ
C_{in}	1.1 pF

have a severely lower resistance of ∼12 MΩ in the range of cyclotron frequencies of interest. Several resistors were tested, and a 1 GΩ-resistor of type *Vishay CRHV1206AF1G00FMFT*, with a resistance of ∼50 MΩ in the frequency range of interest, was found to be the most suitable candidate. Two of these resistors are connected in series to bias the gate in a new layout of the amplifier.

The amplifiers are mounted on top of the resonator housing. To prevent a gain-reduction due to the strong magnetic field (see [115]), which is directed perpendicular to the amplifier board, a perpendicular mounting of the FETs was foreseen in the new amplifier layout. A picture of the amplifiers is shown in Fig. 3.28b. Important performance parameters of the amplifiers are listed in Tab. 3.5. Further details on the resonator and the amplifier as well as details about the varactor diode can be found in [115].

Room temperature electronics The signal from the cryogenic cyclotron amplifier is first amplified with a *Mini-Circuits ZFL-500LN* amplifier. Afterwards, it can either be directly detected with a *Rohde & Schwarz FSP3* spectrum analyzer or, after down-conversion with a *Mini-Circuits ZAD-6+* mixer, it can be analyzed with an *HP 35670A* FFT-analyzer.

3.4.4.7. Systematic shifts

In the following, systematic shifts related to the image-current detection with resonant LCR-circuits will be discussed. One shift is the so-called coil pulling shift that is related to the interaction of the ion with the reactance of the LCR-circuit. Another shifts is the so-called equilibrium position shift [172], which is related to the fact that electrostatic field-gradients, arising i.e. from charge-patches, shift the electrostatic trap center differently for different depths of the trapping potential. A variant of this shift is the multi-trap equilibrium position shift, a PENTATRAP-specific shift, that is related to the fact that the gradients of the electrostatic potential of one trap shift the ion equilibrium positions in the neighboring traps.

Coil pulling shift As has been pointed out in Sec. 3.4.4.1, the voltage across the detector due to an image current acts back on the ion, leading to a damping term in the ion's equation of motion. The damping constant is given by

$$\gamma(\omega) = \frac{q^2 Z_{LCR}(\omega)}{m D_{\text{eff}}^2}. \tag{3.49}$$

The real part of the damping term leads to an exponential decay of the amplitude of an excited ion. Whenever the ion is not exactly tuned in resonance with the LCR-circuit, the damping term will also have an imaginary component. This imaginary damping term will lead to a shift in the corresponding eigenfrequency [65, 173]:

$$\Delta\omega_{z,+} \approx -\frac{1}{2}\mathfrak{Im}(\gamma_{z,+}(\omega_{z,+})). \tag{3.50}$$

In [65], it has been pointed out that for an ultra-high-precision measurement of the cyclotron frequency by means of the PnA-method, the shift due to the interaction with the cyclotron detection circuit can be of relevance. Therefore it is necessary to shift away the cyclotron detection circuit during the measurement by many linewidths.

In the axial dip detection, the axial frequency is tuned closely to the resonance frequency of the LCR-circuit. In this case, the near-resonance expression of the imaginary impedance can be used, and Eq. (3.50) becomes:

$$\Delta\omega_z \approx -\gamma_0 \frac{Q\left(\frac{\omega_z-\omega_0}{\omega_z}\right)}{1+4Q^2\left(\frac{\omega_z-\omega_0}{\omega_z}\right)^2}, \tag{3.51}$$

where γ_0 is the on-resonance damping constant, ω_0 is the LCR-circuit's resonance frequency and Q is the LCR-circuit's quality factor. In Fig. 3.29, the calculated axial frequency dependence of the shift is shown exemplarily. On the one hand, the shift vanishes, when the ion is tuned to the center of the resonator. On the other hand, it is most sensitive to changes of $\nu_z - \nu_0$ there. For the quite realistic parameters, for which Fig. 3.29 was calculated, the relative coil pulling shift around the center is

$$\frac{\Delta\nu_z}{\nu_z} \approx -2.5\cdot 10^{-8}(\nu_z-\nu_0)/\text{Hz}. \tag{3.52}$$

Continuing the example given in Fig. 3.29, for a mass-ratio measurement with a precision better than 10^{-12}, assuming a free space cyclotron frequency of 20 MHz (and a corresponding axial suppression factor $(\nu_z/\nu_c)^2$ of 1/2500), the two ion-species have to be tuned to the same axial frequency within less than 100 mHz. Furthermore the resonance-frequency of the detector must be very stable. These difficulties could be circumvented by a phase-sensitive axial frequency determination.

Equilibrium position shift One implication of the axial frequency determination by means of the image-current technique using resonant LCR-circuits is that the axial

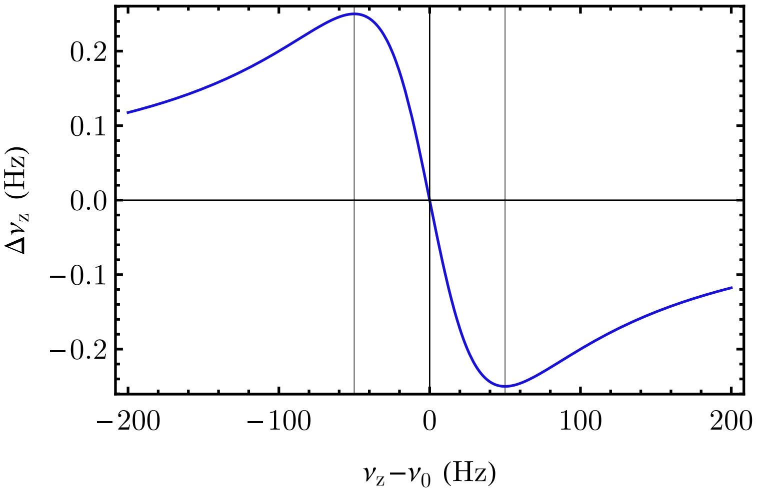

Figure 3.29.: The calculated coil pulling shift of ν_z for different ν_z is plotted for an LCR-circuit with a resonance frequency of 400 kHz and a quality factor of 4000. The on-resonance dip width is assumed to be $\delta\nu_z$=1 Hz. The vertical lines at $\nu_0(1 \pm 1/2Q)$ indicate the frequency, at which the shift has its minimum/maximum value of $\Delta\nu_z = \mp\delta\nu_z/4$.

frequencies of different ion species are equal. Therefore, the ring-voltages are given by

$$U_r = \frac{m\omega_0^2}{2qc_2}, \tag{3.53}$$

where ω_0 is the resonance frequency of the LCR-circuit. If an electrostatic potential gradient C_1 is present in the trap, which might be for instance due to charge patches, the electrostatic trap center shifts by

$$\Delta z = -\frac{C_1}{2c_2 U_r} = -\frac{qC_1}{m\omega_0^2}. \tag{3.54}$$

In the presence of a magnetic field gradient, this leads to a charge-to-mass ratio dependent shift in the determination of the free-space cyclotron frequency.

The following numerical example of a mass-ratio measurement of $^{36}\mathrm{Cl}^{8+}$ and $^{35}\mathrm{Cl}^{8+}$ is intended to illustrate the effect. For the sake of simplicity, it is assumed that the measurement is carried out by performing sequential free-space cyclotron frequency determinations in just one trap. The B_1 in this trap is assumed to be 1 µT/mm and the LCR-resonance frequency is 400 kHz. The potential gradient is introduced artificially by applying a 10 mV offset to the upper endcap, resulting in

$$C_1 = c_{1,\mathrm{UEC}} U_{\mathrm{offset}} \approx 0.33\mathrm{V/m}. \tag{3.55}$$

This results in a shift of the measured mass ratio of

$$\frac{\Delta R}{R} = -\frac{C_1}{\omega_0^2}\left(\frac{8e}{36u} - \frac{8e}{35u}\right)\frac{B_1}{B} \approx 4.6 \cdot 10^{-12}. \tag{3.56}$$

This means that for this moderately chosen numbers, the effect might be relevant for non-mass doublets at the aimed-at precision. This emphasizes the importance of advanced trap tuning techniques that address different offsets to the different trapping voltages [121] and charge patch effects [172]. Furthermore, it would be favorable to use a ν_c-determination technique that allows for identical trapping voltages even for non-q/m-doublets. Such a technique is introduced in App. E.

Multi-trap equilibrium position shift Since the traps of PENTATRAP are cylindrical and close to each other, the potential of one trap has a non-negligible influence on the potential of neighboring traps. This has been taken into account in the trap design concerning harmonicity and orthogonality of the trap [119]. Furthermore it was pointed out in [119] that different trapping voltages in neighboring traps increase electrostatic anharmonicities. Another effect is that the equilibrium positions of ions in neighboring traps change in case the trapping voltage at one of the traps is changed. In the interplay with magnetic field gradients, this results in a systematic shift of the ratio of the magnetic field strengths of the two traps[22]. This shift will be discussed in the following.

If a ring-voltage U_R is applied to a properly tuned trap, the electrostatic field gradient in the center of the neighboring traps is $\pm c_1 \cdot U_R$, where $c_1 \approx 0.03/\text{m}$ is a gradient coefficient, which depends on both the trap geometry and the exact tuning ratio that is used[23]. With $c_2 = 1.496 \cdot 10^4/\text{m}^2$ it can be concluded from Eq. (3.54) that the center positions z_A and z_B in two neighboring traps A and B are shifted by

$$\Delta z_A = +\frac{c_1}{2c_2}\frac{U_B}{U_A} \approx +1\ \mu\text{m} \cdot \frac{U_B}{U_A}, \tag{3.57}$$

$$\Delta z_B = -\frac{c_1}{2c_2}\frac{U_A}{U_B} \approx -1\ \mu\text{m} \cdot \frac{U_A}{U_B} \tag{3.58}$$

assuming that $z_A < z_B$. U_A and U_B are the respective ring voltages. It should be noted that for the three inner traps, the shifts arising from the potentials of the two neighboring traps add up to a total shift.

As long as the shifts are constant, they are of no concern. If however trapping potentials are changed during a mass-ratio determination, they can be of concern. The most extreme example would be to set the ring voltage of the container traps in Fig. 3.13 to 0 V while they are unused and to the same voltage as the measurement traps, when an ion is stored in them. In this case, the equilibrium positions in the measurement traps would be different by ~1 µm from measurement cycle to measurement cycle. With magnetic field gradients on the order of 1 µT/mm, this would give rise to magnetic field changes on the order of nT.

---

[22] This shift is just a variant of the equilibrium position shift described in the last paragraph. However, due to its potentially strong impact on mass-ratio measurements at PENTATRAP, it is treated independently.

[23] Since the value of this coefficient is crucial for a proper estimate of the effect, it has been determined both by an analytical calculation and a Comsol-simulation. Both methods gave good agreement. For a tuning ratio of 0.881, the value was found to be $\sim 0.032/\text{m}$, while for a tuning ratio of 0.85, it was $\sim 0.031/\text{m}$.

However, the shift is not only relevant for unfavorable choices of the trapping potential of container traps, but also for mass-ratio measurements with non-q/m-doublets. Again, the determination of the mass-ratio of ^{35}Cl and ^{36}Cl is a good example. For simplicity it is assumed, that the resonance frequencies of the axial detectors in the two measurement traps are identical. Furthermore, the charge states are identical. Then the relative systematic shift in the mass-ratio R as determined by the two-trap scheme (see Sec. 3.4.3.1) using two neighboring traps would be

$$\frac{\Delta R}{R} \approx \frac{1}{2}\frac{c_1}{2c_2}\left(\frac{35}{36}-\frac{36}{35}\right)\left(\frac{B_{1,B}}{B}-\frac{B_{1,A}}{B}\right), \tag{3.59}$$

where $B_{1,A}$ and $B_{1,B}$ are the magnetic field gradients in the two measurement traps A and B. For a difference of 1 µT/mm between the magnetic field gradients, this would result in a shift of $\sim 4 \cdot 10^{-12}$.

Whether the changes of the equilibrium positions can be compensated by suitably chosen ring voltages at surrounding traps not being used for the mass-ratio determination or by offset voltages at the endcaps will have to be studied in the future. More favorable however would be to improve the homogeneity of the magnetic field or to apply a measurement scheme that allows for identical ring voltages during the ν_c-determination even for non-mass doublets. For such a scheme, see App. E.

3.4.5. Trap voltage supplies and further electronics

Trap voltage supplies Besides the stability of the magnetic field, the stability of the electrostatic trapping potential is crucial for high-precision free-space cyclotron frequency determinations. A change of ΔU_r in the ring-voltage leads to a relative change of the axial frequency of

$$\frac{\Delta\nu_z}{\nu_z} = \frac{\Delta U_r}{2U_r}. \tag{3.60}$$

In the determination of the cyclotron frequency, the influence of the voltage-source stability depends on the measurement technique. For the double-dip technique, the relative change of ν_+ equals the relative change of ν_z. For the PnA-technique, the relative change is given by

$$\frac{\Delta\nu_+}{\nu_+} \approx -\left(\frac{\nu_z}{\nu_+}\right)^2\frac{\Delta\nu_z}{\nu_z} = -\left(\frac{\nu_z}{\nu_+}\right)^2\frac{\Delta U_r}{2U_r}. \tag{3.61}$$

For typical eigenfrequency hierarchies, a determination of the free-space cyclotron frequency by means of the invariance theorem with a relative precision of 10^{-11} thus requires a stability of the ring-voltage on the level of a few 10^{-8} during the measurement. The stability requirements for the correction electrode voltages are much less severe for an orthogonal trap [115].

For commissioning experiments, the trap voltages are provided by the well-established ultra-high precision voltage source *Stahl electronics UM 1-14 LN* [174]. The voltage range of the source is 0 to -14 V. Three high-precision channels, which have 1 µV resolution, provide voltages with temporal stabilities $\leq 4 \cdot 10^{-8}$ on time-scales of 40 s to several 100 s [162][24]. The temperature stability is typically ≤ 1 ppm/K [174]. The high-precision channels feature a ramping option where the voltage ramping is carried out with lower resolution ($\sim$ 0.2 mV) digital-to-analog converters (DACs). 13 additional DACs with $\sim$ 0.2 mV resolution are provided as auxiliary channels. Main drawbacks of the source are the limited voltage-range and the low number of high-precision channels. A minor drawback is that the ramping can only be triggered software-wise (see Sec. 4.2.2).

Therefore, a new ultra-high-stability voltage source called StaReP[25] is currently developed at the Max-Planck-Institut für Kernphysik in Heidelberg in collaboration with the Physikalisch-Technische Bundesanstalt in Braunschweig. The source will have 25 high-precision channels with a resolution ≤ 1.5 µV and a voltage range of 0 to -100 V. Its temporal stability was specified to be $\leq 4{\cdot}10^{-8}$ on a typical measurement time-scale of 10 min and its temperature stability was specified to be ≤ 0.4 ppm/K. All channels will have a ramping option where the ramping is triggered externally. Further details will be provided in the Ph.D. thesis of Christine Böhm [144].

Function generators Function generators are required for RF-excitations and -couplings of eigenmotions and as local oscillators in the down-conversion of signals. The function generators in use are of type *Agilent 33250* (single channel, frequencies up to 80 MHz) and *Agilent 33522* (dual channel, frequencies up to 30 MHz). Both types provide arbitrary waveform generation that can be used for SWIFT[26]-cleaning [175]. All function generators are connected to a *Stanford FS725* Rubidium frequency standard.

Auxiliary voltage supplies The gate- and drain-voltages of the cryogenic amplifiers are supplied by customized *Stahl electronics BS-10* voltage sources [176]. They provide voltages between +5 V and -5V with low temporal drift, low noise and low temperature drift. Currents are limited to 10 mA.

In the setup, there are three different versions of this device, which either feature additional channels for the control of cryogenic GaAs-switches, additional channels for the control of a varactor diode or a sense-input for a PID[27]-controller. The PID-control loop can be used to stabilize the drain voltage across the cascode input stage of the cryogenic axial amplifier by regulating the gate-voltage at the common-source input stage. This might be helpful to keep the resonance frequencies and quality factors of the detector stable.

Room temperature electronics like the *AF-DC-c* pre-amplifier and down-converter or the *Mini-Circuits ZFL-500LN* amplifiers are supplied by *Hameg HMP4040* or *Hameg HM7044* power supplies.

---

[24] The measurement in [162] was carried out at an output voltage of -1 V. The stability might be slightly different at other output voltages.

[25] Stable Reference for Penning-Trap Experiments

[26] Stored Waveform Inverse Fourier Transform

[27] Proportional-Integral-Derivative

Communication devices Most of the devices in use like voltage supplies, function generators or devices for signal analysis have to be controlled or read-out by a computer. The interfaces for this purpose in our lab are GPIB, USB, Ethernet and RS-232. During the first experimental run, all devices were either directly plugged to a computer or to the institute's network. Other experiments have identified their computer as a major source of noise [177]. Therefore for the next experimental runs, the control computer will be situated in a remote location outside the magnet laboratory, and for communication with the devices in the laboratory, *Agilent E5810B* GPIB/RS-232/USB-to-Ethernet gateways will be used.

Grounding, mains supply and noise-avoidance strategies Within the PENTATRAP experimental setup, there are two distinct ground potential regions: One for the EBIT, the beamline and related electronic devices - called $0V_{EBIT}$ in the following - and one for all devices in the magnet laboratory - called $0V_{lab}$ in the following. The central $0V_{EBIT}$-point is a copper plate at the *Dresden EBIT-W* which is connected to an earthed grounding bar in the EBIT-hall. A lot of other experiments with a lot of noisy equipment are connected to this grounding bar as well. The central $0V_{lab}$-point is a copper bar mounted at the magnet. For a start, this plate is connected to the protective earth (PE) of the mains supply. Other options, e.g. an earthing rod in a location away from the transformer station, might be considered in case this solution causes problems.

$0V_{EBIT}$ and $0V_{lab}$ are separated by a ceramic isolator in the beamline below the lower diagnostic station (see Fig. 3.1). Only during loading, they are connected by means of a relay. During measurements in the trap, the relay is opened, such that noise present on $0V_{EBIT}$ will not disturb the measurement. Any other connection between $0V_{EBIT}$ and $0V_{lab}$ is either broken during the measurement, or realized such that galvanic isolation is ensured (e.g. by means of opto-couplers).

For the connections of devices to $0V_{lab}$ the following rules are taken into account:

- The connections should be realized in a tree-like structure to avoid ground loops.
- Measurement electronics and power electronics should not have common ground paths.
- Outer conductors of coaxial cables should not carry any current.
- If a device draws current from a power supply, the return current should not be carried by ground connections.

None of these rules can be fulfilled completely - the difficulty is to find a good compromise. What this compromise will look like cannot be foreseen at this point.

For the mains supply of the magnet laboratory, there is a distribution cabinet that is exclusively used by our experiment and the ALPHATRAP-experiment. In the distribution cabinet, space is foreseen to introduce a DC-intermediate circuit, optionally with a battery for short power cuts. The benefit of the DC-intermediate circuit might be to trade mains disturbances for disturbances of the intermediate circuit that do not change over time. There is a direct connection from a transformer station to the distribution cabinet, such that other experiments (except for ALPHATRAP) do not interfere with the mains supply.

To minimize noise-interference, a combination of many different measures is required. Some measures that already have been realized, or that can be anticipated, are listed exemplarily in the following:

- No noisy equipment like pumps should be placed in the laboratory.
- As many devices as possible should be switched off during measurements (e.g. lights or liquid helium/nitrogen level sensors).
- If possible, switched-mode power supplies should be avoided.
- Being connected to the institutes LAN (i.e. the closest-by Ethernet-switch) by means of common Ethernet-cables is known to introduce excessive noise [178]. Therefore an Ethernet-switch is situated in the laboratory that is connected to the LAN by means of fiber optics.
- Power cords are chosen as short as possible.

3.4.6. Trap splitting and cabling

In the decision, which trap electrodes have to be split, how trap electrodes are biased, how excitation lines are set up and how both detectors and excitation lines have to be distributed to the electrodes within a trap, several points have to be considered:

- The detectors should be attached to an electrode with properly chosen effective electrode distance D_{eff}: For a given ion-species, ion-signal properties (of both dip and peak) and cooling time constants can only be influenced by D_{eff} and the effective parallel resistance $R_{p,\mathrm{eff}}$ of the detector. The choice of D_{eff} by means of an electrode and the choice of $R_{p,\mathrm{eff}}$ by means of a certain amplifier-detector coupling κ are thus closely related. The considerations to decide for a certain pick-up electrode therefore are the same as the considerations to decide for a certain κ (see Sec. 3.4.4.3). Values of D_{eff} are listed in Tab. 3.7.
- For the direct cyclotron frequency detection, for radial dipolar excitations and for quadrupolar couplings, some electrodes have to be split in halves. For axial-radial quadrupolar coupling, the electrode should not be the ring electrode.
- For axial excitation, it is favorable to either have a non-split electrode or a split electrode where both halves can be supplied with an RF-signal independently. Otherwise, there is the risk of accidental axial-magnetron coupling, either via the upper or the lower sideband.
- All trapping voltages should be low-pass filtered for noise-reduction.
- A capacitive voltage-divider for excitation signals reduces the influence of external noise sources.

Table 3.7.: Effective electrode distances for direct axial detection are shown in (a). Effective electrode distances for direct cyclotron detection at halves of split electrodes are shown in (b). Values are taken from [115].

electrode	D_{eff} (mm)
EC	32.5
CE	11.1
ring	-
EC+CE	8.1

(a)

electrode	D_{eff} (mm)
EC	62.5
CE	23.1
ring	31
EC+CE	21.1

(b)

- A grounding of excitation lines if not in use reduces the influence of external noise sources.
- The impedances to ground at electrodes next to detector-pick-up electrodes should not load the detectors. These impedances can be influenced for instance by the RF- and DC-filters.

During the first experimental run, the trap was cabled as shown in Fig. 3.30. In retrospective, the cabling was not optimal in several ways:

- The Faraday cup, which had a connection to room temperature by means of a cryogenic coaxial cable, loaded the axial detector heavily, since it could only be grounded at room temperature (see Sec. 3.4.4.4).
- The ion charge-states could not be chosen as high as anticipated (due to vacuum problems), and the quality factor of the axial detector was not as high as anticipated (see Sec. 3.4.4.4). Therefore the signal pick-up at the lower endcap with its comparably high D_{eff} prohibited axial dip detection.
- Axial dipolar excitation at the split upper endcap always involved the risk of accidental axial-magnetron coupling.

For the coming experimental runs, the cabling scheme shown in Fig. 3.31 is considered to be optimal. Important changes compared to the previous setup and the setup described in [115] are the following:

- The axial signal is picked-up at a correction electrode, which reduces D_{eff} by nearly a factor of three. This will allow for axial dip detection during commissioning experiments with comparably low charged ions. As soon as the vacuum is good enough for high charge states, a relocation of the axial detector to an endcap can be considered.
- Separate RF-excitation lines to both halves of the split endcap will allow for a purely dipolar axial excitation by applying identical RF-signals to both halves, without any quadrupolar axial-radial components of the excitation field.

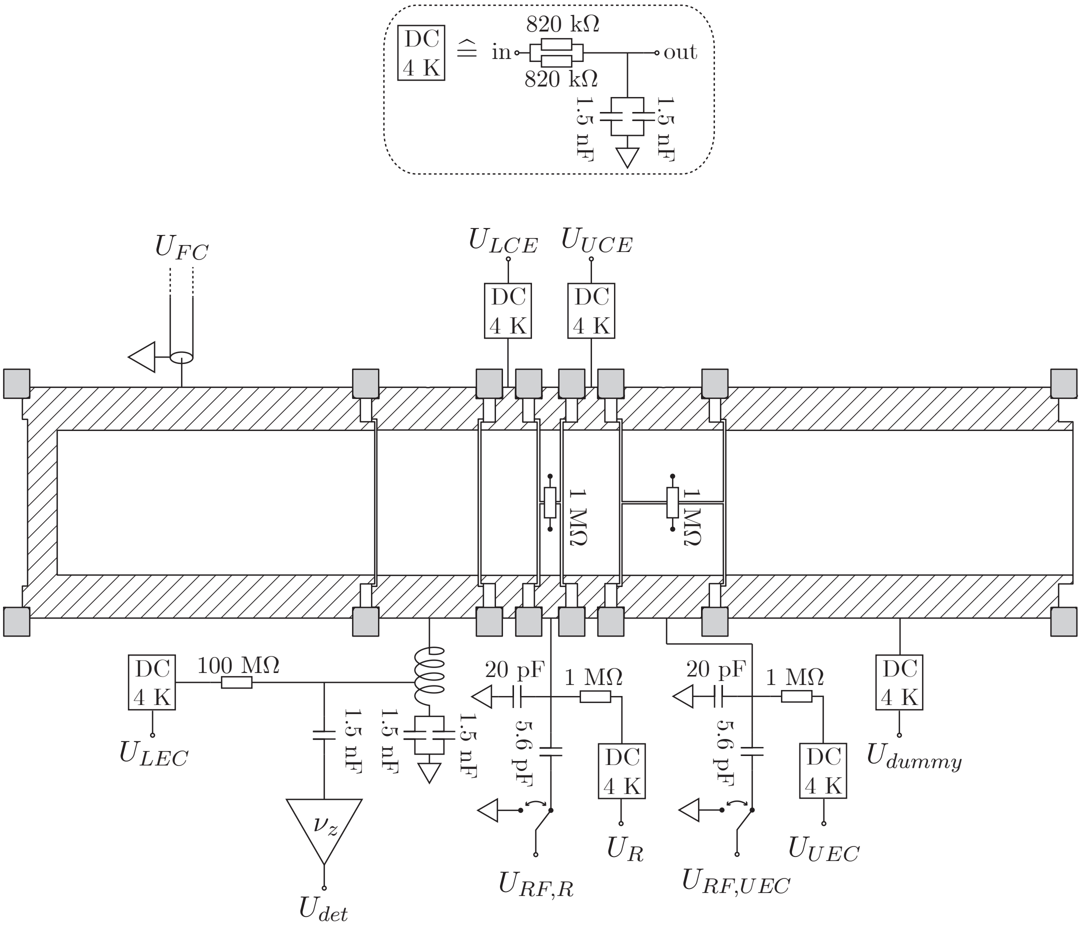

Figure 3.30.: The cabling of the trap stack in the cryogenic region for the first experimental run is shown. For further details see text.

- Electrodes next to the axial detector are DC-biased only, without an RF-filter or a cyclotron-detector attached. The capacitors of the DC-filters provide a proper AC-ground connection, such that the axial resonator is not loaded. Therefore, significantly higher Q-values of the detector are expected.

- It was previously planned to provide identical DC-biasing of both halves of the split electrode at which the cyclotron signal is picked up by a 1 MΩ-resistor across the slit. Calculations show that this loads the cyclotron resonator heavily - even if the resistance is chosen higher[28]. The biasing scheme shown in Fig. 3.31 does not load the resonator at all.

- In the RF-/DC-filter unit which is connected to electrodes, to which excitations are applied, the 1 MΩ-resistor to decouple the DC-filter from the RF-filter is replaced by a 10 kΩ-resistor to reduce the resistor's thermal noise. However, this requires that the capacitance to ground can be switched from 15 pF (the value that is used in the capacitive voltage divider) to some higher value, e.g. 3 nF, when the cyclotron resonator at the neighboring electrode needs to be used. Otherwise the 10 kΩ-resistor would load the cyclotron resonator such that the cyclotron cooling time would increase by more than an order of magnitude.

3.5. Control system

At the PENTATRAP-experiment, a multitude of devices distributed over two laboratories has to be controlled and read out. Among the devices for a complete setup are:

- HV supplies (up to 30 channels),
- trap voltage supplies (25 channels),
- function generators (20 channels used for RF excitations or as local oscillators),
- auxiliary voltage supplies (40 channels for the cryogenic detectors),
- ten phase shifters for axial and cyclotron feedback cooling,
- FFT-analyzers (ten channels for axial and cyclotron detectors).

These and other devices are controlled (and in some cases read out) with the PENTATRAP control system (CS), which is based on the *CS-framework* that was developed at GSI [179]. The framework is based on *National Instruments LabVIEW*. Since LabVIEW-drivers are available for most instruments, this facilitates the integration of new devices.

---

[28] Furthermore, resistors with a higher resistance than 1 MΩ in a non-magnetic grade were found to be rare and very difficult to purchase.

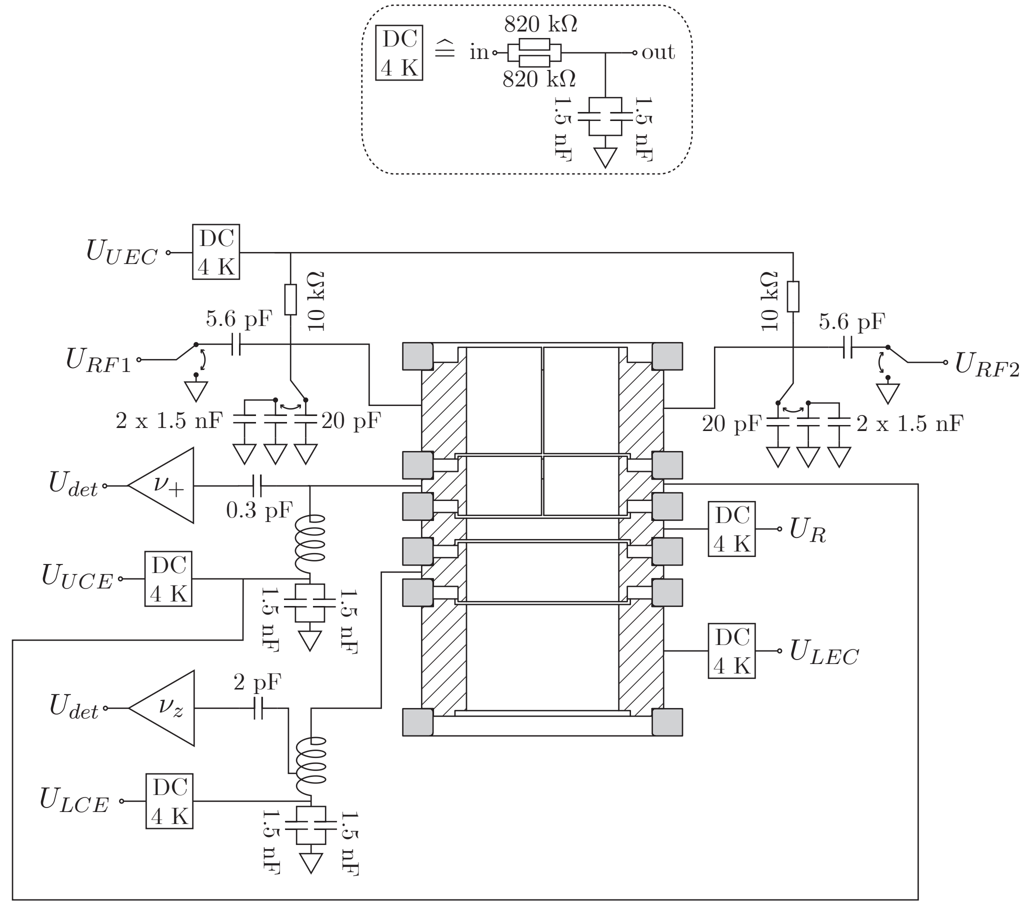

Figure 3.31.: The cabling of an individual trap for the coming experimental runs is shown. For further details see text.

The automation of measurements is a major task of every control system. For this purpose, the PENTATRAP CS features three main classes, called PTScanner, PTSequencer and PTDataHandler. The PTScanner allows to perform multi-dimensional parameter-scans, e.g. for the optimization of certain beamline settings to obtain a high transport efficieny. With the PTSequencer, measurements which consist of sequences of device operations can be set up (for an example see Fig. 3.32a). The PTDataHandler is used for data acquisition.

Device operations that are not time-critical are directly controlled from the CS. If a device operation has to be timed precisely, it can be triggered by an FPGA-card that is used as a PPG (see Sec. 3.3.1). The graphical user interface to control the FPGA-card is shown in Fig. 3.32b.

During the first experimental run, it turned out to be most practical to use the CS and LabVIEW side by side: While established techniques can be implemented in the CS, it is convenient to set up small LabVIEW routines to test new procedures. Further details on the PENTATRAP CS can be found in [180].

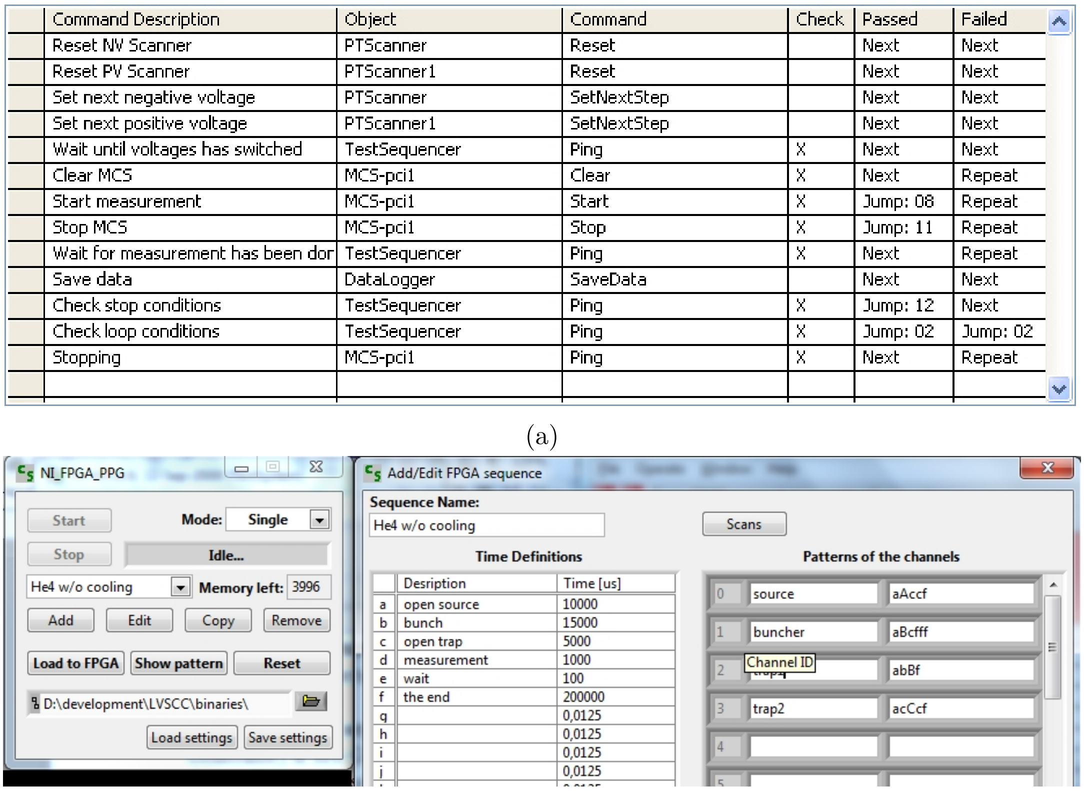

Command Description	Object	Command	Check	Passed	Failed
Reset NV Scanner	PTScanner	Reset		Next	Next
Reset PV Scanner	PTScanner1	Reset		Next	Next
Set next negative voltage	PTScanner	SetNextStep		Next	Next
Set next positive voltage	PTScanner1	SetNextStep		Next	Next
Wait until voltages has switched	TestSequencer	Ping	X	Next	Next
Clear MCS	MCS-pci1	Clear	X	Next	Repeat
Start measurement	MCS-pci1	Start	X	Jump: 08	Repeat
Stop MCS	MCS-pci1	Stop	X	Jump: 11	Repeat
Wait for measurement has been dor	TestSequencer	Ping	X	Next	Repeat
Save data	DataLogger	SaveData		Next	Next
Check stop conditions	TestSequencer	Ping	X	Jump: 12	Next
Check loop conditions	TestSequencer	Ping	X	Jump: 02	Jump: 02
Stopping	MCS-pci1	Ping	X	Next	Repeat

(a)

Mode: Single

Idle...

He4 w/o cooling

Memory left: 3996

D:\development\LVSCC\binaries\

Sequence Name: He4 w/o cooling

Time Definitions

	Desription	Time [us]
a	open source	10000
b	bunch	15000
c	open trap	5000
d	measurement	1000
e	wait	100
f	the end	200000
g		0,0125
h		0,0125
i		0,0125
j		0,0125

Patterns of the channels

0	source	aAccf
1	buncher	aBcfff
2	Channel ID	abBf
3	trap2	acCcf
4		
5		

(b)

Figure 3.32.: Two graphical user interfaces (GUIs) of the PENTATRAP control system are shown. In (a), the GUI of the sequencer is shown. The sequence in this example is used to record Wien filter spectra, i.e. to scan a certain range of Wien filter voltages and to record the counts accumulated on the MCP for each set of voltages. In (b), the GUI to control the FPGA-card is shown. Pulse patterns for several output channels of the FPGA can be defined. These patterns can be applied either one time or continuously. Courtesy of M. Goncharov.

4. Experimental procedures and results

4.1. Ion production and transport

Aim of this section and the following one is to describe the procedures that are performed to obtain high production rates of the ions of interest and a high efficiency of the transport from the EBIT[1] down to the Penning-trap system.

4.1.1. Preparing ions of interest

EBIT offset potential First one has to decide on the offset of the EBIT-trapping potential U_A (see Fig. 3.4), which mainly[2] defines the minimum energy of ions being ejected from the EBIT. The following aspects have to be considered in this decision:

- The emittance after the Wien filter is independent of U_A. Therefore a lower U_A leads to a lower increase in emittance, when the ions are decelerated to a certain energy by means of a drift tube.
- Electron-impact ionization cross sections are energy-dependent. Since the cathode potential is fixed to the recommended value of -3 kV, U_A defines the electron energy and thus influences ionization rates.
- One of the three electrodes forming the ion-guiding lens after the EBIT has to be on a potential below the cathode potential of -3 kV in order to reflect electrons passing through the hole in the electron collector. This gives a practical lower limit of about 2 kV for U_A. It was experienced that for a lower U_A, the lens voltages would all have to be above the cathode potential to guide the ion beam properly towards the Wien filter.

Starting guesses for optimization procedure For the optimization of the production rate and the guiding of the ions of interest, it is crucial to have good starting guesses of all relevant parameters. To obtain these guesses, the Wien filter has to be disabled by shorting its' electrodes and removing the permanent magnet. Otherwise the initial count rates would be unnecessarily low. Then, the following parameters are varied, until a bright and well-focused spot appears on the phosphor screen of one of the diagnostic stations installed:

1. EBIT electron current,

---

[1] Within this chapter, the term EBIT refers to the *Dresden EBIT-W* (see Sec. 3.2.3), which has been used during the commissioning experiments.

[2] Electron-beam parameters are slightly modifying the shape of the EBIT-trapping potential, see e.g. [118].

2. charge breeding time,
3. pressure in the EBIT volume,
4. EBIT trapping potential depth (see Sec. 3.2.3),
5. extraction-voltage at the EBIT's extraction-endcap,
6. voltages at the lens system $L_{1,2,3}$ (see Fig. 3.4) in front of the Wien filter,
7. voltage at the einzel lens D1 after the Wien filter (see Fig. 3.5).

The first four points influence the production rate of the ions of interest. The production rate is governed by a complex rate equation taking into account electron-ion interaction, ion-ion-interaction and ion-neutral interaction. A detailed treatment of this topic can be found in [181] and goes beyond the scope of this thesis. Points 5 and 6 determine the efficiency of the transport of the ions through the entrance- and exit-apertures of the Wien filter. The voltage at the einzel lens affects the focus of the ion beam.

Wien filter spectra After having obtained good starting guesses for all parameters that have been listed in the previous paragraph, the Wien filter can be enabled again by inserting the magnet and connecting the electrodes to HV-supplies. To obtain the Wien filter voltage[3] U_{Wien}, at which the ions of interest are transmitted through the filter, U_{Wien} is scanned and the counts on the MCP of one of the diagnostic stations, averaged over several bunches, are detected for each voltage. As an example, a Wien filter spectrum with medium charged argon ions[4] is shown in Fig. 4.1a. The detection efficiency of the MCP used during the measurements presented here turned out to be highly dependent on the position and the focusing of the beam, leading to a distortion of some of the peaks. A new MCP or the use of the Faraday cup in the diagnostic station instead of the MCP will solve this problem.

The positions of the peak can be described by the relation

$$U_{\text{Wien}} = \frac{\kappa_{\text{Wien}}}{\sqrt{m/q}} + U_{\text{corr}}. \tag{4.1}$$

For $U_{\text{corr}}=0$, this formula describes the behaviour of an ideal Wien filter where κ_{Wien} incorporates the magnetic field strength and the geometry of the Wien filter electrodes. κ_{Wien} scales linearly with the ion velocity and therefore shows a $\sqrt{U_A}$-dependence.

---

[3] The term Wien filter voltage refers to the two voltages applied to the two electrodes of the Wien filter with equal magnitude and opposite sign.

[4] During most of the commissioning experiments, Ar-ions were used. The main motivation for this was the large m/q-distance between the different argon charge states due to the relatively low mass and the high isotopic purity (more than 99% ^{40}Ar [182]). Furthermore Ar-ions in certain charge states (e.g. Ar^{8+}) are quite well separated in m/q from rest-gas ions. These large m/q-distances simplify the loading of an ion bunch to the trap without a lot of contaminations. Xenon, which had been used in the very beginning, was abandoned after some time due to the large abundances of various isotopes (>10% for ^{132}Xe, ^{129}Xe, ^{131}Xe and ^{134}Xe [182]) and the inability to properly clean the ion cloud in the trap (see Sec. 4.2.3).

U_{corr} accounts for imperfections of the Wien filter like e.g. fringe fields. From the fit of Eq. (4.1) to the data shown in Fig. 4.1b, which was recorded with argon ions and an EBIT offset potential of $U_A = 4.9$ kV, one obtains $\kappa_{\mathrm{Wien}} = 429.0(2.2)$ V and $U_{\mathrm{corr}} = -2.9(1.0)$ V.

The calibration of the Wien filter, i.e. the determination of κ_{Wien} and U_{corr}, is particularly important, when peaks of neighboring charge states are overlapping, leading to a broad hill in the Wien filter spectrum. In this case, Eq. (4.1) is required to set the Wien filter voltages properly for a certain charge state.

Optimization procedure After having determined a proper Wien filter voltage from a Wien filter spectrum, starting guesses for all relevant parameters to optimize the production rate and the transport of the ions of interest are available.

First, the EBIT electron current, the charge breeding time, the pressure in the EBIT as well as the EBIT potential depth are optimized simultaneously. For this optimization, the Faraday cups incorporated in the diagnostic stations are mainly used. Their main advantage over the MCP is that the signal height obtained from a measurement as described in Sec. 3.3.2.2 is independent of peak position and focus as long as the ions hit the cup. The optimization consists mainly of a systematic variation of the corresponding parameters until the height of the signal on the Faraday cup is maximized. It has to be pointed out that some of the parameters are interrelated: For instance, the optimum charge breeding time depends on the electron current.

After that, first the extraction-voltage at the EBIT's extraction-endcap and then the voltages at the lens system $L_{1,2,3}$ are varied until the height of the signal on the Faraday cup is maximized. Following, the Wien filter voltage is varied in smaller steps (0.1 or 0.2 V) compared to the recording of a Wien filter spectrum until the Faraday cup signal is maximized. Then, the einzel lens D1 and the SX-steerers (S1, S2, S3, S4) are set such that a well-focused spot appears on the phosphor screen of the lower diagnostic station.

4.1.2. Ion deceleration with room temperature drift tube

The purpose of the room-temperature drift tube D4 (see Fig. 3.5) is to decelerate ions, which are ejected from the EBIT at energies of several keV/q, to energies of only a few 100 eV/q. Since the EBIT-extraction energy of the ions is quite close to q$\cdot eU_A$ (within a few 10 eV/q), a proper drift tube voltage can be found easily. Thus the main task is to find the right timing for the pulsing of the drift tube. For this purpose, the drift tube is set to different static voltages $U < U_A$, and TOF spectra, summed over several bunches, are recorded using the MCP of the lower diagnostic station. As an example, TOF spectra of argon ions for several static voltages U are shown in Fig. 4.2. With the mean flight time T from the EBIT to the MCP, the proper time to

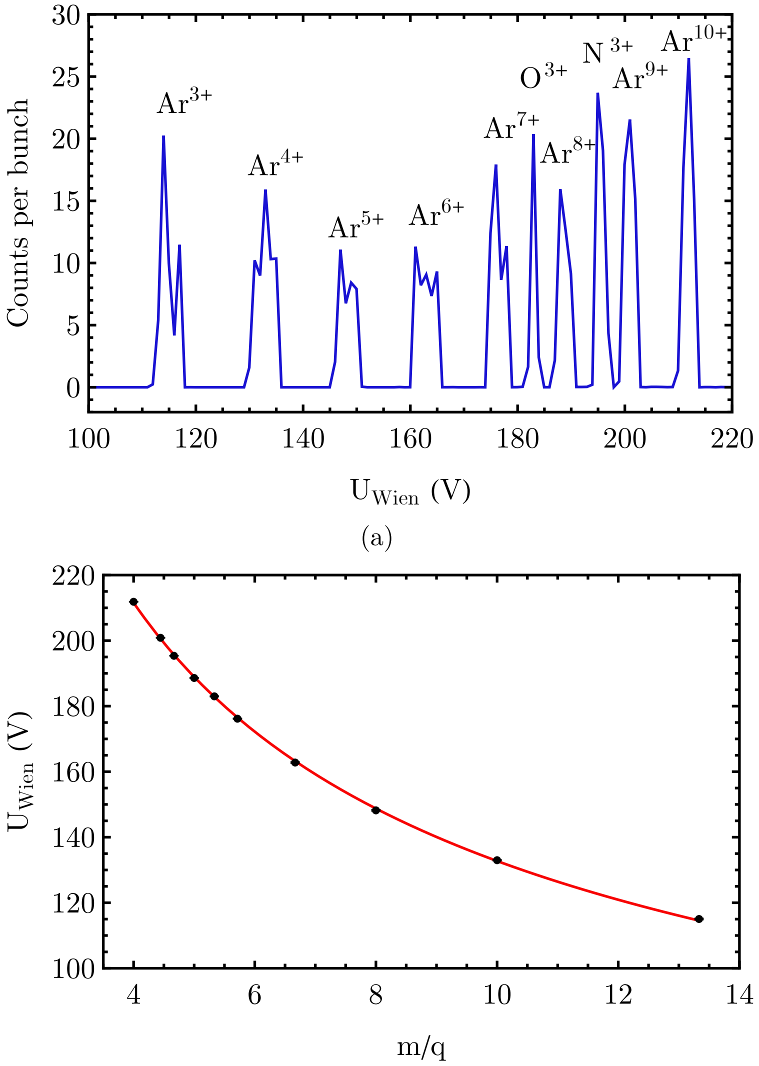

(a)

(b)

Figure 4.1.: (a) Wien filter spectrum of argon for U_A=4.9 kV, a cathode current of 21.5 mA and a charge breeding time of 10 ms. (b) Peak positions versus m/q of the different ions. The dots indicate the peak positions obtained from (a) by fitting a Gaussian to each individual peak. Error bars are smaller than the dot size. The red line is a fit of Eq. (4.1) to this data. For further details, see text.

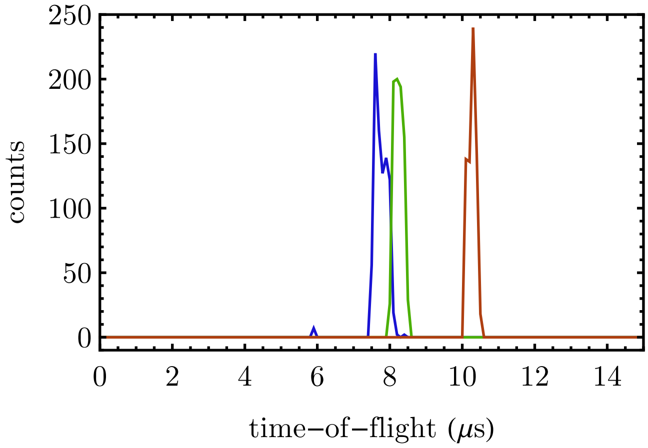

Figure 4.2.: TOF-spectra of Ar^{8+}-ions being extracted from the EBIT at a potential of $U_A = 2380$ V. The lines correspond to static voltages applied to D4 of 0 V (blue), 1000 V (green) and 2000 V (brown).

pulse down D4 at a certain drift tube voltage U is given by:

$$T_{\text{pulse}} = T(0\text{ V}) - \frac{l}{\sqrt{2qeU_A/m}} + \frac{T(U) - T(0\text{ V})}{2} \tag{4.2}$$

$$= \frac{T(U) + T(0\text{ V})}{2} - \frac{l}{\sqrt{2qeU_A/m}}, \tag{4.3}$$

where $l \approx 41$ cm is the distance between the center of the drift tube and the MCP. The first two terms in Eq. (4.2) give the mean TOF of non-decelerated ion bunches from the EBIT to the center of the drift-tube (which is the location, at which the ions should be situated during the pulse-down of the drift tube). The last term gives the additional time that the ions need to “climb up the potential hill” to the center of the drift tube being set to U.

After choosing U and finding the corresponding pulse-down time T_{pulse}, the drift tube can be operated in pulsed mode. Following, the einzel lens D1 and the SX-steerers have to be reconfigured such that a well-focused spot appears on the phosphor screen of the lower diagnostic station.

4.1.3. Ion transport to the cryogenic region

Adjusting SX-steerers and D1 After being able to slow down ions in the room-temperature region, the next task is to transport these ions into the cryogenic region where the traps are located. For this purpose, fast ions (which are not decelerated by D4) are transported to the cryogenic region first. This is much easier than transporting slow ions to the cryogenic region, for the following reasons:

- The bunch emittance increases when ions are decelerated.

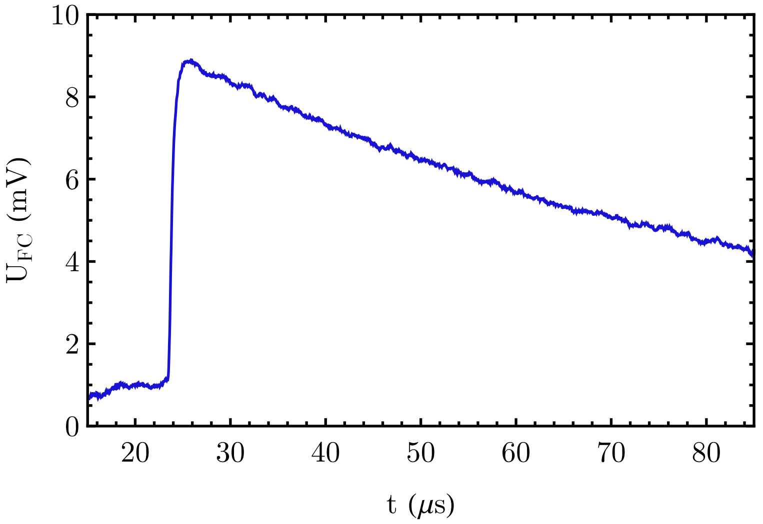

Figure 4.3.: A cryogenic Faraday cup spectrum of fast Ar^{8+}-ions having started at an EBIT-potential of $U_A = 2380$ V is shown. Times are relative to the time of the ejection of the ions from the EBIT. This spectrum, as well as all other spectra presented within this chapter, is an average of 512 single spectra.

- It was experienced, that fast bunches are easier to steer and to focus than slow bunches. The behaviour of slow bunches under changes of beamline settings was difficult to predict, especially when the alignment of the EBIT with the beamline was bad (see Sec. 3.3.1).

The transport of fast ions to the cryogenic region is realized by scanning the SX-steerer voltages until an ion-signal appears on the cryogenic Faraday cup below the trap. Subsequently, the voltage at the einzel lens D1 and the voltages at the SX-steerers are varied, until the minimum-to-maximum amplitude on the Faraday cup is maximized. A resulting Faraday cup spectrum of Ar^{8+}-ions is shown in Fig. 4.3.

After this step, the MCP of the lower diagnostic station is moved back into the beamline and the ion spot on the phosphor screen is recorded (see Fig. 4.4a). Afterwards, the ions get slowed down again by means of the upper drift tube. In the following, the voltages at the einzel lens D1 and at the SX-steerers are varied, until the ion spot on the phosphor screen of the lower diagnostic station is properly focused and approximately in the same position as the spot of the fast ions. Afterwards, the MCP is moved out of the beamline again.

After this procedure, an ion signal can usually be seen right away on the cryogenic Faraday cup in the trap tower. Then the voltages at the einzel lens D1 and at the SX-steerers are varied to maximize the height of the signal on the cryogenic Faraday cup. In Fig. 4.4b it is shown, how the ion spot on the phosphor screen of the lower diagnostic station looks like afterwards. It can be seen that the two spots in Fig. 4.4a and Fig. 4.4b are quite close to each other and partly overlap. That their centers

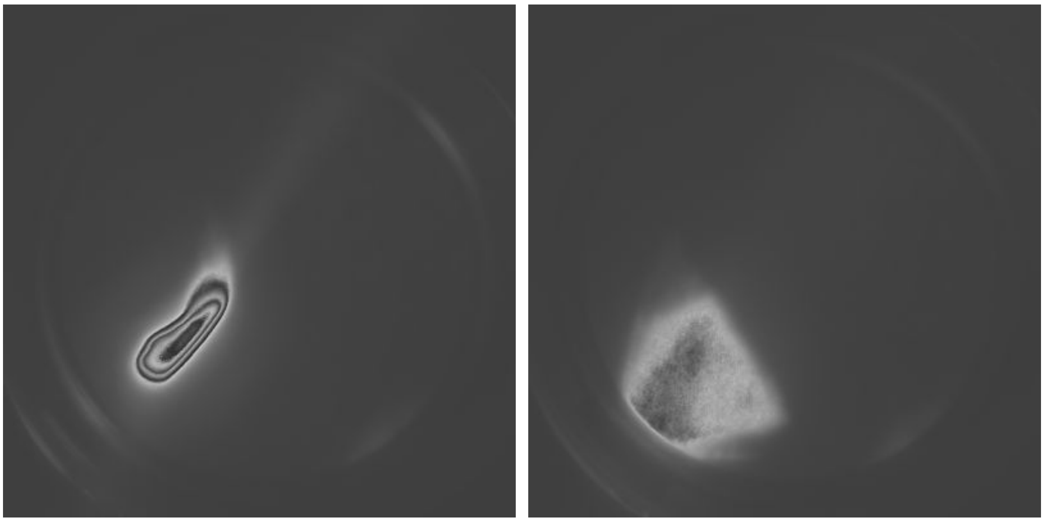

(a) (b)

Figure 4.4.: Averaged spots of fast and slow Ar^{8+}-ions on the phosphor screen of the lower diagnostic station are shown in (a) and (b), respectively. The beamline configurations were such that the ions would have been transported into the cryogenic region with the MCP out of the beamline.

do not coincide with the center of the MCP is for two reasons: First of all, the manipulator was set to some arbitrary, but fixed position. Therefore the center of the MCP does not necessarily coincide with the center of the beamline. Furthermore, the EBIT and the beamline have not been perfectly aligned (see Sec. 3.3.1).

Steering of ions onto the trap axis Afterwards, the last ion-optical element in the room temperature region, the combined einzel lens and steerer-unit incorporating the electrodes S2-1/2/3/4 (see Fig. 3.5) is configured. Aim of this configuration is to set the focus of the beam in the trap region and to steer the ions onto the trap axis in order to capture ions in the trap center.

In a first step, all four segments S2-1/2/3/4 are set to the same bias-voltage in order to set the focus of the beam. The bias-voltage is varied, until the height of the signal on the cryogenic Faraday cup is maximized. In the following, two of the four segments are held on the optimum bias potential U_b, while the voltages of the other two segments are scanned around U_b. These two segments are adjacent to each other and thus allow for steering in all directions in the plane perpendicular to the beam flight direction. For each pair of voltages, the minimum-to-maximum amplitude of the signal on the cryogenic Faraday cup is recorded. The result of such a scan with Ar^{8+}-ions is shown in Fig. 4.5.

Two important information can be extracted from such a scan:

1. The size of the beam in the plane perpendicular to the flight direction is comparable to the size of the Faraday cup, which has a diameter of 10 mm. Since

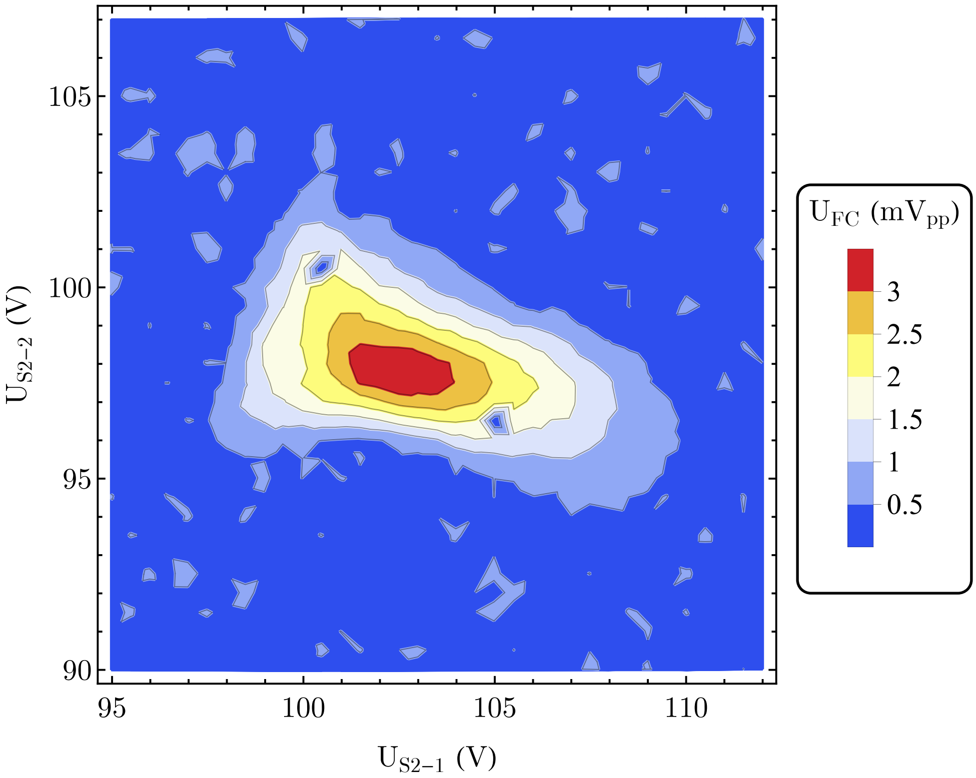

Figure 4.5.: The result of a scan of the voltages at two adjacent S2-X-steerers is shown. For each pair of voltages, the minimum-to-maximum amplitude of the signal on the cryogenic Faraday cup was recorded. The other two steerers were held at 102 V. The measurement was carried out with Ar^{8+}-ions, which were ejected from an EBIT-potential of 2380 V and decelerated by D4 by 2220 eV/q.

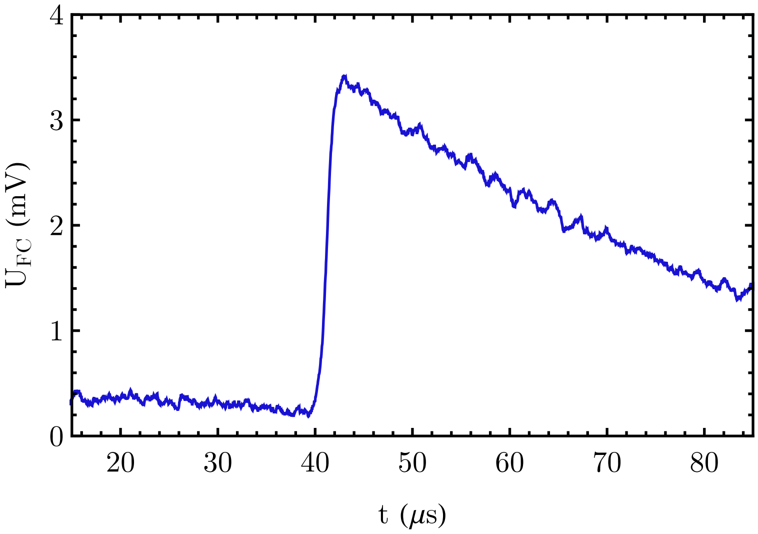

Figure 4.6.: A cryogenic Faraday cup spectrum of slow Ar^{8+}-ions is shown. The ions were ejected from an EBIT-potential of $U_A = 2380$ V and decelerated by D4 by 2220 eV/q. Times are relative to the time of the ejection of the ions from the EBIT.

the beam profile is more elliptic than round (see for instance Fig. 4.4a), it can be stated that the lengths of the principal axes are several mm.

2. The voltage-combination at which the Faraday cup signal height is maximal provides best steering of the bunch onto the trap axis.

Transport efficiency and ion numbers With proper settings of all room temperature ion optical elements, a signal as shown exemplarily in Fig. 4.6 can be obtained with the Faraday cup in the trap tower. The measurement was carried out with Ar^{8+}-ions, which were ejected from an EBIT-potential of $U_A = 2380$ V and decelerated by the room temperature drift tube D4 by 2220 eV/q.

Comparing the signal heights in Fig. 4.3 and Fig. 4.6, one obtains an efficiency of the transport of slow ions compared to the transport of fast ions to the cryogenic region of about 40%. This number is of course only valid for the particular EBIT and beamline settings during the measurement, but it shows that transport efficiencies of several 10% are achievable.

The gain of the amplifier in use was measured to be $A = 710(14)$ where a conservative uncertainty of 2% was estimated for the gain. The capacitance of the Faraday cup and the cabling was measured to be 115(5) pF. The input capacitance of the amplifier is estimated to be 10(8) pF. Thus the total capacitance C_{tot} is 125(10) pF. From the minimum-to-maximum amplitude of 3.3 mV of the Faraday cup signal shown in Fig. 4.6 it can be concluded that the mean number of Ar^{8+}-ions in the corresponding bunches was 450(40).

4.1.4. Ion deceleration with cryogenic drift tube

Ion bunch energy distribution For the deceleration of the ions by means of the room temperature drift tube, a rough guess of the mean ion energy is sufficient to set all parameters properly. The cryogenic drift tube on the other hand serves the purpose to decelerate the ions to only a few eV/q. Therefore, the energy distribution of the ion bunch has to be known with eV/q-precision.

The determination of the ion bunch energy distribution is based on the following idea: When the cryogenic drift tube is set to a static voltage U_{DT}, which corresponds to an energy $q{\cdot}\mathrm{e}{\cdot}U_{DT}$ being represented in the ion bunch energy distribution, then part of the ions in the bunch will be reflected from the drift tube. The other part of the ions will overcome the drift tube's potential hill and will be re-accelerated towards the cryogenic Faraday cup. If $p(E)$ is the ion kinetic energy probability density function, the fraction

$$R_{ref}(U_{DT}) = \int_0^{qU_{DT}} p(E')dE' \tag{4.4}$$

of the ions is reflected, whereas the fraction

$$R_{trans}(U_{DT}) = 1 - R_{ref} = 1 - \int_0^{qU_{DT}} p(E')dE' \tag{4.5}$$

of the ions is transmitted, assuming that no ions are lost during the deceleration-re-acceleration sequence.

The ion bunch energy distribution can thus be determined by scanning U_{DT} and measuring the corresponding minimum-to-maximum amplitudes of the signals on the cryogenic Faraday cup. The result of such a scan is shown in Fig. 4.7. The measurement was carried out with Ar^{8+}-ions, which were ejected from an EBIT-potential of $U_A = 2380$ V and subsequently decelerated by D4 by 2220 eV/q. From the fit of Eq. (4.5), scaled by a constant factor and with an offset added, assuming a Gaussian energy distribution, a mean energy of 149.1 eV and a standard deviation of 8.9 eV can be obtained. It can be seen that the energy distribution with an offset of q·2220 eV added is slightly below $\mathrm{q}{\cdot}\mathrm{e}{\cdot}U_A$. This can be explained by the electrostatic potential of the electron beam, which shifts the minimum potential energy of the ions below $\mathrm{q}{\cdot}\mathrm{e}{\cdot}U_A$.

Deceleration voltage and timing Knowing the ion bunch energy distribution, the deceleration voltage at the cryogenic drift tube can be chosen. The deceleration voltage and the depth of the trap, into which the ion bunch should be loaded, determine which ions from which part of the initial energy distribution can be captured in the trap.

When many ions should be loaded into the trap, a voltage corresponding to an energy slightly below the middle of the energy distribution shown in Fig. 4.7 is chosen. Since the trap voltage source used during the first experiments (see Sec. 3.4.5) did not provide less than -14 V, it was not possible to capture all ions of a bunch, since the typical full width at half maximum (FWHM) of the ion bunch energy distribution

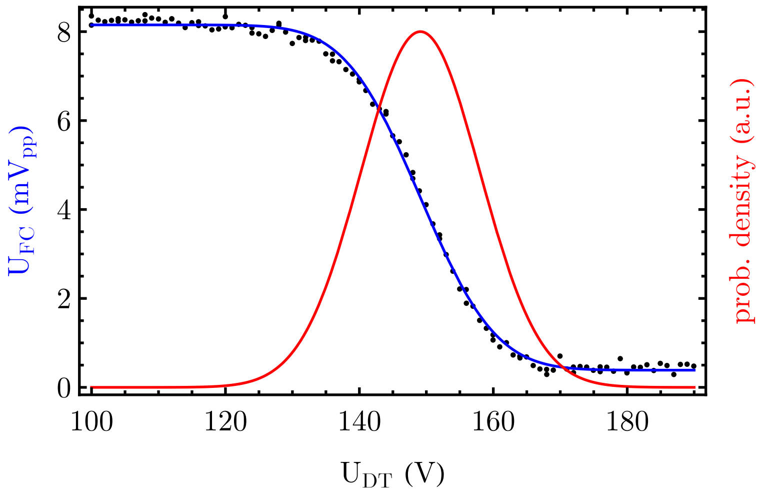

Figure 4.7.: The black dots represent measurements, in which the cryogenic drift tube was set to a static voltage U_{DT}, and the corresponding minimum-to-maximum amplitude of the signal on the cryogenic Faraday cup was measured. The blue line represents a fit of $a \cdot R_{trans}(U_{DT}) + b$ to the data. $R_{trans}(U_{DT})$ is given by Eq. (4.5), assuming a Gaussian energy distribution. a and b are a scaling-factor and an offset, respectively. The red line represents the resulting Gaussian probability density function. The measurement was carried out with Ar^{8+}-ions, which were ejected from an EBIT-potential of $U_A = 2380$ V and decelerated by D4 by 2220 eV/q.

was 21 eV/q. But this was not a major disadvantage due to the large number of ions in one bunch. Furthermore it is possible to accumulate several bunches in the trap.

When only a few ions should be loaded into the trap, a voltage corresponding to the low-energy tail of the energy distribution shown in Fig. 4.7 is chosen. Then most ions of the bunch, except for the few ones in the low-energy tail, aren't trapped but hit the Faraday cup instead.

When a certain deceleration voltage U_{DT} has been chosen, the proper timing for pulsing the drift tube down has to be determined. For this purpose, the following steps are carried out:

1. The cryogenic drift tube is set to ground and a TOF spectrum using the cryogenic Faraday cup is recorded.
2. The TOF-distribution $p_{\mathrm{TOF},0}(t)$ of the ion bunch is determined by fitting Eq. (3.11) with a Gaussian TOF-distribution and an offset added to the TOF-spectrum. $p_{\mathrm{TOF},0}(t)$ is corrected for the step-response function[5] of the Faraday cup amplifier by down-shifting all times by 0.26 µs.
3. The fraction f of the ions that would be reflected by setting the cryogenic drift tube statically to U_{DT} is calculated using the ion bunch energy distribution.
4. The TOF T_0 of the ions that would just pass the cryogenic drift tube, if it were set statically to U_{DT}, is determined. Assuming that the TOF-distribution width of the ion bunch when being extracted from the EBIT is negligible compared to the TOF-distribution width acquired during the flight because of the non-zero width of the velocity-/energy-distribution, T_0 is determined by solving

$$\int_0^{T_0} p_{\mathrm{TOF},0}(t)dt = f. \tag{4.6}$$

   A Faraday cup spectrum, the result of the fit and the resulting T_0 are shown exemplarily in Fig. 4.8a.
5. The cryogenic drift tube is set statically to U_{DT} and a TOF-spectrum using the cryogenic Faraday cup is recorded.
6. For the determination of the TOF-distribution $p_{\mathrm{TOF},U_{DT}}(t)$ it has to be taken into account that the energy distribution is cut at q·e·U_{DT}. Therefore, the TOF-distribution will be cut at the time-of-flight of ions having initially a kinetic energy of q·e·U_{DT}. To perform a fit of Eq. (3.11) with such a cut distribution to the full Faraday cup spectrum is difficult, since the fit function would be a piecewise defined function.

---

[5] The step-response function of the amplifier can be described reasonably well by an integrated Gaussian with a mean-value of 0.26 µs and a standard deviation of 0.13 µs. Assuming the TOF-distribution of the ions is Gaussian as well, the rising edge of the TOF-spectrum measured at the Faraday cup is basically the integration of the convolution of two Gaussian distributions (which is a Gaussian distribution as well). Since the standard deviation of the amplifier's step-response function is typically much smaller than the width of the TOF-distribution, the main effect of the amplifier's step response function is an up-shift of the measured spectrum by 0.26 µs.

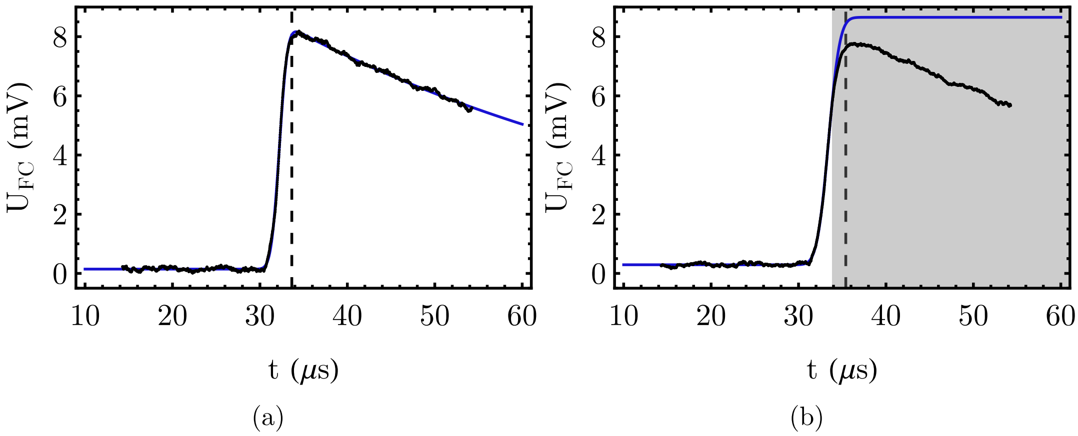

Figure 4.8.: Time-of-flight spectra are shown for static voltages at the cryogenic drift tube of 0 V in (a) and 132 V in (b). The measurements were carried out with Ar^{8+}-ions, which arrived at the cryogenic drift tube with an energy distribution as shown in Fig. 4.7. In (a) the blue line represents the result of the fit of Eq. (3.11) with a Gaussian TOF-distribution and an offset added to the Faraday cup spectrum. The dashed line marks T_0 (see text). In (b), the Faraday cup spectrum is divided into a fit-region (white background) and the rest of the spectrum (gray background). The blue line represents the result of the fit of an integrated Gaussian, scaled by the scale-factor of the fit in (a) and with an offset added to the data of the fit-region. The dashed line marks $T_{U_{DT}}$. Times are relative to the time of the ejection of the ions from the EBIT.

To circumvent this problem, the data set for the fit is limited in time to slightly below the point where the cut is suspected to be. Since in this data set the effect of the exponential decay of the signal is small, a simplified fit function $p'_{\mathrm{TOF},U_{DT}}(t)$ can be used: $p'_{\mathrm{TOF},U_{DT}}(t)$ is simply an integrated Gaussian with an offset added. For the scaling of the Gaussian, the amplitude extracted from the $p_{\mathrm{TOF},0}(t)$-fit is used. The cut in the TOF-distribution is then accounted for in the next steps. The step-response function of the Faraday cup amplifier is accounted for by down-shifting all times by 0.26 µs.

7. The time-of-flight $T_{U_{DT}}$ of the ions that just pass the cryogenic drift tube being set statically to U_{DT} is determined by solving

$$\int_0^{T_{U_{DT}}} p'_{\mathrm{TOF},U_{DT}}(t)dt = f. \tag{4.7}$$

   A Faraday cup spectrum, separated into a fit-region and the rest of the data, the result of the fit and the resulting $T_{U_{DT}}$ are shown for $U_{DT} = 132$ V in Fig. 4.8b.

8. The proper time T to pulse down the drift tube is calculated similar to Eq. (4.2):

$$T = \frac{T_0 + T_{U_{DT}}}{2} - \frac{l}{\sqrt{2qeU_{DT}/m}}, \tag{4.8}$$

   where l is the distance between the center of the drift tube and the Faraday cup, which was ∼100 mm for the experiments presented here and will be ∼157 mm for the experiments with the five-trap tower.

4.2. Ions in the trap

With a sufficient number of ions available in the trap region, the first steps in the commissioning of the trap are:

1. To load ions into the trap (see Sec. 4.2.1).

2. To analyze the trap content (see Sec. 4.2.2).

3. To prepare the ion cloud such that only a few ions of interest are left in the trap (see Sec. 4.2.3 and Sec. 4.2.4). Otherwise ion-ion interaction (especially with contaminating ions) would complicate the optimization of the trap potential.

4. To tune the trap potential, i.e. make it as harmonic as possible (see Sec. 4.2.5).

While the first three steps were successfully completed, tuning of the trap was unfortunately precluded by too large radial amplitudes and vacuum problems.

4.2.1. Loading ions into the trap

At time T (see Eq. (4.8)) after the extraction of ions from the EBIT, the cryogenic drift tube is pulsed down from U_{DT} (see Sec. 4.1.4) to the voltage U_0 that is applied during the loading-process to all electrodes in the trap tower down to the lower correction electrode (see Fig. 3.15a). The lower endcap and all following electrodes are held at ground. In contrast to the upper drift tube D4, the cryogenic drift tube has to be pulsed up again after only a few µs. Otherwise, the ions would leave the trap region again. In case several bunches are loaded to the trap, the pulse-down-pulse-up cycle is repeated for several EBIT extraction cycles. Once the loading is finished, the cryogenic drift tube is grounded, such that its potential does not disturb the electrostatic trapping potential.

After the loading, the ions are trapped in the wide potential minimum created by all electrodes which are set to U_0. To work with the ions, they have to be confined within a single trap. With the single-trap setup used during the experiments presented here, there are two possibilities to move the ions into the trap region:

1. The first option is to directly ramp all electrodes to the voltages that are applied when just a single trap is formed (step 1 and 2a in Fig. 4.9). With this option, only in a few cases excited ions could be seen on the resonator when the ring voltage was scanned afterwards. This leads to the conclusion that the ions in the trap are relatively cold[6] after the loading process.

2. The second option is to first trap the ions in a potential minimum created by the dummy electrode, afterwards to create a second potential minimum with the trap electrodes and then to ramp up the voltage at the dummy electrode, such that the initially cold ions get accelerated into the trap (step 1, 2b, 3, 4 and 5 in Fig. 4.9). The energy of the ions can be controlled by the voltage at the upper endcap during the ramping of the voltage at the dummy electrode. With this procedure, excited ions could be seen on the resonator in most cases.

The second option is an easy way to excite ions without having to know much about the trap or the ions (which would be required for instance when axial dipolar excitation is used). Therefore it was used in many cases. In Fig. 4.10 the noise spectrum of the axial detector with several excited ions tuned near resonance is shown exemplarily.

4.2.2. Analyzing the trap content

Parametric excitation With large excitation amplitudes $h \gg h_T$ (see Eq. (2.47)), a response to parametric excitation can be observed for a wide range of trap potential depths U_0 (several 100 mV variation), anharmonicity coefficients $c_{4,6,8,...}$ (several 10 mUnit tuning ratio variation) and radial amplitudes $a_\pm$ (few mm). If a response to a parametric excitation at frequency ν_d is observed, the ion is at an axial amplitude a_z where all axial anharmonicity shifts $\Delta\nu_z$ sum up such that the resulting axial

---

[6] In this context, cold means that no peak is observable on the resonator, when the axial frequency of an ion is tuned to the resonance frequency of the axial detector.

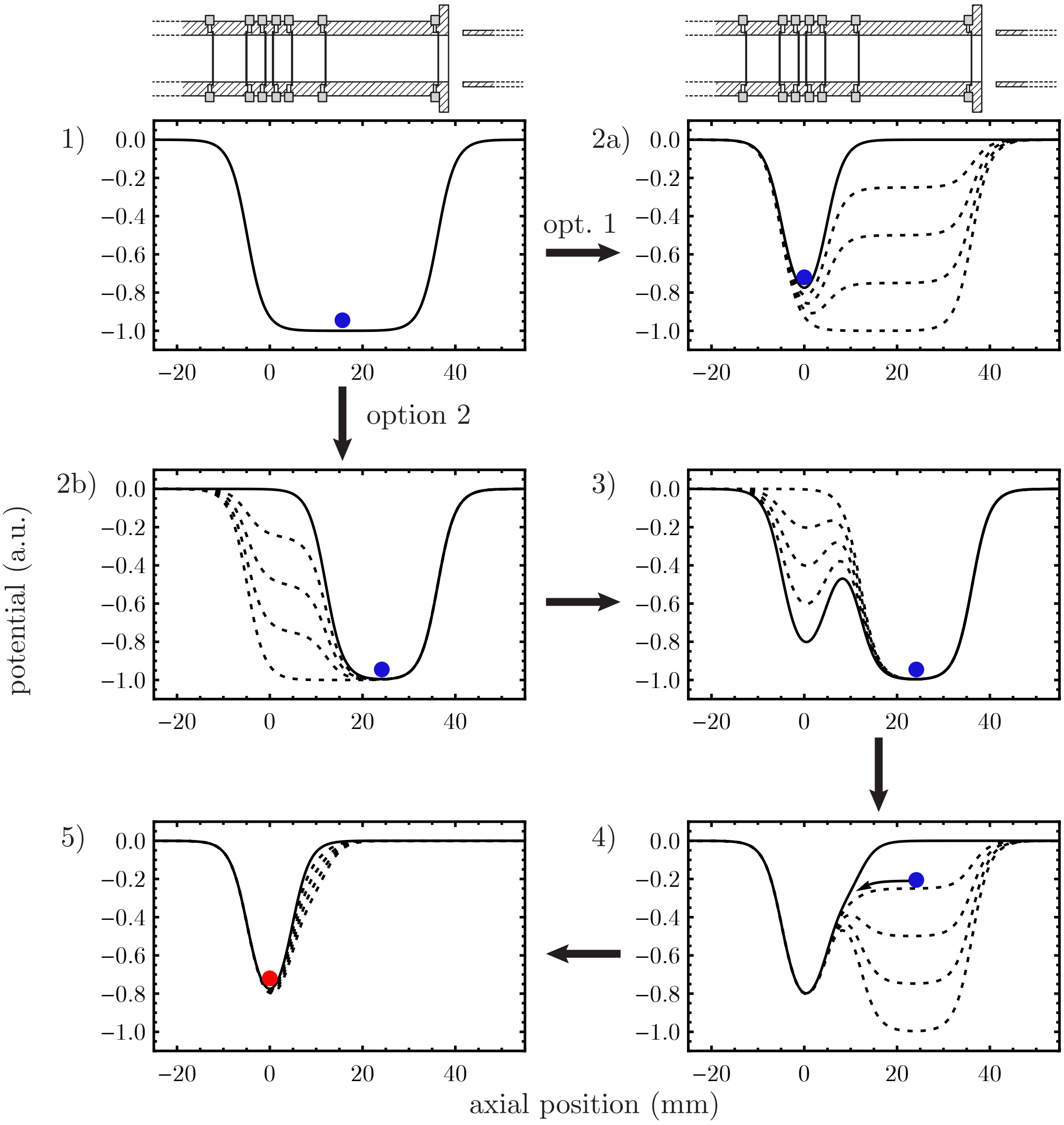

Figure 4.9.: In 1) the trap potential after the loading process is shown. The blue dot indicates cold ions. The position of the electrodes (including the grounded holder plate and the drift tube at the right) is sketched at the top. When all voltages are directly ramped to their final values, the ions stay cold (see 2a). The dashed lines indicate intermediate potentials in the ramping process. Another option is to first trap the ions in a minimum created by the dummy electrode (step 2b), then to create a second potential minimum with the trap electrodes (step 3) and finally to ramp up the voltage at the dummy electrode (step 4). This results in hot ions (red dot) in the trap. In 5), the upper endcap, which controls the energy of the ions, is ramped to ground.

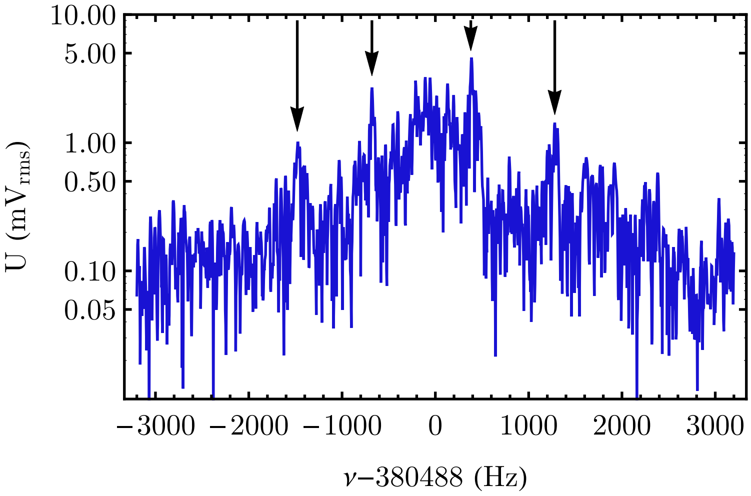

Figure 4.10.: The noise spectrum of the axial detector with several excited Ar^{8+}-ions is shown. The four most pronounced peaks are marked with arrows. To record this spectrum, several bunches were loaded into the trap. The ions were excited by the excitation scheme shown in Fig. 4.9 following the sequence of option 2.

frequency ν_z coincides with $\nu_d/2$. The robustness of the parametric excitation makes it a useful tool to test whether there are ions in the trap (even after they have cooled down).

One way to detect a response of an ion to a parametric excitation is to observe the noise spectrum of the axial detector where a peak appears at the center frequency of the detector (as was shown in Fig. 3.18). A more convenient way is to down-convert the ion signal at $\nu_d/2$ to a low frequency (a few Hz or less) and to observe the resulting signal with an oscilloscope (see Fig. 4.11).

Besides testing the presence of ions in the trap, parametric excitation has proven to be very convenient for further purposes:

- Determine the trapping-time of ions: The maximum time a parametrically excited cloud of Ar^{8+}-ions was observed continuously was ∼30 minutes.
- Getting some information about neutral or ionic contaminants: Collisions with contaminants can have two effects: First of all, they can lead to an unlocking of an ion from the parametric drive. Furthermore, since the parametric excitation is bi-stable [123], collisions can lead to a phase-jump of the ion's axial motion by 180°. These phase-jumps can be detected easily, when the ion-signal is down-converted and observed with an oscilloscope.

Mass scans When the ring voltage and the correction electrode voltages are ramped simultaneously, different ions come into resonance with the detector either in ascending or descending m/q-order (depending on the ramping direction). If the power

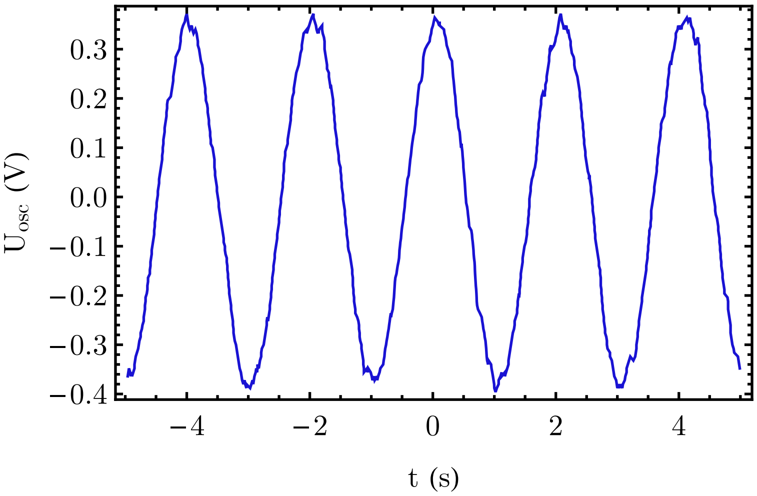

Figure 4.11.: The response of Ar^{8+}-ions to parametric excitation is shown. Prior to detection with an oscilloscope, the ion signal has been amplified, down-converted to a frequency of 0.5 Hz and low-pass filtered.

dissipation on top of the resonator is recorded during such a ramp, different trapped ion species can be identified. This procedure is called mass scan. An exemplary result of a mass scan with different ion species in the trap is shown in Fig. 4.12.

The implementation of mass scans is illustrated in Fig. 4.13. During the ramping of the voltages, the integrated power P_{det} on top of the resonator from both the detector's thermal noise and the ion signal is recorded with a spectrum analyzer in zero-span mode. In this mode, the analyzer records a time-domain series.

For an accurate assignment of a ring voltage to a time in the analyzer's spectrum, the voltage-ramping and the spectrum analyzer recording have to be synchronized. Since only the spectrum analyzer recording can be triggered externally, but not the voltage-ramping with the trap voltage source used during the experiments presented here (see Sec. 3.4.5), a self-made comparator is used for the synchronization: To one input of the comparator, the desired starting voltage U_{start} of the scan is applied. To the other input, the ring voltage U_r is applied. The ring voltage ramp starts slightly below U_{start}, and as soon as U_r is above U_{start}, the output of the comparator changes from low to high. The rising edge is used to trigger the spectrum analyzer recording.

4.2.3. Cleaning attempts

Having loaded many ions of different species into the trap, it was attempted to clean the trap, i.e. to remove contaminating ions. A common approach is to axially excite the contaminating ions while cooling the axial mode of the ions of interest and then to raise the trap potential. Then the hot contaminating ions leave the trap, while the cool ions of interest stay in the trap.

The cleaning attempts did not give satisfying results:

- Although they were not excited by dipolar excitation, ions of interest were lost

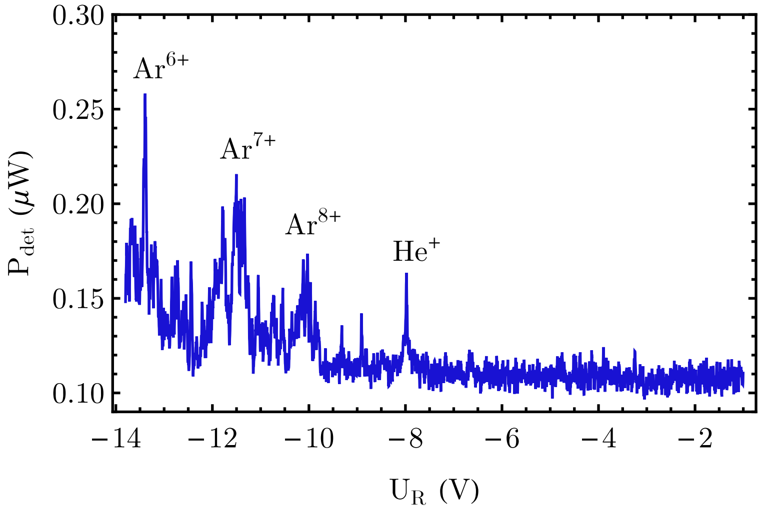

Figure 4.12.: A mass scan with different ion species in the trap is shown. For this measurement, load parameters to obtain many Ar^{8+}-ions in the trap were chosen. As can be seen from the further trap content (Ar^{7+}, Ar^{6+}, He^{+}), the vacuum was rather poor at that time, probably due to a leak in the cryogenic feedthrough flange (see Sec. 3.4.2). For further details see text.

from the trap just like the contaminating ions. The ions of interest were most probably heated by the contaminating ions due to Coulomb interaction. In order to reduce the interaction, it was tried to also excite the cyclotron motion of the contaminant ions, for instance by applying quadrupolar excitation at the $\nu_+ + \nu_z$-sideband. Unfortunately, this did not result in a discrimination between contaminants and ions of interest in the cleaning process. In retrospect, this can be explained with initially large radial amplitudes $a_\pm$ (see Sec. 4.2.5) and a correspondingly large scatter of $a_\pm$, such that ions were spread over the whole trap radius.

- When the trap potential was raised to evaporate hot ions, not as many ions were lost as expected. Even after making the trap completely flat, ions were still detectable when the trap was made deep again. A possible explanation for that would be charge patches on the dummy and the Faraday cup, which were not gold-plated (see Sec. 3.4.3.3). The potential due to the charge patches could have formed a large trap. This hypothesis is supported by the fact that a negative voltage (typically below -10 V) had to be applied to the Faraday cup to empty the trap volume. Since the exact surface charge densities were not known and probably changed over time due to the loading of the trap, the charge patches made a controlled evaporation of ions very difficult.

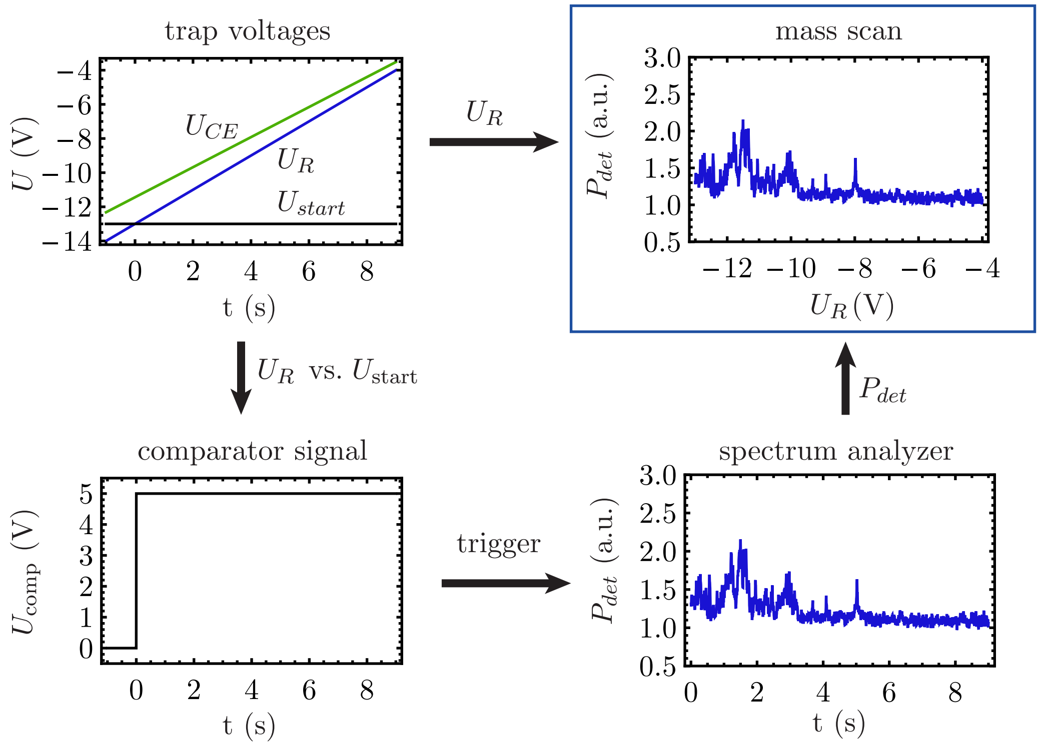

Figure 4.13.: The implementation of mass scans at PENTATRAP is illustrated. Both the ring voltage and the voltages at the correction electrodes are ramped simultaneously. The integrated power on top of the detector is recorded with a spectrum analyzer in zero-span mode. The spectrum analyzer recording is triggered by a comparator, which compares the ring voltage to the start voltage of the mass scan. The mass spectrum is then obtained by combining the spectrum analyzer signal and the ring voltage ramp. For further details see text.

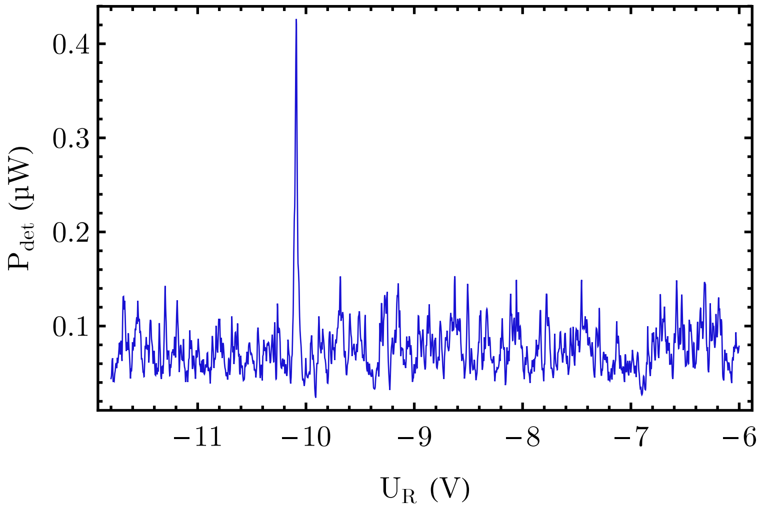

Figure 4.14.: A mass scan with only a few Ar^{8+}-ions in the trap is shown. For details, see text.

4.2.4. Few-ion loading

Improved loading When the cleaning attempts turned out to be unsuccessful, it was tried to improve the loading process to get control over the number of loaded ions. At that time, several ten ion capture attempts[7] were usually required to trap ions. This was due to fluctuations of the (at that time insufficiently buffered) HV-supplies that provided the voltages at the HV-switches (see Sec. 3.3.1). This problem was solved by increasing the buffer capacitances at the switch inputs by factors of 10 to 100. Furthermore detailed investigations of the deceleration by means of the cryogenic drift tube were carried out (see Sec. 4.1.4). With stable voltages at the HV-switches, properly chosen voltages at the cryogenic drift tube and a proper timing of the cryogenic drift tube, it was possible to load ions with just a single ion capture attempt and to get some control over the number of ions that were loaded into the trap. In Fig. 4.14, a mass scan with only a few Ar^{8+}-ions in the trap is shown.

Indications for low ion numbers With a better control over the loading process, two strong indications were found that loading of only a few ions is possible:

1. When the trap was loaded anew, in about 20% of the cases only a single peak appeared in the mass spectrum. For a fixed tuning ratio, the ring voltage at which these peaks appeared showed a large scatter of several 100 mV. As will be shown in Sec. 4.2.5, this scatter can be attributed to large scatters both in the initial axial amplitude a_z and in the radial amplitudes $a_\pm$. Because of this large amplitude-scatter from loading to loading, it can be considered unlikely,

---

[7] Ion capture attempt means that ions are transported to the cryogenic region and the drift tube is pulsed down and up again.

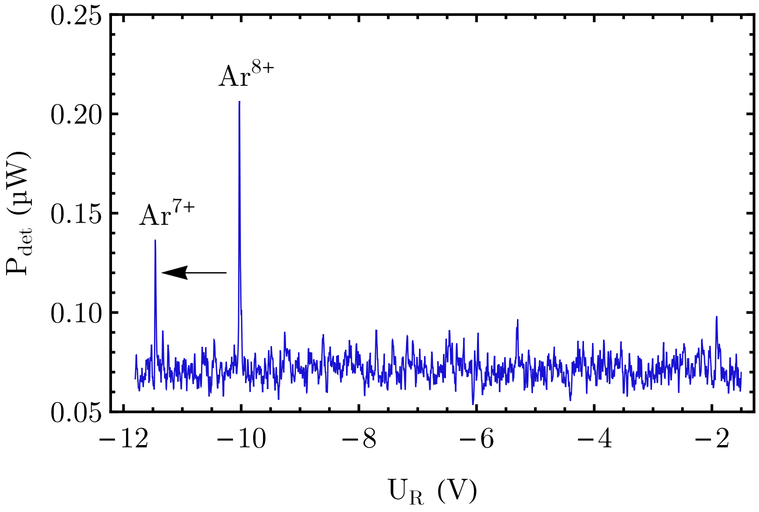

Figure 4.15.: An averaged mass scan is shown. In the first mass scans contributing to the average, an Ar^{8+}-peak was visible. From one mass scan to the next, the position of the peak jumped to the voltage corresponding to Ar^{7+}. Since after none of these jumps, a jump back to the voltage corresponding to Ar^{8+} was observed, this is a strong indication for a charge exchange reaction. For further details see text.

that there are many ions captured in one loading process that incidentally have the same initial axial and radial amplitudes.

2. When several fast mass scans were performed with the same trap content, it was observed in several cases that a peak appeared in the first mass scans at approximately the same ring voltage (corresponding to some charge state q) and then suddenly jumped to a lower voltage (corresponding to a charge state $q-1$). Such an event is illustrated in Fig. 4.15. It was never observed that the peak jumped back to it's initial voltage, which would have been a sign for energy exchange between two ions, one being in charge state q, the other one being in charge state $q-1$. Therefore the jump was attributed to a charge exchange reaction. Since a charge exchange of several ions during one mass scan (lasting a few s) is unlikely for the observed charge exchange rates (below 1/min), this indicates that even single ions were observed in the mass spectra on several occasions.

4.2.5. Trap tuning attempts

With strong indications for a low number of ions in the trap, the tuning of the trap was attempted. In the first of the following paragraphs, favorable methods to tune the trap that are routinely used at other experiments will be described. Unfortunately, these methods were out of reach with the setup used during the first experimental run. In the last three paragraphs of this section, the trap tuning methods that were available and the reasons for their failure will be described.

Favorable methods The most favorable methods to determine the optimum tuning ratio would have been based on axial dip-detection (see Sec. 3.4.4.1), having the benefit of a defined temperature of the axial mode. By means of dip-detection, the tuning ratio can be optimized in two steps:

1. Under the assumption of negligible shifts due to non-zero radial amplitudes, a rough guess of the right tuning ratio (to about 100 µUnit [121]) can be obtained by observing the depth of the dip as a function of the tuning ratio: In an anharmonic trap, the dip is smeared out due to variations of the ion's axial frequency caused by thermal fluctuations of the axial energy during the averaging time. The smaller the leading-order anharmonic coefficient c_4 is, the smaller the axial frequency variations are and thus the deeper the dip gets.

2. Further optimization of the tuning ratio would have involved the variation of either the energy of a radial mode (e.g. by means of dipolar excitation) or the temperature of the axial mode (e.g. by coupling white noise to the detection system). The observation of the axial frequency shifts due to the anharmonicity coefficients $c_{4,6,...}$ as a function of the energy/temperature for different tuning ratios can then be used to find the optimum tuning ratio (see e.g. [65, 87, 121]).

Unfortunately, dip-detection was precluded by a low quality factor of the axial detector in use (see Sec. 3.4.4.4) and a too large effective electrode distance D_{eff} (see Sec. 3.4.6) for the Ar^{8+}-ions that were used during the commissioning experiments.

Parametric excitation As was already mentioned in Sec. 4.2.2, the axial amplitude a_z of a parametrically excited ion in an anharmonic trap has to be such that the sum of all electrostatic anharmonicity shifts[8] $\Delta\omega_z$ compensates the difference between $\omega_d/2$ and $\omega_z = \sqrt{2c_2qU_R/m}$. When U_R is varied, the amplitude a_z changes according to the anharmonicity coefficients and the radial amplitudes. For negligible radial amplitudes, it should thus be possible to draw conclusions about the anharmonicity coefficients of the trap from the shape of the U_R-a_z-curve where a_z can be extracted for instance from the amplitude of the down-converted ion signal (see Fig. 4.11).

The attempt to tune the trap by recording U_R-a_z-curves for different tuning ratios failed for the following reasons:

- In those cases, in which ions stayed parametrically excited for several minutes, no significant variation of the ion's amplitude was observable. Most probably, this was the result of too large electrostatic anharmonicities (see [123] for details). Unfortunately, none of the ions could be excited parametrically long enough to repeat the measurement for different tuning ratios.

---

[8] Within this section, it is assumed that electrostatic anharmonicities are the dominant source of systematic axial frequency shifts.

- For a fixed tuning ratio, the ring voltages, at which the ions became parametrically excited varied from ion to ion by several 100 mV. This pointed at significant contributions by non-zero radial amplitudes to the axial frequency anharmonicity shifts.

Peak positions Both the axial as well as the radial energies of ions from different loadings are distributed randomly following some (unknown) energy distributions of non-zero width. The ring voltages at which the ions come into resonance with the resonator are distributed according to these energy distributions and the electrostatic anharmonicity coefficients.

It was attempted to tune the trap by means of the following measurement cycle that was carried out multiple times for different tuning ratios:

1. Load the trap.
2. Perform a mass scan.
3. In order to avoid systematic shifts due to ion-ion interaction, go back to 1.) in case multiple peaks can be found in the mass scan. In case only one peak appears in the mass scan, record the position of the peak. Then go back to 1.).

In case of negligible radial amplitudes and not too big axial amplitudes (at which shifts due to c_4 and c_6 dominate over shifts due to $c_{8,10,\ldots}$), it should be possible to draw conclusions about c_4 and c_6 from the peak position distributions at different tuning ratios. In particular, the distribution should become narrow around the ideal tuning ratio where c_4 and c_6 vanish simultaneously (see Sec. 3.4.3.2).

Two typical peak position distributions are shown in the form of histograms in Fig. 4.16. In Fig. 4.16a the distribution is comparably broad with a lot of scattering around the main peak. In Fig. 4.16b on the other hand, the distribution is comparably narrow. Unfortunately, similarly narrow distributions could be found for several tuning ratios, being several 10 mUnits different from each other. This ambiguity prohibited the tuning of the trap by means of this method.

An explanation for the ambiguous behavior might be the following: Both the axial as well as the radial amplitudes might have been so large that also $c_{8,10,\ldots}$ lead to significant shifts. Thus for the right tuning ratio, at which $c_{4,6} \approx 0$, the distribution gets broadened nonetheless. On the other hand for tuning ratios being far from the optimum, the interplay of the mean radial amplitudes $\bar{a}_\pm$ and $c_{8,10,\ldots}$ might have lead to a compensation of the $c_{4,6}$-shifts.

Peak tracking After the failed attempt to tune the trap by means of peak position distributions, the main question was whether anharmonicity shifts in the axial frequency were mainly caused by large axial or by large radial amplitudes. To answer this question, the following measurement routine was carried out:

1. Load the trap.
2. Perform a mass scan.

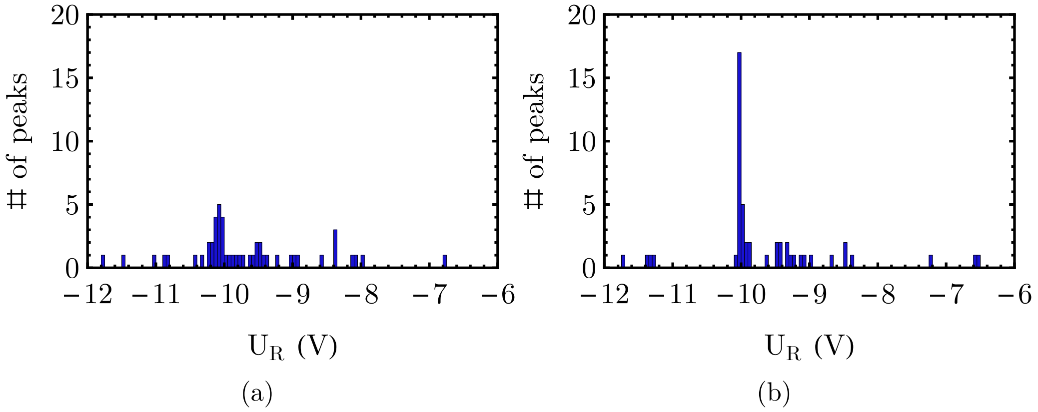

Figure 4.16.: Peak position distributions of Ar^{8+}-ions for two different tuning ratios (0.878 in (a) and 0.902 in (b)) are shown exemplarily. Each count in the histograms corresponds to the position of a (sole) peak in a mass scan.

3. If multiple peaks are found during the mass scan, go back to 1.) (to avoid systematic shifts due to ion-ion-interaction). If only a single peak is found, go to 4.).
4. Perform a mass scan. The mass scan is carried out at a comparably low voltage-ramping speed of a few 100 mV/s.
5. If the ion-peak is still detectable (i.e. has a height above a certain threshold), record the position of the peak and go to 4.). Else, go to 1.).

Each time the ions were ramped across the resonator, the axial energy of the ions was reduced. Due to the comparably low voltage-ramping speed during the mass scans, the cooling of the ions lead to observable shifts of the peak positions due to electrostatic anharmonicities. The method is illustrated in Fig. 4.17 where eight successive mass scans with the same trap content are shown. It can be seen that the ramping across the resonator has two effects: First of all, the peak shifts to lower ring voltages. Furthermore, the height of the peak is reduced. The corresponding peak track (i.e. peak position vs. mass scan number) is shown Fig. 4.18.

Recording multiple peak tracks for the same tuning ratio, the influence of radial amplitudes can be investigated: In case the influence of the radial amplitudes on the overall axial frequency electrostatic anharmonicity shift is negligible, the shapes of different peak-tracks should be similar, the main differences being a horizontal translation and a correspondingly different vertical intercept, caused by different initial axial energies. If on the other hand the radial amplitudes give a significant axial frequency shift, the peak-tracks should be dissimilar: First of all, the shapes of the tracks should be different from each other, as can be seen for instance from the mixed axial-radial-terms in Eq. (2.31). Furthermore, due to the purely radial contributions to the axial frequency shift, the tracks should converge to different voltages.

In Fig. 4.19, peak tracks for fifty different trap loadings are shown. It can be clearly seen that the shapes of the peak-tracks are quite dissimilar (further explanations about

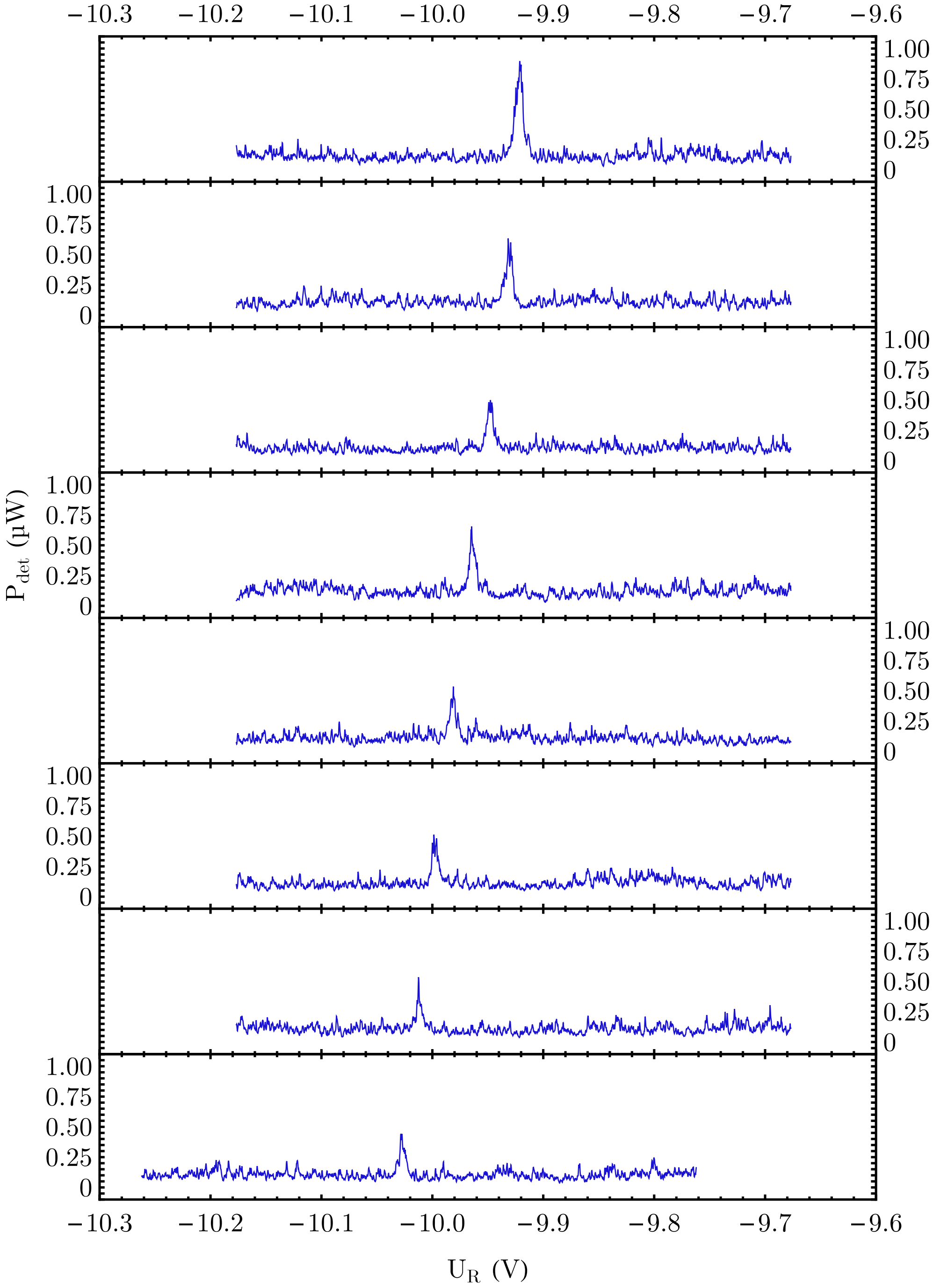

Figure 4.17.: Several successive mass scans with the same trap content are shown, with the first mass scan on top and the last one at the bottom. By means of this method, successive cooling of the axial mode can be observed. For further details, see text.

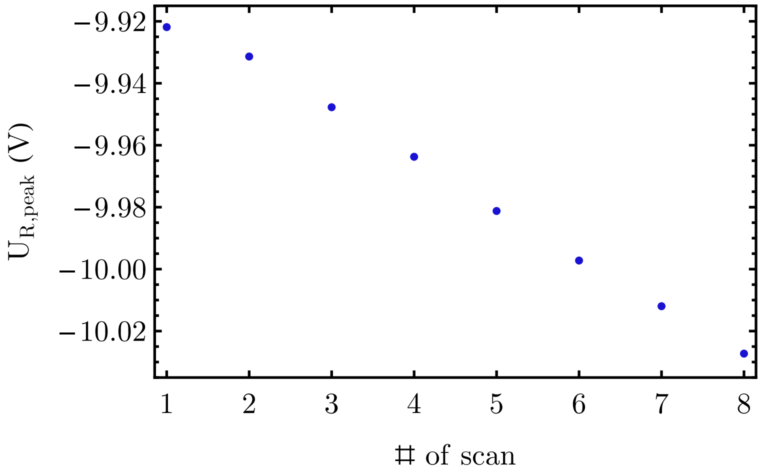

Figure 4.18.: The center positions of the peaks shown in Fig. 4.17 are plotted.

the peak tracks can be found in App. D). Furthermore, the tracks converge to ring voltages spread over more than 200 mV. Thus, it can be concluded that the radial amplitudes $a_\pm$ give significant contributions to the axial frequency anharmonicity shifts. Recalling that the radial diameter of the ion bunches was determined to be on the order of mm (see Sec. 4.1.3), it can be assumed that the radial amplitudes are on the same order of magnitude.

Nevertheless, it was tried to tune the trap by means of peak-tracks: For tuning ratios in a range from 0.82 to 0.895, multiple peak tracks were recorded. Unfortunately, at none of the tuning ratios the tracks converged to a certain ring voltage. Furthermore, for any of the tuning ratios the different tracks were of dissimilar shape. Thus, the tuning of the trap by means of this method failed. Furthermore, since c_4 and c_6 should vanish at some tuning ratio simultaneously (see Sec. 3.4.3.2), it can be concluded that for both the typical radial amplitudes as well as for the initial axial amplitudes, anharmonicity terms beyond c_6 (i.e. $c_{8,10,\ldots}$) contributed significantly to the overall axial frequency shift. Due to the axial cooling during the mass scans, the large initial axial amplitudes were of no concern. But since the radial amplitudes stay constant during the mass scans, a reduction of the radial amplitudes was required to tune the trap.

The very first attempt was to change the focus of the S2-x einzel lens in order to reduce the beam diameter in the trap region. Unfortunately, the change of the einzel lens voltage did not show any effect. An explanation for this might be that the einzel lens not only affects the beam diameter, but also the transverse energy of the ions in the bunch. When a decrease in beam diameter is accompanied by an increase in transverse energy, the decreased diameter might not result in a decrease of the radial amplitudes $a_\pm$.

After this, it was tried to cool the radial modes by means of sideband cooling (see Sec. 3.4.4.2). First it was tried to exchange the actions of the magnetron mode and the

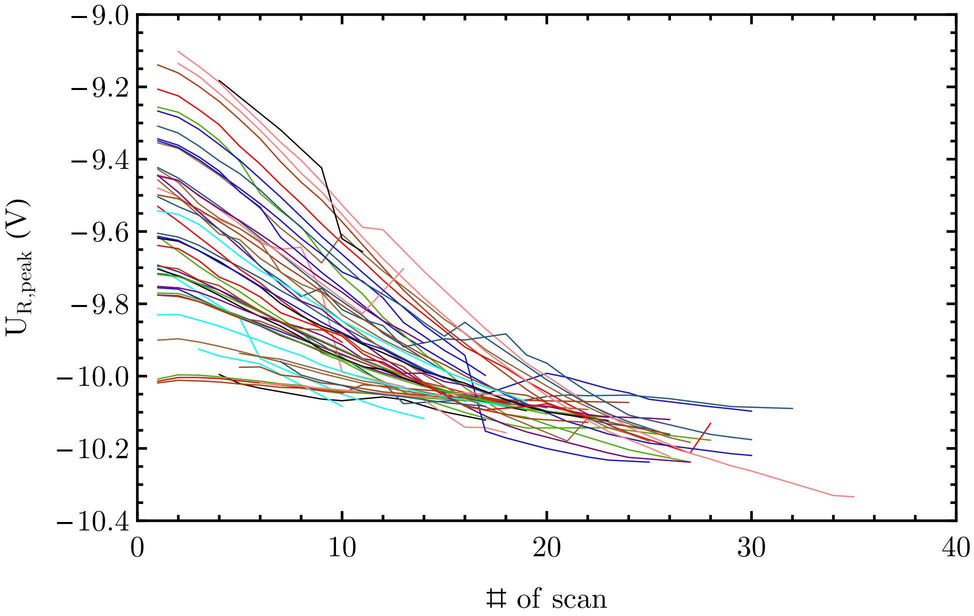

Figure 4.19.: Several peak tracks with Ar^{8+}-ions for a tuning ratio of 0.895 are shown. For each track the trap was loaded anew. For further details, see text.

axial mode by means of a strong quadrupolar excitation employing a slow frequency sweep in the frequency range, in which the sideband was expected to be. It has been observed at the THe-Trap experiment that in the case of the corresponding cyclotron-axial sideband, this leads to an efficient exchange of actions between the axial and the cyclotron mode [183]. When this form of sideband coupling was applied, the particle was unfortunately lost from the trap in most cases. This was probably for the following reason: Following Tab. 2.1, an exchange of actions between either of the radial modes and the axial mode results in an axial amplitude of

$$a_z = \sqrt{\frac{\nu_+}{\nu_z}} a_\pm . \tag{4.9}$$

For an Ar^{8+}-ion with frequencies of ν_z=380 kHz and ν_+=21.525 MHz, a magnetron amplitude of 2 mm for instance would result in theory in an axial amplitude of 15 mm. In practice, the ion would be lost.

After this, it was attempted to exchange the actions more slowly, such that the axial mode could be cooled in the process. Unfortunately at that time, the vacuum conditions had become bad: It was not possible to trap ions for more than ten minutes (in contrast to 30 minutes in the beginning). Thus, the attempt to slowly cool the radial modes failed due to a lack of trapping time.

5. Summary and outlook

The novel Penning-trap mass spectrometer PENTATRAP aims at mass-ratio measurements of medium-heavy to heavy ions with relative uncertainties below 10^{-11}. To reach such ultra-high precision, highly-charged ions and extremely stable electrostatic and magnetic trapping fields are used. Furthermore, a novel two-trap approach, realized with a tower of five identical traps, is employed to suppress the effect of magnetic field fluctuations. Cryogenic detectors with a sensitivity that allows for measurements with single ions are used to determine eigenfrequencies. These and many other features make PENTATRAP an experiment with excellent prospects to contribute to fundamental studies in different fields of physics. Within the presented thesis work, considerable progress towards the tuning of the traps and first precise eigenfrequency measurements was made. Part of the detection electronics was set up and tested. Axial detectors were integrated into the setup and characterized under experimental conditions. Possible limitations of the detector performance in the experimental setup were identified and solutions to the identified problems were proposed. Furthermore, a direct axial-frequency phase-shifter for feedback cooling of the axial mode has been designed.

For the first time, the complete assembly of all parts for a single trap except for a cyclotron resonator was realized. The cyclotron resonator was omitted since the proper ion species to work with was not clear beforehand. The setup worked very reliable during the commissioning experiments presented in this thesis.

For this setup, a provisional Faraday cup taking the place of a trap was designed. This Faraday cup has proven to be a crucial diagnostic tool without which the transport of ions into the trap region could hardly have been realized. Therefore, a Faraday cup below the five-trap tower (designed by Alexander Rischka [142]) will be an inherent part of this installation.

In the course of the commissioning experiments, the first successful transport of ions to the trap region was realized. Particularly important for this was the internal re-alignment of all parts of the *Dresden EBIT-W* and the alignment of the *Dresden EBIT-W* with the beamline. This allowed for trapping of ions in a trap of the PENTATRAP experiment for the very first time, as described in Chapter 4.

Increasing the input buffer capacitances at the HV-switches that are used to switch the voltages at the extraction-endcap of the EBIT and at the two drift tubes for ion deceleration resulted in an increased stability of the corresponding voltages. This allowed for reliable capturing of single ion bunches extracted from the EBIT. Together with detailed studies of the bunch characteristics using the Faraday cup in the trap tower, this enabled reproducible capture of only a few down to single ions. Loading the trap anew became a matter of seconds, possible with just the push of a button.

Mainly two diagnostic tools, namely parametric axial excitation and mass scans, were used to analyze the trap content. By means of mass scans indications for the trapping of only a few down to single ions were found. Several methods were tested to find the reason for unsuccessful trap tuning attempts. Peak tracking, i.e. tracking of the ring voltages at which an ion comes into resonance with the axial detector in repeated mass scans, finally gave the strongest hints towards overly large initial radial amplitudes. Attempts to cool the radial modes failed. Besides other reasons, this was due too short trapping times, which were caused by vacuum problems. In future setups, a 5 cm long and 1.2 mm wide tube above the cryogenic drift tube will both circumvent the problem of large initial radii and act as pumping barrier.

There have been mainly two factors that prevented carrying out more than one commissioning run in the course of this thesis, which are both related to the cryogenic insert. Problems arising from the large diameter of the cryogenic setup compared to the diameter of the magnet's bore in the interplay with air ice frozen to the walls of the bore prevented an insertion of the setup into the magnet at an early stage. A persistent cause of trouble throughout the whole thesis work have been vacuum problems, arising mainly from leaks in the cryogenic feedthroughs. However, to the end of this thesis, a bullet-proof concept has been found to ensure good vacuum conditions: First of all, all but two cryogenic feedthroughs will be removed from the setup. Instead, the feedthroughs will be placed at room temperature and cables will run through capillaries from the room temperature vacuum to the cryogenic vacuum. Furthermore, as mentioned above, a pumping barrier will be employed to reduce the gas load through the beamtube into the cryogenic region. Additionally, to prevent leakage of He through the indium seals or through small leaks in the remaining two feedthroughs, the whole setup will be enclosed in a pre-vacuum chamber. These concepts will be first tested in a modified version of the current setup. Furthermore, a complete re-design of the cryogenic insert has been initiated. In this re-design, which is part of the Ph.D. thesis of Alexander Rischka, the concepts for an improved vacuum will be adopted and the diameter of the setup will be considerably reduced.

The above mentioned improvements of the setup are all underway. It is expected that the modified setup will be completed within the next few month. With the transport procedures developed during the first commissioning run it should be a matter of only a few days to get from the start-up of the EBIT to the capture of single ions (assuming that the internal alignment of the components of the EBIT has not changed). With improved vacuum conditions and smaller initial radial amplitudes cooling of the magnetron mode should be much easier. Furthermore, cyclotron detectors will allow for a direct cooling of the reduced cyclotron mode.

In the new setup limitations of the axial detector identified during the first commissioning run will be circumvented. The improved detector performance together with a smaller effective electrode distance will enable axial dip detection. This should simplify a first rough tuning of the traps. Furthermore, dip detection will allow to count the number of ions of interest that are actually loaded into the traps. Whether contaminating ions have been loaded as well (which might lie outside the range or below the detection threshold of a mass scan) might be diagnosed with different methods, e.g. by observing the stability and the depth of an axial dip [148] or by looking for anomalies in the relativistic shift of ν_+ during the direct cooling of the reduced cyclotron mode [121].

Having a single cooled ion in a clean and roughly tuned trap will allow for trap tuning to high harmonicity and first precise eigenfrequency measurements. This will enable studies of trapping field stabilities and systematic eigenfrequency shifts. Since two of the traps will be equipped with detectors, the stability of the magnetic field ratio between two traps, which is a cornerstone of PENTATRAP, can be tested.

Whether all of this can be accomplished in one experimental run without modifications of the setup and which level of precision will be reached in the studies of systematic eigenfrequency shifts is difficult to foresee. However, if things go really well, tackling a first application might be feasible: Reducing the uncertainty in the mass of ^{35}Cl by more than a factor of ten to below 3 eV/c^2 for an ultra-precise determination of the ^{36}Cl – ^{35}Cl mass-difference (see Sec. 1.4.2). This could be accomplished by a determination of the mass-ratio between e.g. $^{35}\mathrm{Cl}^{10+}$ and $^{28}\mathrm{Si}^{8+}$ with a relative uncertainty below $9 \cdot 10^{-11}$. Trapping-voltage fluctuations should not present a problem at this level of precision, especially not with the recently developed highly stable voltage source StaReP [144]. While of course exact electrostatic field anharmonicities, magnetic field inhomogeneities, effective detector temperatures and employed measurement procedures are yet unclear, there is a fair chance that amplitude dependent shifts (including relativistic shifts) might not be a limiting factor at this level of precision. Image-charge shifts are expected to have a difference below $2 \cdot 10^{-11}$. Due to the small q/m-difference of less than $2 \cdot 10^{-5}$ [104], shifts arising from different equilibrium positions should not be of concern. Special care should be taken concerning coil pulling shifts: Since the axial damping constants would be different with a ratio of 10/8, it would not be sufficient simply to match axial frequencies, but they would have to be close to the resonance frequency of the resonator. While the final detector performance is not clear, it can be estimated that for a quality factor of 4000, a coil inductance of 3 mH and a detector resonance frequency ν_0 of 400 kHz, a difference between ν_z and ν_0 of 10 Hz would result in a shift of the mass ratio of $\sim 1 \cdot 10^{-11}$.

To reach the aimed-at ultra-high precision level required for most applications presented in Sec. 1.4 will be very challenging (some challenges are discussed in App. E). Once this level has been reached, the first goal will be to determine the Q-value of the electron-capture decay in ^{163}Ho with an uncertainty of less than 1 eV. However, a production of ^{163}Ho-ions with the *Dresden EBIT-W* seems difficult due to small available samples and the high sample-consumption with currently available techniques. Thus, highly-charged ^{163}Ho-ions will have to be produced by the HD-EBIT, where the implementation of a very economical wire-probe technique is planned (see Sec. 3.2.4). The beamline for the coupling of PENTATRAP to the HD-EBIT will be set up in the near future in the framework of the thesis of Hendrik Bekker [136]. However, once access to the highest charge states will be provided by the HD-EBIT, there might be a fascinating alternative way to load ^{163}Ho into the Penning traps (ignoring for a moment all arguments that might be against using the highest charge states for this measurement): With excellent vacuum conditions, it might be possible to load a number of $^{163}\mathrm{Dy}^{66+}$-ions into the traps and store them for several days. With one ion in each of the five traps, one of the five ions is likely to undergo a bound-state β^- decay to $^{163}\mathrm{Ho}^{66+}$ on a time scale of $\sim$ 10.5 days [184]. Recoil energies on the order of 100 meV will not lead to a loss of the ion. Thus, in-trap production of $^{163}\mathrm{Ho}^{66+}$ might be possible.

With these exciting perspectives, the thesis is concluded.

A. Thermal expansion issues

Since the field of the PENTATRAP magnet is not perfectly homogeneous, the magnetic field strengths in the traps depend on the relative position of the trap tower and the magnets' coils. The vertical positions of both the magnets' coils and the trap tower will change due to thermal expansions of the corresponding support structures in case the temperature distribution along these support structures changes. The vertical position of the trap tower is defined by the length of the stainless steel beamtube, which will be treated in the following. Since the construction of the magnet's coil support structure is not known, it is difficult to judge the exact effect of e.g. a change in laboratory temperature. But is is very likely that the thermal expansions of beamtube and coil support structure are different.

Thermal expansion of stainless steel 316 The thermal expansion of a stainless steel tube at temperature T, which has a length of $L_{4.2\ \mathrm{K}}$ at 4.2 K, is given by

$$\delta_{\mathrm{th}}(T) = \frac{L(T) - L_{4.2\ \mathrm{K}}}{L_{4.2\ \mathrm{K}}} = \begin{cases} a + bT + cT^2 + dT^3 + eT^4 & T \geq 23\ \mathrm{K} \\ 0 & T < 23\ \mathrm{K} \end{cases} \tag{A.1}$$

where the values of the parameters a, b, c, d, e are given in Tab. A.1.

If the same tube is at a fixed temperature of 4.2 K at end A and at temperature T at the other end B, assuming a linear temperature gradient along the tube, the thermal expansion is given by

$$\delta_{\mathrm{grad}}(T) = \frac{1}{T - 4.2\mathrm{K}} \int_{4.2\ \mathrm{K}}^{T} \delta_{\mathrm{th}}(T')dT'. \tag{A.2}$$

If the temperature T at end B changes by a small amount ΔT, the relative length change of the tube is given by

$$\frac{\Delta L}{L} = \alpha_{\mathrm{grad}}(T)\Delta T = \frac{d\delta_{\mathrm{grad}}(T)}{dT}\Delta T. \tag{A.3}$$

The linear expansion coefficient[1] α_{grad} at 293 K is roughly $6.6 \cdot 10^{-6}$/K.

Implications for the two-trap scheme In the presence of magnetic field gradients $B_{1,\mathrm{A}}$ and $B_{1,\mathrm{B}}$ in the two measurement traps A and B (see Sec. 3.4.3.1), which are usually different from each other, the magnetic field ratio $\rho = B_{\mathrm{A}}/B_{\mathrm{B}}$ depends on the

---

[1] The linear expansion coefficient α_{grad} for a linear temperature gradient along the tube must not be confused with the linear expansion coefficient for a tube of uniform temperature, which is roughly $15.4 \cdot 10^{-6}$/K

Table A.1.: Coefficients for the calculation of the thermal expansion of stainless steel 316 using Eq. (A.1). Values have been derived from [185].

a	b (K^{-1})	c (K^{-2})	d (K^{-3})	e (K^{-4})
$4.5089\cdot10^{-5}$	$-3.9931\cdot10^{-6}$	$9.2962\cdot10^{-8}$	$-2.0322\cdot10^{-10}$	$1.7179\cdot10^{-13}$

relative position of the traps to the magnetic field. In the following, it will be assumed that the absolute thermal expansions of the magnet coil support structure and the beamtube are matched to 10%. The distance between the liquid helium level in the bore and the flange at the top of the magnet is given by L. If the temperature T in the laboratory, and thus the temperature at the upper end of the beamtube changes by ΔT, ρ changes by

$$\Delta\rho \approx \left(\frac{B_{1,\mathrm{A}}}{B_\mathrm{A}} - \frac{B_{1,\mathrm{B}}}{B_\mathrm{B}}\right) \cdot 0.1 \cdot L \cdot \alpha_{\mathrm{grad}}(T) \cdot \Delta T. \tag{A.4}$$

Plugging in exemplary numbers ($B_{1,A} - B_{1,B} = 1$ µT/mm, L=0.5 m), one finds:

$$\Delta\rho/\Delta T \approx 4.7 \cdot 10^{-11}/\mathrm{K}. \tag{A.5}$$

Although the value in Eq. (A.5) is exemplary, and can easily be different by an order of magnitude in one or the other direction, two points should be noted:

- A stabilization of the temperature in the magnet laboratory on the level of 100 mK or possibly even below is crucial for performing mass-ratio measurements at the aimed-at precision level.
- The magnetic field gradients in the measurement traps should be minimized (e.g. by means of compensation coils) or matched.

To summarize, a list of questions is given that can be answered as soon as ν_c-measurements can be carried out at a relative statistical uncertainties $< 10^{-10}$:

1. Is there a dependence of the magnetic field strength on the temperature in the laboratory? If the answer to this question is (as expected) yes, question 2.) arises.
2. Is $B(T)$ linear? If so, question 3.) arises.
3. Does $\partial B/\partial T$ depend on the level in the LHe-/LN$_2$-reservoirs - i.e. does the thermal expansion of the coil support structure depend on the cryogen-level? If not, or if only a very weak dependence is found, question 4.) arises.
4. Is there a LHe-level in the bore, for which $\partial B/\partial T$ becomes minimal? Or, to rephrase the question, can the linear absolut thermal expansions of the coil support structure and the beamtube be matched?
5. Is it possible to monitor changes of the trap position relative to the magnet by means of the comparably large magnetic field gradients in the two outer traps?

B. Cryogenic feedthroughs

To find suitable feedthroughs for the cryogenic feedthrough flange (see Sec. 3.4.2) has been an issue for quite some time at PENTATRAP. The boundary conditions for the feedthroughs at PENTATRAP are the following:

- At least 80 isolated pins are required. The magnetic susceptibility of the feedthroughs should be kept low. This excludes for instance the use of nickel as coating material.
- During the experiments presented in Chapter 4, the feedthroughs were in direct contact with LHe.
- The cryogenic feedthrough flange is cooled by lowering the whole cryogenic setup into the LHe-filled bore of the magnet. To prevent air-ice formation, this has to be done fast.

In Sec. 3.4.2 the realization of the feedthrough flange using 20 *Kyocera* four-pin feedthroughs as well as associated difficulties were described. Most probably it is the fast cool-down of the cryogenic insert (maybe in an interplay with the four-pin geometry) that leads to a damaging of the feedthroughs. Since the cool-down procedure cannot be altered, the four-pin feedthroughs are not suitable for the experiment.

***Stycast*-based feedthroughs** While trying (unsuccessfully) to find a way to treat the flange based on the four-pin feedthroughs properly, alternatives were tested. The alternative that looked most promising was to use self-made *Stycast*-feedthroughs: For these, the void between a hole in the flange and a copper pin protruding through the hole is filled with beforehand degassed *Emerson and Cuming Stycast 2850 FT (catalyst 24 LV)* epoxy resin. Tests have shown that feedthroughs of this kind can be leak-tight at room temperature at a level $< 10^{-12}$ mbar·l/s and can withstand more than 50 cycles of being shock-cooled with liquid nitrogen.

For an experiment-scale test, four-pin feedthroughs were used instead of single-pin feedthroughs[1]. Unfortunately, the holes in the available flange had a rather large diameter of 14 mm. It is suspected that a first test feedthrough using simply *Stycast* and four copper pins developed a leak during thermal cycling due to a mismatch between the thermal contractions of *Stycast 2850 FT* and copper: The thermal contraction of *Stycast 2850 FT* from 300 K to 4 K is ~30% larger than the thermal contraction of copper [186]. To compensate this, it was tried to fill the epoxy with SiO_2-powder

---

[1] This was done due to the fact that the flange was readily available, since it had been milled for a third version of the ceramic feedthrough-based flange.

as was done in [186]. Unfortunately, the epoxy became highly viscous then and was impossible to handle.

The next approach was to glue a borosilicate glass body (12 mm diameter cylinder with four 2 mm holes for the pins), having a much lower thermal contraction than copper, into the 14 mm holes. The void between the 2 mm holes and the copper pins was also filled with *Stycast*. It was hoped that the compression of the *Stycast* between the copper flange and the glass body during a cool-down would prevent leaks. While this worked well for a test feedthrough, the flange with 20 four-pin feedthroughs developed several leaks after shock-cooling with LN_2. Small holes at the surface of the *Stycast* indicated that small caves of entrapped air might have imploded during the cool-down, leading to leakage paths in the *Stycast*.

Another approach was to encapsulate the leaking *Kyocera* four-pin feedthroughs in the flange that was used during the experiments presented in Chapter 4 with *Stycast 2850 FT*. This time, to prevent leaks due to caves of entrapped air, the *Stycast* was degassed twice: Once before and once after being poured onto the feedthroughs. While showing no leaks on a 10^{-10} mbar·l/s-scale before the shock-cooling with LN_2, the flange showed a total leak-rate of several 10^{-5} mbar·l/s after being lowered into LN_2. This emphasizes once again, that the *Kyocera* feedthroughs are not suitable for the experimental boundary conditions at PENTATRAP. A reason for the failure of the epoxy might have been, that the flange could not be cleaned beforehand in an ultrasonic bath due to the very fragile edge-welded bellow soldered to it (see Fig. 3.11). Thus small amounts of grease or solder flux might have lead to weak joints between the epoxy and the feedthroughs.

Despite all setbacks with *Stycast*-based feedthroughs, a number of properly working prototypes indicate that it should be possible to find a reliable thermal-shock resistant feedthrough layout. However, for the next setups, cryogenic feedthroughs will be abandoned from the setup completely (see App. C). In case this decision is reverted some time, *Stycast*-based feedthroughs certainly would be worth being investigated further.

Cryogenic feedthroughs at other Penning-trap experiments PENTATRAP is not the only Penning-trap experiment having cryogenic feedthroughs. In Tab. B.1, details about cryogenic feedthroughs and related experimental boundary conditions are given for six different Penning-trap experiments. The following points are particularly remarkable:

- Except for one experiment (g(HCI) Mainz), all experiments solely use single-pin feedthroughs.

- With the exception of the MIT-/FSU-Trap, all experiments have several ten isolated pins. Thus, although none of the experiments needs as many pins as PENTATRAP, the need for 80 pins should not be a major obstacle. The MIT-/FSU-Trap incorporates only one cryogenic feedthrough (the other electrical connections are realized by means of cables running through a direct vacuum connection from room temperature into the cryogenic region).

- Four of the experiments (g(p) Mainz and Harvard, g(HCI) Mainz and $g(e^-/e^+)$ Harvard) have isolation vacuums around the trap vacuum enclosures. Isolation vacuum pressures like the quoted ones, with possibly even lower partial helium pressures, reduce the helium gas flow through potential leaks by nine or more orders of magnitude compared to experiments with a trap vacuum enclosure having direct LHe-contact[2].
- The same four experiments also have cool-down times of many hours. Thus the feedthroughs in these experiments are cooled very slowly and the temperature distributions across the feedthroughs are nearly homogeneous at all times.
- In the THe-Trap apparatus, the feedthroughs have direct contact to LHe. In [187] it was reported that feedthroughs in the original feedthrough flange had developed cold-leaks on at least two occasions. On the other hand, two replacement flanges, prepared in a different manner than the original flange, have proven to work reliable at 4 K.

From this comparison it can be seen, that only the THe-Trap experiment has boundary conditions similar to those at PENTATRAP. Unfortunately, with the current cryogenic insert at PENTATRAP, a feedthrough flange based on the same feedthroughs as used by the THe-Trap experiment is very difficult to realize: The single-pin feedthroughs would require a lot more space than the four-pin feedthroughs. For a future version of the experiment, the design of the cryogenic insert could be modified to make the single-pin feedthroughs fit into the setup. But currently, the most appealing approach is to abandon all feedthroughs from the flange at the top of the cryogenic detection electronics chamber and to guide all cables through a direct vacuum connection between the cryogenic region and room temperature, as it is done at the MIT-/FSU-Trap.

---

[2] For the sake of completeness it must be added that for these four experiments, low helium leak rates are of utmost importance, since the trap vacuum enclosures are not pumped by some pump at room temperature but are solely cryo-pumped.

Table B.1.: Details about cryogenic feedthroughs and related experimental boundary conditions at different Penning-trap experiments.

experiment	feedthroughs	isolation vacuum	cool-down times	references
g(p) Mainz	31 1-kV and 2 2-kV *Kyocera* copper pin - ceramic - copper sleeve	$5 \cdot 10^{-8}$ mbar	>12 h	[121, 188]
g(HCI) Mainz	3 8-pin and 9 single-pin of unknown type	$1 \cdot 10^{-7}$ mbar	several h	[189]
UW-PTMS/ THe-Trap	24 *Ceramaseal* copper pin - ceramic - CuNi sleeve	direct LHe-contact	∼10 min	[183, 187]
MIT-/FSU-Trap	one self-made single-pin Stycast feedthrough	direct LHe-contact	?	[173]
g(p) Harvard	3 5-kV and 51 500-V single pin feedthroughs of unknown type	10^{-6} torr	∼24 h	[190]
$g(e^-/e^+)$ Harvard	41 *Insulator Seal* copper pin - ceramic - CuNi sleeve	10^{-7} torr	∼4 h	[61, 62]

C. Near-future modifications of the cryogenic insert

For the near future, the following modifications of the existing setup, which address the problem of too short storage times caused by vacuum problems (see Sec. 4.2.5), are planned:

- Feedthrough flange: All cryogenic feedthroughs will be abandoned from the flange sitting on top of the detection electronics chamber. Instead, cables for the trap voltages, the amplifier voltages, the Faraday cup signal, RF-excitation signals, amplifier output signals and feedback signals will be guided through direct connections between the cryogenic vacuum and the room temperature vacuum. For these connection copper-capillaries (within the pre-vacuum chamber (see below)) and stainless steel capillaries (above the pre-vacuum chamber) will be used. The capillaries will be connected to the beamline vacuum above the magnet's top flange. The vacuum-to-atmosphere transition of the voltages and signals will be realized by means of commercial room-temperature D-sub vacuum feedthroughs.

- Pre-vacuum chamber: The cryogenic setup will be housed in a pre-vacuum chamber. Thus direct contact of the remaining two cryogenic feedthroughs and the cryogenic seals with LHe is avoided. This will significantly reduce the sensitivity to leaks.

  The chamber will reach from slightly below the top flange of the detection electronics chamber to a flange above to the bronze flange, beneath which the actual trap chamber is located. The wall of the chamber will be made of 0.7 mm thick copper sheet. The chamber will be pumped through two 1/2" *Swagelok* stainless steel tubes. Furthermore it will be cryo-pumped, since it is in direct contact with LHe. Since it is a rather provisional setup to bridge the time until PENTATRAP V2 is ready to be used, the tube will be joined with the holder flanges using *Stycast 2850 FT* epoxy resin (see App. B).

  Main difficulty with this chamber is the limited space in the bore. To obtain an outer diameter $\leq$156 mm over the whole length of the cryogenic insert, the bulky translation and tilt stage has to be removed. But even then, the pre-vacuum chamber will have an outer diameter of 157.5 mm. To lower the setup with the pre-vacuum chamber into the 160 mm-bore will be challenging.

- Pumping barrier: To reduce the gas-flow from the room temperature vacuum region into the cryogenic vacuum region, it is planned to introduce a pumping barrier above the cryogenic drift tube (see Fig. C.1). Besides the reduced gas

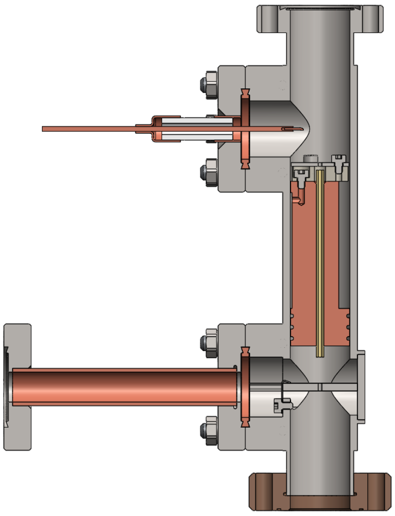

Figure C.1.: A cross-sectional drawing of the pumping barrier that will be placed in the cryogenic region above the drift tube is shown. Besides the pumping barrier itself, it contains a planar Faraday cup with a hole in the middle above the barrier for beam alignment purposes and a pump port that can be pinched off below the barrier.

flow, this will have the benefit of limiting the initial radial amplitudes of trapped ions (see Sec. 4.2.5). The pumping barrier will consist of a gold tube of length 5 cm and inner diameter 1.2 mm soldered into a copper-holder. A planar Faraday cup with a hole of 1 mm diameter in the middle will aid the optimization of the transport. For the pumping of the part below the pumping barrier prior to the cool-down of the experiment, an annealed OFHC copper tube is used. This tube will be pinched off before the setup is lowered into the bore.

- Charcoal absorber: In order to increase the surface for cryogenic pumping, charcoal absorbers have been placed at the bottom of the detection electronics chamber and at the bottom of the trap chamber so far [118]. However, in order to regenerate the charcoal, it has to be heated under vacuum to temperatures $\gtrsim 400$ K [191]. This is possible in neither of the two locations: In the detection electronics chamber, the heating might damage the detectors. In the trap chamber, such high temperatures would lead to an increased interdiffusion between the copper trap electrodes and their gold coating. Being not regenerated, the charcoal significantly prolonged the pumping before the lowering of the setup due to outgassing. For the coming experimental run, the charcoal will be removed from the setup. A rough estimate indicates that the surface of the cryogenic setup should be sufficient for cryogenic pumping of hydrogen over years.

D. Peak tracks

Within this appendix, a few more details on peak tracks will be provided. First of all, unusual features of some of the tracks shown in Fig. 4.19 will be explained. Second, the possibility to fit a model function based on theoretical axial frequency anharmonicity shifts to the peak tracks will be discussed.

Peak track features Some of the peak tracks show the following features:

- The track does not start at scan number one. This is for the following reason: In case a peak does not re-appear in a mass scan (i.e. there is no peak above the peak detection threshold), a few more mass scans are carried out to see whether the peak can be detected again. Thus, if the peak is lost after the first mass scan after the loading and re-appears after n mass scans, the track starts at scan number n.

  That a peak is lost and re-appears after some mass scans usually happens, when the peak height is close to the detection threshold. The re-appearance of the peak is related to the fact, that not only the axial energy defines the peak height, but also the trap anharmonicity: As will be explained in more detail in the next paragraph, the time T_{diss} an ion dissipates energy on top of the resonator not only depends on the voltage ramping speed but also on the axial frequency anharmonicity shift. A reduction of T_{diss} can lead to a reduction of the peak height below the detection threshold. But since the axial frequency anharmonicity shift changes during the cooling of the axial mode, T_{diss} can increase again after further mass scans, and the peak can re-appear again.

- The track shows one or multiple jumps. This indicates a change in the energies of the ions' eigenmotions due to a collision of the ion either with neutral rest-gas atoms or with ions, that were not detected in the mass scan after loading.

Peak track fitting Assuming that the relative axial energy loss per mass scan is constant throughout a peak track, a model function for the peak track can be obtained using the axial frequency anharmonicity shifts $\Delta\nu_z(a_z, a_+, a_-, c_{4,6,8,\ldots})$ (see Sec. 2.2):

$$U_{R,\text{peak}}(n) = \frac{m}{2c_2 q} \left(\nu_0 - \Delta\nu_z(a_{z,0}e^{-n}, a_+, a_-, c_{4,6,8,\ldots})\right)^2 , \tag{D.1}$$

where ν_0 is the resonance frequency of the detector. This function could be fitted to peak tracks, with the free parameters of the fit being the initial axial amplitude $a_{z,0}$, the radial amplitudes a_+ and a_- as well as the anharmonicity coefficients $c_{4,6,8,\ldots}$ (depending on which anharmonicity orders are taken into account). $c_{4,6,8,\ldots}$ would have to be identical for all peak-tracks measured at a certain tuning ratio. By determining the anharmonicity coefficients for several tuning ratios, the trap could be tuned.

Unfortunately, the relative axial energy loss per mass scan is not a constant: The time that an ion is effectively cooled by the resonator not only depends on the voltage ramping speed, but also on the slope of $\Delta\nu_z(a_z)$. If the sign of the slope of $\Delta\nu_z(a_z)$ and the sign of the slope of the ring voltage $U_R(t)$ during the mass scan are the same, the cooling time is effectively shortened, since the change in the anharmonicity shift due to the cooling and the change of the axial frequency due to the voltage change are of equal sign. If on the other hand the two slopes are of opposite sign, the effective cooling time is prolonged.

Due to the unclear assignment of an axial amplitude to a mass scan number, the trap could not be tuned by means of peak track fits.

E. Challenges on the way to ultra-high-precision mass-ratio measurements

In this section, a (by no means complete) list of possible challenges on the way to ultra-high-precision mass-ratio measurements is given. Furthermore proposals are made, how some of them could be mastered. Possible challenges are:

(A) Instabilities of the ratio of magnetic fields between two traps.

(B) Differences in equilibrium position shifts for ions with dissimilar q/m.

(C) Image charge shifts in case of dissimilar ion masses.

(D) At some level of precision, the stability of the already very stable voltage sources might become a limitation.

If the source of (A) are changes of the relative positions between the magnets' coils and the trap tower in an interplay with magnetic field inhomogeneities (see App. A), improving the homogeneity of the magnetic field might become necessary. Possible measures to obtain this are the reduction of magnetic material in the cryogenic setup (e.g. reduction of the amount of stainless steel close to the trap chamber or replacement of diamagnetic copper by a special CuNi-alloy with close to zero magnetic susceptibility [192, 193]), a re-shimming of the magnet and the use of additional compensation coils around the trap chamber.

The improved magnetic field homogeneity would also reduce problems with (B), since it would reduce the magnitude of individual equilibrium position shifts. A further measure concerning (B) is a careful compensation of asymmetries in the electrostatic trapping potential. However, the ultimate solution to this problem would be to perform cyclotron frequency measurements with identical trapping voltages even for ions with dissimilar q/m. A possible implementation of this will be discussed at the end of this section.

A solution to (C) would be to determine cyclotron frequencies not by means of the invariance theorem $\omega_c^2 = \omega_+^2 + \omega_-^2 + \omega_z^2$, but to use the sum-relation $\omega_c = \omega_+ + \omega_-$ instead. In this relation image charge shifts of ν_+ and ν_- cancel each other, as can be seen from Eq. (2.37). Furthermore, the sum-relation is unaffected by electrostatic anharmonicity shifts when magnetron- and cyclotron-amplitudes are equal[1] [116]. In contrast to the invariance theorem, eigenfrequency shifts due a tilt between the trap symmetry axis and the magnetic field or due to an elliptic trap potential do not cancel

---

[1] To which level of precision the two amplitudes can be made equal is difficult to foresee at this point.

in the sum relation Eq. (2.23). However, it is planned to incorporate a cryogenic-piezo-motor based hexapod into the new design of the cryogenic insert, which will allow for an extremely precise alignment of the trap tower with respect to the field [150]. Whether an ellipticity of the potential will prevent using the sum-relation will have to be tested. However, due to the precise and careful manufacturing of the PENTATRAP electrodes, chances are good that ellipticity will not be a limiting factor. Furthermore, the influence will be suppressed by many orders of magnitude when ions are close to each other in q/m (see Eq. (2.23)).

A solution to (D) would be to perform simultaneous eigenfrequency measurements: Both in the invariance theorem and in the sum relation, fluctuations of eigenfrequencies cancel exactly in case the eigenfrequencies are measured simultaneously. In the following, a measurement technique which would allow for a simple implementation of simultaneous eigenfrequency measurements is briefly presented.

A *Ramsey separated oscillatory fields* (SOF) technique was developed at the MIT-Trap to overcome difficulties with equilibrium position shifts [49, 194]. In this technique, an eigenmotion is initially excited by a dipolar pulse, and after some waiting time T during which the phase of the eigenmotion evolves freely, it is excited again by a second identical pulse. The relative phase between the eigenmotion and the second excitation pulse is encoded in the amplitude of the eigenmotion afterwards. If the amplitude is determined for different T, an interference pattern, being a rectified sine at the difference δ of the ion's eigenfrequency ν_i and the excitation frequency ν_exc shows up. From ν_exc and δ, which can be determined from the interference pattern, the eigenfrequency ν_i can be determined.

A huge benefit of the SOF technique is that the phase information is stored in the amplitude. Thus the trapping voltage can be changed after the SOF-excitation pattern without losing the phase information. This allows for instance to apply the SOF-excitation pattern to one of the radial modes at a trapping voltage, at which the ion is not in resonance with the axial detector. Afterwards, the trapping voltage can be changed to bring the ion into resonance with the axial detector, such that the amplitude of the radial mode can be determined by means of sideband coupling. Thus, equilibrium position shifts can be avoided. This could furthermore allow to cool the axial mode to below 100 mK by means of sideband coupling to a cyclotron detector prior to the application of the SOF-excitation pattern for the reduction of systematic eigenfrequency shifts.

Furthermore, the feature that the phase information can be stored for extended periods could enable simultaneous eigenfrequency measurements. One variant would be to apply the SOF-excitation pattern simultaneously to the cyclotron and the magnetron mode and read out the amplitudes one after the other. Then, ν_c could be determined by means of the sum-relation $\nu_c = \nu_+ + \nu_-$. Alternatively, one could apply the SOF-technique for the determination of ν_+ and ν_- as before, and determine ν_z simultaneously, e.g. by dip detection. Then, ν_c could be determined by means of the invariance theorem.

The finally attainable precision by means of this method is difficult to predict, but should certainly be analyzed in detail in the future. One crucial factor will be the stability of the trapping fields, which will limit the maximum waiting time T, for which unambiguous phase-unwrapping (i.e. counting of the number of full interference fringes before the final fringe around time T) is possible [173]. The same holds true for the maximum phase-accumulation time in phase-sensitive detection techniques. This emphasizes the importance of ultra-stable trapping fields at PENTATRAP, even with the possibility to perform simultaneous cyclotron frequency measurements in two traps and the possibility to perform simultaneous eigenfrequency measurements in one trap.

Bibliography

[1] R. Karplus and N. M. Kroll, “Fourth-Order Corrections in Quantum Electrodynamics and the Magnetic Moment of the Electron”, Physical Review **77**, 536–549 (1950).

[2] C. M. Sommerfield, “Magnetic Dipole Moment of the Electron”, Physical Review **107**, 328–329 (1957).

[3] S. H. Koenig, A. G. Prodell, and P. Kusch, “The Anomalous Magnetic Moment of the Electron”, Physical Review **88**, 191–199 (1952).

[4] R. Beringer and M. A. Heald, “Electron Spin Magnetic Moment in Atomic Hydrogen”, Physical Review **95**, 1474–1481 (1954).

[5] J. H. Gardner, “Measurement of the Magnetic Moment of the Proton in Bohr Magnetons”, Physical Review **83**, 996–1004 (1951).

[6] P. Franken and S. Liebes Jr., “Magnetic Moment of the Proton in Bohr Magnetons”, Physical Review **104**, 1197–1998 (1956).

[7] H. G. Dehmelt, “Spin Resonance of Free Electrons Polarized by Exchange Collisions”, Physical Review **109**, 381–385 (1958).

[8] F. M. Penning, “Die Glimmentladung bei niedrigem Druck zwischen koaxialen Zylindern in einem axialen Magnetfeld”, Physica **3**, 873–894 (1936).

[9] J. R. Pierce, *Theory and design of electron beams*, 2nd (D. Nostrand Company, Inc., 1954).

[10] H. G. Dehmelt, *Hans G. Dehmelt - Biographical*, Nobel Media, 1989.

[11] G. Gräff, F. G. Major, R. W. H. Roeder, and G. Werth, “Method for Measuring the Cyclotron and Spin Resonance of Free Electrons”, Physical Review Letters **21**, 340–342 (1968).

[12] B. N. Taylor, W. H. Parker, and D. N. Langenberg, “Determination of e/h, Using Macroscopic Quantum Phase Coherence in Superconductors: Implications for Quantum Electrodynamics and the Fundamental Physical Constant”, Reviews of Modern Physics **41**, 375–496 (1969).

[13] G. Gräff and E. Klempt, “Messung der Zyklotronfrequenz freier Elektronen im Vierpolkäfig”, Zeitschrift für Naturforschung **22 a**, 1960–1962 (1967).

[14] C. B. Richardson, K. B. Jefferts, and H. G. Dehmelt, “Alignment of the H_2^+ Molecular Ion by Selective Photodissociation. II. Experiments on the Radio-Frequency Spectrum”, Physical Review **165**, 80–87 (1968).

[15] H. G. Dehmelt and F. L. Walls, “"Bolometric" Technique for the rf Spectroscopy of Stored Ions”, Physical Review Letters **21**, 127–131 (1968).

[16] F. L. Walls and T. S. Stein, "Observation of the $g-2$ Resonance of a Stored Electron Gas Using a Bolometric Technique", Physical Review Letters **31**, 975–979 (1973).

[17] E. R. Cohen and B. N. Taylor, "The 1973 Least-Squares Adjustment of the Fundamental Constants", Journal of Physical and Chemical Reference Data **2**, 663–734 (1973).

[18] D. Wineland, P. Ekstrom, and H. Dehmelt, "Monoelectron Oscillator", Physical Review Letters **31**, 1279–1282 (1973).

[19] R. S. Van Dyck Jr., D. J. Wineland, P. A. Ekstrom, and H. G. Dehmelt, "High mass resolution with a new variable anharmonicity Penning trap", Applied Physics Letters **28**, 446–448 (1976).

[20] R. Van Dyck Jr., P. Ekstrom, and H. Dehmelt, "Axial, magnetron, cyclotron and spin-cyclotron-beat frequencies measured on single electron almost at rest in free space (geonium)", Nature **262**, 776–777 (1976).

[21] H. G. Dehmelt, "Entropy reduction by motional sideband excitation", Nature **262**, 777 (1976).

[22] R. S. Van Dyck Jr., P. B. Schwinberg, and H. G. Dehmelt, "Precise Measurements of Axial, Magnetron, Cyclotron, and Spin-Cyclotron-Beat Frequencies on an Isolated 1-meV Electron", Physical Review Letters **38**, 310–314 (1977).

[23] G. Gärtner and E. Klempt, "A Direct Determination of the Proton-Electron Mass Ratio", Zeitschrift für Physik A **287**, 1–6 (1978).

[24] G. Gräff, H. Kalinowsky, and J. Traut, "A direct determination of the proton electron mass ratio", Zeitschrift für Physik A **297**, 35–39 (1980).

[25] R. S. Van Dyck Jr. and P. B. Schwinberg, "Preliminary Proton/Electron Mass Ratio using a Compensated Quadring Penning Trap", Physical Review Letters **47**, 395–398 (1981).

[26] R. S. Van Dyck Jr., F. L. Moore, D. L. Farnham, and P. B. Schwinberg, "New measurement of the proton-electron mass ratio", International Journal of Mass Spectrometry and Ion Processes **66**, 327–337 (1985).

[27] P. B. Schwinberg, R. S. Van Dyck Jr., and H. G. Dehmelt, "New Comparison of the Positron and Electron g Factors", Physical Review Letters **47**, 1679–1682 (1981).

[28] L. S. Brown and G. Gabrielse, "Precision spectroscopy of a charged particle in an imperfect Penning trap", Physical Review A **25**, 2423–2425 (1982).

[29] L. S. Brown and G. Gabrielse, "Geonium theory: Physics of a single electron or ion in a Penning trap", Reviews of Modern Physics **58**, 233–311 (1986).

[30] R. S. Van Dyck Jr., P. B. Schwinberg, and H. G. Dehmelt, "New high-precision comparison of electron and positron g factors", Physical Review Letters **59**, 26–29 (1987).

[31] P. J. Mohr and B. N. Taylor, "CODATA recommended values of the fundamental physical constants: 2002", Reviews of Modern Physics **77**, 1–107 (2005).

[32] *The Nobel Prize in Physics 1989*, Nobel Media, 1989.

[33] G. Gabrielse et al., "First Capture of Antiprotons in a Penning Trap: A Kiloelectronvolt Source", Physical Review Letters **57**, 2504–2507 (1986).

[34] G. Bollen et al., "First absolute mass measurements of short-lived isotopes", Hyperfine Interactions **38**, 793–802 (1987).

[35] J. Dilling et al., "The SHIPTRAP project: A capture and storage facility at GSI for heavy radionuclides from SHIP", Hyperfine Interactions **127**, 491–496 (2000).

[36] V. S. Kolhinen et al., "JYFLTRAP: a cylindrical Penning trap for isobaric beam purification at IGISOL", Nuclear Instruments and Methods in Physics Research A **528**, 776–787 (2004).

[37] J. Dilling et al., "Mass measurements on highly charged radioactive ions, a new approach to high precision with TITAN", International Journal of Mass Spectrometry **251**, 198 –203 (2006).

[38] M. Smith et al., "First Penning-Trap Mass Measurement of the Exotic Halo Nucleus ^{11}Li", Physical Review Letters **101**, 202501 (2008).

[39] M. Block, "Direct mass measurements of the heaviest elements with Penning traps", International Journal of Mass Spectrometry **349-350**, 94–101 (2013).

[40] S. Eliseev et al., "Phase-Imaging Ion-Cyclotron-Resonance Measurements for Short-Lived Nuclides", Physical Review Letters **110**, 082501 (2013).

[41] K. Blaum, "High-accuracy mass spectrometry with stored ions", Physics Reports **425**, 1–78 (2006).

[42] C. Gerz, D. Wilsdorf, and G. Werth, "Measurement of the ^{4}He-D$_2$ mass difference", Zeitschrift für Physik D **17**, 119–121 (1990).

[43] R. Jertz et al., "Direct determination of the mass of ^{28}Si as a contribution to a new definition of the kilogram", Physica Scripta **43**, 399–404 (1993).

[44] C. Carlberg et al., "The SMILETRAP facility", Physica Scripta **1995**, 196–202 (1995).

[45] S. A. Eliseev, Y. N. Novikov, and K. Blaum, "Search for resonant enhancement of neutrinoless double-electron capture by high-precision Penning-trap mass spectrometry", Journal of Physics G **39**, 124003 (2012).

[46] D. A. Nesterenko et al., "Direct determination of the atomic mass difference of ^{187}Re and ^{187}Os for neutrino physics and cosmochronology", Physical Review C **90**, 042501(R) (2014).

[47] E. A. Cornell et al., "Single-Ion Cyclotron Resonance Measurement of $M(CO^+)/M(N_2^+)$", Physical Review Letters **63**, 1674–1677 (1989).

[48] R. S. Van Dyck Jr., F. L. Moore, D. L. Farnham, and P. B. Schwinberg, "Mass Ratio Spectroscopy and the Proton's Atomic Mass", in *Frequency standards and metrology* (Springer Berlin Heidelberg, 1989), pp. 349–355.

[49] V. Natarajan, "Penning trap mass spectroscopy at 0.1 ppb", PhD thesis (Massachusetts Institute of Technology, 1993).

[50] E. A. Cornell, K. R. Boyce, D. L. K. Fygenson, and D. E. Pritchard, "Two ions in a Penning trap: Implications for precision mass spectroscopy", Physical Review A **45**, 3049–3059 (1992).

[51] S. R. Rainville, J. K. Thompson, and D. E. Pritchard, "An Ion Balance for Ultra-High-Precision Atomic Mass Measurements", Science **303**, 334–338 (2004).

[52] R. S. Van Dyck Jr., D. L. Farnham, S. L. Zafonte, and P. B. Schwinberg, "Ultrastable superconducting magnet system for a penning trap mass spectrometer", Review of Scientific Instruments **70**, 1665–1671 (1999).

[53] E. G. Myers, "The most precise atomic mass measurements in Penning traps", International Journal of Mass Spectrometry **349-350**, 107–122 (2013).

[54] R. S. Van Dyck Jr., D. B. Pinegar, S. Van Liew, and S. L. Zafonte, "The UW-PTMS: Systematic studies, measurement progress and future improvements", International Journal of Mass Spectrometry **251**, 231–242 (2006).

[55] J. K. Thompson, S. Rainville, and D. E. Pritchard, "Cyclotron frequency shifts arising from polarization forces", Nature **430**, 58–61 (2004).

[56] S. Rainville et al., "A direct test of $E = mc^2$", Nature **438**, 1096–1097 (2005).

[57] B. Odom, D. Hanneke, B. D'Urso, and G. Gabrielse, "New Measurement of the Electron Magnetic Moment Using a One-Electron Quantum Cyclotron", Physical Review Letters **97**, 030801 (2006).

[58] D. Hanneke, S. Fogwell, and G. Gabrielse, "New Measurement of the Electron Magnetic Moment and the Fine Structure Constant", Physical Review Letters **100**, 120801 (2008).

[59] P. J. Mohr, B. N. Taylor, and D. B. Newell, "CODATA recommended values of the fundamental physical constants: 2010", Reviews of Modern Physics **84**, 1527–1605 (2012).

[60] D. Hanneke, S. Fogwell Hoogerheide, and G. Gabrielse, "Cavity control of a single-electron quantum cyclotron: Measuring the electron magnetic moment", Physical Review A **83**, 052122 (2011).

[61] S. Fogwell Hoogerheide, "Trapped Positrons for High-Precision Magnetic Moment Measurements", PhD thesis (Harvard University, 2013).

[62] J. Dorr, "Quantum Jump Spectroscopy of a Single Electron in a New and Improved Apparatus", PhD thesis (Harvard University, 2013).

[63] T. Aoyama, M. Hayakawa, T. Kinoshita, and M. Nio, "Tenth-Order QED Contribution to the Electron $g - 2$ and an Improved Value of the Fine Structure Constant", Physical Review Letters **109**, 111807 (2012).

[64] F. Terranova and G. M. Tino, "Testing the a_μ anomaly in the electron sector through a precise measurement of h/M", Physical Review A **89**, 052118 (2014).

[65] S. Sturm, "The g-factor of the electron bound in ^{28}Si^{13+}: The most stringent test of bound-state quantum electrodynamics", PhD thesis (Johannes Gutenberg-Universität Mainz, 2011).

[66] S. Sturm et al., "g-factor measurement of hydrogenlike ^{28}Si^{13+} as a challenge to QED calculations", Physical Review A **87**, 030501 (2013).

[67] A. Wagner et al., "g Factor of Lithiumlike Silicon ^{28}Si^{11+}", Physical Review Letters **110**, 033003 (2013).

[68] S. Sturm, G. Werth, and K. Blaum, "Electron g-factor determinations in Penning traps", Annalen der Physik **525**, 620–635 (2013).

[69] D. von Lindenfels et al., "Bound electron g-factor measurement by double-resonance spectroscopy on a fine-structure transition", Canadian Journal of Physics **89**, 79–84 (2011).

[70] Y. Fukuda et al., "Evidence for Oscillation of Atmospheric Neutrinos", Physical Review Letters **81**, 1562–1567 (1998).

[71] R. N. Mohapatra et al., "Theory of neutrinos: a white paper", Reports on Progress in Physics **70**, 1757–1867 (2007).

[72] E. A. Cornell, *Eric A. Cornell - Biographical*, Nobel Media, 2001.

[73] E. W. Otten, J. Bonn, and C. Weinheimer, "The Q-value of tritium β-decay and the neutrino mass", International Journal of Mass Spectrometry **251**, 173–178 (2006).

[74] R. S. Van Dyck Jr., D. L. Farnham, and P. B. Schwinberg, "Tritium-helium-3 mass difference using the Penning trap mass spectroscopy", Physical Review Letters **70**, 2888–2891 (1993).

[75] S. Nagy et al., "On the Q-value of the tritium β-decay", Europhysics Letters **74**, 404–410 (2006).

[76] S. Streubel et al., "Toward a more accurate Q value measurement of tritium: status of THe-Trap", Applied Physics B **114**, 137–145 (2014).

[77] F. T. Avignone, S. R. Elliott, and J. Engel, "Double beta decay, Majorana neutrinos, and neutrino mass", Reviews of Modern Physics **80**, 481–516 (2008).

[78] B. J. Mount, M. Redshaw, and E. G. Myers, "Double-β-decay Q values of ^{74}Se and ^{76}Ge", Physical Review C **81**, 032501(R) (2010).

[79] Z. Sujkowski and S. Wycech, "Neutrinoless double electron capture: A tool to search for Majorana neutrinos", Physical Review C **70**, 052501 (2004).

[80] M. Agostini et al., "Results on Neutrinoless Double-β Decay of ^{76}Ge from Phase I of the GERDA Experiment", Physical Review Letters **111**, 122503 (2013).

[81] D. L. Farnham, R. S. Van Dyck Jr., and P. B. Schwinberg, "Determination of the Electron's Atomic Mass and the Proton/Electron Mass Ratio via Penning Trap Mass Spectroscopy", Physical Review Letters **75**, 3598–3601 (1995).

[82] S. Sturm et al., "High-precision measurement of the atomic mass of the electron", Nature **506**, 467–470 (2014).

[83] R. Bouchendira et al., "New Determination of the Fine Structure Constant and Test of the Quantum Electrodynamics", Physical Review Letters **106**, 080801 (2011).

[84] B. J. Mount, M. Redshaw, and E. G. Myers, "Atomic masses of ^{6}Li, ^{23}Na, ^{39,41}K, ^{85,87}Rb and ^{133}Cs", Physical Review A **82**, 042513 (2010).

[85] V. M. Shabaev et al., "g-Factor of Heavy Ions: A New Access to the Fine Structure Constant", Physical Review Letters **96**, 253002 (2006).

[86] A. Einstein, "Ist die Trägheit eines Körpers von seinem Energieinhalt abhängig?", Annalen der Physik **18**, 639–631 (1905).

[87] S. Rainville, "A two-ion balance for high precision mass spectrometry", PhD thesis (Massachusetts Institute of Technology, 2003).

[88] R. Bluhm, V. A. Kostelecky, and N. Russell, "CPT and Lorentz tests in Penning traps", Physical Review D **57**, 3932–3943 (1998).

[89] G. Gabrielse et al., "Precision Mass Spectroscopy of the Antiproton and Proton Using Simultaneously Trapped Particles", Physical Review Letters **82**, 3198–3201 (1999).

[90] G. Gabrielse, "Antiproton mass measurements", International Journal of Mass Spectrometry **251**, 273–280 (2006).

[91] C. Smorra et al., "Towards a high-precision measurement of the antiproton magnetic moment", Hyperfine Interactions, 1–6 (2014).

[92] A. Mooser et al., "Direct high-precision measurement of the magnetic moment of the proton", Nature **509**, 596–599 (2014).

[93] J. DiSciacca et al., "One-Particle Measurement of the Antiproton Magnetic Moment", Physical Review Letters **110**, 130801 (2013).

[94] A. Nucciotti, "The MARE Project", Journal of Low Temperature Physics **151**, 597–602 (2008).

[95] G. Audi et al., "The Nubase2012 evaluation of nuclear properties", Chin. Phys. C **36**, 1157–1286 (2012).

[96] M. Sisti et al., "New limits from the Milano neutrino mass experiment with thermal microcalorimeters", Nuclear Instruments and Methods in Physics Research A **520**, 125–131 (2004).

[97] E. Ferri et al., "Preliminary Results of the MARE Experiment", Journal of Low Temperature Physics **176**, 885–890 (2014).

[98] G. Audi et al., "The Ame2012 atomic mass evaluation", Chinese Physics C **36**, 1287–1602 (2012).

[99] M. R. Gomes et al., "Status of the MARE Experiment", IEEE Transactions on Applied Superconductivity **23**, 2101204 (2013).

[100] A. Nucciotti, *Statistical sensitivity of 163-Ho electron capture neutrino mass experiments*, arXiv:1405.5060v2 [physics.ins-det], 2014.

[101] L. Gastaldo et al., "The Electron Capture ^{163}Ho Experiment ECHo", Journal of Low Temperature Physics **176**, 876–884 (2014).

[102] P. C.-O. Ranitsch, "Development and characterization of metallic magnetic calorimeters for the calorimetric measurement of the electron capture spectrum of ^{163}Ho for the purpose of neutrino mass determination", PhD thesis (Ruprecht-Karls Universität Heidelberg, 2014).

[103] J. Krempel, "A new spectrometer to measure the molar Planck constant", PhD thesis (Ludwig-Maximilians-Universität München, 2010).

[104] M. Wang et al., "The Ame2012 atomic mass evaluation", Chinese Physics C **36**, 1603–2014 (2012).

[105] G. C. Rodrigues et al., "Systematic calculation of total atomic energies of ground state configurations", Atomic Data and Nuclear Data Tables **86**, 117–233 (2004).

[106] V. A. Yerokhin, A. N. Artemyev, and V. M. Shabaev, "QED treatment of electron correlation in Li-like ions", Physical Review A **75**, 062501 (2007).

[107] V. A. Yerokhin and K. Pachucki, "QED treatment of electron correlation in Li-like ions", Physical Review A **81**, 022507 (2010).

[108] A. V. Volotka, D. A. Glazov, G. Plunien, and V. M. Shabaev, "Progress in quantum electrodynamics theory of highly charged ions", Annalen der Physik **525**, 636–646 (2013).

[109] A. Gumberidze et al., "Quantum Electrodynamics in Strong Electric Fields: The Ground-State Lamb Shift in Hydrogenlike Uranium", Physical Review Letters **94**, 223001 (2005).

[110] H. Goldstein, *Classical mechanics*, 2nd (Addison-Wesley Publishing Company, Inc., 1980).

[111] E. A. Cornell, R. M. Weisskoff, K. R. Boyce, and D. E. Pritchard, "Mode coupling in a Penning trap: π pulses and a classical avoided crossing", Physical Review A **41**, 312–315 (1990).

[112] J. Ketter et al., "Classical calculation of relativistic frequency-shifts in an ideal Penning trap", International Journal of Mass Spectrometry **361**, 34–40 (2014).

[113] G. Gabrielse, L. Haarsma, and S. L. Rolston, "Open-endcap Penning traps for high precision experiments", International Journal of Mass Spectrometry and Ion Processes **88**, 319–332 (1989).

[114] G. Gabrielse, "Why Is Sideband Mass Spectrometry Possible with Ions in a Penning Trap?", Physical Review Letters **102**, 172501 (2009).

[115] C. Roux, "High-Resolution Mass Spectrometry: The Trap Design and Detection System of Pentatrap and New Q-Values for Neutrino Studies", PhD thesis (Ruprecht-Karls Universität Heidelberg, 2012).

[116] J. Ketter et al., "First-order perturbative calculation of the frequency-shifts caused by static cylindrically-symmetric electric and magnetic imperfections of a Penning trap", International Journal of Mass Spectrometry **358**, 1–16 (2014).

[117] J. L. Verdú, "Ultrapräzise Messung des elektronischen g-Faktors in wasserstofähnlichem Sauerstoff.", PhD thesis (Johannes Gutenberg-Universität Mainz, 2003).

[118] J. Repp, "The setup of the high-precision Penning trap mass spectrometer PENTATRAP and first production studies of highly charged ions", PhD thesis (Ruprecht-Karls Universität Heidelberg, 2012).

[119] C. Roux et al., "The trap design of PENTATRAP", Applied Physics B **107**, 997–1005 (2012).

[120] K. Blaum et al., "Recent developments at ISOLTRAP: towards a relative mass accuracy of exotic nuclei below 10^{-8}", Journal of Physics B **36**, 921–930 (2003).

[121] S. Ulmer, "First Observation of Spin Flips with a Single Proton Stored in a Cryogenic Penning Trap ", PhD thesis (Ruprecht-Karls Universität Heidelberg, 2011).

[122] M. König et al., "Quadrupole excitation of stored ion motion at the true cyclotron frequency", International Journal of Mass Spectrometry and Ion Processes **142**, 95–116 (1995).

[123] L. Lapidus, "Synchronization and Stochastic Behavior of Electrons in a Penning Trap", PhD thesis (Harvard University, 1998).

[124] J. Tan and G. Gabrielse, "Parametrically pumped electron oscillators", Physical Review A **48**, 3105–3122 (1993).

[125] S. L. Zafonte, "A Determination of the Mass of the Deuteron", PhD thesis (University of Washington, 2012).

[126] S. Ulmer et al., "Direct Measurement of the Free Cyclotron Frequency of a Single Particle in a Penning Trap", Physical Review Letters **107**, 103002 (2011).

[127] M. A. Levine et al., "The Electron Beam Ion Trap: A New Instrument for Atomic Physics Measurements", Physica scripta **T22**, 157–163 (1988).

[128] R. E. Marrs, S. R. Elliott, and D. A. Knapp, "Production and Trapping of Hydrogenlike and Bare Uranium Ions in an Electron Beam Ion Trap", Physical Review Letters **72**, 4082–4085 (1994).

[129] P. Beiersdorfer et al., "X-Ray Emission from Highly Charged Ions Colliding with a Relativistic Electron Beam in the SuperEBIT Electron Beam Ion Trap", AIP Conference Proceedings **652**, 131–140 (2003).

[130] G. Zschornak et al., *DRESDEN ELECTRON BEAM ION SOURCES: LATEST DEVELOPMENTS*, tech. rep. (Technische Universität Dresden and DREEBIT GmbH, 2009).

[131] M. Schmidt, H. Peng, G. Zschornack, and S. Sykora, "A compact electron beam ion source with integrated Wien filter providing mass and charge state separated beams of highly charged ions", Review of Scientific Instruments **80**, 063301 (2009).

[132] *Instruction manual - dresden ebit with wien filter* (DREEBIT GmbH, Dresden, 2010).

[133] H. Koivisto, J. Arje, and M. Nurmia, "Metal ions from the volatile compounds method for the production of metal ion beams", Review of Scientific Instruments **69**, 785–787 (1998).

[134] J. R. Crespo López-Urrutia, A. Dorn, R. Moshammer, and J. Ullrich, "The Freiburg Electron Beam Ion Trap/Source Project FreEBIT", Physica Scripta **T80B**, 502–503 (1999).

[135] H. Bekker, Private communication, 2014.

[136] H. Bekker, "To be submitted", PhD thesis (Ruprecht-Karls Universität Heidelberg, 2015).

[137] S. R. Elliott and R. E. Marrs, "A wire probe as an ion source for an electron beam ion trap", Nuclear Instruments and Methods in Physics Research B **100**, 529–535 (1995).

[138] J. R. Crespo López-Urrutia et al., "Progress at the Heidelberg EBIT", Journal of Physics: Conference Series **2**, 42–51 (2004).

[139] *A1523 A1524 A1526 AG523 AG524 AG526 HV Boards User Manual*, Caen S.p.A. (2013).

[140] *MOD. A 1733 - A 1833 A 1733B - A 1833B 12/28 CHANNEL HV BOARDS MANUAL REV.10l*, Caen S.p.A. (2013).

[141] *http://www.caen.it/csite/*.

[142] A. Rischka, "Aufbau eines Heliumdruck- und Heliumlevel-Stabilisierungssystems und Konstruktion eines kryogenen Faraday-Bechers für PENTATRAP", MA thesis (Ruprecht-Karls Universität Heidelberg, 2014).

[143] M. Redshaw, "Precise Measurements of the Atomic Masses of ^{28}Si, ^{31}P, ^{32}S, ^{84,86}Kr, ^{129,132,136}Xe, and the Dipole Moment of PH^{+} Using Single-Ion and Two-Ion Penning Trap Techniques", PhD thesis (Florida State University, 2007).

[144] C. Böhm, "To be submitted", PhD thesis (Ruprecht-Karls Universität Heidelberg, 2014).

[145] A. Rischka, "Aufbau und Charakterisierung eines Systems zur Stabilisierung des Magnetfeldes an PENTATRAP", Bachelor's thesis (Ruprecht-Karls Universität Heidelberg, 2011).

[146] J. Repp et al., "PENTATRAP: a novel cryogenic multi-Penning-trap experiment for high-precision mass measurements on highly charged ions", Applied Physics B **107**, 983–996 (2012).

[147] G. Gabrielse and J. Tan, "Selfshielding superconducting solenoid systems", Journal of Applied Physics **63**, 5143–5148 (1988).

[148] A. Wagner, "The g-factor of the valence electron bound in lithiumlike silicon $^{28}\mathrm{Si}^{11+}$: The most stringent test of relativistic many-electron calculations in a magnetic field", PhD thesis (Ruprecht-Karls Universität Heidelberg, 2013).

[149] R. Schüssler, "To be submitted", MA thesis (Ruprecht-Karls Universität Heidelberg, 2015).

[150] A. Rischka, "To be submitted", PhD thesis (Ruprecht-Karls Universität Heidelberg, 2017).

[151] J. K. Thompson, "Two-ion control and polarization forces for precise mass comparisons", PhD thesis (Massachusetts Institute of Technology, 2003).

[152] C. Roux, Private communication, 2014.

[153] W. Shockley, "Currents to Conductors Induced by a Moving Point Charge", Journal of Applied Physics **9**, 635–636 (1938).

[154] S. Ramo, "Currents Induced by Electron Motion", Proceedings of the IRE **27**, 584–585 (1939).

[155] S. Stahl, "Aufbau eines Experimentes zur Bestimmung elektronischer g-Faktoren einzelner wasserstoffähnlicher Ionen", PhD thesis (Johannes Gutenberg-Universität Mainz, 1998).

[156] J. B. Johnson, "Thermal Agitation of Electricity in Conductors ", Physical Review **32**, 97–109 (1928).

[157] H. Nyquist, "Thermal Agitation of Electric Charge in Conductors", Physical Review **32**, 110–113 (1928).

[158] D. J. Wineland and H. G. Dehmelt, "Principles of the stored ion calorimeter", Journal of Applied Physics **46**, 919–930 (1975).

[159] H. Häffner, "Präzisionsmessung des magnetischen Moments des Elektrons in wasserstoffähnlichem Kohlenstoff ", PhD thesis (Johannes Gutenberg-Universität Mainz, 2000).

[160] J. L. Verdú et al., "Determination of the g-Factor of Single Hydrogen-Like Ions by Mode Coupling in a Penning Trap", Physica Scripta **T112**, 68–72 (2004).

[161] S. Sturm, A. Wagner, B. Schabinger, and K. Blaum, "Phase-Sensitive Cyclotron Frequency Measurements at Ultralow Energies", Physical Review Letters **107**, 143003 (2011).

[162] A. Mooser, "Der g-Faktor des Protons", PhD thesis (Johannes Gutenberg-Universität Mainz, 2013).

[163] S. Ulmer et al., "The quality factor of a superconducting rf resonator in a magnetic field", Review of Scientific Instruments **80**, 123302 (2009).

[164] P. Horowitz and W. Hill, *The art of electronics*, 2nd (Cambridge University Press, 1989).

[165] S. N. Buckley, P. Agnew, and G. P. Pells, "Cryogenic dielectric properties of sapphire at 2.45 GHz", Journal of Physics D **27**, 2203–2209 (1994).

[166] S. Stahl, *Axialfrequenzverstärker mit integriertem Abwärtsmischer AF-DC-b / AF-DC-c*, Stahl Electronics (2010).

[167] A. Dörr, "Setup, test and optimization of detection electronics for high-precision mass measurements at PENTATRAP", Diploma thesis (Ruprecht-Karls Universität Heidelberg, 2011).

[168] B. D'Urso, B. Odom, and G. Gabrielse, "Feedback Cooling of a One-Electron Oscillator", Physical Review Letters **90**, 043001 (2003).

[169] H. Kracke, "Detection of individual spin transitions of a single proton confined in a cryogenic Penning trap", PhD thesis (Johannes Gutenberg-Universität Mainz, 2012).

[170] C. D. Hökel-Schmöger, "Realisierung des axialen Feedbacks bei PENTATRAP", Diploma thesis (Ruprecht-Karls Universität Heidelberg, 2013).

[171] S. Ulmer et al., "A cryogenic detection system at 28.9 MHZ for the non-destructive observation of a single proton at low particle energy", Nuclear Instruments and Methods in Physics Research A **705**, 55–60 (2013).

[172] K. R. Boyce, "Improved single ion cyclotron resonance mass spectroscopy", PhD thesis (Massachusetts Institute of Technology, 1992).

[173] M. P. Bradley, "A sub-ppb measurement of the mass of cesium for a new determination of the fine-structure constant", PhD thesis (Massachusetts Institute of Technology, 2000).

[174] S. Stahl, *UM 1-14 and UM 1-5b*, Data Sheet, 2011.

[175] T.-C. L. Wang, T. L. Ricca, and A. G. Marshall, "Extension of Dynamic Range in Fourier Transform Ion Cyclotron Resonance Mass Spectrometry via Stored Waveform Inverse Fourier Transform Excitation", Analytical Chemistry **58**, 2935–2938 (1986).

[176] S. Stahl, *BS - Series*, Data Sheet, 2012.

[177] S. Sturm, Private communication, 2013.

[178] T. Busch, Private communication, 2014.

[179] D. Beck et al., "A new control system for ISOLTRAP", Nuclear Instruments and Methods in Physics Research A **527**, 567–579 (2004).

[180] M. Goncharov, "High-precision Penning-trap mass spectrometry at SHIPTRAP and PENTATRAP for neutrino physics research", PhD thesis (Ruprecht-Karls Universität Heidelberg, 2014).

[181] B. M. Penetrante et al., "Evolution of ion-charge-state distributions in an electron-beam ion trap", Physical Review A **43**, 4861–4872 (1991).

[182] W. M. Haynes, ed., *Handbook of chemistry and physics*, 95th (CRC Press, 2014).

[183] M. Höcker, Private communication, 2014.

[184] M. Jung et al., “First observation of bound-state β^- decay”, Physical Review Letters **69**, 2164–2167 (1992).

[185] *www.cryogenics.nist.gov*.

[186] W. O. Hamilton, D. B. Greene, and D. E. Davidson, “Thermal Expansion of Epoxies between 2 and 300 °K”, Review of Scientific Instruments **39**, 645–648 (1968).

[187] C. Diehl, “First mass measurements with the MPIK/UW-PTMS ”, PhD thesis (Ruprecht-Karls Universität Heidelberg, 2011).

[188] S. Kreim, “Direct observation of a single proton in a Penning trap”, PhD thesis (Johannes Gutenberg-Universität Mainz, 2009).

[189] J. Alonso Otamendi, “Development of an Experiment for Ultrahigh-Precicion g-Factor Measurements in a Penning-Trap Setup”, PhD thesis (Johannes Gutenberg-Universität Mainz, 2007).

[190] N. Guise, “Spin-Flip Resolution Achieved with a One-Proton Self-Excited Oscillator”, PhD thesis (Harvard University, 2010).

[191] C. Day, “The use of active carbons as cryosorbent”, Colloids and Surfaces A **187-188**, 187–206 (2001).

[192] S. R. Jefferts, “A compensated penning ion trap mass spectrometer”, PhD thesis (University of Colorado, 1992).

[193] T. P. Heavner et al., “The JILA Penning Trap Mass Spectrometer”, Physica Scripta **1995**, 414–417 (1995).

[194] V. Natarajan, K. R. Boyce, F. DiFilippo, and D. E. Pritchard, “Precision Penning Trap Comparison of Nondoublets: Atomic Masses of H, D and the Neutron”, Physical Review Letters **71**, 1998–2001 (1993).

Danksagung

Zu allererst möchte ich *Klaus Blaum* danken. Klaus, vielen Dank für deine Unterstützung in allen Belangen dieser Arbeit und für dein Vertrauen. Danke für deine herzliche und positive Art und für den Freiraum, den du mir bei meiner Arbeit gelassen hast. Du hast wirklich ein einmaliges Arbeitsumfeld geschaffen.

Herzlichen Dank an *Selim Jochim* für die Bereitschaft als Zweitgutachter zu fungieren.

Vielen Dank an das PENTATRAP-Team *Sergey Eliseev, Christine Böhm, Mikhail Goncharov, Hendrik Bekker, Alexander Rischka und Rima Schüssler* und an die Ex-PENTATRAPper *Julia Repp und Christian Roux.* Gemeinsam haben wir nicht wenige Rückschläge erlebt - trotzdem haben wir das Experiment Stück für Stück vorangebracht. Ich schlage hiermit eine Umbenennung der Gruppe in *Die Unerschütterlichen* vor. Sergey, vielen Dank für's Durchlesen von Kapitel 2 und 3, für zahlreiche Diskussionen und die Einführung an SHIPTRAP. Christine, Danke für deine Hilfe beim Toroidwickeln und gute Unterhaltungen. Mikhail, thanks for all the LabView- and CS-support, even in the final phase of writing your thesis. Hendrik, Danke für deine Infos zur HD-EBIT. Alexander, Danke für den vielen Spaß im Labor und im Büro. Danke für die reibungslose Übernahme vieler Aufgaben als ich mich zunehmend dem Schreiben dieser Arbeit gewidmet habe. Dein Engagement ist wirklich außergewöhnlich. Rima, Danke für deine große Hilfsbereitschaft. Ich hoffe sehr, dass du dem PENTATRAP-Team erhalten bleibst. Julia, vielen Dank für die gute Zusammenarbeit im Labor und deine positive Art, auch bei Rückschlägen. Christian, Danke für eine Vielzahl hilfreicher Diskussionen sowie für lehrreiche Stunden im Labor und am Kickertisch.

Mein Dank gilt auch dem THe-Trap-Team *Jochen Ketter, Sebastian Streubel, Martin Höcker, Marc Schuh* inklusive den Ehemaligen *Tommi Eronen und Marius Tremer.* Jochen und Martin, euch möchte ich besonders für eure Bereitschaft danken, jederzeit über jedes erdenkliche Thema rund um Penningfallen zu diskutieren. Marius, Danke für die angenehme Büroatmospäre. Den Mitgliedern des ALPHATRAP-Teams um *Sven Sturm, Robert Wolf und Andreas Weigel* möchte ich ebenfalls für erhellende Diskussionen danken. Allen anderen aktuellen und früheren Heidelberger Penning-Trappern danke ich für berreichernde Diskussionen und eine angenehme Arbeitsatmospäre. Besonderer Dank auch an *Hendrik Golzke* für jede Menge Spaß im Büro.

Der Austausch mit den verschiedenen Penningfallengruppen außerhalb des MPIK war ein große Bereicherung. Dabei seien besonders die Mitglieder der g-Faktor $p/\bar{p}$ und g-Faktor HCI Experimente in Mainz und am CERN erwähnt. Besonderer Dank gilt dabei *Stefan Ulmer, Anke Wagner und Holger Kracke*, die mit Rat (Stefan) und

Tat (Anke und Holger) zur Seite standen. Den SHIPTRAPpern möchte ich für ihre Gastfreundschaft danken.

Danke an *Stefan Stahl* für interessanten Austausch und außergewöhnlich guten technischen Support.

Ganz besonders möchte ich *Ralf Zilly* für seine tatkräftige Unterstützung danken. Neben deinen handwerklichen Fertigkeiten weiß ich auch deine Expertise in vielen technischen Belangen zu schätzen.

Frau Dücker möchte ich für die Unterstützung in organisatorischen Angelegenheiten danken.

Den Mitarbeitern in den verschiedenen Werkstätten, in der Konstruktion, in der zentralen Elektronik und in sonstigen Infrastruktureinrichtungen möchte ich für eine Vielzahl wichtiger Beiträge zu PENTATRAP und die gute Zusammenarbeit danken.

Meinen Eltern möchte ich für die bedingungslose Unterstützung in allen Belangen während der vergangenen Jahre danken. Danke für euren Glauben an mich. Danke an meine Schwester *Antje*, meinen Freund und Schwager *Fabian* und meine Patentochter *Johanna.* Ihr seid nicht nur Familie, wie man sie sich erhofft, sondern auch wunderbare Freunde. Meinen Schwiegereltern *Juliane, Susanne und Claus* möchte ich für ihre Unterstützung danken - auf euch ist immer Verlass. Danke an meine Großeltern, die fortwährendes Interesse an meiner Arbeit zeigen.

Zu guter Letzt möchte ich meiner Frau *Katharina* und meinem Sohn *Jonathan* danken. Katha, Danke für deine Unterstützung während der vergangenen Jahre. Danke für deine Liebe und dass du immer an mich glaubst. Jonathan, Danke für die Freude, die du in unser Leben gebracht hast. Mit dir zu spielen ist die denkbar beste Ablenkung.

Katha und Jonathan, ihr macht mich glücklich. Euch ist diese Arbeit gewidmet.